Université de Paris-Sud
Centre d'Orsay

THESE

pour obtenir le grade de

DOCTEUR EN SCIENCES

Spécialité: Physique des Solides

présentée par

Francesca CHIODI

Dynamical effects in Superconductor/Normal metal/ Superconductor long Josephson Junctions

Soutenue le 5 juillet 2010 devant la commission d'examen:

Hélène Bouchiat	Co-directrice de thèse
Olivier Buisson	Rapporteur
Frank Hekking	Président
Alfredo Levy Yeyati	
Hugues Pothier	
Bertrand Reulet	Directeur de thèse
Christoph Strunk	Rapporteur

Contents

Résumé

Introduction

L'évolution de l'électronique, dans ses efforts de miniaturisation, a permis la fabrication de dispositifs dont les échelles caractéristiques sont au dessous du micromètre. Cette réduction progressive des dimensions, unie à la possibilité de refroidir les échantillons jusqu'à des températures de l'ordre du mK, a permis de sonder des régimes de la matière dans lesquels la mécanique classique n'est plus valable, et il faut avoir recours à la mécanique quantique.
Le caractère ondulatoire des électrons se manifeste alors, donnant lieu à des phénomènes d'interférence et de diffraction qui modifient fortement le transport électronique. La phase des électrons joue alors un rôle fondamental.
On définit L_φ comme la longueur sur laquelle un électron conserve sa phase. Dès que la taille de l'échantillon L est inférieure à L_φ, les électrons gardent mémoire de leur phase, et l'échantillon est dit cohérent.
L_φ dépend fortement de la température, et en dessous de 1 K elle peut dépasser $1\mu m$. Il est ainsi possible d'observer des phénomènes d'origine quantique, associés normalement à des systèmes de taille atomique, dans des échantillons qu'on peut aisément observer au microscope optique. Ces phénomènes font l'objet de la Physique Mésoscopique.
Dans les supraconducteurs, on observe une cohérence de phase qui, à la différence de la cohérence dont nous avons parlé jusqu'à maintenant, concerne des états à deux électrons, les paires de Cooper. Ces paires sont condensées dans un état quantique cohérent macroscopique, défini par le paramètre d'ordre $\Delta\, e^{i\,\theta}$. Le condensat est caractérisé par une résistance nulle.
Á l'interface entre un supraconducteur et un non-supraconducteur, les paires de Cooper pénètrent dans le matériau non-supracondcuteur sur la longueur de corrélation de paires ξ (dans le Niobium, par exemple, $\xi \sim 40\, nm$).
Une jonction formée par deux électrodes supraconducttrices (S) séparées par une couche isolante (I) d'épaisseur inférieure à ξ, est appelée jonction Josephson, ou jonction SIS. Comme les corrélations supraconductrices s'étendent

d'un contact à l'autre, un courant non-dissipatif peut circuler dans la jonction. En présence d'une différence de phase entre les contacts supraconducteurs, les paires de Cooper traversent par effet tunnel la couche isolante, et portent le supercourant: c'est l'effet Josephson dc.
Une relation très simple relie le supercourant I_J à la différence de phase δ: $I_J = I_c \sin \delta$, où I_c et le supercourant maximum que la jonction peut porter. Dès que la jonction est dans l'état résistif, tant que $eV < \Delta$, la différence de phase δ varie avec le temps: l'effet Josephson ac prédit en fait que $V = \frac{\hbar}{2e}\dot{\delta}$.

Quand on met en contact un métal normal (N) avec un supraconducteur (S), la cohérence de phase électronique dans N interagit avec la cohérence des paires de Cooper dans S.
Les corrélations supraconductrices peuvent alors pénétrer dans le métal normal, sur des longueurs supérieures à ξ, sous la forme de paires d'Andreev, paires cohérentes électron-trou.
Le transport est assuré par les paires d'Andreev, qui se propagent tant que la cohérence dans le métal normal est préservée, c'est à dire sur une longueur $L \lesssim L_\varphi, L_T$. L_T est la longueur thermique, au delà de laquelle l'agitation thermique tue la cohérence.
Quand un fil métallique cohérent ($L << L_\varphi, L_T$) est connecté par deux supraconducteurs, un courant non-dissipatif traverse la jonction en présence d'une différence δ entre les phases des deux électrodes supraconducteurs. Une relation semblable, mais plus compliquée que celle décrite par l'effet Josephson dc, est valable aussi dans ces jonctions. En fait, de la simple relation sinusoïdale des jonctions tunnel, on passe dans les jonctions SNS à la relation anharmonique $I_J = \sum_n I_{c,n} \sin(n\,\delta)$.
Grâce à l'effet de proximité des contacts, le conducteur normal acquiert donc des propriétés supraconductrices. Hormis le supercourant, un minigap, réminiscence du gap supraconducteur, s'ouvre dans sa densité des états. La particularité de ce minigap, beaucoup plus petit que le gap dès que $L > \xi$, est qu'il est fortement dépendant de la phase: à $\delta = 0$, son amplitude est maximale, tandis que à $\delta = \pi$ il se ferme complètement.
Comme nous nous intéressons aux modifications des propriétés du métal normal dues à la supraconductivité de proximité, nous étudions des jonctions longues diffusives, où le fil normal est plus long que ξ. Dans ce régime, les contacts supraconducteurs n'imposent que les conditions aux limites, agissant comme des réservoirs de phase. La densité des états du métal normal devient un quasi-continuum d'états liés, appelés états d'Andreev, formant un minigap.
La physique d'une telle jonction SNS est régie par la diffusion des paires d'Andreev dans N. Par exemple, l'amplitude du minigap $\tilde{\Delta}$ ne dépend que

de la longueur du fil normal L et de la constante de diffusion D dans N: $\tilde{\Delta} = 3.1\, E_{Th}$, où $E_{Th} = \hbar\, D/L^2$ est appelée énergie de Thouless.
Les propriétés dc de l'effet de proximité mésoscopique dans une jonction longue métallique sont pratiquement universelles, dans le sens qu'elles dépendent peu du métal lui-même, mais plutôt de sa géométrie et du régime de transport, diffusif ou balistique.
Ces propriétés sont théoriquement bien comprises: on peut calculer, par exemple, la densité des états du métal normal, la dépendance en température du supercourant, l'influence de la transparence des interfaces NS...
Par contre, la dynamique des jonctions SNS longues est encore loin d'être complètement comprise, même si elle suscite l'intérêt des physiciens depuis les années 60. En fait, par rapport aux jonctions Josephson tunnel, où la seule dynamique présente est celle de la phase, il faut prendre maintenant en compte l'interaction entre la dynamique de la phase supraconductrice et celle des quasiparticules hors équilibre dans le métal normal.

Le but de cette thèse est d'étudier la dynamique des jonctions longues diffusives SNS.
En particulier, nous nous proposons d'identifier les temps caractéristiques de réponse du courant. Nous avons distingué plusieurs temps qui jouent un rôle fondamental dans la dynamique des jonctions longues SNS:

- Temps de diffusion $\tau_D = \frac{D}{L^2}$: il s'agit du temps nécessaire à une paire d'Andreev pour diffuser à travers la partie normale de longueur L.

- Temps électron-phonon τ_{e-ph}: il s'agit du temps inélastique d'interaction électron-phonon. À haute température, c'est le processus inélastique qui contrôle la relaxation de l'énergie du gaz d'électrons. La température électronique tend donc vers la température du bain de phonons avec un temps caractéristique τ_{e-ph}.

- Temps électron-électron τ_{e-e}: il s'agit du temps inélastique d'interaction électron-électron. C'est le temps nécessaire au gaz d'électrons, après une excitation, pour reformer une distribution d'équilibre de Fermi-Dirac.

Le courant Josephson à l'équilibre est la somme des courants i_n portés par chaque niveau d'Andreev d'énergie ϵ_n, ponderés par l'occupation du niveau, p_n. On a donc:

$$I_J(\delta) = \sum_n i_n(\delta)\, p_n(\epsilon_n(\delta)) \tag{1}$$

Si l'on augmente progressivement la fréquence de l'excitation, on s'attend à observer des effets hors-équilibre dès qu'on dépasse les fréquences caractéristiques de la jonction.
En particulier, nous nous attendons à détecter deux temps: le temps de réponse des fonctions de distribution p_n, qui interviennent directement dans l'expression du courant, et le temps de diffusion des paires d'Andreev. En fait, dès que les paires d'Andreev n'ont plus le temps de traverser la partie normale pendant le temps de mesure, les états liés d'Andreev ne sont plus définis et la densité des états devient hors-équilibre; dans ce cas, le courant porté par chaque niveau n'est plus défini, et le courant I_J est affecté.

Pendant ma thèse, après avoir caractérisé le comportement dc des jonctions SNS,

- nous avons observé les effets d'une modulation haute fréquence du courant sur la caractéristique dc tension-courant. En particulier, le courant critique augmente dès que la fréquence de l'excitation est supérieure au taux de diffusion dans la partie normale, tandis que le courant de retrapping est fortement affecté dès que la fréquence de l'excitation dépasse le taux électron-phonon.

- nous avons observé les effets d'une irradiation haute fréquence, comparable à une modulation de tension, sur la caractéristique dc tension courant pour $I > I_c$, quand la jonction est ohmique et la phase varie avec le temps. Nous avons mesuré des paliers de Shapiro entiers et fractionnaires, jusqu'à des énergies supérieures au minigap. La dépendance en champ magnétique des paliers fractionnaires a montré qu'ils sont générés par des effets hors équilibre.

- nous avons observé dans un anneau SNS la réponse haute fréquence du courant à une modulation haute fréquence de la différence de phase δ. Pour des fréquences supérieures au taux de relaxation inélastique, la réponse présente des composantes en-phase (χ') et hors-phase (χ'') qui dépendent de la phase dc et de la fréquence. χ' et χ'' suivent en fréquence une relaxation de Debye caractérisée par un temps du même ordre de grandeur que le temps de diffusion.

Propriétés dc d'une jonction SNS longue

Nous avons commencé par étudier les caractéristiques dc tension-courant de nos jonctions longues SNS, en l'absence de toute excitation.

Nous avons étudié de simples jonctions SNS et des SQUIDs dc, anneaux formés par deux jonctions SNS en parallèle. L'avantage des SQUIDs consiste à pouvoir contrôler la différence de phase δ aux bords des deux jonctions SNS en imposant un flux magnétique dans l'anneau. L'avantage des jonctions, par contre, est leur simplicité: dans un SQUID, le fait que les deux jonctions ne sont jamais exactement identiques complique l'interprétation des résultats.
Nous avons fabriqué les contacts supraconducteurs de nos jonctions avec trois métaux différents: Aluminium (Al), Niobium (Nb) et Tungstène (W). La partie normale de toutes nos jonctions est de l'Or (Au) de grande pureté (99.9999%) avec un contenu d'impuretés magnétique inférieur à 0.1 ppm.
Les jonctions en Al-Au ont été faites par évaporation thermique sous angles; les jonctions en Nb-Au par la gravure, en différentes étapes, d'une bicouche Nb-Au; les jonctions en W-Au par une étape de lithographie et évaporation du fil d'or, suivie par le dépôt de contacts de W en décomposant avec un faisceau d'ions de Gallium focalisés un gaz organométallique de Tungstène.
Cette variété de méthodes de fabrication mène à des interfaces NS très différentes. Malgré cela, les dépendances en température et champs magnétique des caractéristiques dc tension-courant ont pu être interprétées par le même modèle.

Characteristiques dc tension-courant

Nous polarisons nos jonctions en courant, et nous mesurons la tension V aux bornes de l'échantillon.
À basse température, la jonction est supraconductrice par effet de proximité en dessous du courant I_c, appelé courant critique; la tension est donc nulle. À $I = I_c$, la jonction transite brusquement vers un état résistif, dans lequel sa caractéristique est ohmique. Si on diminue le courant de polarisation à partir de l'état résistif (N), la jonction retourne dans l'état supraconducteur (S) seulement au dessous du courant de repiègeage $I_r < I_c$. Nous observons une hystérésis d'amplitude $I_r/I_c \sim 0.15 - 0.4$. Un exemple de la caractéristique V(I) à basse température est montré en figure 1 (a).
À haute température, l'hystérésis disparaît, et les transitions entre les états S et N s'adoucissent. Un exemple de la caractéristique V(I) à haute température est montré en figure 1 (b).

Nous avons examiné plusieurs causes possibles de l'hystérésis à basse température.
D'abord, nous avons supposé une origine thermique. La jonction serait alors intrinsèquement non-hystérétique, mais la valeur du courant critique

dépendrait de l'état de la jonction.
Quand la jonction est supraconductrice, sa résistance est nulle, et la puissance dissipée par effet Joule est nulle aussi. Le courant de transition entre l'état S et l'état N est donc $I_c(T_e) = I_c(T_{ph})$, où T_e est la température électronique, qui coïncide avec la température du bain des phonons T_{ph}.
Dès que la jonction transite dans l'état résistif, elle est chauffée par une puissance $R\,I^2$. La thermalisation des électrons s'opère par émission de phonons. Comme à basse température le couplage électron-phonon n'est pas efficace, la puissance injectée n'est pas complètement évacuée, et la température électronique augmente. La jonction transite donc de N à S au courant $I_c(T_e) < I_c(T_{ph})$, étant donné que $I_c(T)$ diminue exponentiellement avec la température.
Nous avons trouvé un très bon accord entre théorie et expérience en modélisant la puissance de refroidissement des phonons par $P_{ph} = \Sigma' V (T_e^6 - T_{ph}^6)$, où $\Sigma' \sim 5\ 10^{-8} W\,\mu m^{-3} K^{-6}$ et V est le volume du fil normal (voir figure 2). La dépendance de P_{ph} en T_e^6, et la valeur de Σ', sont compatibles avec les prédictions théoriques, mais , étonnamment, n'ont été mesuré qu'une fois par Karvonen et al. [33], alors que d'autres obtiennent une dépendance en T_e^5 [49] [61].

Nous avons ensuite supposé une hystérésis intrinsèque, générée par la dynamique de la phase. Nous nous sommes pour cela inspiré des jonctions SIS.

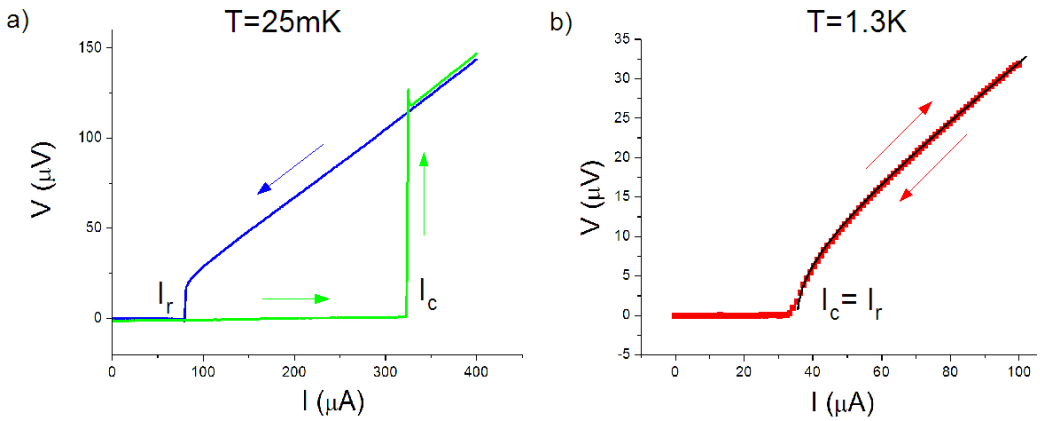

Figure 1: *(a) Characteristique dc tension-courant à T=25 mK: on observe une hystérésis dans la transition, très raide, entre l'état normal et l'état supraconducteur. Les flèches indiquent le sens du courant (b) Characteristique dc tension-courant à T=1.3 K: la transition devient douce, et l'hystérésis disparaît. Le fit décrit la dépendance* $V = R\sqrt{I^2 - I_c^2}$.

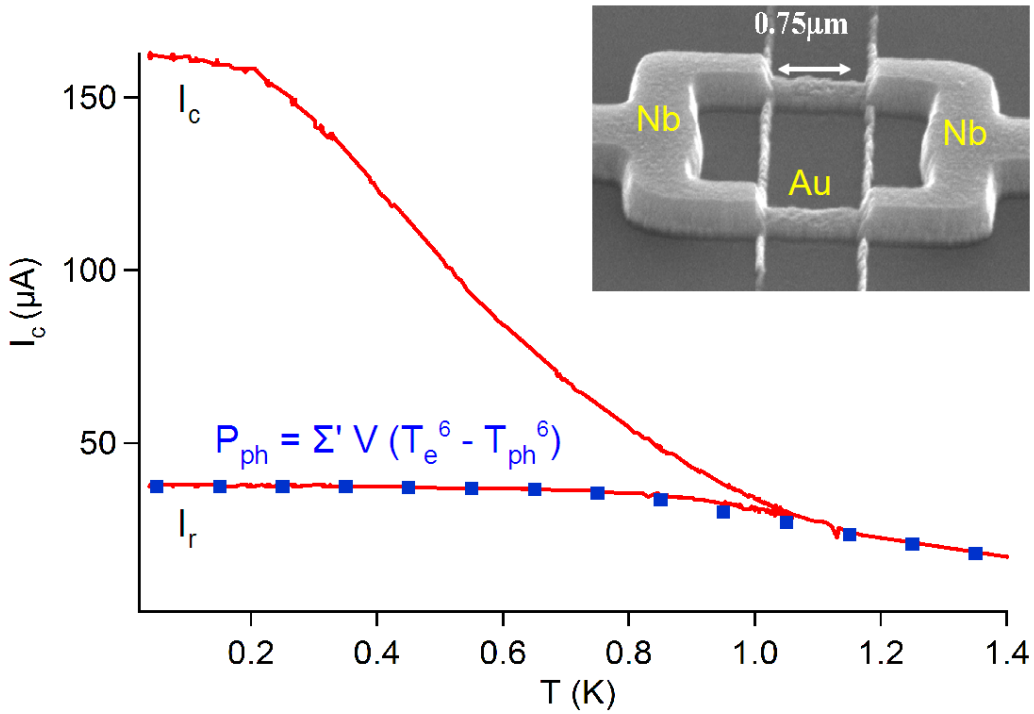

Figure 2: *Dépendance en température du courant critique et du courant de repiègeage pour le SQUID dc Nb-Au dont l'image SEM est montré en inset. Les symboles carrés montrent les prédictions pour I_r en supposant que l'hystérésis est d'origine thermique et que la puissance de refroidissement des phonons suit la loi de puissance $P_{ph} = \Sigma' V (T_e^6 - T_{ph}^6)$, avec $\Sigma' = 5.5\,10^{-8} W\,\mu m^{-3} K^{-6}$.*

Dans une jonction SIS on prédit dans le modèle RCSJ une courbe V(I) hystérétique pour des facteurs de qualité $Q > 1$. Q est défini par $Q = \tau\,\omega_p$, où $\tau = R\,C$ est le temps de relaxation de la phase (R et C sont la résistance et la capacité de la jonction SIS), et ω_p est la fréquence plasma.
Song a montré [54] que l'hystérésis de liens faibles supraconducteurs pouvait être expliquée par la dynamique de la phase si on remplaçait le temps de relaxation RC d'une jonction SIS par le temps de relaxation caractéristique du nouveau système.
Nous avons remplacé le temps RC par le temps de relaxation inélastique de l'énergie τ_{in}, déduite de façon indépendante (voir sec. 3.6). Puisque RC est le temps qu'il faut à la phase pour perdre l'énergie cinétique acquise dans l'état N, et relaxer dans l'état S, de façon analogue, τ_{in} est le temps qu'il faut aux électrons pour perdre l'énergie acquise dans l'état N par collision inélastique et relaxer dans l'état S.

À partir de la relation du modèle RCSJ, $Q = \tau\,\omega_p = (4/\pi)\,(I_c/I_r)$, et des courbes expérimentales $I_c(T)$, $I_r(T)$ et $\tau_{in}(T)$, nous avons déduit une fréquence plasma effective. Nous avons trouvé une fréquence indépendante de la température et proportionnelle au taux de diffusion.
Les deux temps caracteristiques d'une jonction longue SNS sont donc le temps de relaxation inélastique de l'énergie et le temps de diffusion.
Nous avons jusqu'à maintenant supposé la corréspondance entre le temps τ_{in}, déduit expérimentalement, et le temps RC, et nous avons déduit dans le cadre du modèle RCSJ la corréspondance $\omega_p \leftrightarrow \tau_D^{-1}$.
Pour confirmer cette déduction, nous avons ensuite raisonné à l'inverse: en supposant la corréspondance $\omega_p \leftrightarrow \tau_D^{-1}$ nous avons déduit le temps inélastique pour les échantillons où une mesure de τ_{in} n'avait pas été effectuée. Si nos suppositions sont bonnes, on devrait retrouver la dépendance en température du temps électron-électron à $T \lesssim 1\,K$ et du temps électron-phonon à $T \gtrsim 1\,K$.
Nous observons à $T \sim 1\,K$ un taux de relaxation $\tau^{-1} \sim 1.3\ 10^8\ T^{1.5}\,s^{-1}\,K^{-1.5}$, et à plus basse température une saturation progressive, qui pourrait être due à une rélaxation de l'énergie liée aux impuretés magnétiques [45].
Ce résultat pourrait être compatible avec le taux de relaxation inélastique prédit dans un système de taille finie [6], mais des mesures ultérieures sont nécessaires pour avoir une réponse définitive.

Dépendance en température du courant critique

La dépendance en température typique du courant critique est montrée en figure 2. À basse température, nous observons une saturation du courant critique I_c. À haute température, par contre, $I_c(T)$ décroit exponentiellement sur une échelle de température qui correspond au minigap.
Les expressions analytiques obtenues par P. Dubos en ajustant le calcul numérique des équations d'Usadel [18] reproduisent très bien nos dépendances $I_c(T)$. Ces ajustements nous permettent de déduire avec une bonne précision l'énergie de Thouless et la résistance intrinsèque de nos jonctions.
La seule déviation de la théorie est le régime de très basses températures, où nous observons une région de saturation plus large que prévu, et un courant critique inférieur à la valeur attendue. Même en prenant en compte une transmission non parfaite des interfaces, la largeur de la région de saturation reste incomprise. Nous n'avons pas trouvé d'explication satisfaisante à cet effet.

Dépendance en champ magnétique du courant critique

Nous avons mesuré la dépendance du courant critique en fonction d'un champ magnétique appliqué perpendiculairement à l'échantillon.
Nous observons dans les SQUIDs dc deux échelles caracteristiques du champ magnétique: $H = \Phi_0/S$ et $H = \Phi_0/S_J$, où S est la surface de l'anneau et S_J la surface de la partie normale.

À faible champ magnétique, $I_c(H)$ oscille avec une période Φ_0/S. Nous arrivons à décrire complètement la forme et la période des oscillations en utilisant un modèle développé pour des jonctions SIS par C. D. Tesche et V. Lefevre-Seguin, et repris par F. Balestro [55] [38] [4] (voir la figure 3). Nous ne trouvons donc aucune signature de la physique de la partie normale.

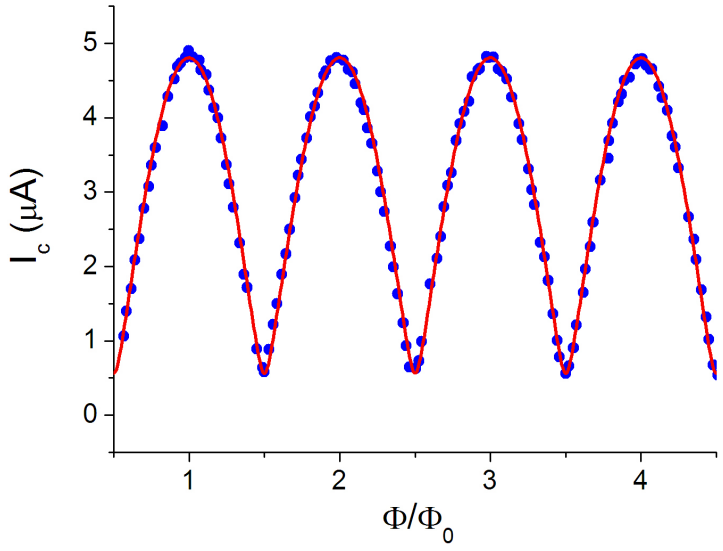

Figure 3: *Dépendance à faible champ magnétique du courant critique d'un SQUID Al-Au en fonction du flux dans l'anneau renormalisé,* $\Phi/\Phi_0 = HS/\Phi_0$. *Le fit (ligne rouge) est la dépendance d'un SQUID SIS de même surface et avec une asymétrie en courant critique entre les deux jonctions.*

À fort champ magnétique, la dépendance des jonctions et des SQUIDs dc s'éloigne de la figure d'interférence de Fraunhofer attendue pour une jonction SIS.
En particulier, nous avons remarqué que la géométrie du fil normal influence grandement les courbes $I_c(H)$: dans les jonctions avec des fils normaux longs et fins, $I_c(H)$ décroit comme une gaussienne, tandis que dans le cas de fils

larges et de rapport d'aspect $L/w \lesssim 1$, $I_c(H)$ ressemble de plus en plus à une figure de Fraunhofer.
Le modèle 1D semiclassique développé par G. Montambaux [41], et les calculs numériques résolvant les équations d'Usadel proposés par J. C. Cuevas [13], reproduisent bien nos expériences.

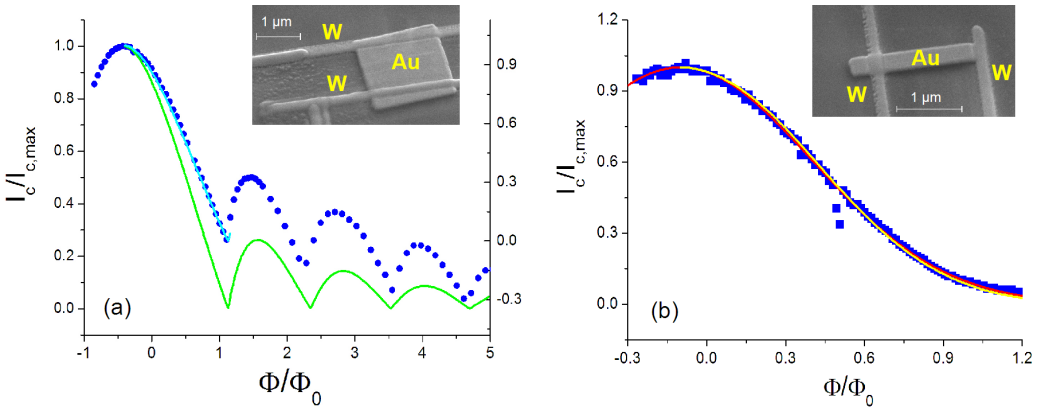

Figure 4: *Courant critique en fonction du flux magnétique dans le fil de métal normal, pour deux jonctions W-Au de géométrie très différente. (a) Dans le cas d'une jonction presque carré de rapport d'aspect $L/w = 0.7$ (image SEM en inset), I_c oscille en rappelant une fonction de Fraunhofer. Le fit vert est donné par la résolution des équations d'Usadel. La ligne bleue est la première période du fit vert à l'échelle des données. (b) Dans le cas d'une jonction longue et fine de rapport d'aspect $L/w = 4.5$ (image SEM en inset), I_c décroit comme une fonction gaussienne. La ligne rouge est une fonction gaussienne, la ligne jaune est donné par la résolution des équations d'Usadel.*

Dans certains échantillons Al-Au, nous avons observé une surprenante réentrance du courant critique à faible champ magnétique ($H \lesssim 45\,G$) et à basse température ($T \lesssim 100\,mK$), montrée en figure 5.
Une possible explication de cette réentrance est donnée par la présence d'un faible contenu en impuretés magnétiques. À faible champ, H aligne les moments magnétiques des impuretés, diminuant ainsi le spin-flip et augmentant la supraconductivité. À fort champ, par contre, l'effet de brisure de paires par le champ magnétique est prédominant.
Cette supposition explique bien l'échelle de température d'apparition de la réentrance et son amplitude, mais l'échelle de champ magnétique prédite est deux ordres de grandeur supérieure à celle observée. De plus, comment échantillons fabriqués en même temps peuvent-ils différer par leur concentration en impuretés magnétiques?
Une deuxième explication possible est que la réentrance soit due à un ef-

fet mésoscopique semblable à la localisation faible. Dans ce cas, l'échelle de champ magnétique prédite est compatible avec les expériences, mais l'amplitude de la réentrance mesurée est 20 fois plus grande que celle attendue.
Nous cherchons encore une explication satisfaisante.

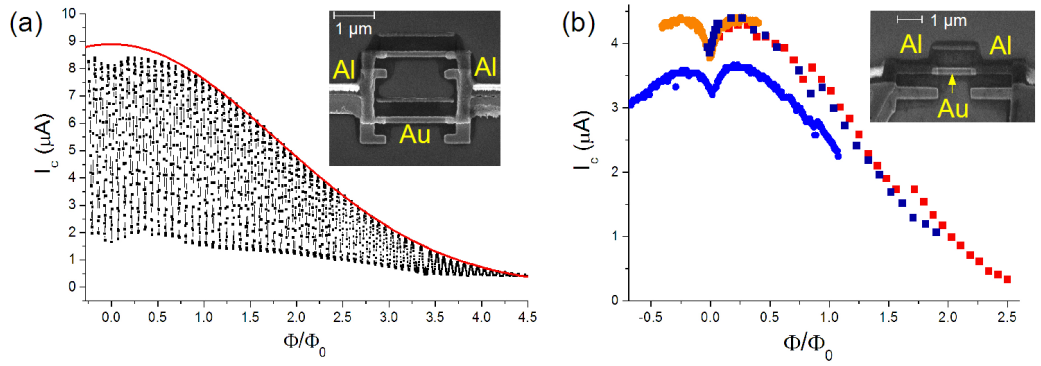

Figure 5: *Courant critique en fonction du flux magnétique dans le fil de métal normal pour un SQUID (a) et trois jonctions (b) Al-Au. On remarque dans tous les cas une réentrance du courant critique à des petits champs. Le fit rouge est une fonction gaussienne.*

Paliers de Shapiro

Nous avons mesuré la caractéristique dc d'une jonction W-Au en présence d'irradiation rf.
Quand une jonction est dans l'état résistif, la différence de phase δ varie avec le temps ($2eV \propto \hbar\dot{\delta} = \hbar\omega_J$). Irradier l'échantillon de micro-ondes revient à moduler la tension V à la fréquence rf. Quand $\omega_J = n\,\omega_{rf}$, une composante dc du courant Josephson apparaît, et des plateaux de courant se forment dans la relation tension-courant: ils s'agit des paliers de Shapiro. Une relation courant-phase $I_J(\delta)$ sinusoïdale génère des paliers à n entier, tandis qu'une $I_J(\delta)$ contenant des harmoniques produit des paliers avec un indice n fractionnaire.
À basse température ($T \sim 150\,mK$), des paliers de Shapiro entiers et fractionnaires sont visibles jusqu'à des tensions plus grandes que l'énergie de Thouless et pour des fréquences d'irradiation plus grandes que le minigap. Donc, dans l'état résistif et très loin de l'état supraconducteur, les électrons sont encore couplés en paires d'Andreev et le courant Josephson est anharmonique.
Nous avons mesuré la dépendance en champ magnétique des paliers entiers

et fractionnaires. Nous avons trouvé que les paliers entiers dépendent du champ comme le palier à n=0, qui est le courant critique. Les pas fractionnaires (n=1/2, n=1/3), par contre, semblent décroitre plus lentement que $I_c(H)$.
Si ces pas fractionnaires étaient dûs à des réflexions d'Andreev multiples à l'équilibre, on s'attendrait à ce qu'ils décroissent plus vite que $I_c(H)$. Comme ce n'est pas le cas, il faut trouver une autre origine aux harmoniques présentes dans la relation courant-phase. Nous croyons que ces harmoniques sont générées par un effet hors équilibre semblable à ceux qu'on observe en réponse à une modulation de phase, mais d'autres expériences sont nécessaires pour le prouver.

Reponse d'une jonction SNS longue à une modulation du courant haute fréquence

Nous avons mesuré la caractéristique dc tension-courant de jonctions longues Nb-Al excitées par un courant ac dont nous avons varié la fréquence entre 100 kHz et 40 GHz.
Les jonctions Nb-Al ont été fabriquées par évaporation sous angles de Niobium (la partie supraconductrice) et d'Aluminium (la partie normale). Le masque suspendu nécessaire à ce type d'évaporation est une résine spéciale formée par le tricouche PMMA-Si_3N_4-PES. Cette résine peut supporter de très hautes températures sans dégazer ses impuretés, et cette condition est fondamentale pour évaporer un métal réfractaire tel que le Nb.
Les jonctions ont été mesurées à des températures entre $1.4\,K$ (au dessus de la température critique de l'Al, $T \sim 1.2\,K$), et la température de l'He^4 liquide, $T \sim 4\,K$. Dans cette gamme de température, la nature supraconductrice de l'Al, qui forme la partie normale de la jonction, ne semble pas affecter qualitativement les résultats, qui sont les mêmes que pour une jonction contenant un vrai métal normal. Quantitativement, par contre, nous observons une augmentation globale du supercourant d'au moins un ordre de grandeur.
Nous observons dans la caractéristique V(I) à basse température, qui est hystérétique, plusieurs régimes en fonction de la fréquence des micro-ondes.

À basse fréquence ($f \lesssim 50\,MHz$), la tension dc suit adiabatiquement la courbe V(I) dc, de courant critique I_c et de courant de repiègeage I_r.
Pour une petite amplitude du courant ac, $2\,I_{ac} < I_c - I_r$, le courant critique

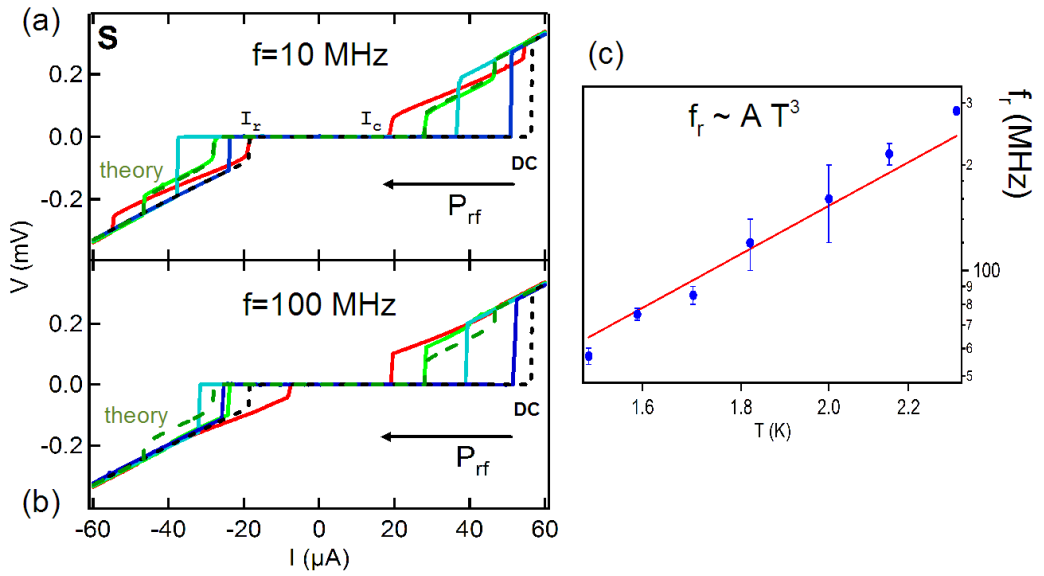

Figure 6: *Caractéristiques tension-courant d'une jonction Nb-Al de longueur* $L = 0.33\,\mu m$ *à (a) f=10 MHz et (b) f=100 MHz pour un courant ac croissant (de la droite vers la gauche). En l'absence d'excitation, la courbe V(I) est donnée par la ligne noire en pointillé. La courbe verte (tirets) correspond à la courbe attendue dans le régime adiabatique. (c) Dépendance en température de la fréquence* f_r*, fréquence seuil au delà de laquelle on sort du régime adiabatique.*

est diminué en $I_c^1 = I_c - I_{ac}$ et le courant de repiègeage est augmenté en $I_r^1 = I_r + I_{ac}$.
Pour une grande amplitude du courant ac, $2\,I_{ac} > I_c - I_r$, deux sauts abrupts de tension sont visibles dans la caractéristique, le premier à $I_c^1 = I_c - I_{ac}$ et le deuxième à $I_c^2 = I_r + I_{ac}$. Entre I_c^1 et I_c^2 la modulation est telle que la jonction oscille entre l'état supraconducteur et l'état résistif. En figure 6 (a) nous montrons la caractéristique dc (en pointillé noir), et les courbes V(I) mesurées pour des valeurs toujours plus grandes de courant ac.
Nos expériences reproduisent exactement les prévisions que nous venons d'exposer. Une comparaison entre la courbe expérimentale verte et la courbe attendue dans le cas adiabatique montre cet excellent accord. La jonction suit donc adiabatiquement l'excitation.

À des fréquences intermédiaires ($50\,MHz < f < 500\,MHz$), le courant de repiègeage est fortement modifié pour des fréquences supérieures à f_r. Sur la caractéristique dc on observe que les deux sauts de tension sont remplacés

continument par un seul saut, à $I_c^1 = I_c - I_{ac}$ (voir la figure 6 (b)).
En mesurant sa dépendance en température, nous avons déduit que la fréquence f_r correspond au taux inélastique électron-phonon τ_{e-ph}^{-1} (voir la figure 6 (c)). Nous mesurons $f_r = 1.9\ 10^7\, T^3\ s^{-1}\, K^{-3}$, en accord avec des expériences précédentes sur des fils d'Al [51].
Cet effet dynamique peut être compris si on suppose que l'hystérésis a, au moins partiellement, une origine thermique. La jonction peut alors transiter de l'état résistif à l'état supraconducteur seulement si la température électronique est assez basse ($I_r = I_c(T_e)$), ce qui nécessite que la puissance Joule soit complètement dissipée dans le substrat par des processus inélastiques. À $T \gtrsim 1\, K$, le processus inélastique prédominant est la collision électron-phonon.
Quand la fréquence est plus grande que le taux électron-phonon, la puissance dissipée par la jonction dans son état résistif n'a plus le temps d'être évacuée. La jonction alors chauffe, et le courant de repiègeage diminue. Le courant ac n'est plus alors suffisant pour cycler entre l'état N et l'état S, et les doubles sauts de tension disparaissent.
Un effet similaire est reproduit par le modèle RCSJ, pour des jonctions SIS de facteur de qualité Q du même ordre que ceux de nos expériences ($Q = 4/\pi\ I_c/I_r \sim 1.5 - 10$), quand la fréquence de modulation ac dépasse $f = 1/RC$. Nous avons donc établi un parallèle entre le temps de relaxation de la phase RC dans une jonction SIS et le temps de relaxation de l'énergie τ_{in} dans une jonction SNS.

À haute fréquence ($f > 5\, GHz$), nous observons une forte augmentation du courant critique sur une large gamme de températures. Le courant de repiègeage, par contre, n'est pas du tout affecté.
Nous montrons en figure 7 l'effet d'une modulation du courant à f=39 GHz sur I_c et I_r. En présence des micro-ondes, I_c est augmenté en I_c^{rf} sur une plage de plus de 2 K.
À $T/E_{Th} \sim 20$, les micro-ondes doublent le courant critique dans les échantillons courts ainsi que dans les longs.
Le courant critique augmente avec la fréquence rf et semble osciller avec la puissance rf (mais nous n'observons qu'une période d'oscillation).
En figure 8 nous montrons le courant critique en fonction de la puissance rf pour des fréquences croissantes.

Le même phénomène avait été vu dans des fils supraconducteurs et des jonctions SIS, pour des fréquences supérieures au taux inélastique, et à des températures très proches de la température critique. L'augmentation du courant critique était dans ce cas due à une augmentation effective du gap

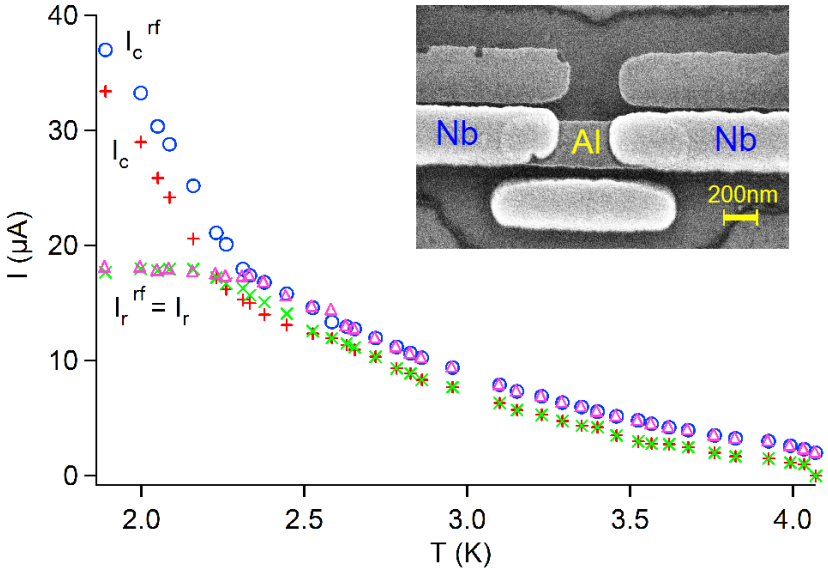

Figure 7: *Dépendance en température du courant critique et du courant de repiègeage d'une jonction Nb-Al de longueur $L = 0.33\,\mu m$, en l'absence de modulation (I_c, I_r), et en présence d'une modulation à fréquence f=39 GHz (I_c^{rf}, I_r^{rf}). Inset: image SEM de l'échantillon mesuré.*

qui se produit lorsque la fréquence de pompage des quasiparticules à basse énergie est plus grande que leur taux de relaxation (voir inset de la figure 8). Dans notre cas, la fréquence caractéristique est 100 fois plus grande que le taux inélastique, et l'augmentation est présente sur une grande gamme de températures.

La fréquence caractéristique f_c pour l'apparition de l'augmentation du courant critique semble liée au taux de diffusion τ_D^{-1}: comme τ_D^{-1}, f_c ne varie pas avec la température et dépend fortement de la longueur du fil normal.

Si on applique un champ magnétique dc, f_c augmente en H^2 pour des températures proches de la température critique de la supraconductivité de proximité, $T_{c,N}$, tandis que pour $T << T_{c,N}$, f_c est non-monotone (voir la figure 9).

Le champs magnétique agit en fait à haute température comme un mécanisme de cassure de paires, avec un taux typique $\tau_H^{-1} \propto H^2$. L'excès de quasiparticules créé par le champ magnétique affaiblit la supraconductivité, et l'augmentation du courant critique est observée seulement si l'excitation est plus rapide que la cassure des paires.

À $T/T_{c,N} = 0.35$, f_c décroit à bas champ, pour augmenter ensuite (voir figure 9). On peut deviner dans ce comportement la compétition entre la cassure

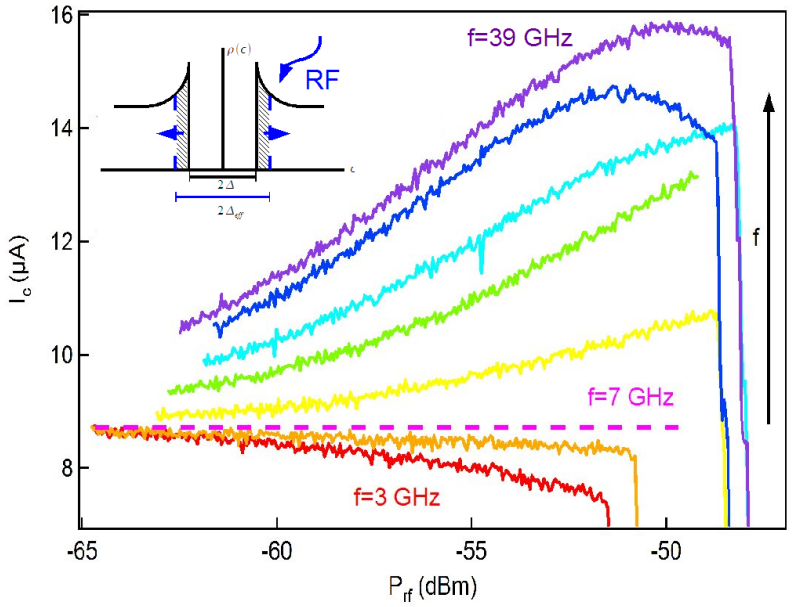

Figure 8: *Courant critique en fonction de la puissance rf d'une jonction Nb-Al de longueur $L = 0.78\,\mu m$ à $T = 1.6\,K$pour des fréquences croissantes entre f=3 GHz et f=39 GHz. Pour $f > 7\,GHz$ le courant critique augmente de façon monotone avec la fréquence.*

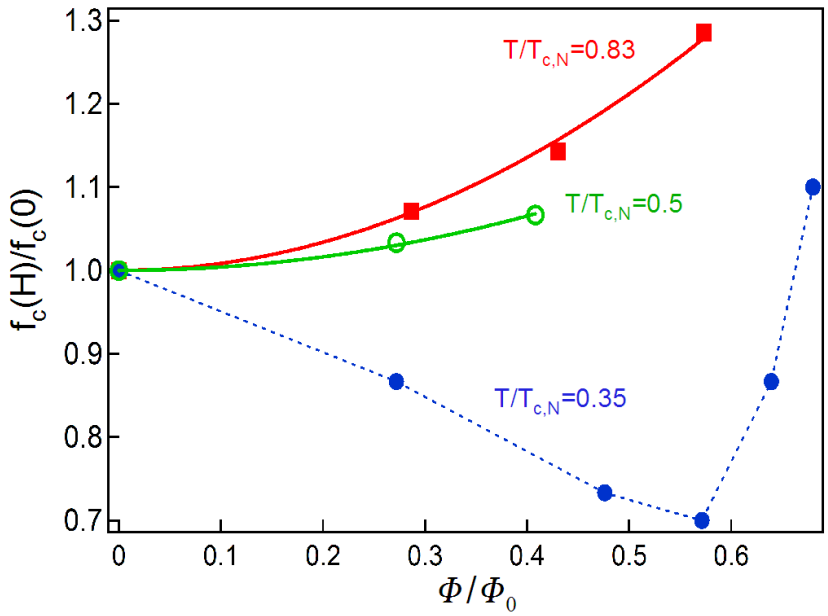

Figure 9: *Fréquence caractéristique pour l'augmentation du courant en fonction du flux magnétique dans la jonction, pour différentes températures.*

de paires à fort champ et la décroissance du minigap en fonction du champ à bas champ.

Réponse d'une jonction longue SNS à une modulation de la phase haute fréquence

Nous avons mesuré la réponse haute fréquence du courant d'une jonction longue W-Au dans une géométrie annulaire.
Nous avons modulé la différence de phase aux bornes du fil normal à haute fréquence ($0.2\,E_{Th} < h\,f < 1.37\,E_{Th}$) et à haute température ($6\,E_{Th} < k_B\,T < 11\,E_{Th}$), et nous avons mesuré les parties du courant en phase et hors phase avec l'excitation.
Pour cela, nous avons couplé inductivement un anneau supraconducteur interrompu par un long fil normal (SQUID ac) à un résonateur multimodal supraconducteur qui opère dans une large gamme de fréquences; nous l'utilisons entre f=365 MHz et f=6 GHz.

Le fil d'or qui constitue la partie normale est fabriqué directement par lithographie et évaporation standard sur le substrat du résonateur. Il est ensuite connecté à une ligne du résonateur en Nb par fils de W, qui sont déposés en décomposant un gaz de Tungstène avec un faisceau d'ions Gallium focalisés (voir la figure 10).
Grâce à l'extrême versatilité du processus de fabrication, il nous a été possible de modifier, après un premier set de mesures, la géométrie de l'anneau, pour l'adapter aux exigences de la mesure, sans par ailleurs toucher à la jonction SNS elle-même.

Le résonateur multimodal supraconducteur génère un flux magnétique haute fréquence dans le SQUID ac autour d'une valeur donnée par un flux dc. Comme le flux dans l'anneau est proportionnel à la différence de phase aux bornes du fil normal, nous modulons ainsi la phase.
Le résonateur est, de plus, un détecteur haute fréquence: en mesurant les variations de la fréquence de résonance et du facteur de qualité du résonateur en fonction de la phase dc, nous pouvons accéder à la réponse en phase et hors phase du courant circulant dans le SQUID.
Grâce au grand facteur de qualité de nos résonateurs, $Q \sim 10^4$, nous arrivons à détecter des variations extrêmement petites: $\delta f/f \sim 10^{-9}$ et $\delta(1/Q) \sim 10^{-10}$. Nous pouvons alors mesurer la réponse d'un seul SQUID ac.

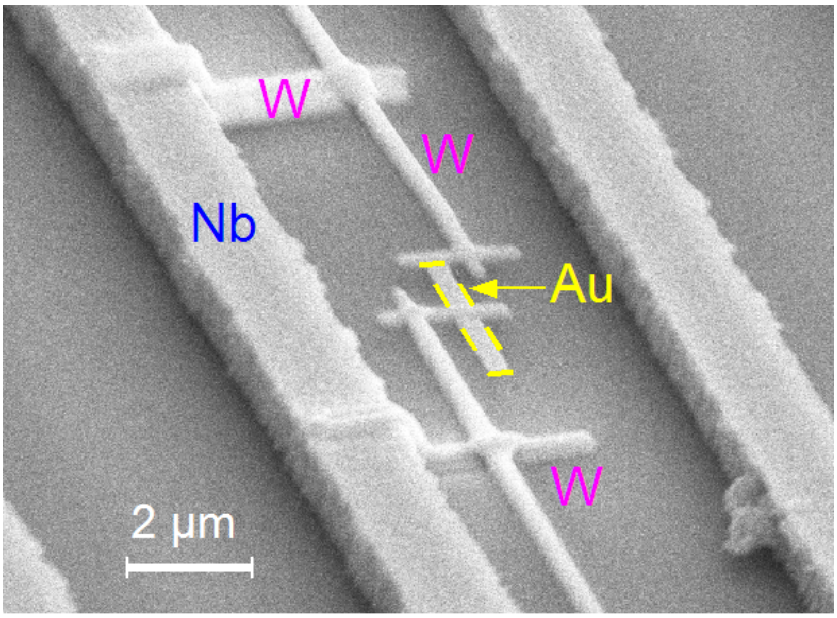

Figure 10: *Image SEM du SQUID ac en W-Au. Le fil d'or, entouré par une ligne jaune en pointillé, est connecté à une ligne du résonateur par fils de W.*

À basse fréquence, on s'attend à ce que le supercourant suive de façon adiabatique l'excitation ac. La réponse sera alors complètement en phase et égale à $\chi'(\omega = 0) = \partial I_J/\partial\Phi \propto I_c\, cos(2\pi\, \Phi/\Phi_0)$.
Quand on dépasse les fréquences caractéristiques de la jonction SNS, la réponse dynamique acquiert une partie dissipative hors phase.
Nous observons, au delà de la réponse en phase χ', une réponse dissipative χ'' plus grande que la réponse en phase elle-même à toutes les températures et fréquences explorées.
Comme la réponse à fréquence nulle, à la fois χ' et χ'' oscillent avec une période Φ_0 à fréquence finie. Mais, dans une gamme de températures où la réponse dc est complètement cosinusoïdale, nous observons à fréquence finie un contenu en harmoniques important (voir la figure 11).

Quand on augmente la température, l'amplitude de χ' décroit exponentiellement, tout comme le courant critique. L'amplitude de χ'', par contre, décroit avec la température deux fois plus vite que χ'.
Quand on augmente la fréquence, l'amplitude des réponses en phase et hors phase, $\delta\chi'$ et $\delta\chi''$ décroit. La figure 12 montre les amplitudes $\delta\chi'$ et $\delta\chi''$ en fonction de la fréquence, à T=0.67 K et T=1K. Dans les deux cas, $\delta\chi'$ décroit plus vite que $\delta\chi''$.
En particulier, $\delta\chi'$ et $\delta\chi''$ correspondent à une relaxation de Debye $\delta\chi =$

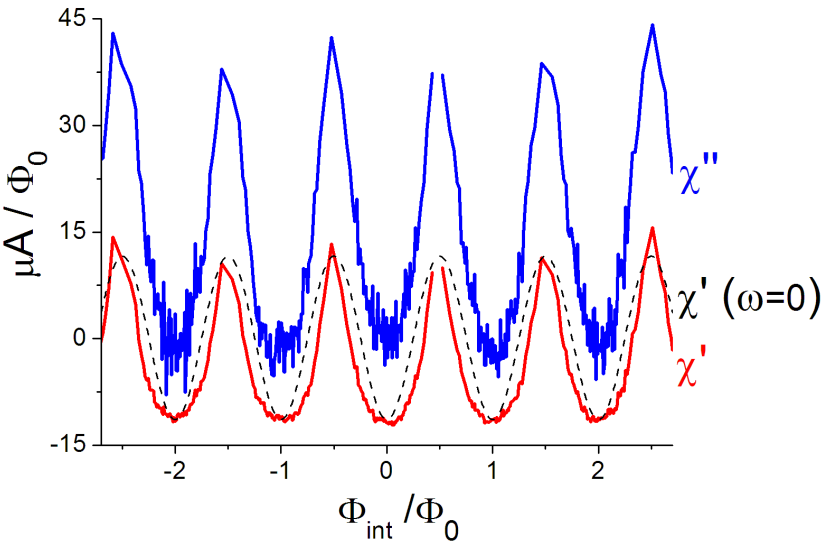

Figure 11: *Réponses en phase (χ') et hors phase (χ'') en fonction du flux dc dans l'anneau Φ_{int} à f=365 MHz et T=0.67 K. Ces réponses à fréquence finie sont comparées à la réponse dc $\chi'(\omega = 0)$, en pointillé.*

$1/(1 + i\omega\,\tau_A)$, caractérisée par un temps de relaxation $\tau_A = 0.6 \pm 0.2\,ns$. Ce temps de relaxation est indépendant de la température, et du même ordre de grandeur que le temps de diffusion: $\tau_A = 7.5\,\tau_D$. On peut donc supposer que nous observons une décroissance de la réponse due à une situation hors-équilibre des niveaux d'Andreev.

Il est possible de calculer l'amplitude et la dépendance en flux des réponses en phase et hors phase à f=365 MHz si on considère la dynamique des populations des niveaux d'Andreev. Ces populations relaxent avec un temps caractéristique correspondant au temps inélastique, que nous estimons être dans notre cas $\tau_{in} = 50\,ns$. Ce temps correspond à une fréquence f=3 MHz. Comme nous travaillons à des fréquences 100 fois plus grandes, nous pouvons considerer que les populations sont complètement gelées.
La réponse du courant, qui s'écrit en général en fonction des populations p_n et des courants i_n du $n^{ième}$ niveau d'Andreev:

$$\chi = \frac{\partial I}{\partial \Phi} = \sum_n \frac{\partial p_n}{\partial \epsilon_n} \frac{1}{1 + i\omega\,\tau_{in}} \frac{\partial \epsilon_n}{\partial \Phi}\, i_n + \sum_n p_n \frac{\partial i_n}{\partial \Phi} \tag{2}$$

se simplifie pour $\omega >> \tau_{in}^{-1}$:

$$\chi = \sum_n p_n \frac{\partial i_n}{\partial \Phi} \tag{3}$$

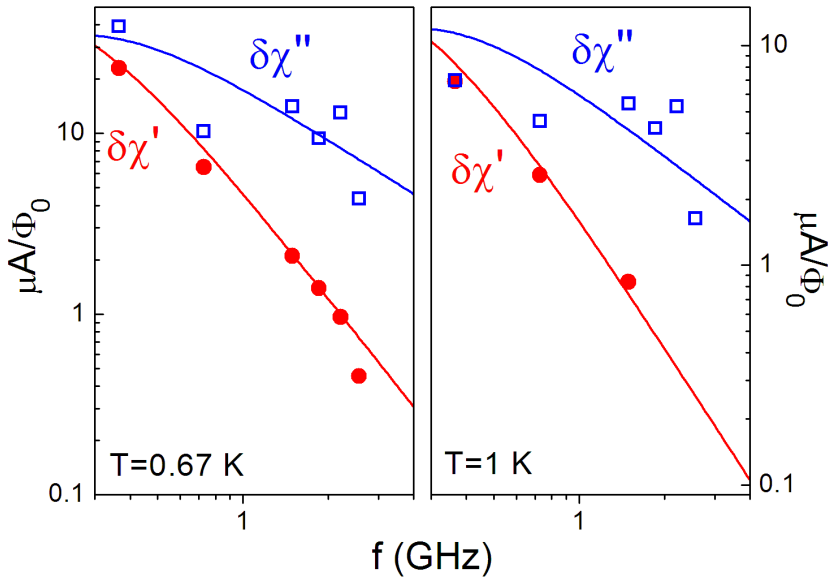

Figure 12: *Amplitude de la réponse en phase $\delta\chi'$ et hors phase $\delta\chi''$ en fonction de la fréquence à T=0.67 K et T=1K. Les expériences sont comparées aux parties en phase et hors phase d'une relaxation de Debye, $1/(1+\omega^2\tau_A^2)$ et $\omega\tau_A/(1+\omega^2\tau_A^2)$, avec $\tau_A = 0.6 \pm 0.2\, ns$.*

Nous ajoutons à cela la rélaxation observée en figure 12:

$$\chi = \left[\sum_n p_n \frac{\partial i_n}{\partial \Phi}\right] \frac{1}{1+i\omega\tau_A} \tag{4}$$

Cette expression a été calculée par P. Virtanen et T. T. Heikkilä; leurs résultats pour la réponse en phase sont comparés à nos mesures en figure 13. On peut voir qu'on obtient un accord excellent entre la forme et l'amplitude des courbes expérimentales et théoriques.

Abandonnant le régime de réponse linéaire, nous avons augmenté la puissance rf et mesuré la réponse hors-équilibre du courant.
Les effets non-linéaires apparaissent au dessus de la puissance critique P_c, qui varie en fonction de la température et de la fréquence. En particulier, aux fréquences et températures les plus hautes, il est difficile d'atteindre le régime de réponse linéaire.
Dans ce régime, la réponse dissipative, proportionnelle à $\delta(1/Q)$, augmente grandement en correspondance des multiples impairs de $\Phi_0/2$. C'est justement pour ces valeurs de flux que le minigap se ferme complètement, ce qui fait que la moindre excitation peut transférer des quasiparticules à la

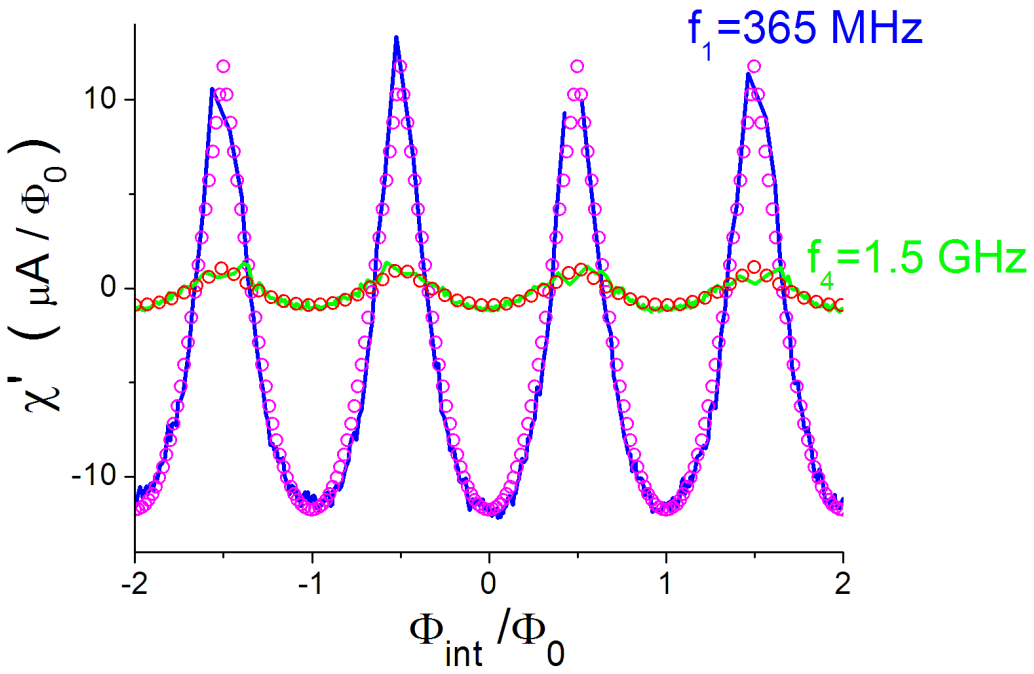

Figure 13: *Comparaison des expériences et de la théorie pour la réponse en phase à f=365 MHz et f=1.5 GHz et à T=0.67 K.*

bande de conduction, augmentant ainsi la dissipation. Quand on augmente la puissance rf, les pics de dissipation deviennent des plateaux de largeur grandissante (voir la figure droite de 14). La réponse en phase, proportionnelle à $-2\delta f/f$, est aussi modifiée en correspondance des multiples impaires de $\Phi_0/2$, avec l'apparition de pics négatifs. Le comportement observé rappelle la relation dc courant-phase mesurée sous irradiation de micro-ondes par C. Strunk: une deuxième harmonique importante apparaît en fait à des multiples impair de $\Phi_0/2$ [25].

Conclusions

Nous avons exploré les propriétés dynamiques de jonctions longues Supraconducteur-Métal normal-Supraconducteur.
Nous avons utilisé une ample gamme d'échantillons, dont nous avons variés les matériaux composant les contacts supraconducteurs, la longueur et la géométrie des fils normaux, et le type d'interfaces.
Nous avons imposé une excitation à haute fréquence de différentes façons:

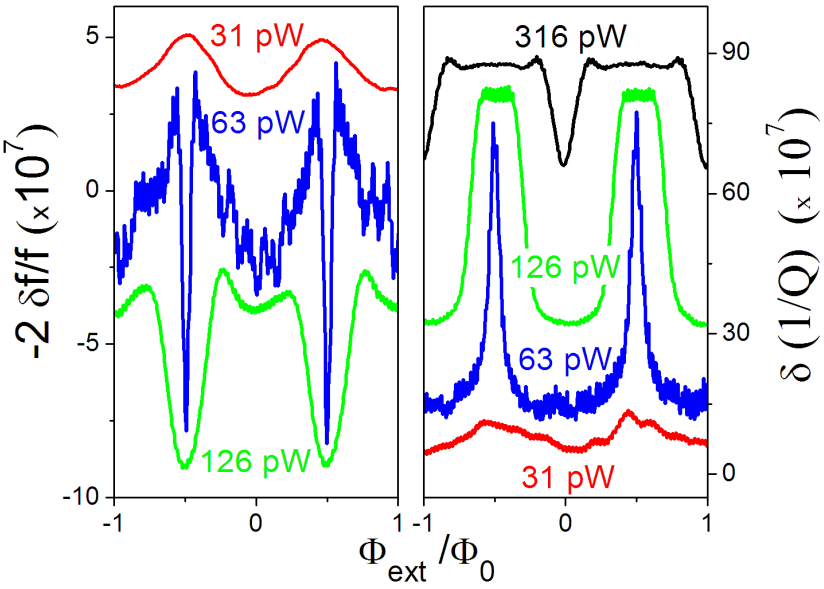

Figure 14: *Réponse en phase, proportionnelle à* $-2\delta f/f$*, et réponse hors phase, proportionnelle à* $\delta(1/Q)$*, dans le régime non-linéaire pour des puissances rf croissantes.*

par le biais d'une antenne couplée faiblement à l'échantillon, en modulant le courant ou en modulant la différence de phase aux bords de la jonction normale. Nous avons exploré aussi bien le régime de réponse linéaire que le régime fortement hors-équilibre.
Le but de ces expériences est de repérer les mécanismes qui contrôlent la dynamique dans une jonction longue supraconducteur-normal, où la physique de la partie normale a une importance fondamentale. En particulier, nous nous attendons à voir de forts changements dans la caractéristique dc tension-courant, ou dans la réponse haute fréquence de la jonction, quand la fréquence de l'excitation dépasse une des fréquences caractéristiques de la jonction SNS. Nous avons idintifié deux temps caractéristiques: le temps de relaxation inélastique de l'énergie τ_{in} et le temps de diffusion τ_D à travers la partie normale de la jonction.
Ces deux temps régissent les transitions entre l'état supraconducteur et l'état résistif de la jonction et la réponse du courant à haute fréquence.

Chapter 1

Introduction

In a classical BCS superconductor, electrons with opposite spins form coherent pairs, called Cooper pairs. These pairs condense in a macroscopic quantum state, described by a wave function $|\psi| e^{i\theta}$. The condensate is characterised by a zero electrical resistance.
The superconducting correlations extend over a length ξ, the pair correlation length ($\xi \sim 40\, nm$ in clean niobium).
When two superconductors are separated by an insulating layer a few $\mathring{A}$ thick, the superconducting wave functions of the two contacts overlap. Cooper pairs can then tunnel from one contact to the other when a macroscopic phase difference between the two superconductors is present. This non-dissipative current of Cooper pairs is called supercurrent.
If, instead, we separate the two superconducting contacts by a normal metal wire longer than ξ, in which no attractive potential is present, we would expect the superconductivity to exist only at the NS interfaces.
However, surprisingly, the superconducting correlations manage to propagate in the normal wire [44] [11] by means of the Andreev pairs. Andreev pairs are electron-hole coherent pairs, created by a coherent quasiparticle reflexion at the NS interface. Indeed, an electron colliding with the NS interface is retro-reflected in a hole whose phase depends on the incident electron phase and on the superconductor phase. In this way, the information about the phase of a superconducting contact is carried along the normal metal to the other superconducting contact. This is evidently possible only as long as the Andreev pair remains coherent. Two conditions are then imposed to the length L of the normal metal:

- $L < L_\varphi$: the normal metal has to be shorter than the phase coherence length L_φ, length over which the electron and the hole lose individually the memory of their phase ($L_\varphi \gtrsim 1\, \mu m$ at $T < 1\, K$).

- $L < L_T$: the normal metal has to be shorter than the thermal length L_T, length over which the electron and the hole composing an Andreev pair are dephased by the thermal energy.
  In fact, the electron and the hole have an energy difference of $2\epsilon \sim k_B\,T$ which gives a phase difference $\frac{2\epsilon}{\hbar}\,t$. The thermal length correspond to the time for a 2π dephasing: $L_T = \sqrt{D\,t} \sim \sqrt{\hbar\,D/k_B\,T}$.

A long Superconductor- Normal metal - Superconductor (SNS) junction is similar, but much more complicated and interesting than a Superconductor - Insulator - Superconductor (SIS) junction.
In both systems, the presence of the superconducting contacts generates a phase dependent, non-dissipative current in the absence of a voltage. But in a SNS junction, the interplay between the superconducting correlations introduced in the normal metal, and the properties of the normal metal itself, more and more important when increasing the wire's length, create a new hybrid system.
Despite the large amount of work devoted to SNS junctions, starting from the pioneering work of J. Clarke [9], their dynamics is still an open issue. What are the relevant times in a SNS junction? In this thesis we try to identify the times that control the current response of an SNS junction, and probe the junction behavior at frequencies larger than the inverse of the characteristic times.

1.1 Josephson Junctions

A Josephson junction is a Superconductor-Insulator-Superconductor tunnel junction.
As we have seen above, the two superconducting states are coupled through the tunneling of Cooper pairs. A supercurrent flows, in the absence of a voltage, when a phase difference is applied across the junction.
Josephson was the first to predict the existence of a supercurrent in an SIS junction, and to deduce how the supercurrent and the dc voltage across the junction are related to the macroscopic phases of the superconducting contacts [32].

1.1.1 DC Josephson effect

Let's define $\psi_1 = |\psi_1|\,e^{i\,\theta_1}$ and $\psi_2 = |\psi_2|\,e^{i\,\theta_2}$ as the complex wave functions of the contacts superconducting states. Because of the system symmetries,

one expects the junction energy to be proportional to $\psi_1 \times \psi_2$, and symmetric in ψ_1 and ψ_2. The simplest general expression is [39]:

$$E \propto \int dy\, dz \left[|\psi_1\, \psi_2| - \frac{1}{2} \left(\psi_1 \psi_2^* + \psi_1^* \psi_2 \right) \right] = \int dy\, dz \left[|\psi_1\, \psi_2| (1 - \cos(\theta_1 - \theta_2)) \right] \tag{1.1}$$

where the junction SI interface is on the $y - z$ plane.
$\theta_1 - \theta_2 = \delta$ is the phase difference between the two superconductors and plays a crucial role in the physics of the Josephson junctions.
The supercurrent density j_s is the derivative of the energy density ϵ with respect to the phase δ:

$$j_s \propto \frac{\partial \epsilon}{\partial \delta} = j_c \, \sin(\delta) \tag{1.2}$$

Integrating over the junction surface we obtain the first Josephson relation, relating the supercurrent I_s to the phase difference across the junction:

$$I_s = I_c \, \sin(\delta) \tag{1.3}$$

where I_c is the critical current, the maximum of the supercurrent.

1.1.2 AC Josephson effect

A voltage across the junction leads to a difference in the chemical potentials at the junction sides:

$$\mu_2 - \mu_1 = -2\,|e|\,V \tag{1.4}$$

Because of the temporal dependence of the wave functions:

$$\psi \propto e^{-i\,\mu\,t/\hbar} \tag{1.5}$$

the phase difference between the superconductors evolves in time:

$$\delta = \frac{-(\mu_2 - \mu_1)\, t}{\hbar} = \frac{2\,|e|V}{\hbar} t \tag{1.6}$$

We derive thus the second Josephson relation:

$$\dot{\delta} = \frac{2\,|e|V}{\hbar} \tag{1.7}$$

Imposing a constant voltage across the junction leads then to a harmonic oscillation of the supercurrent:

$$I_s = I_c \, \sin(\delta_0 + \frac{2\,|e|V}{\hbar} t) \tag{1.8}$$

And, reversing the second Josephson relation, a phase varying in time generates a voltage across the junction.

1.1.3 SQUID

The DC and AC Josephson effects relate the supercurrent and the voltage of an SIS junction to the superconducting phase difference across the junction. But how can one directly control the phase? This is possible in a SQUID geometry.
An AC SQUID is a Superconducting QUantum Interference Device consisting of a superconducting ring interrupted by a SIS junction. When applying a magnetic field, the phase across the junction is proportional to the magnetic flux Φ through the ring (see appendix A):

$$\delta = -2\,\pi\,\frac{\Phi}{\Phi_0} \tag{1.9}$$

where $\Phi_0 = h/(2\,e)$ is the superconducting quantum flux.
The supercurrent in the SQUID is then diamagnetic at low flux:

$$I_s = -\,I_c\,\sin\left(2\,\pi\,\frac{\Phi}{\Phi_0}\right) \tag{1.10}$$

1.2 Hybrid Superconducting - Normal metal long junction

Hybrid Superconducting-Normal metal-Superconducting junctions consist in a non-superconducting metallic wire of length L confined between two superconducting electrodes.
In a long SNS junction, the length of the normal metal wire is greater than the superconducting coherence length in the normal metal, $\xi_N = \sqrt{\hbar\,D/\Delta}$, where D is the diffusion coefficient of the normal metal (for a Nb-Au junction $\xi_N \sim 77\,nm$).
A supercurrent, carried by the coherent electron-hole Andreev pairs, can nevertheless run through the normal metal.
In the case of a diffusive metal ($L >> l_e$, where l_e is the mean free path), the Andreev pairs diffuse across the normal wire in a time of the order of:

$$\tau_D = \frac{L^2}{D} \tag{1.11}$$

The energy associated to the diffusion time in N is the Thouless energy:

$$E_{Th} = \frac{\hbar}{\tau_D} = \frac{\hbar\,D}{L^2} \tag{1.12}$$

E_{Th} is determined exclusively by the normal metal properties, and is independent of the superconducting gap.
In long SNS junctions ($L >> \xi_N$ or $E_{Th} << \Delta$), the characteristic energy is the Thouless energy, while for short SNS junctions ($L << \xi_N$ or $E_{Th} >> \Delta$), the characteristic energy is the superconducting gap Δ.

1.2.1 Andreev reflexions

We now describe in more detail the Andreev reflexions, the mechanism that permits the coherent transfer of a Cooper pair in a normal metal (see Fig. 1.1).
Let's begin by studying what happens to a quasiparticle in a normal metal

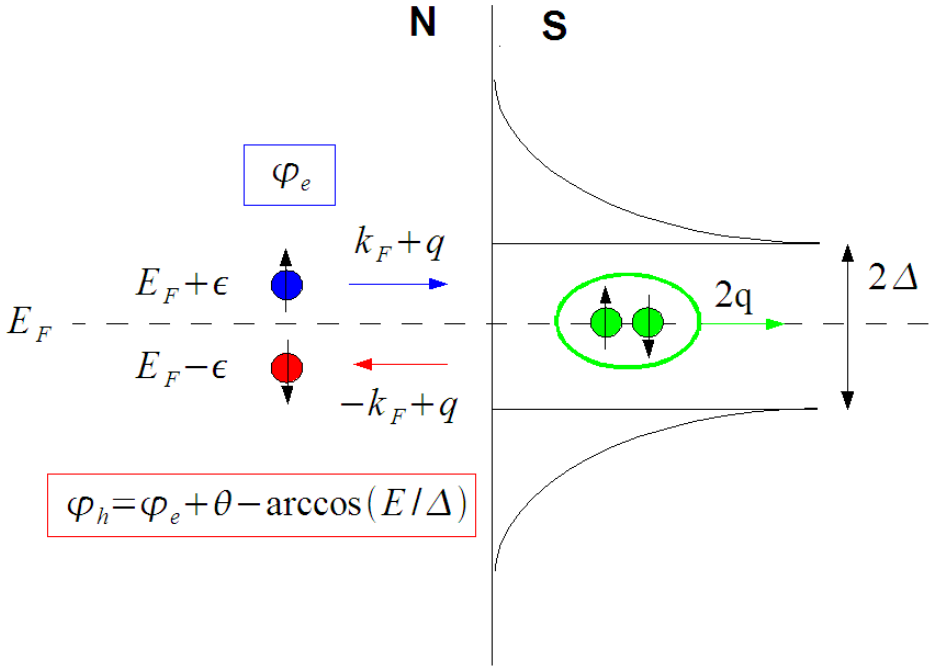

Figure 1.1: *Schematic view of an Andreev reflexion at the NS interface.*

when it hits the NS interface.
Below the superconductor critical temperature T_c, and for low voltages V across the junction, the thermal energy $k_B T$ and the potential energy $e V$ are smaller than the superconducting gap. Thus, an electron with $E - E_F << \Delta$ cannot pass into the superconducting contact, since there are no quasiparticle states at the Fermi level and the electron doesn't have enough energy to access a quasiparticle state above the gap.

The electron is then reflected with a probability equal to one. Moreover, only the reflexion in a hole is possible, the classical reflection of a electron being suppressed at the NS interface.
A normally incident electron, of energy $\epsilon_e = E_F + \epsilon$, wave vector $k_e = k_F + q$ and phase φ_e is thus reflected in a hole, of energy $\epsilon_h = E_F - \epsilon$, wave vector $k_h = -k_F + q$ and phase $\varphi_h = \varphi_e + \theta - \arccos(\epsilon/\Delta) \sim \varphi_e + \theta - \pi/2$. The reflected hole phase depends then on the superconductor phase θ! In a similar way, a hole is coherently reflected in an electron.
The charge transferred into the superconductor is the Cooper pair charge $2\,e$. More precisely, the two electrons enter as evanescent waves in the superconductor and condense within the superconducting coherence length.

If we add a second SN interface, we form a SNS junction.
The hole produced by the reflexion at the first NS interface can then be reflected in an electron at the second interface, closing the cycle. If the length of the normal part is small enough to insure coherence along the whole path, a Cooper pair is transferred coherently from one superconducting contact to the other, and a non-dissipative current flows into the normal wire.

In a long ballistic 1D SNS junction, an electron, starting from a contact, reflected as a hole at the second superconducting contact and coming back to the first one, is dephased of:

$$(k_e - k_h)\,L - 2\,\arccos(\epsilon/\Delta) + \theta_1 - \theta_2 = 2\,\pi\,n \tag{1.13}$$

where the two contacts are made by the same superconductor. This leads to the following excitation spectrum (see Fig. 1.2 (a)):

$$\epsilon = \frac{h\,v_F}{2\,L_N}\left[n \pm \frac{\theta_1 - \theta_2}{2\pi} + \frac{1}{\pi}\arccos\left(\frac{\epsilon}{\Delta}\right)\right] \tag{1.14}$$

The non-dissipative current is given by $I_s \propto \partial\epsilon/\partial(\theta_2 - \theta_1)$, where ϵ is the energy of the eigenstate. This energy differs from the energy of the excited states, since it takes into account the whole spectrum, including the levels above the minigap. The resulting supercurrent is shown in Fig. 1.2 (b) [7]. The jumps of the current at the odd multiples of π smoothes out when introducing the disorder or when increasing the temperature, so that finally the current-phase relation looses some anharmonicity and approaches that of a SIS junction.

Let's now consider long diffusive SNS junctions.
The Andreev bound states spectrum [50] is a quasi-continuum of phase

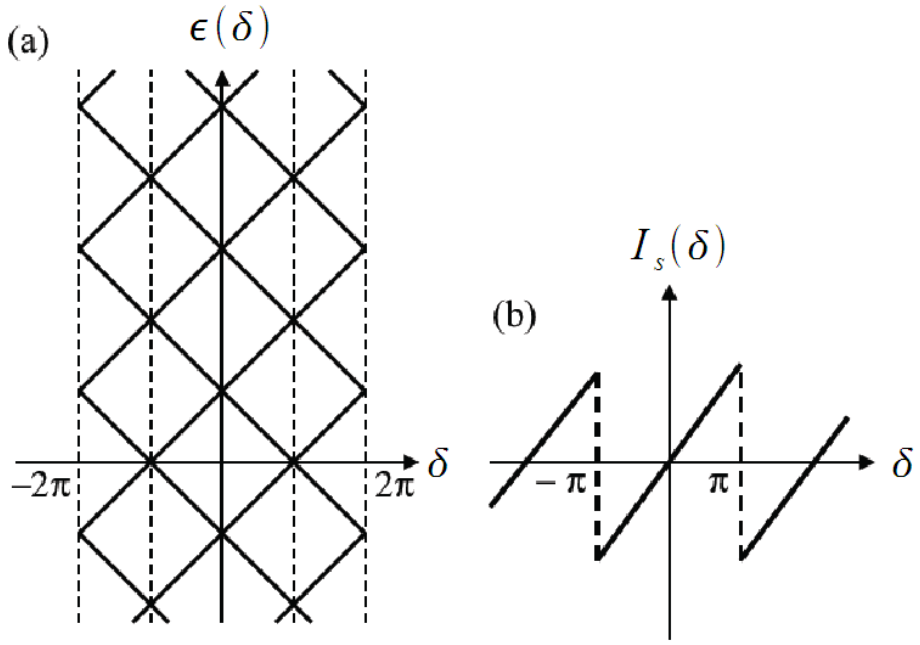

Figure 1.2: *(a) Energy excitation spectrum and (b) non-dissipative current for a long 1D ballistic junction.* $\delta = \theta_1 - \theta_2$ *is the phase difference between the two superconductors.*

dependent levels with a small energy gap, called the minigap (see Fig. 1.3). The minigap $\tilde{\Delta}$ is proportional to the Thouless energy ($\tilde{\Delta} = 3.1\, E_{Th}$), and is fully modulated by the phase difference δ between the two superconductors. $\tilde{\Delta}$ is maximum at $\delta = 0$, and goes linearly to zero at $\delta = \pi$.
This phase dependence was recently measured by scanning tunneling spectroscopy (see Fig. 1.4[37]).

The supercurrent of a long diffusive junction derived from such spectrum is anharmonic [30]:

$$I_s = \sum_n I_{c,n} \sin(n\,\delta) \qquad I_{c,n} = -(-1)^n \frac{10.82\, E_{Th}}{e\, R} \frac{3}{(2n+1)(2n-1)} \tag{1.15}$$

where R is the normal wire resistance. We show in Fig. 1.5 the current-phase relation of a long SNS junction, compared to the harmonic current-phase relation of a SIS junction.

The occurrence of higher harmonics in eq. 1.15 may be interpreted as the transfer through the junction of n Cooper pairs by n coherent Andreev reflexions (see Fig. 1.6). Indeed, if the coherence length is much longer than the normal wire length, a quasiparticle can be Andreev reflected many times

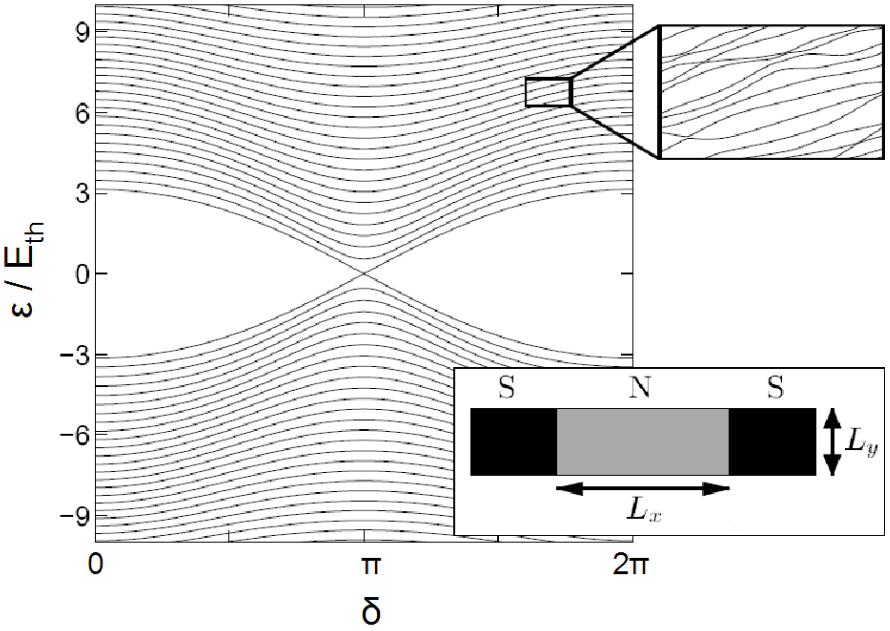

Figure 1.3: *Phase dependent Andreev bound states for a long SNS junction [2].*

coherently, thus transferring a bunch of correlated Cooper pairs.
For $L_\varphi > n\,L$, 2n Andreev reflexions are possible, conveying n Cooper pairs: the effective charge transferred is $n \times 2\,e$, the effective Andreev trajectory time is $n^2\,\tau_D$ and the superconducting phase difference accumulated is $n\,\delta$. A harmonic of order n appears then in the current-phase relation.

1.3 Relaxation times

As we have seen, the dc properties of long SNS junctions are well understood, both theoretically and experimentally. On the contrary, their dynamics is still far from being completely figured out, even if it raised much interest since the '60s.
Indeed, the dynamics of long SNS junctions is much more complicated than that of SIS junctions, where the dynamics is exclusively the phase dynamics. In a SNS junction, one has instead to consider the interaction between the phase dynamics and that of the out-of-equilibrium quasiparticles in the normal metal.

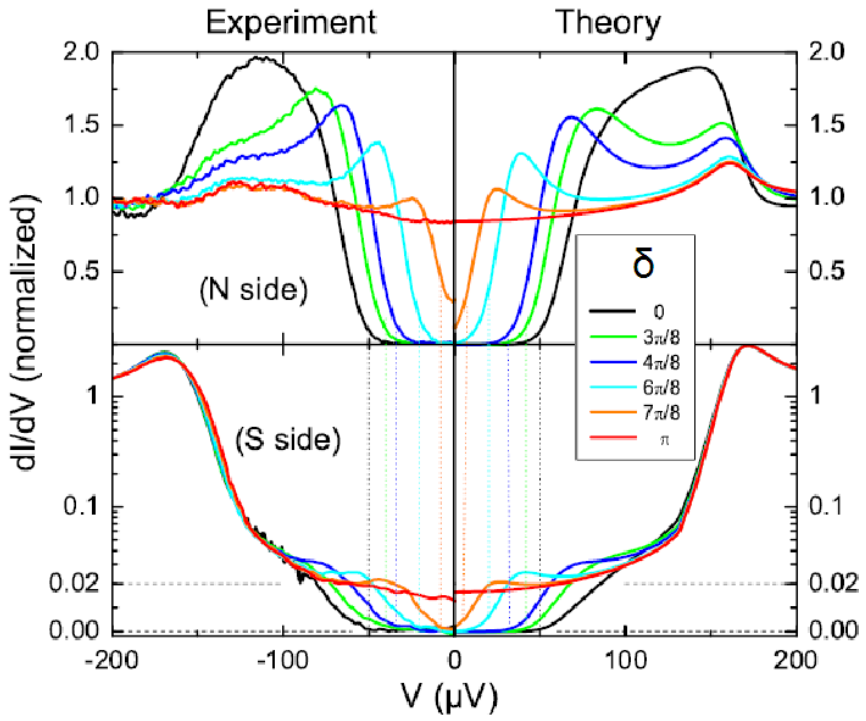

Figure 1.4: *Differential conductance versus voltage, for different values of the phase difference δ across a 300 nm long Ag wire. Left quadrants: measured. Right quadrants: calculated. Top: on the N side; Bottom: on the S side, close to the interface (the scale is linear up to 0.02 and logarithmic above, to magnify the variation for small subgap conductance). This shows that the minigap is also present on the superconductor side with the same value as on the N side [37].*

In this thesis, after the dc characterisation of our junctions, we have observed:

- the effects of a high frequency current modulation on the dc voltage-current characteristic
- the effects of a high frequency irradiation, comparable to a voltage modulation, on the dc voltage-current characteristic at $I > I_c$, in the ohmic regime
- the high frequency current response of a SNS ac SQUID to a high frequency phase modulation

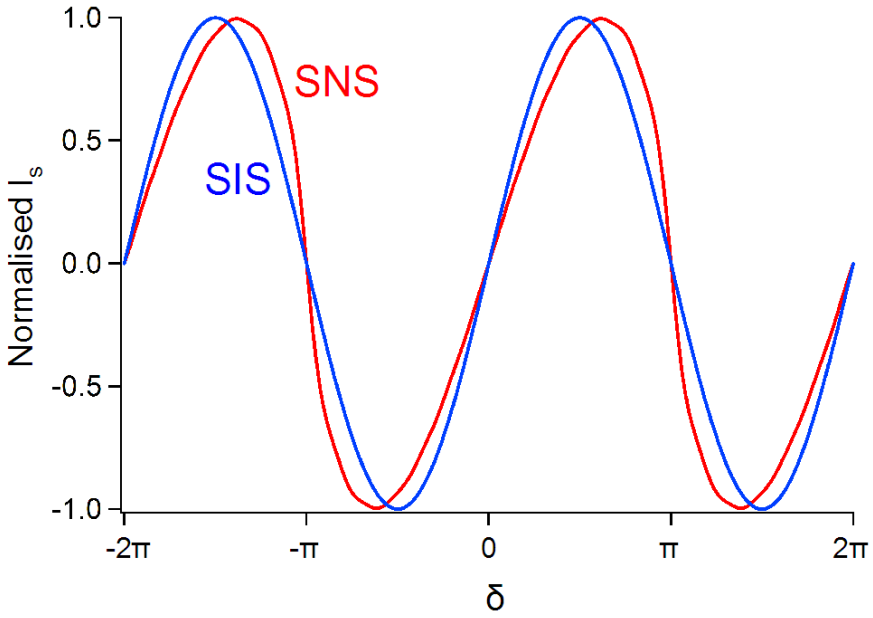

Figure 1.5: *Normalised supercurrent vs phase difference δ for a SIS junction (sinusoidal relation) and for a long SNS junction at low temperature (12 harmonics).*

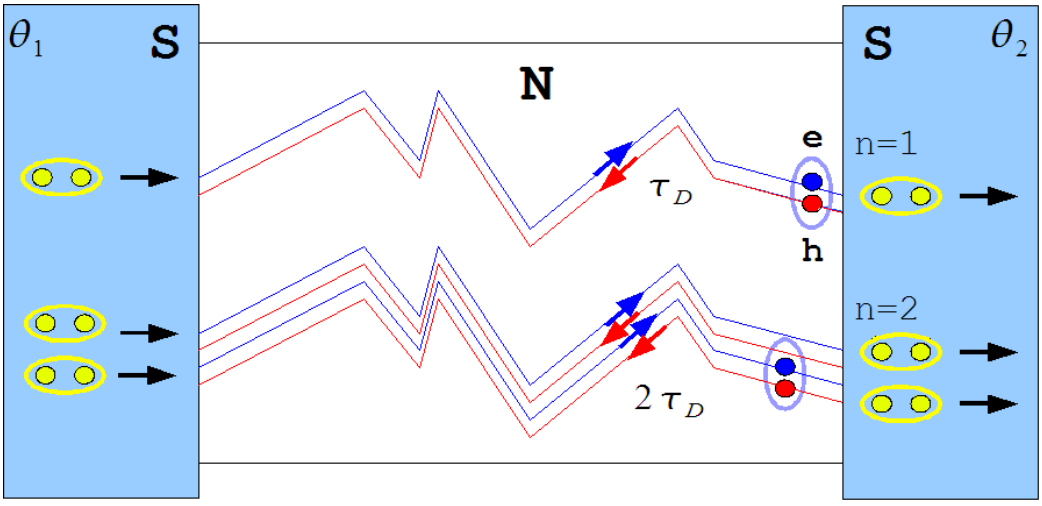

Figure 1.6: *Harmonics in a SNS long junction current-phase relationship: multiple coherent Andreev reflexions.*

In general, we aim to identify the characteristic times of the current response. If we increase the excitation frequency, we expect to observe out-

of-equilibrium effects, in the dc or ac response, as soon as the frequency is greater than the characteristic rates of the junction.
The Josephson current at equilibrium is the sum of the currents i_n carried by the Andreev levels of energy ϵ_n, weighted by the level occupation p_n:

$$I_J(\delta) = \sum_n i_n(\delta)\, p(\epsilon_n(\delta)) \tag{1.16}$$

We should then detect two characteristic times: the response time of the distribution function p_n appearing explicitly in the current expression, and the diffusion time of Andreev pairs. In fact, if the pairs don't have the time to cross the normal wire during the measuring time, the adiabatic approximation fails. The Andreev bound states aren't then defined any more, and the density of states becomes out-of-equilibrium. In this case, the Josephson current is affected through the currents i_n.

The response time of the occupations p_n is the inelastic energy relaxation time.
At high temperature ($T \gtrsim 1\,K$), the inelastic process controlling the energy relaxation of the electronic gas is the electron-phonon time. The electronic temperature tends then towards the phonon bath temperature with a characteristic time τ_{e-ph}.
At low temperature ($T \lesssim 1\,K$), the electron-electron time is the predominant inelastic process. It is the time the electronic gas needs after an excitation to form again an equilibrium Fermi-Dirac distribution.

In section 4.6.1 we show how the current response is affected when the excitation approaches the inelastic rate.

Chapter 2

DC properties of long diffusive SNS junctions

Before beginning the high frequency part of this thesis, we study in this chapter the DC properties of long SNS junctions. On one hand, this helps us understanding how the physics change when the insulating layer of a classic Josephson junction is replaced by a long normal wire, and on the other hand this is a necessary step to characterise the junctions we fabricate when measuring isolated SNS rings (see chapter 4).
We present in this chapter the temperature and field dependence of SNS junctions of different geometries and with the contacts made of different superconductors [23]. We have fabricated both single long SNS junctions and dc SQUIDs, superconducting loops interrupted by two normal metal wires in parallel.
The advantage of single Josephson Junctions is their simplicity: in a SQUID the asymmetry between the two SNS junctions, never exactly identical, has to be taken into account.
The advantage of dc SQUIDs is that they are modulable devices [10]: a dc supercurrent can flow through a dc SQUID, provided that the coherence is maintained. The supercurrent maximum value is periodically modulated by a magnetic field, with a period of one flux quantum $\Phi_0 = h/2e$ through the loop area.
The chapter is arranged as follows: we first outline the sample fabrication and the measurement setup. Then, we present the current-voltage curves at low and high temperature. The temperature dependence of the critical and retrapping current follows. Then, we discuss the dynamics of the SNS junctions to explain the hysteresis and its temperature dependence. We shortly study the low temperature transition towards the proximity induced superconducting state and the critical current statistics. We then concentrate on

the magnetic field dependence of the critical current: we detail the interference pattern in SNS dc SQUID at low field; the large scale field dependence for all samples is then addressed and compared to the theoretical predictions; we report moreover a surprising reentrance for some of the samples. Finally, we study the field dependence of integer and fractional Shapiro steps.

2.1 Sample fabrication

For all SNS samples, we use as normal metal 99.9999% pure gold, with a content in magnetic impurities (Fe) smaller than 0.1 ppm. In a separated weak localisation measurement P. Billangeon determined the phase coherence length of this gold: he obtained $L_\Phi \sim 10\,\mu m$ below 50 mK.
Three different superconductors contact the normal wires: Aluminum (Al), Niobium (Nb), and Tungsten (W).
We label the samples as follows: if they are SQUIDs, the first two letters of the name are SQ; then we indicate the superconductor (S) and then the normal metal (N) materials; finally, we add a letter to distinguish the samples with different normal wire lengths or geometries.
Our samples are:

- SQ-NbAu-L and SQ-NbAu-S
  SQUIDs, Nb (S) and Au (N), Long (L) or Short (S)

- SQ-AlAu-a, SQ-AlAu-b and SQ-AlAu-c
  SQUIDs, Al (S) and Au (N), labelled from the shortest (a) to the longest (c)

- AlAu-a, AlAu-b and AlAu-c
  wires, Al (S) and Au (N), labeled from the shortest (a) to the longest (c)

- WAu-N and WAu-Sq
  wires, W (S) and Au (N), Narrow (N) and Square (Sq)

The sample parameters, obtained by scanning electron microscopy (SEM) visualization or transport measurements, are gathered in Table 2.1 and 2.2. All the samples SQ-AlAu were produced on the same chip and have the same material parameters (for example the diffusion coefficient D); the same is also true for the samples SQ-NbAu-x, AlAu-x and WAu-x.

sample	$L(\mu m)$	$w(\mu m)$	$t(nm)$
SQ-NbAu-L	1.2	0.4	50
SQ-NbAu-S	0.75	0.4	50
WAu-N	1.53	0.34	50
WAu-Sq	1.2	1.75	50
AlAu-a	0.9	0.125	50
AlAu-b	1.25	0.125	50
AlAu-c	1.3	0.125	50
SQ-AlAu-a	0.9	0.13	50
SQ-AlAu-b	1.5	0.15	50
SQ-AlAu-c	1.9	0.2	50

Table 2.1: *Geometric characteristics of the different samples. The length L and width w have been deduced from the SEM images. The tickness t was measured by a quartz cristal during the metal deposition.*

sample	$E_{Th}(K)$	$\Delta(K)$	Δ/E_{Th}	$R_{J,fit}(\Omega)$	$R_J(\Omega)$	$R_{J,\square}(\Omega)$
SQ-NbAu-L	0.051	16.2	318	1	1.4	0.34
SQ-NbAu-S	0.13	16.2	125	0.46	0.78	0.26
WAu-N	0.041	7.04	185	2	3	0.44
WAu-Sq	0.0618	7.04	123	0.31	0.31	0.45
AlAu-a	0.033	2.07	63	3	5	0.42
AlAu-b	0.044	2.07	47	6	6	0.6
AlAu-c	0.036	2.07	58	5	5	0.48
SQ-AlAu-a	0.047	2.07	44	3.8	5.2	0.44
SQ-AlAu-b	0.03	2.07	69	4.8	6.6	0.48
SQ-AlAu-c	0.026	2.07	80	5.4	6	0.56

Table 2.2: *Characteristics of the different samples obtained by transport measurements. The Thouless energy* $E_{Th} = \hbar D/L^2$ *and the resistance* R_{fit} *have been deduced from the fit of* $I_c(T)$*. The diffusion coefficient is* $D \sim 1.2\,10^{-2}\,m^2/s$*. The superconducting gap* Δ *has been deduced from the transition temperature* T_c *of the superconducting contacts, using the relation* $\Delta = 1.76\,k_B T_c$*. We find* $T_c = 9.2\,K$ *for the Nb,* $T_c = 4\,K$ *for the W and* $T_c = 1.17\,K$ *for the Al.*

The length of the normal metal, which varies between $0.75\,\mu m$ and $1.9\,\mu m$, is much larger than the superconducting coherence length in the normal part $\xi_S^N = \sqrt{\hbar D/\Delta} = L/\sqrt{\Delta/E_{Th}}$, where $D \sim 1.2\ 10^{-2}\,m^2/s$ is the diffusion coefficient in the normal wire, Δ is the superconductor gap and the Thouless energy is $E_{Th} = \hbar D/L^2$. For all our samples, $\Delta/E_{Th} > 40$ (see table 2.2), and $L \gtrsim 7\xi$: the devices are in the long-junction regime . If $\Delta/E_{Th} > 10^5$ [19], the properties of the normal metal determine completely the proximity effect. In our case, the superconductor still influences the junction behavior, but the normal metal properties are predominant.

The three superconductors used (Al, Nb and W), differ by their transition temperature.
The fabrication procedure also produces different S/N interface conditions.
In the angle-evaporated samples of Al-Au, at the SN junction, the bare Au wires overlap with the Al; in addition, the Al loop is, at some point covered by Au (depending on the loop shape, see Fig. 2.1). Therefore, the superconductor in this configuration is not completely homogeneous.
In contrast, in the Nb-Au samples, the superconductor is a homogeneous bilayer of Nb and Au, and the normal metal is a bare Au region. The interface is thus a very different one, not horizontal in the overlap region, but vertical between the proximity superconducting Au under the Nb and the bare Au.
Finally, in the W-Au samples, the SN junction is made by the overlap of W and Au, but contamination (a thin layer of discontinuous W) is present around the W wires (see Fig. 2.4).

2.1.1 Al-Au wires and SQUIDs

The proximity wires and dc SQUIDs made from Al and Au are obtained by conventional double angle thermal evaporation through a PMMA-MMA suspended mask.
At first, we evaporate a Au layer of thickness t=50 nm, and then an Al layer of thickness t=200 nm, both at a rate of 1 nm/s; the evaporation order is important to assure the continuity of the thinner layer.
The double-angle evaporation technique permits to obtain very low contact resistances between the normal wire and the superconductor, the two evaporations following each other in a vacuum of 10^{-6} mbar.
The SEM images of four Al-Au samples are shown in Fig. 2.1.

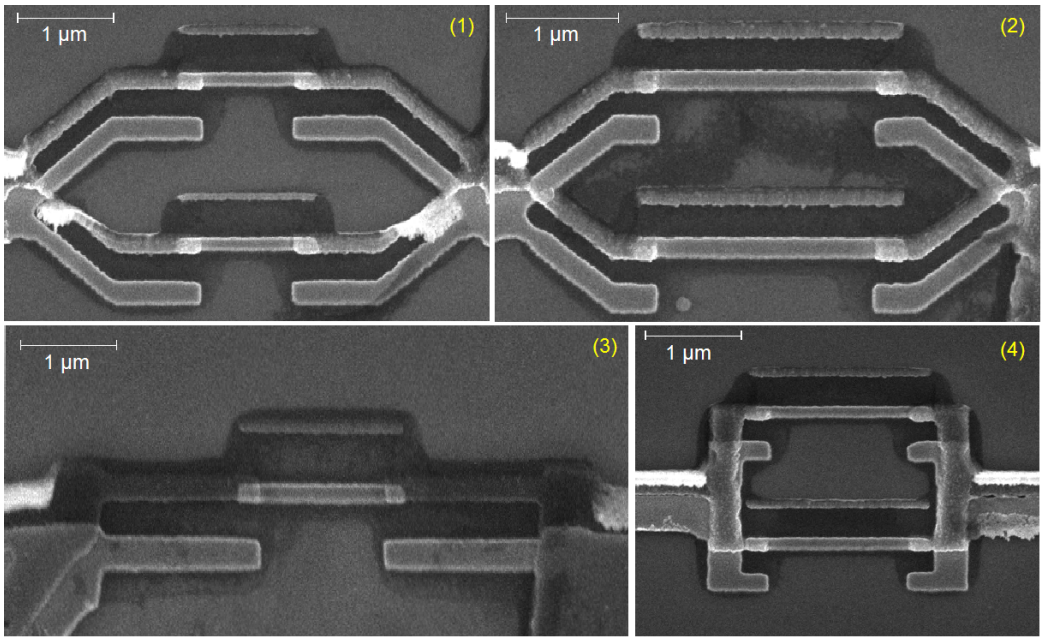

Figure 2.1: *Scanning Electron Microscope images of samples SQ-AlAu-a (1), SQ-AlAu-c (2), AlAu-b (3), SQ-AlAu-b (4).The white regions in the contacts are probably PMMA resist.*

2.1.2 Nb-Au SQUIDs

The process with Niobium as a superconductor, developed by L. Angers, is more involved (see Fig. 2.2). It is indeed difficult to create good Nb-Au interfaces using standard techniques. For example, classical double angle evaporation is very difficult to use: the Nb is evaporated at such high temperatures that the usual organic resists melt, and the lift-off of a thick Nb layer becomes impossible. The solution L. Angers found is detailed below.
First, the surface is cleaned with an Oxygen plasma, to ensure adhesion of a Au layer (we cannot use the classical adhesion layers, such as Cr or Pt, because their magnetic properties would weaken the proximity effect).
In a 10^{-7} mbar vacuum we thermally evaporate a 50 nm thick Au layer, we sputter a 200 nm thick Nb layer and finally we evaporate a 70 nm thick aluminum layer. Since the Au and the Nb layers are deposited in the same vacuum, we obtain a high quality SN interface.
Then by e-beam lithography we draw a rectangular window of the same width as the desired normal wires (Fig. 2.2 (1)).
We wet-etch open the window in the Al mask with a MF319 solution, through which we locally etch away the Nb using an SF_6 RIE (Reactive Ion Etching).

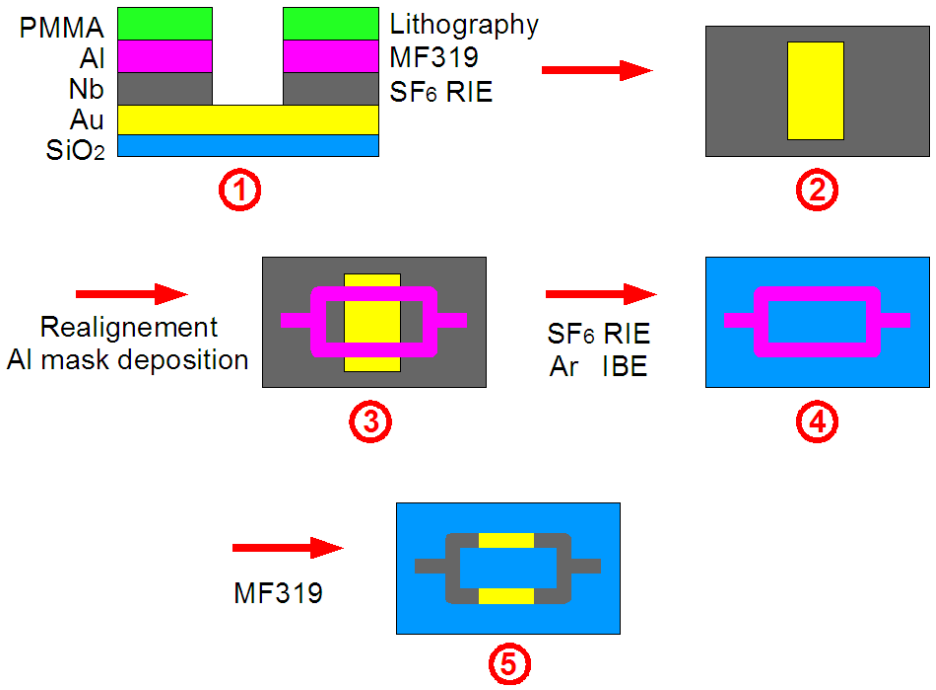

Figure 2.2: *Fabrication steps for samples SQ-NbAu-L and SQ-NbAu-L. (1) Multilayer mask and description of the processes used to etch each layer; (2) upper view of the future sample when PMMA and Al have been removed and only the Au-Nb bilayer, with the Nb etched in a rectangular zone, remains; (3) deposition of a ring-shaped Al mask over the rectangular window opened in the Nb; (4) elimination of all Nb and Au not covered by the Al mask; (5) the sample, after dissolving the Al protective mask.*

We finally eliminate all the remaining Al mask, obtaining a Nb-Au bilayer with a window in the Nb layer (Fig. 2.2 (2)).
In a realignment step, we lithograph and evaporate a ring shaped Al mask passing across the window designed previously; this mask protects the Nb-Au bilayer forming the future dc SQUID (Fig. 2.2 (3)).
The remaining bilayer is removed by a SF_6 RIE followed by an Argon IBE (Ion Beam Etching) (Fig. 2.2 (4)).
Finally, the Al mask is removed (Fig. 2.2 (5)); SEM images of the samples are shown in Fig. 2.3.
An important part of the fabrication was done at LPN (Laboratoire de Photonique et Nanostructures) in Marcoussis.

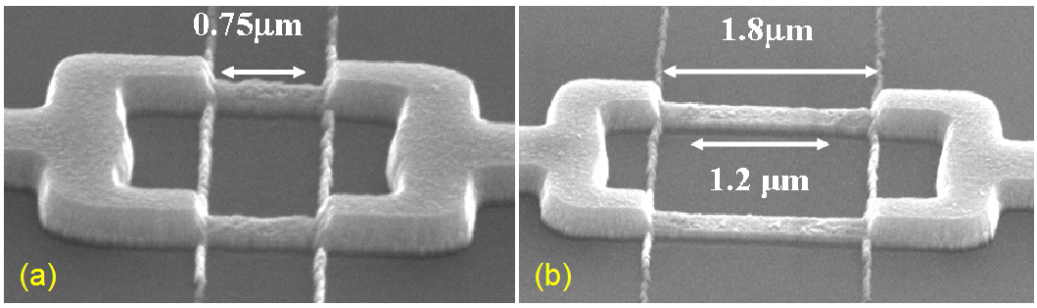

Figure 2.3: *Scanning Electron Microscope images of samples SQ-NbAu-S (a) and SQ-NbAu-L (b). In sample SQ-NbAu-L, one can see at the edges of the normal wires that the Nb hasn't been completely etched; this causes the reduction of the normal region length from the designed* $1.8\mu m$ *to* $1.2\mu m$*. One can also see the traces of the rectangular window used to define the normal parts of the junctions (see Fig. 2.2 (2)), etched in the* $Si0_2$ *substrate; this is due to the fact that in step (4), while the etching times are set to permit the removal of a Nb-Au bilayer, in the window zone there is only a Au layer, which is etched faster than the bilayer; the remaining time, the plasma etches the substrate.*

2.1.3 W-Au wires

The W-Au wires are made with a different method.
First, Au wires of the desired width are drawn by e-beam lithography and evaporated on a substrate (we used either $Si0_2$ or sapphire substrates); alignment marks are also created.
The superconducting contacts are fabricated in a Dual beam microscope, formed by a Scanning Electron Beam (SEM) aligned with a Focused Ion Beam (FIB).
First, we slightly etch the Au wire with the FIB to remove possible oxidation or impurities on its surface.
Then, we place at a few tens of μm above the sample a nozzle, which injects a metallo-organic vapor of tungsten hexacarbonyl. This vapor is decomposed by the focused Ga^+ ion beam, and a dirty W metal is deposited on the substrate. The wires produced are composed by tungsten, carbon, gallium and oxygen with varying proportions (in our case, probably 75% W, 10% C, 5% Ga and 40% O_2).
The superconducting critical temperature of the wires produced is not $12\,mK$, like in bulk W, but, in all our samples, $T_c \sim 4\,K$! This could be due to the injection of Ga, which is itself a superconductor with $T_c = 1\,K$.
The critical magnetic field of the wires is also surprising high: at $1\,K$,

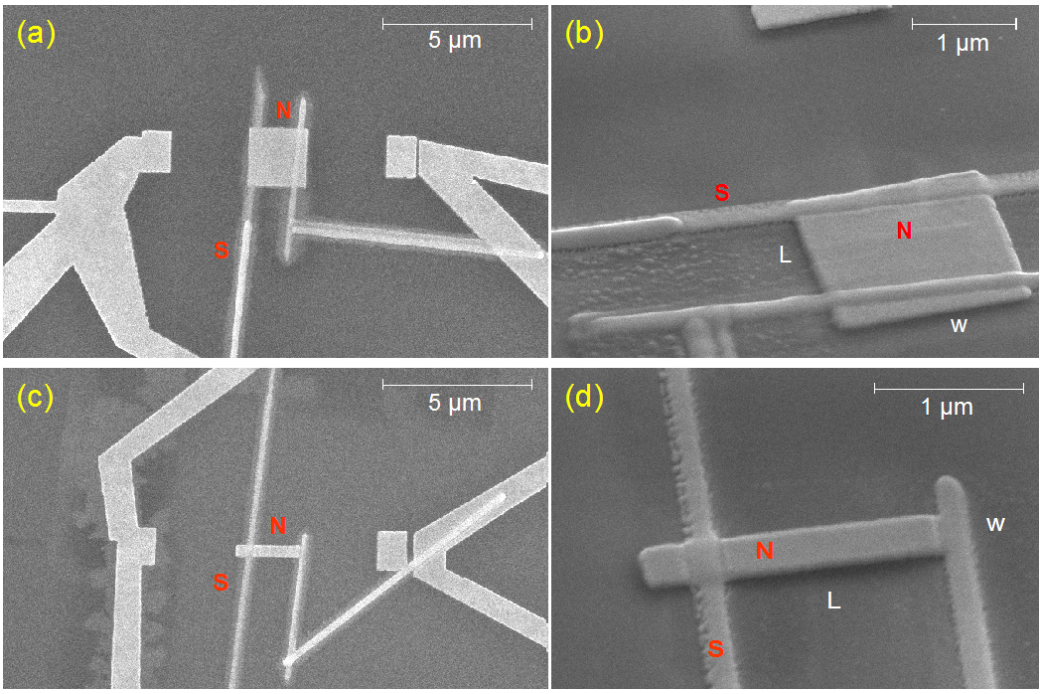

Figure 2.4: *Scanning Electron Microscope images of samples WAu-Sq ((a) and (b)) and WAu-N ((c) and (d)). One can see as a clear halo the W contamination around the superconducting contacts.*

$H_c = 7\,T$ [34].
By changing the scanning parameters of the ion beam, we can fabricate superconducting wires of the desired geometry at the desired position. The minimum W wires width is about $100\,nm$, and their thickness is controlled by the irradiation time. A FIB current of $10\,pA$, with $40\,ns/pixel$ and 10^7 scans produces a wire 100 nm wide and 100 nm thick in 20s.
The deposition is done with a ion beam energy of 30 keV and a focused ion-beam current of $30\,pA$. The gas temperature is set to $90\,°C$; during the wire deposition the pressure in the chamber is $4\,10^{-4}$ mbar.
After one wire deposition, thanks to the dual system, one can control the result by SEM observation and determine the position of the next wire. This can be particularly useful in the case of an insulating substrate such as sapphire, where the accumulation of charge on the substrate can deflect the ion beam and thus shift the position of the deposited wire.
The main advantages of this technique are the deposition of the material of practically any shape and size, without any mask, directly onto the substrate. There are, of course, some disadvantages. An example is the extreme proximity needed for the nozzles injecting the W vapor. The nozzles have to

be lowered manually, and the distance nozzle-sample is determined by the darkness of the nozzle's shade on the substrate. An excessive lowering, like in Fig. 4.6, can strongly affect the sample!
In conclusion, this technique is quite difficult and demanding, but gives a great amount of freedom and possibilities for fabrication.
We were strongly helped for the fabrication by A. Kasumov and F. Fortuna.

2.1.4 Measurement setup

All measurements are done by biasing the sample with a dc current (up to $400\mu A$), often modulated by a small ac current $\delta I = 10 - 100nA$ at a few tens of Hertz for differential resistance measurements.
In our setup, superconducting leads, in a four wire configuration, connect the SQUIDs or the wires. Since the samples are connected at each end by two wires, the current flows through the junction using two of the wires; the voltage is measured across the two remaining ones, where no current passes, so that the voltage drop is directly the junction voltage drop.
Samples Al-Au, SQ-AlAu and Nb-Au were cooled down to $15\,mK$ in a $He^3 - He^4$ dilution refrigerator. The samples were bonded to 150 pF capacitors on the sample holder with Al-Si wires, in order to assure a good filtering of the high frequency noise. Homemade lossy coaxial cables connected the sample holder to room temperature low pass π filters.
Samples W-Au were cooled down to $50\,mK$ in a second $He^3 - He^4$ dilution refrigerator. In this case the sample holder was connected to the room temperature π filters by simple lossy cables, but the dilution was equipped with a high frequency (up to 18 GHz) coaxial cable we used for microwave irradiation.
The temperature is varied up to $1.3\,K$ by a resistance on the sample holder (at higher temperatures the dilution fridge is unstable).
A superconducting coil at the bottom of the cryostat provides a magnetic field up to 5 T.

2.2 Voltage-current characteristic

The V(I) curve for sample SQ-NbAu-S at T=25mK is shown in Fig. 2.6 (a). We polarise the sample with a dc current and we read the dc voltage across the junction in a four-wire configuration.
Below the critical current I_c the junction is in a superconducting state, the voltage is zero and a non dissipative supercurrent flows in the junction.

For $I = I_c$, the junction abruptly jumps to a resistive state, a non-zero voltage appears across the junction and the V(I) relationship becomes ohmic.
If we decrease the bias current from $I > I_c$, the junction returns to the superconducting state only at a current I_r lower than the critical current, called the retrapping current .

When increasing the temperature (Fig. 2.6 (b)), the curve becomes non-hysteretic and the transition becomes smoother. Near the superconducting transition the V(I) curve has a square root dependence given by $V = R\sqrt{I^2 - I_c^2}$ (see Fig. 2.6 (b)).
All our samples, SQUIDs or simple wires, show the same qualitative behavior than SQ-NbAu-S sample, but the temperature at which the hysteresis disappears depends strongly on the length of the normal part.

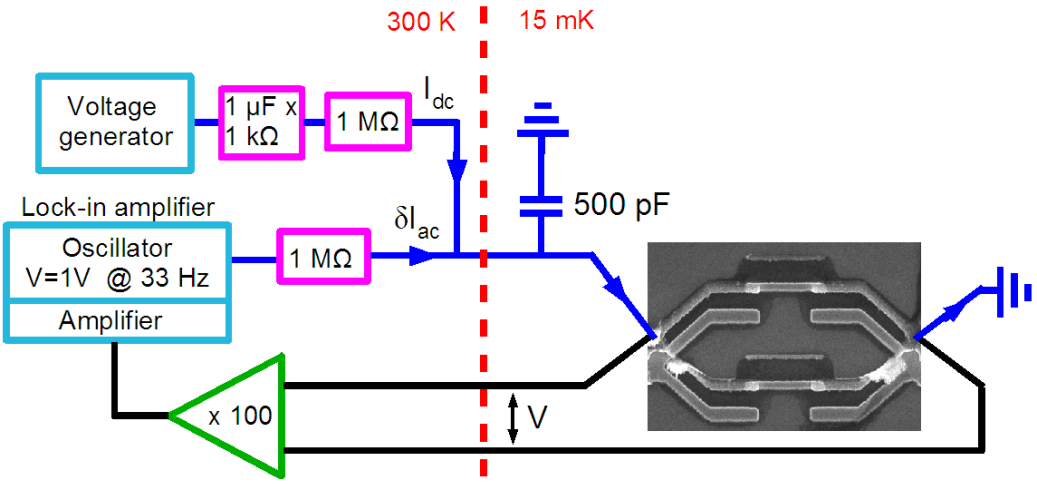

Figure 2.5: *Measurement setup. A voltage generator through a $1M\Omega$ resistance, supplies after filtering the dc current bias, while the Lock-in SR830 oscillator modulates the dc current at $f \sim 33Hz$. The bias current, flowing through the blue wires, is then $I = I_{dc} + \delta I_{ac} \cos(2\pi ft)$. The voltage across the sample, $V = V_m + \delta V_m \cos(2\pi ft)$, is amplified by a low-noise amplifier and arrives to the Lock-in. We then measure the differential resistance R_{diff}: $\delta V_m = \frac{\partial V}{\partial I}\delta I_{ac} = R_{diff}\,\frac{\delta V_{ac}}{1M\Omega}$.*

2.3 Temperature dependence and Thouless energy

In Fig. 2.7 we show the temperature dependence of the critical current in sample WAu-Sq. At low temperature, the critical current saturates, while at high temperature I_c decays exponentially as:

$$I_c(T) \propto e^{-T/\alpha E_{Th}} \tag{2.1}$$

This same dependence is observed in all our long SNS junctions, with α varying between 2.5 and 4. The decay of the critical current at high temperature is thus controlled by an energy scale of about three times the Thouless energy. This suggests that the important energy scale here is not the Thouless energy itself but the minigap $\tilde{\Delta}$, which, in the absence of a magnetic field, is $\tilde{\Delta} = 3.1E_{Th}$.

As we see in Fig. 2.7, the exponential behavior differs from the exact dependence at the highest temperatures. This is quite a common feature, so we use, instead of the exponential law, a more complete expression to fit the temperature dependence.

Dubos et al. [18] have numerically calculated the exact $I_c(T)$ curve for a long SNS junction solving the Usadel equations, and have found analytical expressions valid in the low and the high temperature limits.

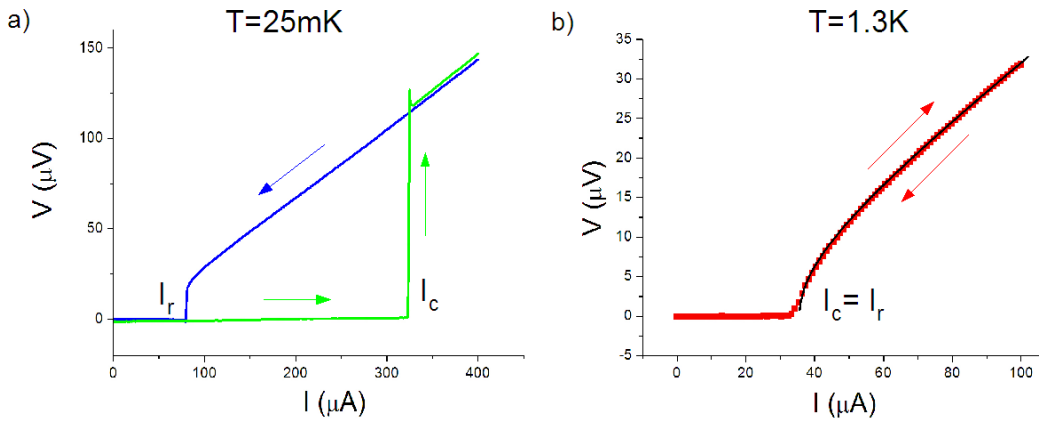

Figure 2.6: *Dc voltage vs dc current for sample SQ-NbAu-S at (a) T=25 mK and (b) T=1.3 K. The bias current is increased from zero and then, when in the normal state, decreased back to zero; the arrows indicate the direction of the current. We notice a strong hysteresis at T=25mK, that disappears when increasing the temperature up to T=1.3 K. The fit is given by* $V = R\sqrt{I^2 - I_c^2}$ *with* $R = 0.343\Omega$ *and* $I_c = 35.6\mu A$.

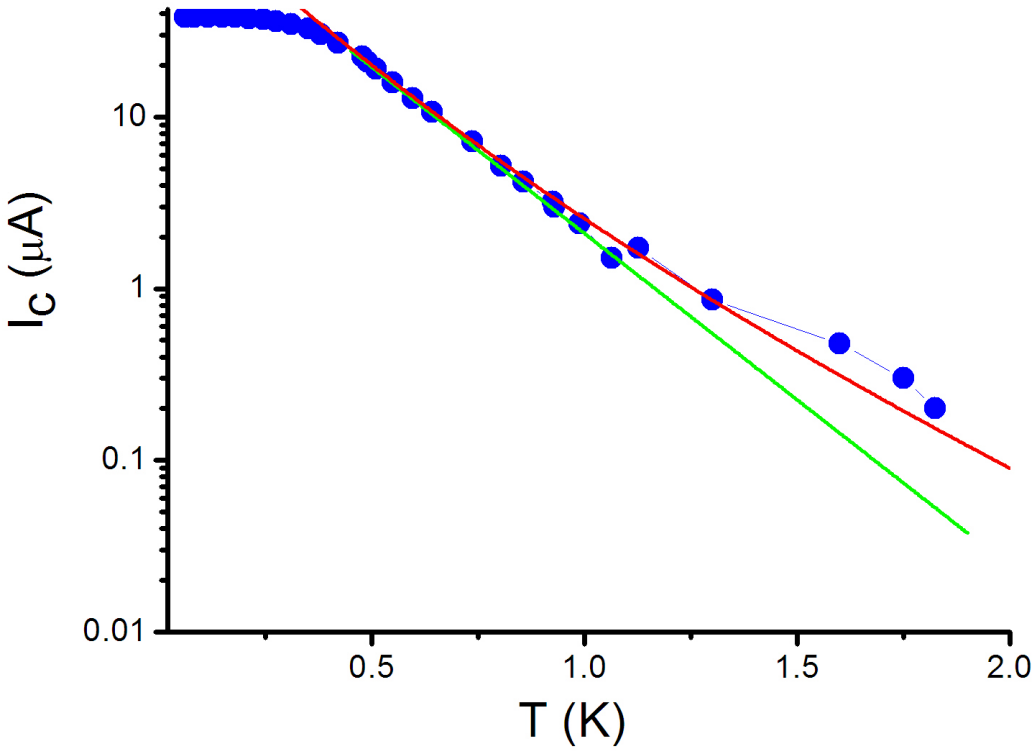

Figure 2.7: *Critical current vs. temperature for sample WAu-Sq. The green straight line shows an exponential fit of equation* $I_c(T) = 183\, e^{-T/3.66\, E_{Th}}\, \mu A$, *while the red line is the complete fit in the high temperature regime given by eq.2.4 with parameters* $R = 0.31\,\Omega$ *and* $E_{Th} = 61.8\, mK$.

The low temperature limit of $I_c(T)$, valid for $k_B T < 2.5\, E_{Th}$, within a 1% error, is given by:

$$\frac{eRI_c}{E_{Th}} = b\left(1 - a\, e^{-bE_{Th}/(3.2\, k_B T)}\right) \tag{2.2}$$

In the case of a very long wire ($\Delta/E_{Th} > 5\ 10^4$), the numerical values for a and b are:

$$a = 1.3 \qquad\qquad b = eRI_c(T=0)/E_{Th} = 10.82 \tag{2.3}$$

In our samples, the ratio Δ/E_{Th} ranges between 40 and 300, so that the parameter b ranges between 8.8 and 10.48.
At high temperature, for $k_B T > 5E_{Th}$, the analytical approximation, within a 3% error, is:

$$eRI_c = 64\pi k_B T\sqrt{\frac{2\pi k_B T}{E_{Th}}}\frac{\Delta^2 e^{-\sqrt{\frac{2\pi k_B T}{E_{Th}}}}}{(\pi k_B T + \Delta + \sqrt{2(\Omega^2 + \Omega\pi k_B T)})^2} \tag{2.4}$$

where Δ is the superconductor's gap and $\Omega = \sqrt{\Delta^2 + (\pi k_B T)^2}$.
For a very long junction ($\Delta/E_{Th} \to \infty$), the previous expression simplifies into:

$$eRI_c = \frac{32}{3+2\sqrt{2}} E_{Th} \left(\frac{2\pi k_B T}{E_{Th}}\right)^{3/2} e^{-\sqrt{\frac{2\pi k_B T}{E_{Th}}}} \tag{2.5}$$

We use the expressions for a finite Δ/E_{Th} to fit our data and find the values of the ohmic state resistance R and the Thouless energy E_{Th}.
Of course, R can also be obtained by a differential resistance measurement, and E_{Th} can be calculated from the resistance and the geometrical parameters of the sample (see sec. 3.2), but the fit of the temperature dependence permits, on one hand, to confirm the values found in these other ways, and on the other hand, to precise them.
In general, the normal state resistance R extracted from the fit is smaller than the one extracted from the dV/dI curves. The temperature fit is indeed sensitive only to the SNS junction resistance, ignoring other resistances in series, which are instead present in the dV/dI measurement.
In the case of a symmetric SQUID (which is mostly our case), where two practically identical junctions are in parallel, the above expressions for a single SNS junction are still valid, since the product RI_c is exactly the same: the current in each junction is half the injected current, but the resistance of each junction is the double of the SQUID resistance.

Fig. 2.8 shows the temperature dependence of samples SQ-NbAu-L and SQ-NbAu-S and their fits at low and high temperature.
We proceed in the following way: first, the high temperature dependence is fitted, to find R and E_{Th}. Then the low temperature expression is traced for the values of R and E_{Th} previously determined and with b fixed by the ratio Δ/E_{Th}. Finally, a is adjusted to obtain a good overlap with the high temperature fit. The values of a never differ more than 10% from the $\Delta/E_{Th} \to \infty$ case.
The complete fit at high temperature (eq. 2.4) is moreover compared to the high temperature expression (eq. 2.5) for the same values of R and E_{Th} in the limit of an infinite long junction ($\Delta/E_{Th} \to \infty$). Even for sample SQ-NbAu-L, for which $\Delta/E_{Th} = 318$, the approximation $\Delta/E_{Th} \to \infty$ is not satisfactory. For all our samples it is then necessary to use the expression for a finite Δ/E_{Th}. The error in the value of E_{Th} coming from the approximation $\Delta/E_{Th} \to \infty$ is 6% for sample SQ-NbAu-L and 15% for sample SQ-NbAu-S.
We can see in Fig. 2.8 that while the high temperature fit is very good, the measured critical current at low temperatures is too small by roughly a factor 1.5. The deviations from the theory appear below $T = 150\,mK$ for

sample SQ-NbAu-L, and below $T = 400\,mK$ for sample SQ-NbAu-S.
One possible explanation is that at the lowest temperatures the electronic temperature is higher than the phonon temperature of the mixing chamber; but this seems improbable at temperatures above 100 mK. Indeed, when in the normal state, the junction dissipates a Joule power of the order of 10 nW, which is of the order of the dilution fridge cooling power. However, before each switch, the junction spend a long time ($t \sim 200\,s$) in the superconducting, non-dissipative state, and the electronic temperature should then have the time to decrease to the bath temperature.
Another possible explanation involves the role of nonperfect transparency of the superconducting/normal SN interface. This has been investigated by J. C. Hammer et al. [28]. Numerical integration of the Usadel equations shows

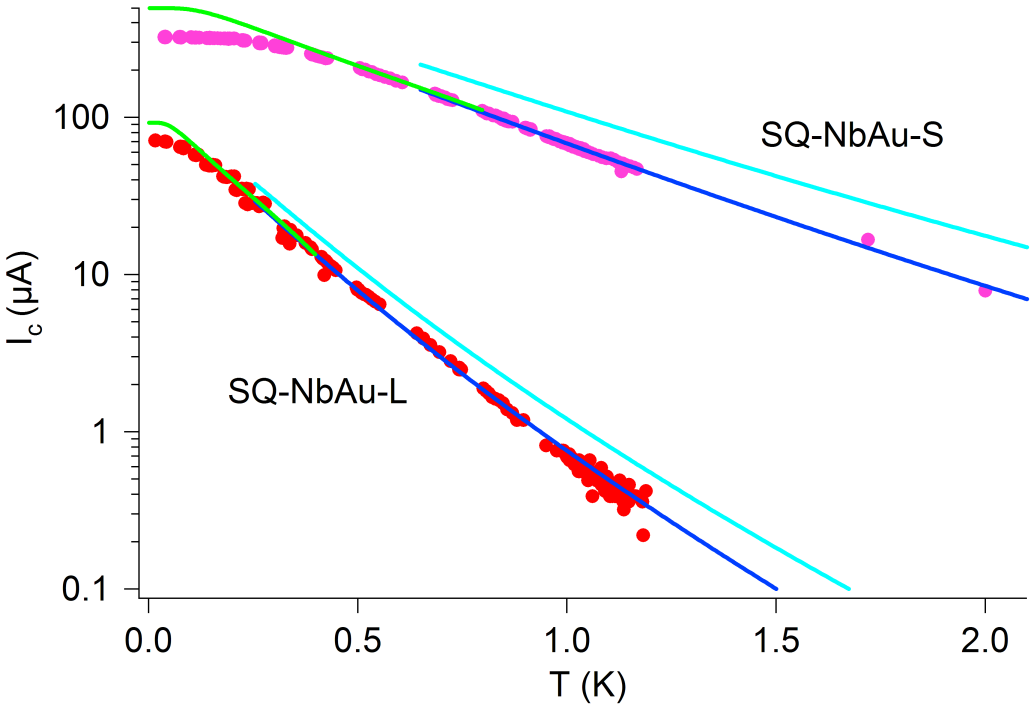

Figure 2.8: *Critical current vs. temperature for samples SQ-NbAu-L (red dots) and SQ-NbAu-S (pink dots). The high temperature fits (blue lines) are valid for $T > 0.66K$ (SQ-NbAu-S) and $T > 0.25K$ (SQ-NbAu-L). The low temperature fits (green lines) are valid for $T < 0.33K$ (SQ-NbAu-S) and $T < 0.13K$ (SQ-NbAu-L). Both take into account the finite ratio Δ/E_{Th}. Notice that the fits continue to be valid well outside their limits. Light blue lines: high temperature approximation for $\Delta/E_{Th} \to \infty$, using the R and E_{Th} found in the complete fit.*

that the main effect of a nontransparent interface is to renormalize the Thouless energy and to decrease the critical current. At the lowest temperatures, a non-ideal interface decreases the amplitude of the critical current, but also the temperature range of the current saturation: thus, an imperfect interface cannot explain the saturation region we observe.
We are still looking for a good explanation of this discrepancy between the experimental the theoretical low temperature behavior.

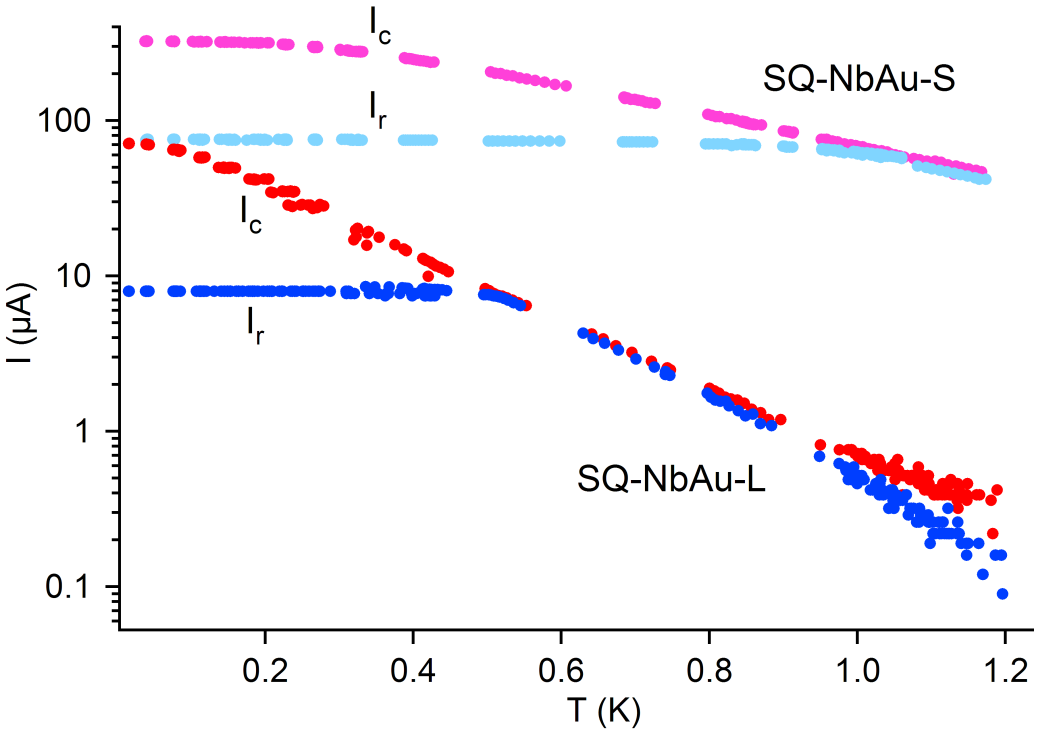

Figure 2.9: *Critical current I_c and retrapping current I_r vs. temperature for samples SQ-NbAu-L (I_c: red dots, I_r: blue dots) and SQ-NbAu-S (I_c: pink dots and I_r: light blue dots). At $T > 1\,K$, one can observe $I_r < I_c$. This is due to an artefact of the measurement technique, I_c, I_r and the current measurement step ΔI being of the same order of magnitude.*

Samples SQ-NbAu retrapping current vs temperature is shown in Fig. 2.9, compared to the critical current.
The retrapping current temperature dependence is strikingly different from the $I_c(T)$ curve: I_r is constant over a large range of temperature (up to $T = 0.76\,K$ for SQ-NbAu-S and up to $T = 0.45\,K$ for SQ-NbAu-L), then decreases slowly up to a point ($T = 1\,K$ for SQ-NbAu-S and $T = 0.51\,K$ for

SQ-NbAu-L), where the hysteresis disappears and I_r becomes equal to I_c. We find the same qualitative dependence in all our samples. In next section, we try to explain the value of the constant retrapping current and the temperature at which the hysteresis disappears in the context of the Resistive and Capacitive Shunted Junction (RCSJ) model.

2.4 Hysteresis in V(I) curves

In this section we examine the possible causes of the hysteretic V(I) curves we have seen in the previous sections. In particular, we compare the predictions of different models to the experimental hysteresis and its temperature dependence.

2.4.1 RCSJ model

The Resistive and Capacitive Shunted Junction (RCSJ) model is, because of its simplicity and efficiency, the most popular model used to describe the static and dynamic properties of SIS junctions [56].
Its main idea is to represent schematically a SIS junction as the sum of three circuit elements in parallel: a resistance R, a capacitance C and a non-linear inductance, which is the Josephson junction itself.
The resistance R corresponds to the total resistance shunting the junction; in a SIS junction at low temperature, the appropriate R is the quasiparticle resistance, while in the case of a SNS junction, the normal state resistance is thought to predominate [56].
In a SIS junction, C is the capacitance formed by the two electrodes and the insulating layer; in the case of a SNS junction, the capacitance is negligible, but an effective capacitance can be defined, so that the main results of the RCSJ model not only apply to SIS junctions but also to SNS junctions.
The bias current I_{dc} is the sum of the currents flowing into these three elements:

$$I_{dc} = I_s + I_R + I_C = I_c \sin\delta + \frac{V}{R} + C\,\frac{\partial V}{\partial t} \tag{2.6}$$

Using the second Josephson relation

$$V = \frac{\Phi_0}{2\pi}\dot{\delta} \tag{2.7}$$

we can write eq. 2.6 as a function of the phase difference δ across the junction:

$$I_{dc} = I_c \sin\delta + \frac{1}{R}\,\frac{\Phi_0}{2\pi}\,\dot{\delta} + C\frac{\Phi_0}{2\pi}\,\ddot{\delta} \tag{2.8}$$

By expressing eq. 2.8 in dimensionless units we can evidence the parameters that determine the phase dynamics: the quality factor and the plasma frequency. The dimensionless equation is:

$$\frac{I_{dc}}{I_c} = \ddot{\delta} + \frac{1}{Q}\dot{\delta} + \sin\delta \tag{2.9}$$

where the quality factor Q is given by:

$$Q = R\,C\,\omega_p \tag{2.10}$$

and where $\dot{\delta} = \partial\delta/\partial\tau$:

$$\dot{\delta} = \frac{\partial\delta}{\partial\tau}, \qquad \tau = \omega_p t \quad and \quad \omega_p = \sqrt{\frac{2\pi I_c}{\Phi_0 C}} \tag{2.11}$$

We can also re-write eq.2.8 in the form of a motion equation:

$$C\left(\frac{\Phi_0}{2\pi}\right)^2 \ddot{\delta} + \frac{1}{R}\left(\frac{\Phi_0}{2\pi}\right)^2 \dot{\delta} + \frac{\partial U(\delta)}{\partial\delta} = 0 \tag{2.12}$$

with

$$U(\delta) = -E_J\left(\cos\delta + \frac{I_{dc}}{I_c}\,\delta\right) \qquad E_J = \frac{\Phi_0\, I_c}{2\pi} \tag{2.13}$$

where $U(\delta)$ is the potential in which the phase evolves and E_J is the Josephson energy.
Equation eq. 2.12 describes the motion of a particle of position δ and of mass proportional to C, submitted to a friction force proportional to 1/R, in the washboard potential $U(\delta)$ whose slope is determined by the current I_{dc} (see Fig. 2.10).

When the particle is in the potential pit, the phase is well defined and oscillates around the minimum at the frequency:

$$\omega = \omega_p\left(1 - \frac{I_{dc}^2}{I_c^2}\right)^{1/4} \tag{2.14}$$

While the phase is trapped, we have $< \dot{\delta} >= 0$, which gives $< V >= 0$: we are in the superconducting state.
When increasing the bias current, the potential tilts, lowering the barrier: the particle has more and more probability to escape the potential pit. We can then distinguish two behaviors, depending on the value of the quality factor Q.

- $Q > 1$, underdamped junction. In this case the friction is small: the particle that has escaped the potential pit accelerates down and gains enough kinetic energy not to be trapped again. When decreasing I_{dc}, the particle slows down, but because of its kinetic energy, it stops in a potential minimum only for a current $I_{dc} = I_r < I_c$. The V(I) curve is then hysteretic, and the hysteresis is controlled by the value of Q:

$$Q = R\,C\,\omega_p = \frac{4}{\pi}\frac{I_c}{I_r} \tag{2.15}$$

- $Q < 1$, overdamped junction. In this case the friction is important: the particle that has escaped the potential pit is slowed down by the friction and is trapped in the following potential minimum; its motion is similar to a Brownian motion. When decreasing I_{dc}, the particle is retrapped at $I_{dc} = I_c$. The V(I) curve is then non-hysteretic.
If $Q << 1$ (for example in the case of a very small capacitance), the differential equation becomes:

$$I_{dc} = I_c \sin\delta + \frac{1}{R}\frac{\Phi_0}{2\pi}\dot{\delta} \tag{2.16}$$

Integrating this differential equation to obtain $\delta(I_{dc})$, and thus $V(I_{dc})$, one finds:

$$V = R\sqrt{I_{dc}^2 - I_c^2} \tag{2.17}$$

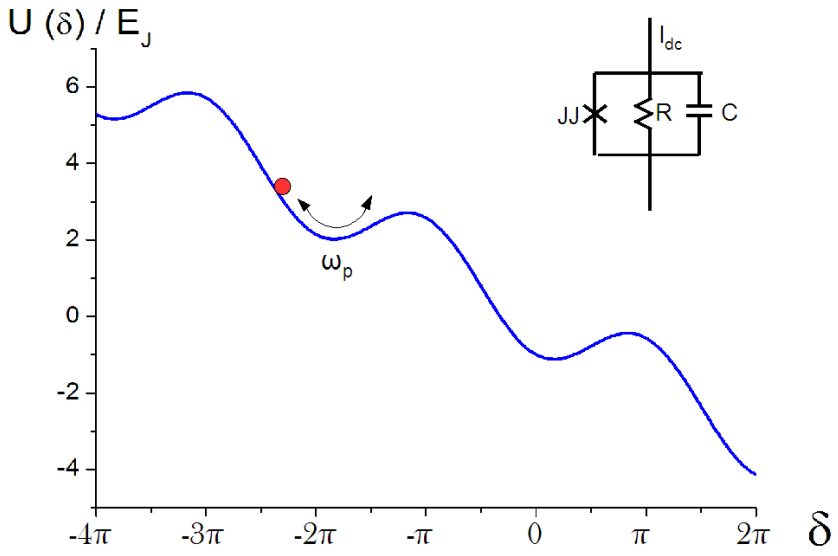

Figure 2.10: *Washboard potential describing the motion of the phase position. Inset: circuit schematics of a SIS junction in the RCSJ model*

This is exactly the voltage-current dependence we measure at $T = 1.3\,K$ in SQ-NbAu-S (see fit in Fig. 2.6 b)). At high temperature, then, our junction behaves exactly as an overdamped SIS junction.

2.4.2 Hysteresis: heating

Let's now examine the low temperature hysteresis of the V(I) curves.
A first possible source of hysteresis is of thermal origin [21].
We suppose that our junction is intrinsically non-hysteretic: then $I_r = I_c$. But, if the electronic temperatures are different in the superconducting state (S) and in the normal state (N), the switching currents are different when passing from S to N ($I_c(T^S)$) and from N to S ($I_r = I_c(T^N)$). I_c depends indeed strongly on T.
When the sample is in the superconducting state, because of its zero resistance, the injected power doesn't heat the normal wire. But, as soon as the junction is resistive, the sample dissipates a power $P_J = RI^2$ and its electronic temperature increases.
Because of the superconducting gap of the contacts, electrons with $E < \Delta$ cannot enter the contacts. Moreover, since the normal wire resistance is small ($R \sim 1\Omega$), the voltage across the junction is also small $V \sim 10^{-4}V << \Delta$, and an electron would need at least 10 incoherent reflections (MAR) to escape the superconducting gap. Therefore, electrons are confined in the normal wire and relax their energy by phonon emission.
At high temperature, phonon cooling is very efficient, so that the electronic temperature T_e and the phonon temperature T_{ph} always coincide, and $I_r = I_c$.
At low temperature, instead, the cooling is poor, T_e^N is greater than T_{ph} and doesn't vary much when T_{ph} varies; we then have $I_r < I_c$, with I_r almost independent on T_{ph}. This qualitatively corresponds to our measurements.

Let's now look if the agreement is also quantitative. The standard phonon cooling power is:

$$P = \Sigma V(T_e^5 - T_{ph}^5) \tag{2.18}$$

where V is the volume of the normal wire and Σ a material dependent parameter.
At every bias current, the equilibrium between the injected power and the phonon cooling power sets the electronic temperature. As soon as the bias current is smaller than the critical current at that electronic temperature, the junction switches into the superconducting state. This means:

$$RI_c^2(T_e) = \Sigma V(T_e^5 - T_{ph}^5) \tag{2.19}$$

We have graphically solved this equation, using the measured $I_c(T)$ curve, to find the retrapping current $I_r = I_c(T_e)$ at various bath temperatures (we assume that $T_{bath} = T_{ph}$). For SQUID samples, we have taken $I_c/2$ as the single junction critical current, and $2\,R$ as the single junction resistance. Our junctions are not completely symmetric in reality, but the error is negligible (see sec.2.7.1).
The comparison between the calculated $I_r(T)$ and the experimental one is shown in Fig. 2.11 for sample SQ-NbAu-S.
One can see that the standard value $\Sigma = 210^{-9} W\,\mu m^{-3} K^{-5}$ yields a heating

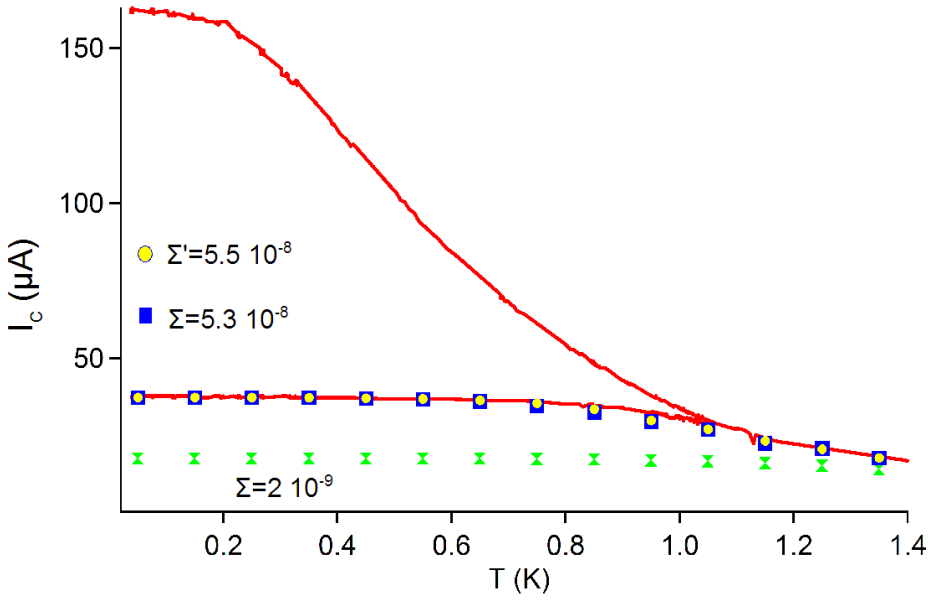

Figure 2.11: *Critical and retrapping currents of sample SQ-NbAu-S (red lines). T^5 power law: $I_r(T)$ for $\Sigma = 2\,10^{-9} W\,\mu m^{-3} K^{-5}$ (green butterflies) and for $\Sigma = 5.3\,10^{-8} W\,\mu m^{-3} K^{-5}$ (blue squares). T^6 power law: $I_r(T)$ for $\Sigma' = 5.5\,10^{-8} W\,\mu m^{-3} K^{-6}$ (yellow dots).*

effect which is too large to account for the experimental results: we obtain half the experimental I_r, even if the constant dependence on temperature is well explained.
To reproduce the amplitude of I_r, we have at first tried to increase the value of Σ, to see if a reasonable change could account for the measured curve. A good agreement is found for $\Sigma = 5.3\,10^{-8} W\,\mu m^{-3} K^{-5}$ (Fig. 2.11). However, this value is 20 times larger that the ones found in literature.
In a second attempt we considered not a fifth power law but a sixth power law for the phonon cooling.
A sixth power law has been first predicted by A. Schmid, and then by A.

sample	T^5 : $\Sigma(W\,\mu m^{-3}K^{-5})$	T^6 : $\Sigma'(W\,\mu m^{-3}K^{-6})$
SQ-NbAu-S	$5.3\,10^{-8}$	$5.5\,10^{-8}$
SQ-NbAu-L	$2.5\,10^{-8}$	$5.3\,10^{-8}$
WAu-Sq	$1.15\,10^{-8}$	$1.98\,10^{-8}$

Table 2.3: *Best fits of the $I_r(T)$ curves for a phonon cooling power proportional to T_e^5 or to T_e^6.*

Sergeev and V. Mitin [52] , and has been measured for 57 nm thick Au wires, and for Cu wires thinner than $140nm$ by Karvonen et al. [33]. The new equation to solve is then:

$$RI_c^2(T_e) = \Sigma' V(T_e^6 - T_{ph}^6) \tag{2.20}$$

We could fit our $I_r(T)$ curve using $\Sigma' = 5.5\,10^{-8} W\,\mu m^{-3}K^{-6}$ (Fig. 2.11). This Σ' value is in good agreement with the one found by Karvonen et al., $\Sigma' = 6\,10^{-8} W\,\mu m^{-3}K^{-5}$.
We report in table 2.3 the best fitting values of Σ for both power laws and for the samples where we can observe an hysteresis over a large temperature range. In all those samples, we didn't find much differences between the fits for a T^5 or a T^6 power law, but only the value of Σ' for the sixth power dependence is consistent with previous measurements.
In conclusion, the heating hypothesis works quite well, if we accept a sixth power law for the phonon cooling and a coefficient $\Sigma' \sim 5\,10^{-8} W\,\mu m^{-3}\,K^{-6}$. It is however not clear why measurements of a sixth power law are so rare in standard normal metal films, (the power law observed is normally slower than T^5 [49] [61]) and what consequently is the peculiarity of our samples.
In the following sections, we then examine other possible causes of hysteresis.

2.4.3 Hysteresis: phase dynamics characteristic time τ_D

As we have seen in sec. 2.4, SIS junctions present hysteretic V(I) characteristics, due to their phase dynamics.
We then wondered if a similar mechanism could also explain the hysteretic V(I) curves of SNS junctions.
The parallel between SIS and SNS junctions, however, is not straightforward, since the geometrical capacitance of a SNS junction is very small (roughly $10^{-16}\,fF$) and the corresponding Q would be much smaller than one. We then expect to be in the overdamped regime, where the $V(I)$ curve is smooth

and non-hysteretic. Instead we observe sharp hysteretic transitions.
Y. Song [54] showed that a large hysteresis in superconducting weak links can be explained by the phase dynamics when replacing the relaxation time RC of a SIS junction with an effective relaxation time, given by $\hbar/\Delta$.
J. Warlaumont and R.A. Buhrman [59] used the approach of Y. Song to explain the hysteresis in SNS junctions. They found the effective relaxation time to be the Ginzburg-Landau time, proportinal to the diffusion time.
Following the suggestion of Ryazanov, we decided to try this approach for our long SNS junctions. But what should replace the RC relaxation time?
At first, we consider like [59] that the characteristic time in SNS junctions is the diffusion time τ_D. We take, like M. Tinkham, as characteristic resistance the normal state resistance R. We then define an effective capacitance C_{eff} such as $R\,C_{eff} = \tau_D$.
The plasma frequency and the quality factor become:

$$\omega_p(T) = \sqrt{\frac{2\,e\,I_c(T)}{\hbar C_{eff}}} = \frac{\sqrt{2b}}{\tau_D}\sqrt{\frac{I_c(T)}{I_c(0)}} \tag{2.21}$$

$$Q(T) = \sqrt{2b}\sqrt{\frac{I_c(T)}{I_c(0)}} \tag{2.22}$$

where

$$e\,R\,I_c(0) = b\,E_{Th} \tag{2.23}$$

Typical values for Q and C_{eff} are $Q \sim 4$ and $C_{eff} \sim 10\,pF$.
Since the quality factor determines the hysteresis (see eq.2.15), the retrapping current is given by:

$$I_r(T) = \frac{4}{\pi}\sqrt{\frac{I_c(0)}{2b}}\,\sqrt{I_c(T)} \tag{2.24}$$

The expected retrapping current for sample SQ-NbAu-S is shown in Fig. 2.12 (blue squares). We used $b = 10$, which is the coefficient expected from the ratio Δ/E_{Th}, also used in the low temperature fit of $I_c(T)$. The agreement in the $I_r(T)$ temperature dependence is not very good, even if the order of magnitude is well reproduced.
One could argue that the low temperature expression of $I_c(T)$ already didn't fit our data at the lowest temperatures, and that maybe the b coefficient we used is for some reason wrong.
But since we can see the saturation region in our experimental data, we know the value of $I_c(0)$ and we can directly measure the b coefficient; we find $b = 6.67$. The retrapping current dependence on temperature for this b is shown in Fig. 2.12. We find a little improvement at the highest temperatures,

but the general agreement is worse than with $b = 10$.
Of course, one could have expected from the start a failure of this simple model, since it is quite difficult to find a temperature independent I_r starting from the relation $I_r \propto \sqrt{I_c(T)}$ and knowing that $I_c(T)$ is exponential in T! However,it is noteworthy that this model predicted roughly the right order of magnitude of I_r.

2.4.4 Hysteresis: phase dynamics characteristic times: τ_{e-ph} and τ_D

A second attempt to attribute the hysteresis to the phase dynamics was motivated by an observation we made on long SNS Nb-Al samples, where the normal part is an Al wire measured at $T > T_c$ (see chap. 3).
When exciting those junctions at low frequency, we see an important change in their V(I) curves for $f > f_r$, where f_r is related to the electron-phonon rate of the Al (we find $\tau_{e-ph}^{-1} = 1.9\ 10^7\, T^3\, s^{-1}\, K^{-3}$).
We numerically solved the RCSJ model for quality factors Q between 1 and 10 (of the same order of magnitude of our experimental I_c/I_r) and in presence of an ac current (see sec.3.6.1).

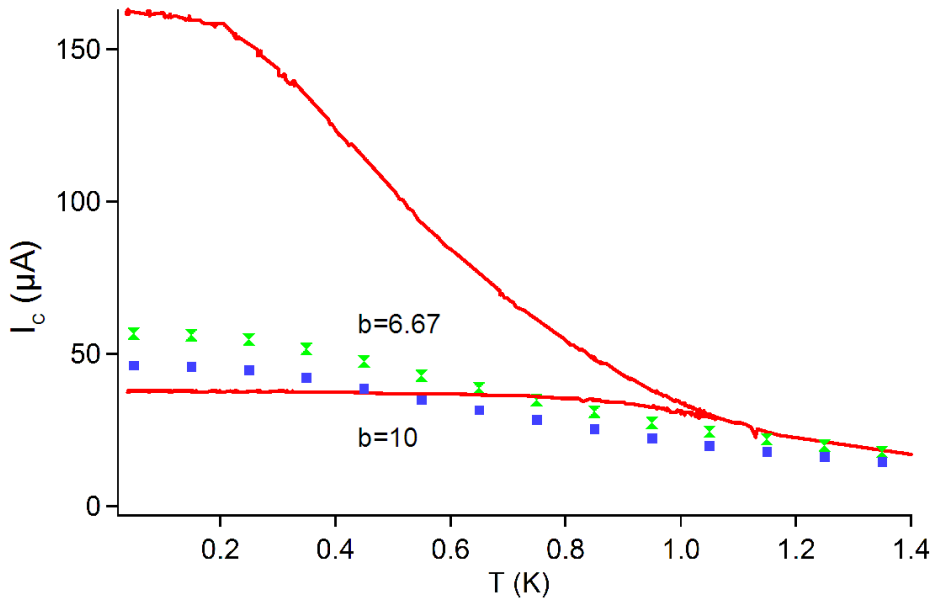

Figure 2.12: *Critical and retrapping currents of sample SQ-NbAu-S (red lines) and expected retrapping current when assuming the hysteresis given by the phase dynamics and the typical relaxation time given by* τ_D.

We observed in the calculated V(I) the same effect seen in the experiments, but this time at a characteristic frequency $2\,\pi\,f_r = 1/RC$.
This correspondence between simulations and experiments suggests a parallel between the RC relaxation time and the electron-phonon time.

Let's now suppose that the phase dynamics controls the behavior of long SNS junctions. We then define an effective RCSJ model, where the two characteristic times RC and ω_p^{-1} are replaced by their equivalent in the SNS junction:

- The relaxation time RC corresponds to the inelastic relaxation time, the electron-phonon time τ_{e-ph} at $T > 1\,K$
- What should correspond to the plasma frequency?

To answer this question, we trace the effective plasma frequency ω_p' for the Nb-Al samples:

$$\omega_p = \frac{Q}{RC} \;\longleftrightarrow\; \omega_p' = \frac{\frac{4}{\pi}\frac{I_c}{I_r}}{\tau_{e-ph}} \tag{2.25}$$

We find in the two different Nb-Al samples that ω_p' is practically constant, its relative variation being about $\sim 10\%$ (see table 2.4).
The effective plasma frequency could then correspond to a temperature independent characteristic time in SNS junctions. The more natural guess is the diffusion time τ_D.
The ω_p' for the Nb-Al samples seems indeed proportional to the Thouless energy $\hbar/\tau_D$: $\omega_p' \sim 0.01\,\tau_D^{-1}$.
Contradicting this guess is the fact that the ratio between the ω_p' in the two samples is not proportional to $(L_L/L_S)^2$ as expected. However, this could depend on these particular samples: the frequency f_c, which controls the high frequency behavior of the Nb-Al samples, and which is proportional to the Thouless energy (see chap.3), behaves in the same way.
In conclusion, the effective plasma frequency ω_p' could indeed be proportional to the diffusion rate.

We have then found two possible replacements for the time scales RC and $1/\omega_p$. Let's now see if they give reasonable prediction for the hysteresis in the other samples.
In general, we have three independent ingredients to introduce in the RCSJ model: $I_c(T)$, RC and ω_p. For the Nb-Al samples we measure, at high temperature, $I_c(T)$, $I_r(T)$ and τ_{e-ph}:

- $I_c(T) \;\longleftrightarrow\; I_c(T)$

- $RC \longleftrightarrow 1/f_r = \tau_{e-ph}(T)$
- $\omega_p(T) \longleftrightarrow \frac{4}{\pi}\frac{I_c(T)}{I_r(T)}\tau_{e-ph}^{-1} \rightarrow 0.01\,\tau_D^{-1}$

In the Nb-Au, W-Au and Al-Au samples, however, we don't access directly the inelastic rate τ_{in}. We start then from the assumption that the plasma frequency is indeed related to the Thouless energy. The correspondence between the RCSJ parameters and the experimental quantities is:

- $I_c(T) \longleftrightarrow I_c(T)$
- $\omega_p \longleftrightarrow \alpha\,\tau_D^{-1}$
- $RC \longleftrightarrow \tau_{in} = \frac{4}{\pi}\frac{I_c(T)}{I_r(T)}\frac{\tau_D}{\alpha}$

where we take $\alpha = 0.01$, like in the case of the Nb-Al samples.

To control the validity of these assumptions we can look at the effective RC time. We expect a time whose amplitude and temperature dependence are coherent with the inelastic time in Au.
Fig. 2.13 shows the effective RC time of sample SQ-NbAu-S, deduced from the diffusion rate and the experimental $I_c(T)$ and $I_r(T)$ curves, in the temperature region $40\,mK < T < 1\,K$, where the hysteresis is present. Note that these temperatures are much lower than in the case of the Nb-Al samples ($1.5\,K < T < 4\,K$).

At the highest temperatures the curve follows the power law $1/(A\ T^x)$, while at the lowest temperatures it saturates. The A and x coefficients for some samples are reported in table 2.5.

The electron-phonon rate expected for a moderate disordered thin Au wire is:

$$\tau_{e-ph}^{-1} \sim 2\ 10^8\ T^3 \tag{2.26}$$

sample	τ_D^{-1}	ω'_p	$\omega'_{p,S}/\omega'_{p,L}$	L_L^2/L_S^2	$f_{c,S}/f_{c,L}$
NbAl-S	29 GHz	280-310 MHz	2.7 - 3.3	3.8	2.43
NbAl-L	8.2 GHz	92-102 MHz			

Table 2.4: *Comparison between the diffusion rate of samples Nb-Al and the effective plasma frequency ω'_p. The ratio between the effective plasma frequencies of the short sample NbAl-S, $\omega'_{p,S}$, and the long sample NbAl-L, $\omega'_{p,L}$, is also compared to the square of the normal length ratio and to the frequency f_c ratio.*

sample	$A\ (s^{-1}\,K^{-x})$	x
SQ-NbAu-S	$1.28\ 10^8$	1.51
SQ-NbAu-L	$1.38\ 10^8$	1.6
WAu-Sq	$1.25\ 10^8$	1.5

Table 2.5: *Coefficients of the power law* $1/(A\,T^x)$ *fitting the high temperature dependence of the effective time RC, corresponding to the electron-phonon time.*

In a proximity superconducting structure, the electron-phonon rate, measured by Minghao Shen for a SNS junction with a disordered Au normal wire $12nm$ thick, $10\mu m$ long and $0.5\mu m$ wide, is:

$$\tau_{e-ph}^{-1} = 1.1\ 10^7\ T^2 \tag{2.27}$$

The relaxation rate we find is even slower than the one measured by Minghao Shen [53]. However, we are here at low temperature, and in particular at $T < 1\,K$, where the energy relaxation rate begins to be controlled by the electron-electron scattering rate.

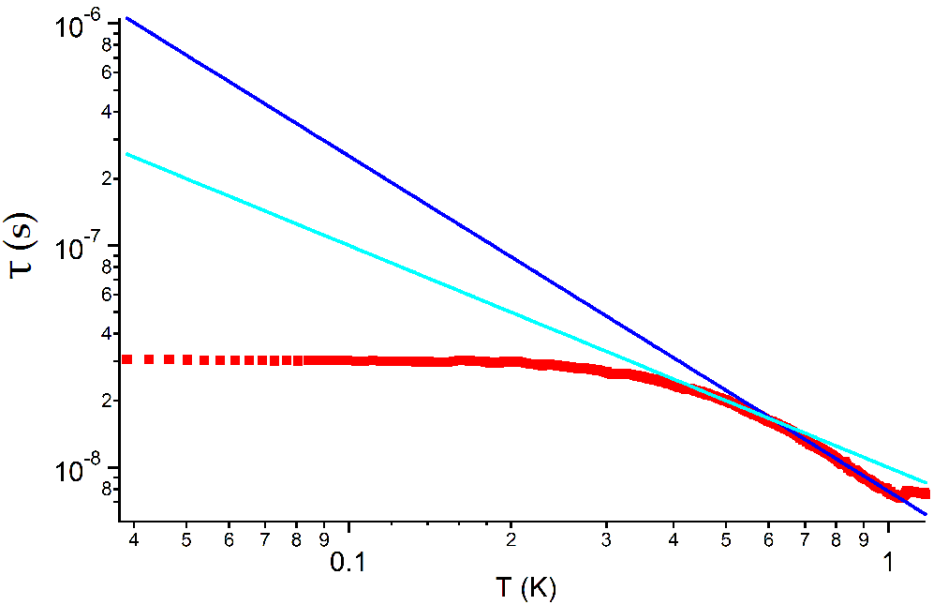

Figure 2.13: *Effective RC time for sample SQ-NbAu-S calculated from* $I_c(T)$, $I_r(T)$ *and* E_{Th} *(red squares). Blue line:* $1/(A\,T^x)$ *with* $A = 1.28\ 10^8$ *and* $x = 1.51$. *Light blue line:* $1/(A\,T^x)$ *with* $A = 10^8$ *and* $x = 1$.

The electron-electron time in a finite quasi-1D system is given by [6]:

$$\tau_{e-e}^{-1} \sim \frac{T}{g} \tag{2.28}$$

where g is the adimensional conductance.
This gives an inelastic rate increasing linearly with the temperature (x=1) and with $A \sim 10^{-7}$.
The relaxation time saturation for $T < 300\,mK$ could be due to the magnetic impurities in the normal wire. It has been shown by F. Pierre [45] that an electron-electron interaction mediated by the magnetic impurities could lead to an energy relaxation when the temperature is below $T = 500\,mK$ in a golden wire.

In conclusion, it is possible to interpret the hysteresis in SNS junctions as the result of the phase dynamics. An effective RCSJ model can describe our V(I) characteristic if we replace the plasma frequency ω_p by $\alpha\,\tau_D^{-1}$ and the relaxation time RC by, at $T \gtrsim 1\,K$, the electron-phonon time and at $T \lesssim 1\,K$, the inelastic time. At the lowest temperatures, the saturation could be explained by a relaxation time, constant in temperature, given by the magnetic impurities present in the Au wire.
Of course, this is at the moment only a possible interpretation, and even if the time obtained is consisten with a relaxation time, our hypothesis should be supported by more experiments to be confirmed.
However, this discussion highlights an important issue: what corresponds to the phase relaxation time in a SNS junction? Is it an elastic, or inelastic energy relaxation time? A charge relaxation time? A phase coherence time?

2.5 Transition temperatures

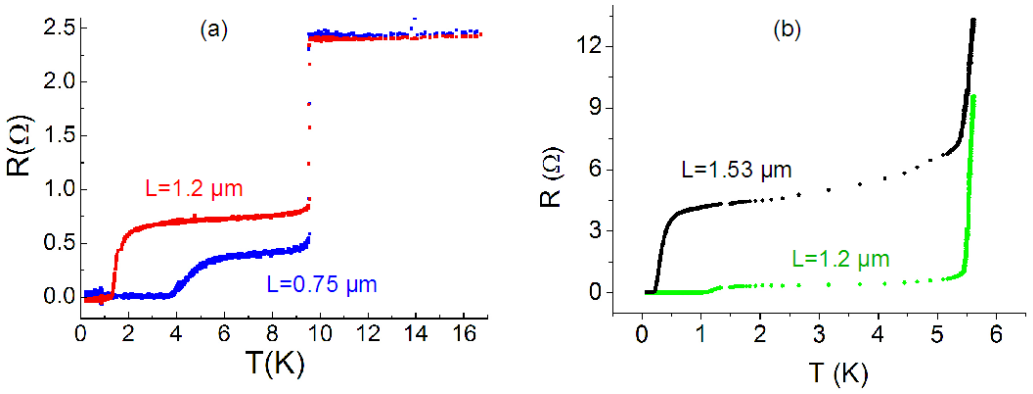

Figure 2.14: *Resistance vs Temperature while cooling: (a) samples SQ-NbAu-S (blue line) and SQ-NbAu-L (red line); (b) samples WAu-Sq (green line) and WAu-N (black line). Temperatures are only approximate above 4 K due to poor calibration of the thermometer in this range (for example, the W switches in the superconducting state around* $4\,K$*, while we read a transition of* $5.5\,K$*).*

We describe in this section the temperature transition towards the proximity induced superconducting regime.
The resistance vs. temperature curves are shown in Fig. 2.14 (a) for samples SQ-NbAu-L and SQ-NbAu-S and in Fig. 2.14 (b) for samples WAu-N and WAu-Sq. There is no qualitative difference between the SQUIDs and the wires behavior.
For all samples, when cooling, one can see two jumps in the R(T) curve. The resistance of the junction decreases abruptly a first time, when passing below the critical temperature of the superconducting contacts, then decreases slowly down to a point where the proximity effect extends to the whole normal region, and the resistance drops to zero. This second transition is often less abrupt than the one of the superconductor, and happens at a temperature strongly dependent on the normal wire length.

In a SIS junction, a supercurrent can flow through the junction only if the thermal fluctuations of the phase are small enough [1]. This means $k_B T \lesssim E_J = \frac{\hbar}{2e} I_c(T)$, where E_J is the Josephson energy.
As we have seen in sec. 2.4, E_J represents the height of the energy barrier that traps the phase. If $k_B T > E_J$, the phase fluctuates freely and is not defined any more.

sample	L (μm)	$T_{exp}(K)$	$T_2(K)$	$T_1(K)$
SQ-NbAu-L	1.2	1.3	1.19	0.2
SQ-NbAu-S	0.75	3.7	3.7	0.52
WAu-N	1.55	0.22	0.5	0.164
WAu-Sq	1.2	1.1	2	0.25
AlAu-b	1.25	0.54	0.62	0.18
AlAu-c	1.3	0.5	0.56	0.14

Table 2.6: *Temperature at which the normal part becomes proximity superconducting T_{exp} compared to the predicted transition temperatures.*

In a SNS junction, the Andreev pair coherence length is the minimum between the temperature coherence length L_T and the phase coherence length L_φ. At low temperature, L_T dominates. One could imagine that as soon as the coherence extends to the whole normal part, the junction becomes superconducting. This would correspond to a transition temperature $T_1 = 4\,E_{Th}/k_B$. We see in table 2.6 that T_1 is about from two to four times smaller than the experimental transition temperature.

We can then try to apply, to our SNS junctions, the argument used above for SIS junctions. The transition would then occur at a temperature T_2 for which $k_B\,T_2 = E_J(T_2)$.
The comparison between the transition temperatures observed T_{exp} and the temperature T_2 calculated from the measured critical current, are shown in table 2.6. The agreement is quite good, except for the WAu samples.
This discrepancy could be explained by an insufficient filtering during the cooling: the external noise could have heated the sample, lowering the transition temperature (we had indeed at the beginning of the experiment unexpected low critical currents that we increased when achieving a better control over the noise).

One should also note that in the experimental determination of the transition temperature, the role of the measurement current I_{meas} is important: the junction becomes superconducting only if $I_{meas} < I_c(T)$.

2.6 Fluctuations of the critical current

The critical current is a stochastic quantity, which means that the values at which the junction switches from the superconducting state to the normal state are characterised by a certain dispersion. This dispersion depends on the possible ways the phase can escape the tilted washboard potential described in section 2.4: at low temperature, quantum tunneling of the phase is possible, while at high temperature the thermal fluctuations cause the phase escape.
We measure the critical current histograms by repeatedly sweeping linearly the current from a slightly negative value to $I > I_c$ at a frequency of 65 Hz. We record the time at which a voltage appears across the junction, time which is proportional to the switching current.
An example of the obtained asymmetric histograms is shown in Fig. 2.15.

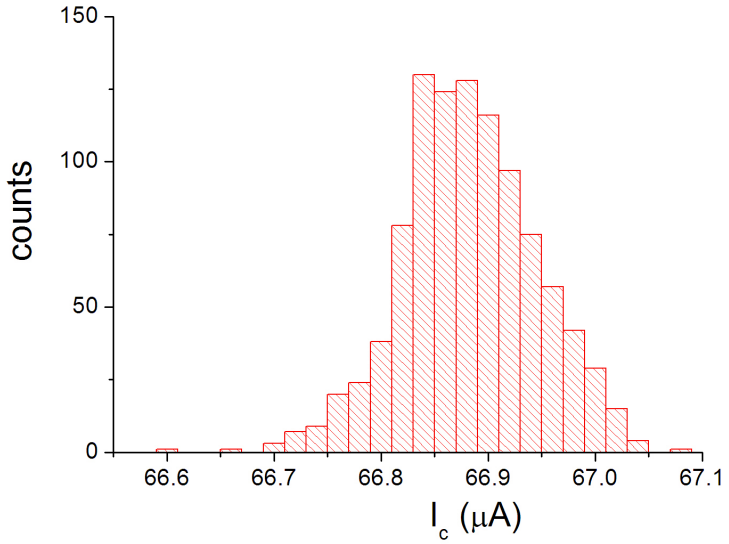

Figure 2.15: *Sample SQ-NbAu-L critical current histogram at T=17 mK, for 1000 counts and* $f = 65\,Hz$.

We have measured the width of the hystograms ΔI at half height (when fitting the hystogram with a gaussian probability, the half height width is a good approximation of the standard deviation SD).
The relative width is $\Delta I_c/I_c < 1\ 10^{-3}$ for SQ-NbAu-S and $\delta I_c/I_c \sim 5\ 10^{-3}$ for SQ-AlAu-a. These values are from 5 to 10 times smaller than the ones measured by Dubos et al. [19] on long SNS Nb-Cu junctions at $T \sim 1.3\,K$.
The temperature dependence of the histogram width is shown in Fig. 2.16 for sample SQ-NbAu-S and in Fig. 2.17 for sample SQ-AlAu-a.

In sample SQ-NbAu-S, the SD is constant up to T=0.7 K, then jumps down and slowly decreases; similarly, in sample SQ-AlAu-a, the SD decreases like the critical current up to T=100 mK, then jumps down and remains nearly constant.
We can compare our results to the histogram width dependence predicted for an underdamped SIS junction within the RCSJ model [26].
At first, let's calculate the escape rate Γ of the phase. For an underdamped junction ($Q >> 1$), we have in the quantum tunneling regime

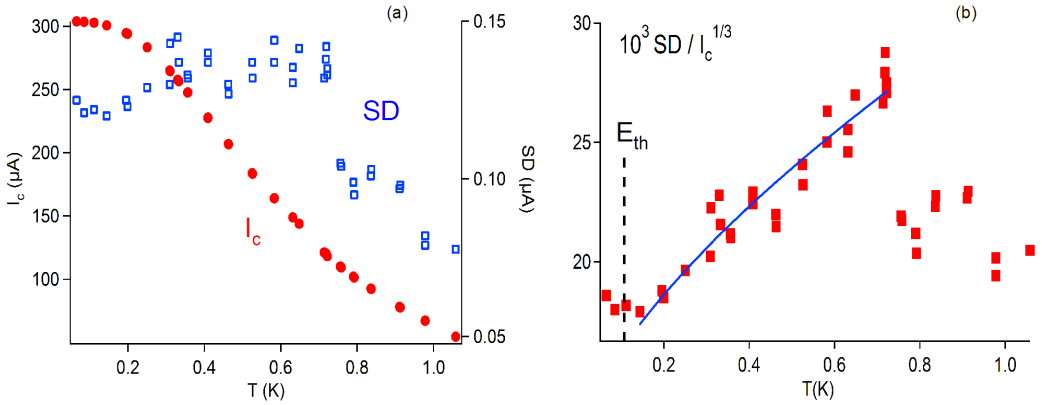

Figure 2.16: *Sample SQ-NbAu-S (a) critical current vs temperature (left scale) compared to SD vs. temperature (right scale); (b)* $10^3 SD/I_c^{1/3}$ *vs. temperature. The blue fit corresponds to* $10^3 SD/I_c^{1/3} = 12.35 + 18.37\,T^{2/3}$.

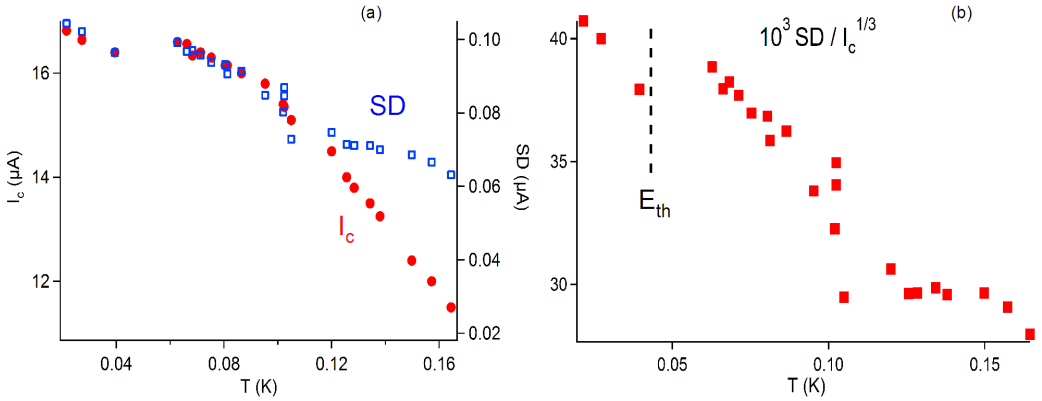

Figure 2.17: *Sample SQ-AlAu-a (a) critical current vs temperature (left scale) compared to SD vs. temperature (right scale); (b)* $10^3 SD/I_c^{1/3}$ *vs. temperature.*

($T < \hbar\omega_p/(2\pi k_B)$) the law:

$$\Gamma_Q = 12\sqrt{6\pi}\,\frac{\omega_p}{2\pi}\sqrt{\frac{\Delta U}{\hbar\omega_p}}\,e^{-7.2\,\Delta U/(\hbar\omega_p)} \tag{2.29}$$

while in the thermal activated regime ($T > \hbar\omega_p/(2\pi k_B)$), the escape rate is:

$$\Gamma_T = a\,\frac{\omega_p}{2\pi}\,e^{-\Delta U/(k_B T)} \tag{2.30}$$

where $a \sim 1$.
The barrier height ΔU and the plasma frequency are:

$$\Delta U = \frac{4}{3}\frac{I_c\Phi_0}{2\pi}\left(1-\frac{I}{I_c}\right)^{3/2} \qquad \omega_p = \sqrt{\frac{2\pi I_c}{\Phi_0 C}}\left(1-\frac{I^2}{I_c^2}\right)^{1/4} \tag{2.31}$$

These rates are related to the escape probability by:

$$P(I) = \frac{\Gamma(I)}{\dot{I}}\,e^{-\int_0^I \Gamma(I)/\dot{I}dI} \tag{2.32}$$

One can then calculate the width of the critical current histogram, which in the tunnel regime is:

$$\Delta I_c \propto I_c^{3/5} \tag{2.33}$$

while in the thermal activation regime we find a width:

$$\Delta I_c \propto I_c^{1/3}\,(k_B T)^{2/3} \tag{2.34}$$

Fig. 2.16 and 2.17 (b) show the ratio $\Delta I_c/I_c^{1/3}$ as a function of temperature. In sample SQ-NbAu-S, the ratio $\Delta I_c/I_c^{1/3}$ between $T = 0.2\,K$ and $T = 0.7\,K$ agrees with the predicted the power law $T^{2/3}$, even if the best fit is linear in temperature. For $T < 0.2\,K$, both I_c and ΔI_c are constant, so that the ratio $\Delta I_c/I_c^{3/5}$ is also constant, as it is expected in the quantum tunneling regime. It is difficult to verify if we are indeed below $T = \hbar\,\omega_p/(2\pi\,k_B)$, because of the uncertainty of the ω_p definition in a SNS junction. We note however that the temperature corresponds well to the Thouless energy. We cannot explain the behavior for $T > 0.7\,K$.

In sample SQ-AlAu-a, a completely different behaviour is observed: the ratio $\Delta I_c/I_c^{1/3}$ initially decreases linearly with the temperature, slightly faster than the critical current, then, at $T = 0.12\,K$, it saturates.
We are still looking for a clear interpretation of our data.

2.7 Magnetic field dependence

We study in this section the variations of the critical current in a perpendicular magnetic field.
As for the conventional SIS dc SQUID, the SNS dc SQUID samples have a periodically oscillating critical current, whose period corresponds to a flux quantum $\Phi_0 = h/(2e)$ through the loop area S, as shown in Figs. 2.19 and 2.21. For all our samples, the oscillation period corresponds exactly to Φ_0/S, where S is the ring surface measured in the SEM images.
The relative oscillation amplitude, defined by $(I_{c,max} - I_{c,min})/I_{c,max}$, which is 100% in a symmetrical SQUID, varies in our samples from 46% to 87%. We explain this imperfect modulation by considering the geometrical differences between the two junctions in a model developed for SIS junctions.
There are, however, features of the field dependence that differ strongly from the SIS case. For instance, the absence in nearly all our samples of the Fraunhofer-like oscillations of $I_c(H)$ at high field: the decay is monotonous and practically Gaussian with a field scale of approximately one flux quantum through the normal wire. We show that the aspect ratio L/w controls the high field behavior of the critical current.

2.7.1 Low field behavior

We now focus on the SQUID interference patterns, that causes the oscillations with a period Φ_0/S.
We can explain every feature of our curves by using a model developed by C. D. Tesche, V. Lefevre-Seguin and F. Balestro [55] [38] [4] for a SIS dc SQUID.
Let's start by analysing what happens to an ideal SIS dc SQUID in a perpendicular magnetic field (see Fig. 2.18 for a sketch).
The phase differences across the two junctions are: $\delta_1 = \varphi_{1,dn} - \varphi_{1,up}$ and $\delta_2 = \varphi_{2,up} - \varphi_{2,dn}$.
When we apply a magnetic flux, a screening current i_s flows into the ring, and the phase differences across the junctions 1 and 2 changes, according to the formula:

$$\delta_1 + \delta_2 = 2\pi \frac{\Phi}{\Phi_0} \tag{2.35}$$

The currents in each junction are then:

$$i_{s1} = i_s - i_1 = i_{c1} \sin \delta_1 \tag{2.36}$$

$$i_{s2} = i_s + i_2 = i_{c2} \sin \delta_2 = -i_{c2} \sin \left(\delta_1 - 2\pi \frac{\Phi}{\Phi_0} \right) \tag{2.37}$$

The total current in the SQUID is:

$$I = i_1 + i_2 = -i_{c1}\, sin(\delta_1) - i_{c2} \sin \left(\delta_1 - 2\pi \frac{\Phi}{\Phi_0} \right) \tag{2.38}$$

and the critical current I_c is its maximum:

$$I_c = \sqrt{(i_{c1} - i_{c2})^2 + 4\, i_{c1}\, i_{c2}\, \cos^2(\pi\Phi/\Phi_0)} \tag{2.39}$$

This simple analysis applies well to the field dependence of sample SQ-AlAu-c: just taking into account the asymmetry in critical current of the two junctions (respectively $i_{c1} = 2.121\mu A$ and $i_{c2} = 2.684\mu A$), we obtain a very good agreement (see Fig. 2.19).

In general, for SQ-AlAu samples, the increase of the minimal critical current (the non perfect modulation), is mainly due to the asymmetry in critical current. This asymmetry is easy to explain, since little differences in the geometry of the normal wires give large differences in the critical current,

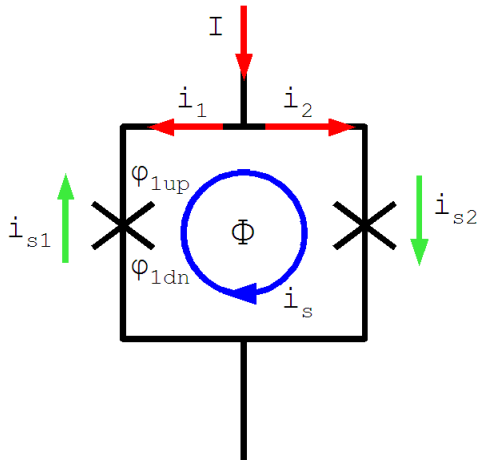

Figure 2.18: *Scheme of a dc SQUID. I is the bias current, splitted in the two branches in i_1 and i_2, $\varphi_{1,up}$ and $\varphi_{1,dn}$ are the superconducting phase before and after the Josephson junction, Φ is the magnetic flux in the ring and i_s is the supercurrent screening the flux.*

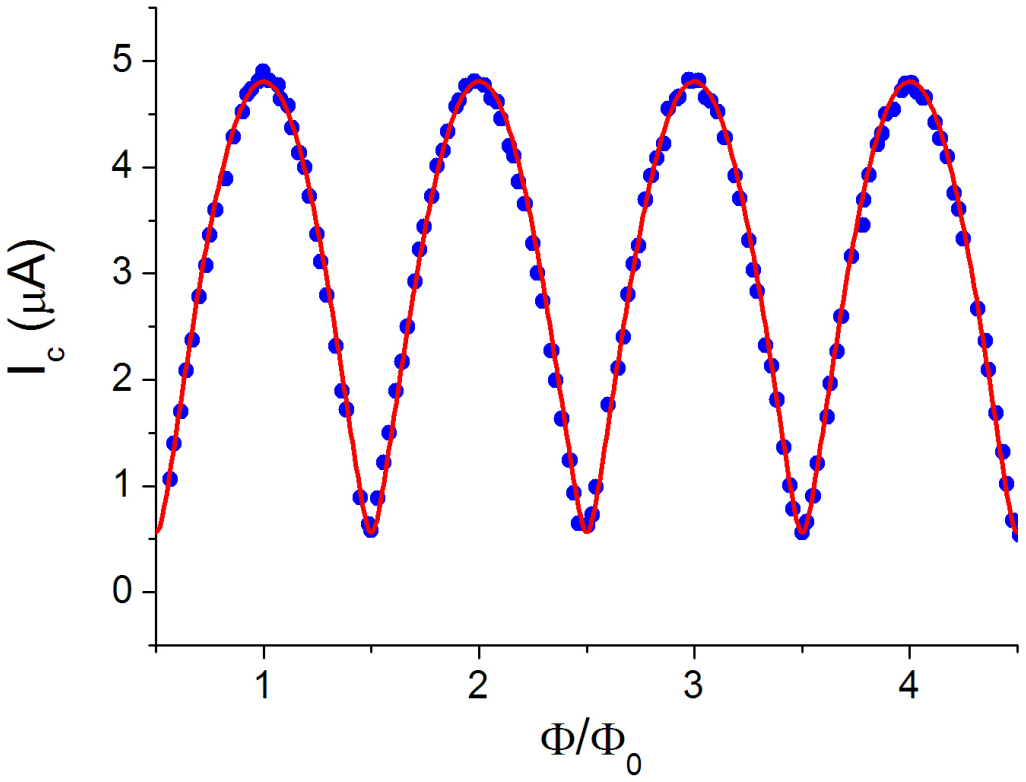

Figure 2.19: *Critical current vs normalised flux* Φ/Φ_0 *for sample SQ-AlAu-c. The fit takes into account the asymmetry in critical currents described in eq. 2.39, with* $i_{c1} = 2.121\mu A$ *and* $i_{c2} = 2.684\mu A$.

which scales like $1/L^3$.
For other samples such as SQ-NbAu, instead, we cannot obtain a satisfactory fit even when considering asymmetric critical currents.
This disagreement can be due to a finite SQUID inductance: the applied flux is screened by the inductances $\mathcal{L}_1$ and $\mathcal{L}_2$ of the two branches of the ring by $\delta\Phi = \mathcal{L}_1 i_{s1} + \mathcal{L}_2 i_{s2}$.
In symmetric SQUIDs with $\mathcal{L}_1 = \mathcal{L}_2 = \mathcal{L}$ and $i_{c1} = i_{c2} = i_c$, the screening flux is:

$$\delta\Phi = \mathcal{L}\, i_c \left(\sin(\delta_1) + \sin(\delta_2)\right) = \mathcal{L}\, i_c \left(\sin(\delta_1) - \sin(\delta_1 - 2\pi\Phi/\Phi_0)\right) \qquad (2.40)$$

We can see that the two contributions cancel each other when the flux imposed in the ring is a multiple of Φ_0, while for a multiple of $\Phi_0/2$ the flux screening is maximal. At Φ_0 we don't expect any effects on the maximum critical current, while around $\Phi_0/2$, we expect the most important change.
In asymmetric SQUIDs, instead, the whole $I_c(\Phi)$ curve is modified.

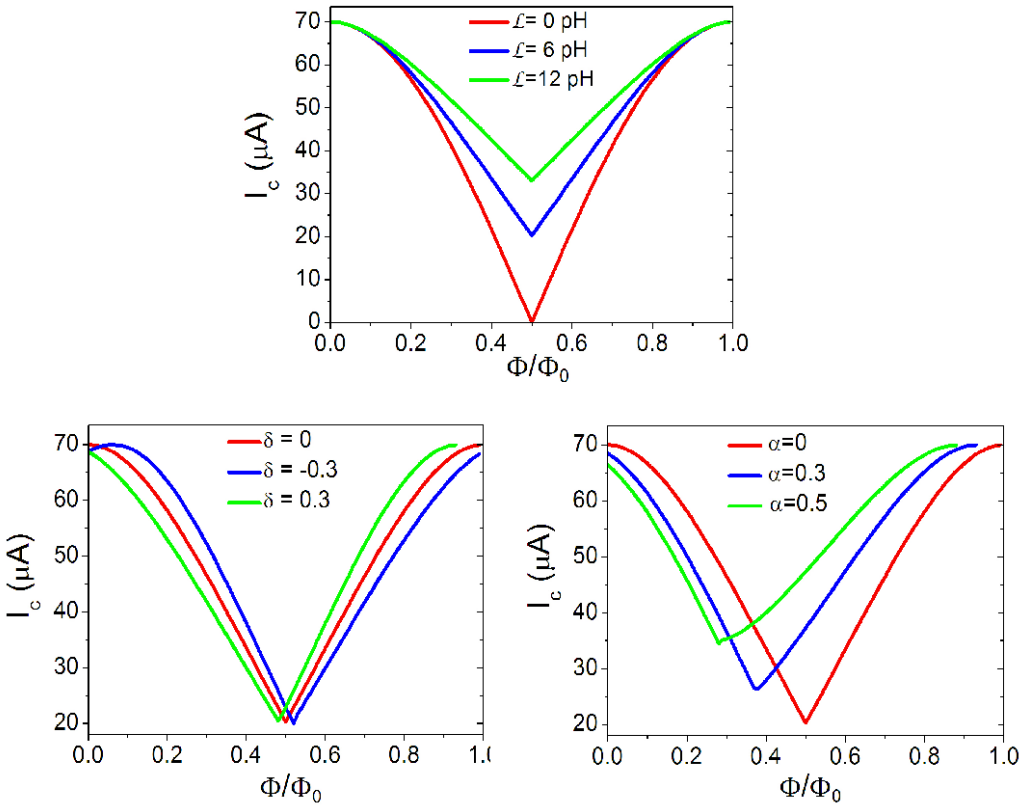

Figure 2.20: *Numerical simulations to understand the tilting and scaling of our $I_c(\Phi/\Phi_0)$ curves. The critical current of the SQUID is $I_c = 70\mu A$. (a) Effects of a global inductance: $\alpha = \delta = 0$, $\mathcal{L} = 0$, $\mathcal{L} = 6pH$, $\mathcal{L} = 12pH$; (b) effects of an inductance asymmetry: $\alpha = 0$, $\mathcal{L} = 6pH$, $\delta = -0.3$, $\delta = 0$ and $\delta = 0.3$; (c) effects of a critical current asymmetry: $\delta = 0$, $\mathcal{L} = 6pH$, $\alpha = 0$, $\alpha = 0.3$ and $\alpha = 0.5$*

We show in Fig. 2.20 how a finite inductance $\mathcal{L}$, an asymmetry in inductance $\delta = (\mathcal{L}_2 - \mathcal{L}_1)/\mathcal{L}$, and an asymmetry in critical current $\alpha = (i_{c2} - i_{c1})/(i_{c2} + i_{c1})$ modify the simple $I_c(H)$ dependence of a SIS dc SQUID. For these numerical simulations we follow the analysis of C. D. Tesche, V. Lefevre-Seguin and F. Balestro [55] [38] [4] for a SIS dc SQUID. We can see that the effect of a global inductance, just like the effect of an asymmetry in critical current, is to increase the minimal value of I_c, reducing the modulation amplitude; this effect is maximum around the odd multiples of $\Phi_0/2$.
When an inductance asymmetry is present, the maximum and the minimum of I_c don't change but their position in flux do. The change is maximum near the multiples of Φ_0.

Finally, a critical current asymmetry in an inductive SQUID changes the minimum of I_c, and shifts both its maximum and minimum (see Fig. 2.20).
In Fig. 2.21 we show the field dependence of sample SQ-NbAu-L, fitted by

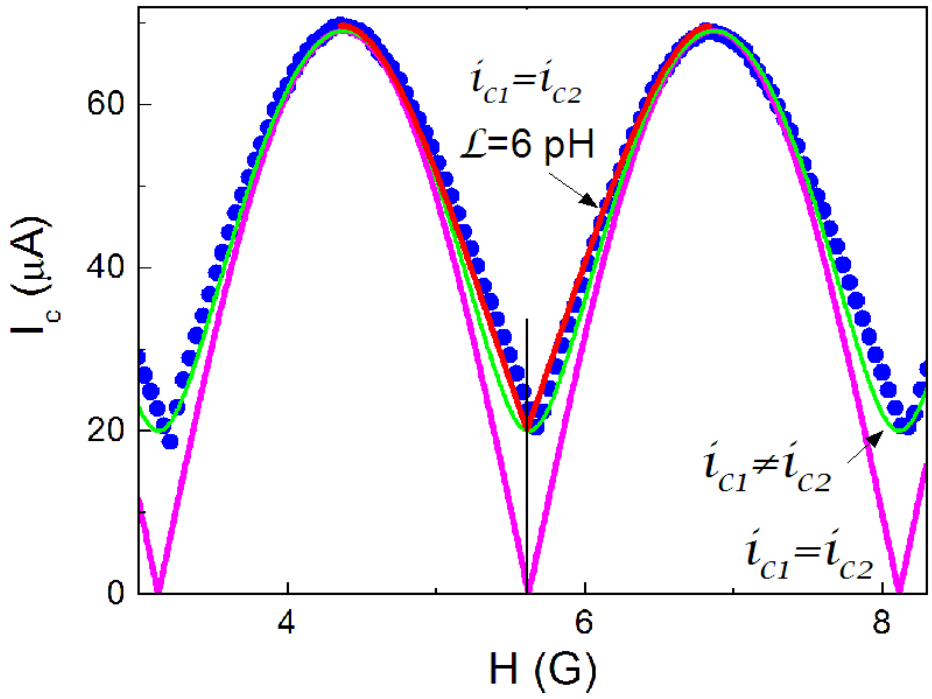

Figure 2.21: *Critical current vs. magnetic field for sample SQ-NbAu-L. Pink line: symmetric SQUID with* $i_{c1} = i_{c2} = 34.5\mu A$. *Green line: fit for a critical current asymmetry given by* $i_{c1} = 47.5\mu A$ *and* $i_{c2} = 21.5\mu A$. *Red line: fit for a symmetric SQUID (*$i_{c1} = i_{c2} = 34.5\mu A$*) with an inductance* $\mathcal{L} = 6pH$*; a slight deviation in the minima position is still visible, probably due to an inductance asymmetry.*

the $I_c(H)$ curve of a symmetric SQUID with a global inductance $\mathcal{L} = 6pH$. This self inductance corresponds well to the value deduced from the perimeter of the ring, using the conversion $1nH \Leftrightarrow 1mm$. The slight shift of the minimum critical current between the data and the fit is probably due to an inductance asymmetry (see Fig. 2.20).
It is easy to understand why we need to take into account the inductance in the SQ-NbAu samples and not in all the SQ-AlAu ones: since the critical current in the SQ-NbAu samples is more than ten times the one in the SQ-AlAu samples, the flux screening is bigger.
The effects due to the inductance are important when $2\pi\mathcal{L}\, I_c/\Phi_0 \sim 1$. At

low temperature, for SQ-NbAu-L, we have:

$$2\pi\frac{\mathcal{L}\,I_c}{\Phi_0} = 2\pi \times 6pH \times 70\mu A/\,2\;10^{-15}\,W \sim 1.3 \tag{2.41}$$

while for SQ-AlAu-c we have:

$$2\pi\frac{\mathcal{L}\,I_c}{\Phi_0} = 2\pi \times 10pH \times 5\mu A/\,2\;10^{-15}\,W \sim 0.15 \tag{2.42}$$

In some cases, the inductance, coupled to a critical current asymmetry, is clearly visible in the magnetic field dependence of the critical current. As we just saw, the asymmetry and anharmonic distortion of the periodic oscillations due to inductance effects are greater in the samples with the largest critical current. Fig. 2.22 shows the $I_c(H)$ curve of sample SQ-AlAu-a, which, being the shortest of the Al-Au samples, is the one with the highest critical current. In this sample, it is possible to see directly the tilting of the $I_c(H)$ curve due to the inductance.
Fig. 2.22 shows not only the critical current measured when increasing from zero the bias current (I_c^{up}) but also when decreasing it from zero (I_c^{dn}). One could be surprised to find those two curves asymmetric with the bias current ($I_c^{up}(H) \neq -I_c^{dn}(H)$).
However, reversing the direction of the time means reversing not only the direction of the current bias but also the direction of the field. We can then see that the time-reversal symmetry still holds:

$$I_c^{up}(H) = -I_c^{dn}(-H) \tag{2.43}$$

One could also interpret the distortion in the SNS $I_c(H)$ curve as an intrinsic anharmonicity of the current-phase relation, not present in a SIS $I_c(H)$ curve: since the amplitude of the n_{th} harmonic is predicted to vary as $1/n^2$ [30], our precision would be sufficient to detect at least the first three harmonics.
However, it is possible to show that the critical current of a symmetric SNS dc SQUID is insensitive to even harmonics so that the harmonic content of the current-phase relation finally does not easily show up.
To calculate the critical current of a symmetric harmonic SQUID, with current-phase relation $I(\delta) = I_c \sin(\delta)$, we maximise the current I (see eq. 2.38):

$$I = -i_c\left[\sin(\delta_1) + \sin\left(\delta_1 - 2\pi\frac{\Phi}{\Phi_0}\right)\right] \tag{2.44}$$

The phases for which I_c is maximum are:

$$\delta_{1,max} = \frac{\pi}{2} + \pi\frac{\Phi}{\Phi_0} \qquad \delta_{2,max} = \frac{\pi}{2} - \pi\frac{\Phi}{\Phi_0} \tag{2.45}$$

If now we consider an anharmonic current-phase relation, and if we suppose that the maximum is still approximately at $\delta_{1,max}$ and $\delta_{2,max}$, the second harmonic is:

$$\begin{aligned} I^2(\delta_1 = \delta_{1,max}) &= -i_c^2\,[\sin(2\,\delta_{1,max}) + \sin(2\,\delta_{2,max})] \\ &= -2\,i_c^2\,\sin(\pi)\,\cos(2\pi\frac{\Phi}{\Phi_0}) = 0 \end{aligned}$$

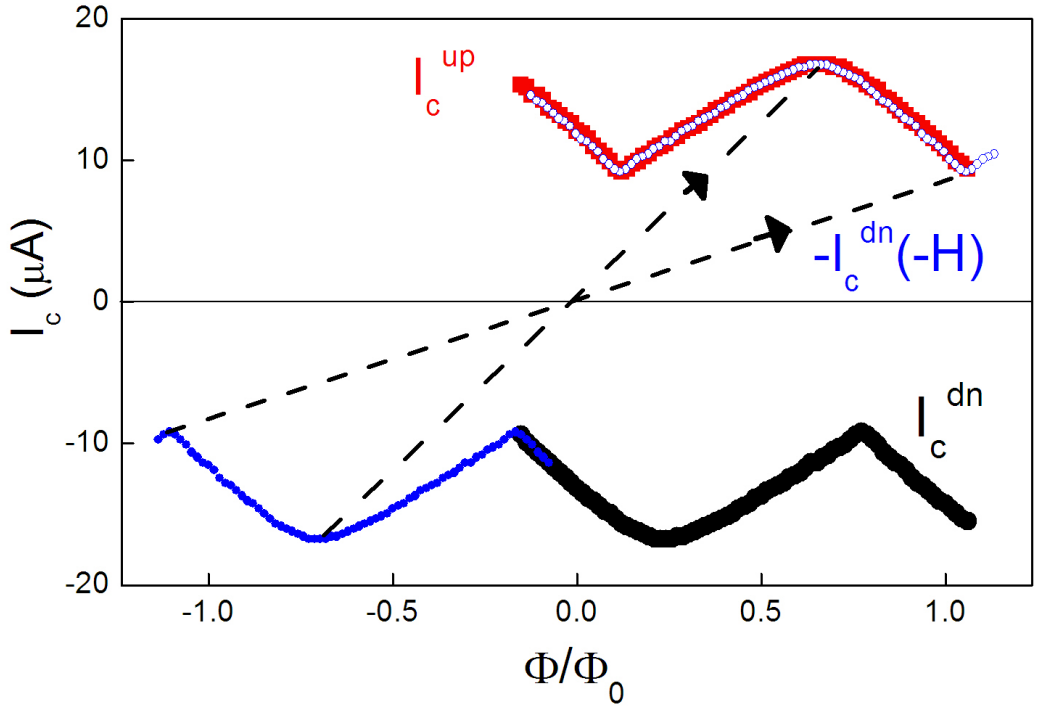

Figure 2.22: *Sample SQ-AlAu-a critical current vs. normalised flux in the SQUID ring. Red dots: I_c measured increasing the bias current from zero (up curve); black dots: I_c measured when decreasing the bias current from zero (dn curve); blue dots: periodisation of the dn curve; blue circles: blue period reflected around $\Phi = 0.0125\Phi_0$ (a small trapped flux can explain the shift of the zero).*

Similarly, we calculate the third harmonic:

$$\begin{aligned} I^3(\delta_1 = \delta_{1,max}) &= -i_c^3 \left(\sin(3\,\delta_{1,max}) + \sin(3\,\delta_{2,max})\right) \\ &= -2\,i_c^3\,\sin(3\pi/2)\,\cos(3\pi\frac{\Phi}{\Phi_0}) \\ &= 2\,i_c^3\,\cos(3\pi\frac{\Phi}{\Phi_0}) \neq 0 \end{aligned}$$

The critical current is then in the form:

$$I_c = 2\sum i_c^n \left|\cos\left((2n+1)\pi\frac{\Phi}{\Phi_0}\right)\right| \tag{2.46}$$

We can then see that only odd harmonics modify the $I_c(H)$ curve, making it more difficult to reconstruct the whole current-phase relation. Therefore, the best way to measure the various harmonics of the current phase relation of long SNS junctions is to directly measure the magnetic orbital response of a single junction SN ring, as was done by C. Strunk [25].

2.7.2 High field dependence

We consider now the dependence of the critical current at higher field scales, i.e. we study the envelope of the oscillations of the dc SQUIDs.
We will see that the SNS junctions, in contrast with the SIS junctions, offer the interesting possibility to explore a wide range of geometries, leading to a large variety of field dependences.

Let's start by considering the simple case of a large and thin SIS junction. When applying a magnetic field on a SIS junction, the field penetrates not only in the insulating layer but also in the superconducting contacts, over a length λ_L, called the London penetration length. $\lambda_{L,d} = \lambda_L\sqrt{\xi/l_e}$ is the penetration length in the dirty limit, $\lambda_L = \sqrt{\frac{2m}{\mu_0 n_s (2e)^2}}$ is the clean penetration length, $\xi = \sqrt{\frac{\hbar D}{\Delta}}$ is the superconducting coherence length and l_e is the elastic mean free path.
Cooper pairs are then dephased over a length $l = d + 2\lambda_{L,d}$ (d is the thickness of the insulating layer) when passing from a superconducting contact to the other.
In a perpendicular magnetic field $\vec{B} = B\hat{z}$, the vector potential is $\vec{A} = -By\hat{x}$,

and thus the field dependent phase shift is:

$$\Delta\theta = 2\pi\frac{2e}{h}\int_{-\lambda_{L,d}}^{d+\lambda_{L,d}} A_x dx = 2\pi\frac{2e}{h}B\,l\,y = 2\pi\frac{\Phi_J(y)}{\Phi_0} \tag{2.47}$$

where Φ_J is the flux in the surface of the normal wire $S_j = l\,w$.
The current density at y is then:

$$j = j_c\,\sin\left(\delta + 2\pi\frac{\Phi_J(y)}{\Phi_0}\right) \tag{2.48}$$

The current in the junction is obtained by integrating in y over the width of the junction and in z over the thickness of the junction. The critical current is its maximum:

$$I_c = I_c(0)\,\frac{\Phi_0}{\pi\Phi_J}\left|\sin\left(\frac{\pi\Phi_J}{\Phi_0}\right)\right| \tag{2.49}$$

which gives the Fraunhofer pattern shown in Fig. 2.24.
In a classical comparison, the Fraunhofer pattern corresponds to a diffraction pattern through a slit of the junction size, created by the interference between

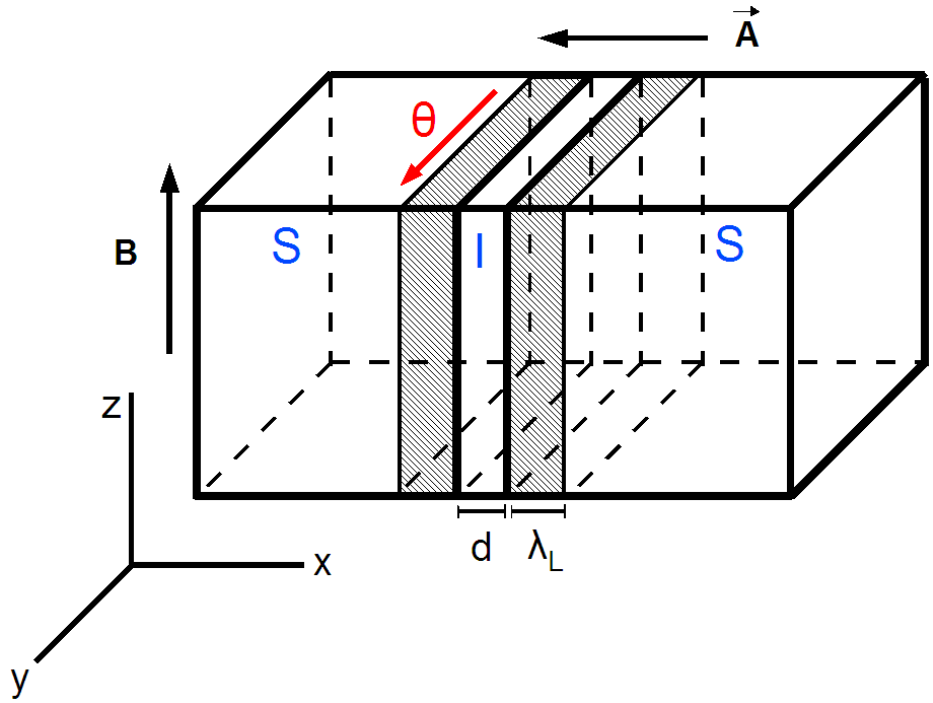

Figure 2.23: *Schematic view of a SIS junction in presence of a perpendicular magnetic field.*

the ballistic trajectories having different phases over the junction width. The characteristic flux for this diffraction is Φ_0/S_j.
The oscillations we have seen in the previous section are, on the other hand, due to an interference phenomenon between the trajectories passing in the two branches of the SQUID. The characteristic flux for this interference is Φ_0/S, where S is the surface of the ring hole.

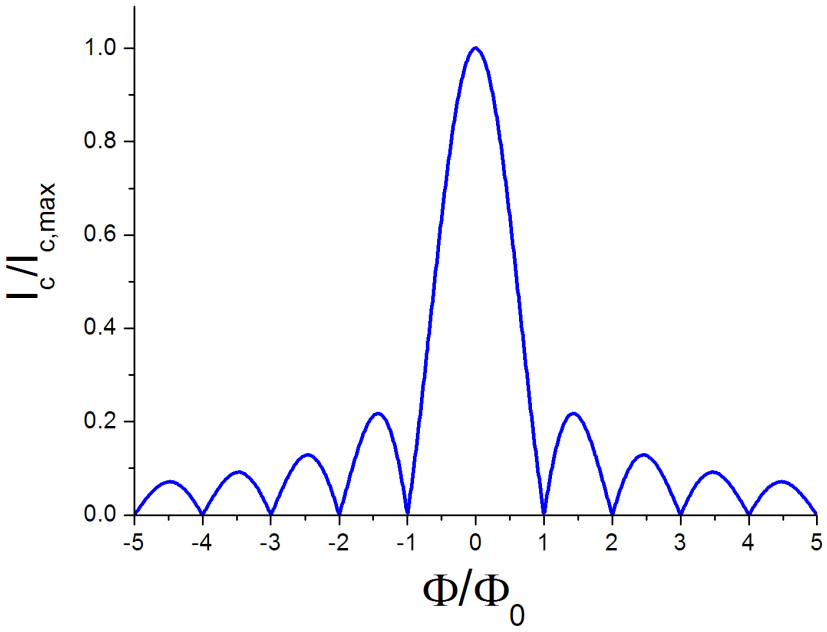

Figure 2.24: *Fraunhofer curve.*

If we now consider SNS junctions, we are not limited any more by a geometry adapted to the tunneling of Cooper pairs. We then expect strong differences between a large and thin or a long and narrow normal wire: in a large and thin junction, the phase difference between the trajectories comes from the phase distribution along the junction width, while in a narrow and long junction, the travel in the normal metal gives the main contribution to the dephasing.
Indeed, what we observe in Figg.2.25 and 2.26 for samples AlAu-a and SQ-NbAu-S is very different from the Fraunhofer pattern seen in a two-dimensional electron gas connected to Nb contacts [29] : I_c decreases with the field as a Gaussian function and never oscillates.
The general fit for our samples is:

$$I_c(\Phi/\Phi_0) = I_c(0)\, e^{-(\Phi/\Phi_0)^2/(2\sigma^2)} \tag{2.50}$$

where the parameter σ, roughly around one, is specified in Table 2.7 for different samples.

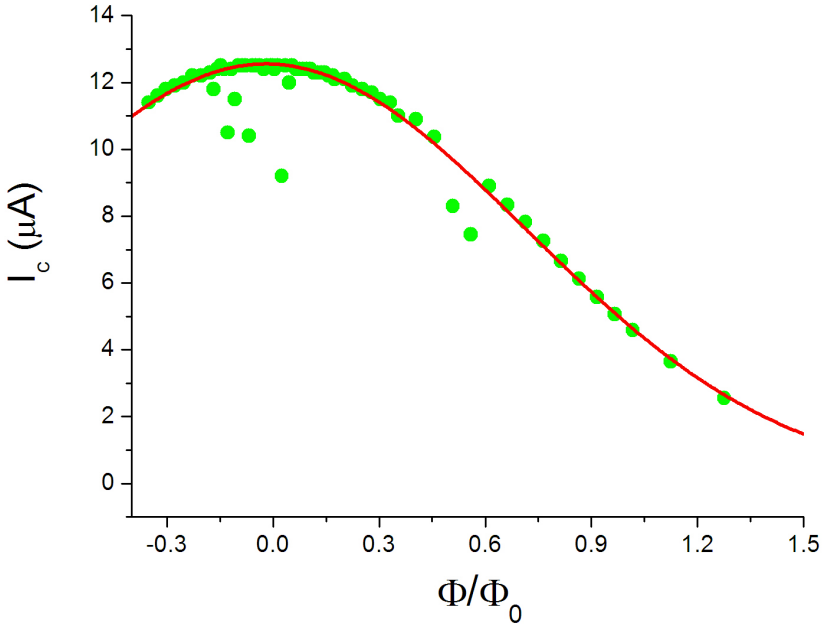

Figure 2.25: *Sample AlAu-a critical current vs normalised flux* $\Phi/\Phi_0 = H\,S_j/\Phi_0$. *The fit is a Gaussian function with* $\sigma = 0.735$.

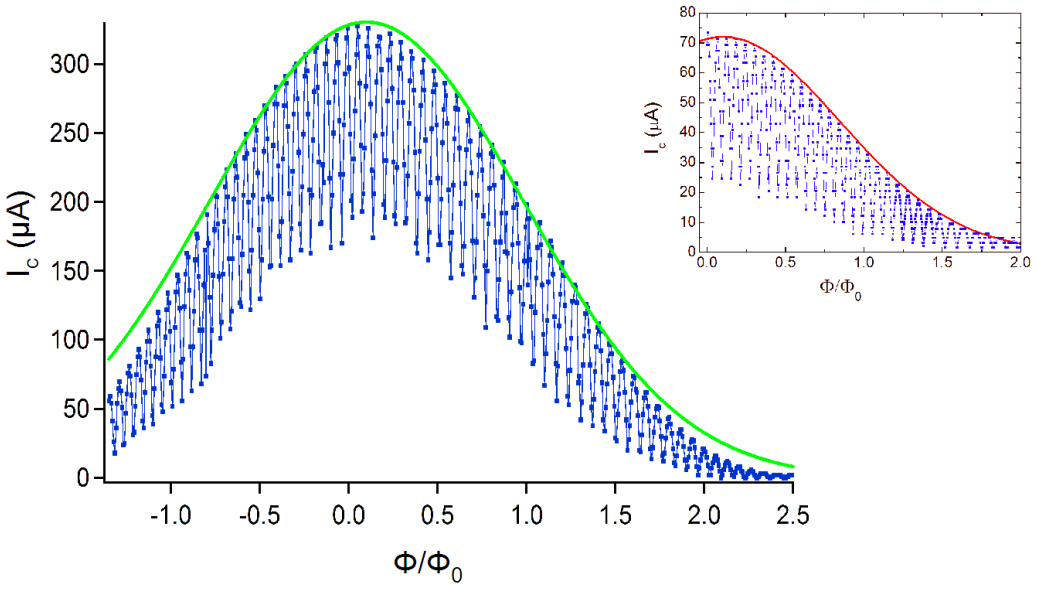

Figure 2.26: *Sample SQ-NbAu-S critical current vs. normalised flux* Φ/Φ_0 *in the surface junction. The fit is a Gaussian function with* $\sigma = 0.88$*. Unlike SQ-NbAu-L (inset), and the other Al-Au samples, the Gaussian fit is here worse at high fields.*

sample	L/w	L (μm)	σ
SQ-NbAu-S	1.875	0.75	0.88
SQ-NbAu-L	3	1.2	0.75
SQ-AlAu-a	6.9	0.9	1.43
AlAu-a	7.2	0.9	0.735
SQ-AlAu-c	9.5	1.9	1.83
AlAu-b	10	1.25	1.07
SQ-AlAu-b	10	1.5	1.8
AlAu-c	10.4	1.3	0.92

Table 2.7: *Comparison between the Gaussian standard deviation found in the fits and the geometrical properties of the samples, normal wire length L and aspect ratio L/w. No trend was found. The only deviation from a Gaussian law was the high field behavior of sample SQ-NbAu-S (see Fig. 2.26), which also has the smallest aspect ratio.*

To explain this behavior, a semi-classical model was developed with the help of G. Montambaux [41].
The aim is to model a long diffusive SNS junction, with $w << L << L_\phi, L_T$ (1D geometry), in presence of a perpendicular magnetic field $\vec{B} = -B\hat{z}$.
We can choose the gauge to have a vector potential $\vec{A} = B\,y\,\hat{x}$. The current density, supposing a harmonic current-phase relation, is then:

$$j = j_c \sin(\delta + \theta_{i,j}) \tag{2.51}$$

δ is the phase difference between the two superconducting contacts, independent of the position of i and j since in this long 1D geometry one can ignore the dephasing along the junction width in comparison to the one along the junction length.
$\theta_{i,j}$ is the phase taken along the trajectory starting at point i and finishing at point j.
The current is the average over all possible trajectories $\mathcal{C}_{i,j}$:

$$I \propto Im\left[< e^{i(\delta+\theta_{i,j})} >_{\mathcal{C}_{i,j}} \right] \tag{2.52}$$

Considering a reference trajectory 1-2 with a dephasing θ_a, we have $\theta_{i,j} = \theta_a + \Delta\theta_{i,j}$ (see Fig. 2.27)

$$I \propto Im\left[e^{i(\delta+\theta_a)} < e^{i\Delta\theta_{i,j}} >_{\mathcal{C}_{i,j}} \right] \tag{2.53}$$

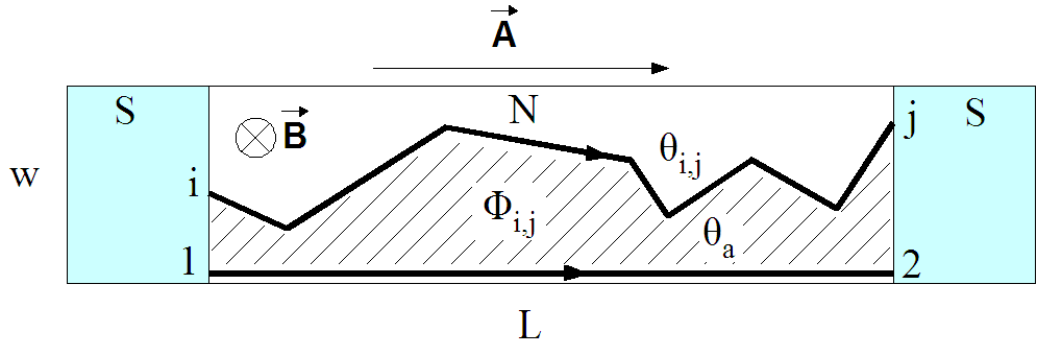

Figure 2.27: *Scheme of the 1D model developped by G. Montambaux.*

The critical current is the maximum of the current I. The constant exponential term has amplitude equal to one:

$$I_c \propto \left| < e^{i\Delta\theta_{i,j}} >_{\mathcal{C}_{i,j}} \right| \tag{2.54}$$

Since there is a great number of possible trajectories, because of the central limit theorem we can suppose that the distribution of the trajectories length is gaussian. The phases $\theta_{i,j}$ of each trajectories follow then also a gaussian distribution. We obtain:

$$I_c \propto \left| e^{-<(\Delta\theta_{i,j})^2>_{\mathcal{C}_{i,j}}/2} \right| \tag{2.55}$$

where $\Delta\theta_{i,j} = \theta_{i,j} - \theta_a$ is:

$$\Delta\theta_{i,j} = \frac{2e}{\hbar}\left[\int_i^j A_x dx - \int_1^2 A_x dx\right] = \frac{2e}{\hbar}\oint A_x dx = \frac{2\pi}{\Phi_0} H\, S_{i,j} = 2\pi\frac{\Phi_{i,j}}{\Phi_0} \tag{2.56}$$

Introducing eq. 2.56 in eq. 2.55, we find that the critical current decays as a gaussian function:

$$I_c \propto \left| e^{-\,2\pi^2\, H^2\, \alpha^2/\Phi_0^2} \right| \tag{2.57}$$

where

$$\alpha^2 = < S_{i,j}^2 >_{\mathcal{C}_{i,j}} \tag{2.58}$$

has the same order of magnitude of the normal wire surface.
If the trajectories are ballistic, we have $\alpha^2 = S^2/3$. This gives:

$$I_c \propto \left| e^{-\,(2\pi^2/3)\,\Phi^2/\Phi_0^2} \right| \tag{2.59}$$

So that, in a rough approximation, we expect a gaussian decay with $\sigma \sim 0.3$, which is 3-4 times smaller than the observed values.
The exact calculation describing the diffusion of trajectories from point i to point j gives however a slightly different distribution for the trajectories. The final magnetic flux dependence is:

$$I_c = I_c(0) \frac{\frac{\pi}{\sqrt{3}} \frac{\Phi}{\Phi_0}}{sinh\left(\frac{\pi}{\sqrt{3}} \frac{\Phi}{\Phi_0}\right)} \tag{2.60}$$

The difference between this distribution and a Gaussian one is shown in

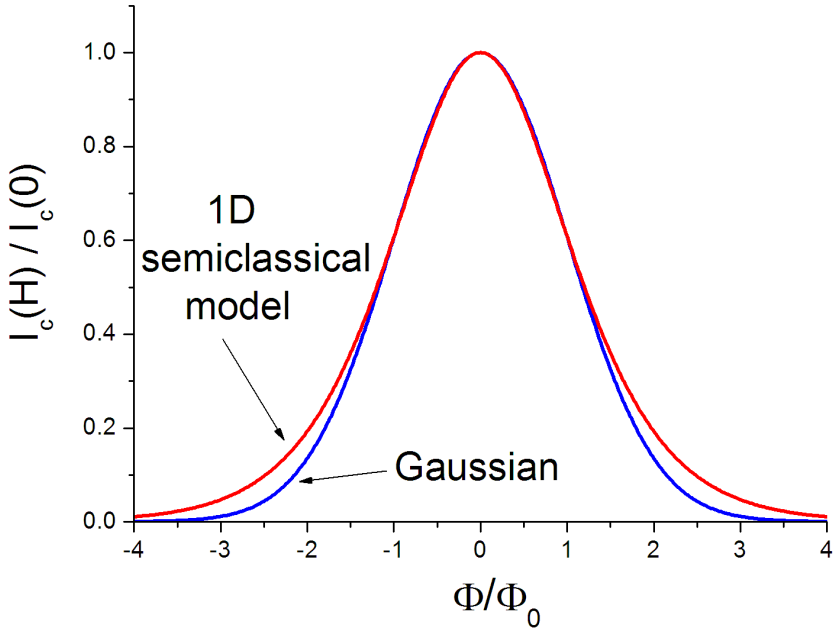

Figure 2.28: *Comparison between a Gaussian decay* $I_c(\Phi/\Phi_0)/I_c(0) = e^{-(\Phi/\Phi_0)^2/2}$ *(blue line) and the semi-classical 1D model decay of eq.2.60 found by G. Montambaux (red line).*

Fig. 2.28. This model reproduces the shape of our $I_c(H)$ curves, but the predicted field decay is slower than in our experimental results.
This semi-classical 1D model is however interesting for its qualitative prediction: the field dependence can strongly differ from a Fraunhofer pattern in a long, 1D geometry.

To study this influence of the geometry on the $I_c(H)$ curve, we designed two new samples with different aspect ratios: sample WAu-Sq, with aspect ratio L/w=0.7, and sample WAu-N, with aspect ratio L/w=4.5.
We can see at first in Fig. 2.33 and Fig. 2.32 that our intuition about the important role of the aspect ratio is good: the WAu-N sample shows a Gaussian decay like the other measured samples, while WAu-Sq sample, which has nearly a square geometry, shows oscillations which remind of a Fraunhofer pattern, even if with some differences (for example, the minima aren't exactly at multiples of a quantum flux).
J.C. Cuevas and F.S. Bergeret [13] have studied the influence of the aspect ratio on the critical current field dependence for a long, diffusive, SNS junction.
They have solved the 2D Usadel equation for different normal wire lengths and widths, at different temperatures, in the limit of high-resistance or low-resistance interfaces. They supposed a complete field penetration in the normal metal ($w < \lambda_{L,d}$), no Josephson currents screening, and the absence of inelastic scattering.
In the low-resistance interfaces (which applies well to our case), they have fixed the normal wire length in the limit of a long junction, and varied the width of the junction; they have found two very different cases for $w < L$ and $w > L$. These two regimes are described below and represented in Fig. 2.29.

- $w << L$: in this 1D limit (w very small), the field acts as a pair-breaking mechanism. It has the same effect than magnetic impurities, which cause spin-flip scattering and thus reduce the critical current. The critical current is then monotonically reduced: at T=0 we have $I_c(H)/I_c(0) \sim e^{-0.145\,\Gamma_H/E_{Th}}$, with $\Gamma_H = De^2H^2w^2/(6\hbar)$.

- $w >> L$ In this case, the main effect of the field is to affect the phase, which varies in the junction width. Linear arrays of proximity vortices appear in the normal wire; these vortices have the same properties than superconducting vortices, such as a normal core or a quantised flux inside the vortex. Because of the phase modulation, an interference pattern emerges, which is identical to a Fraunhofer pattern for a small enough aspect ratio ($L/w < 0.04$).

The authors don't suppose an harmonic current-phase relationship, but calculate the complete, anharmonic $I(\delta)$ relation of a long SNS junction. However, we see that the wide junction limit of SNS junctions corresponds exactly to the Fraunhofer pattern of SIS junctions.

J.C. Cuevas and F.S. Bergeret have then studied in detail the field dependence of the critical current in the case $w >> L$, when the magnetic field only changes the phase difference along the width of the junction. The expected field dependence is then:

$$I(H,\delta) = \sum_n I_n \frac{\sin(n\,\pi\,\Phi/\Phi_0)}{n\,\pi\,\Phi/\Phi_0}\sin(n\delta) \tag{2.61}$$

The harmonics amplitude strongly depends on temperature; at $T = 0$ the harmonic content is maximum, but we can see that even then the changes from a Fraunhofer pattern are very small (Fig. 2.30). We can then conclude that the high field dependence of the critical current is not appropriate to detect the harmonic content of the current-phase relation. In fact, neither the interference pattern of $I_c(H)$ in a SQUID structure (see section 2.7.1) nor

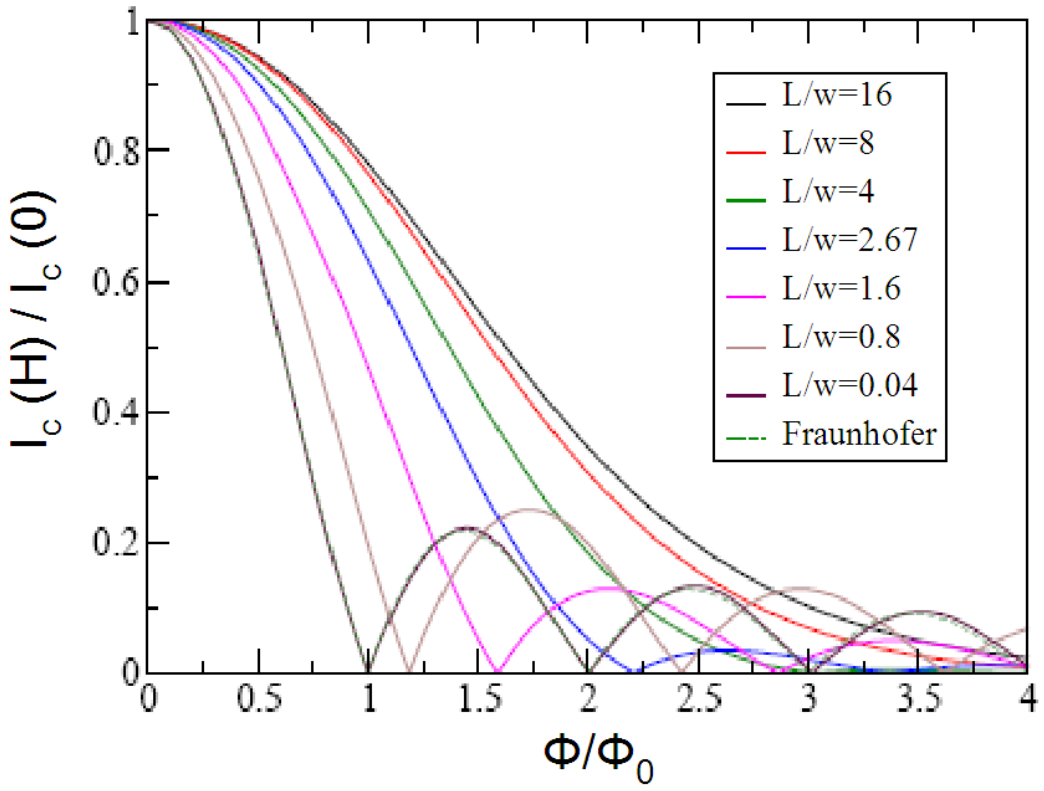

Figure 2.29: *Normalised critical current vs. normalised magnetic flux. The numerical simulation was done for* $L = 8\xi$, $k_BT = 0.01\Delta$, *perfect transparent SN interfaces and an aspect ratio varying from* $L/w = 0.04$ *to* $L/w = 16$. *[13]*

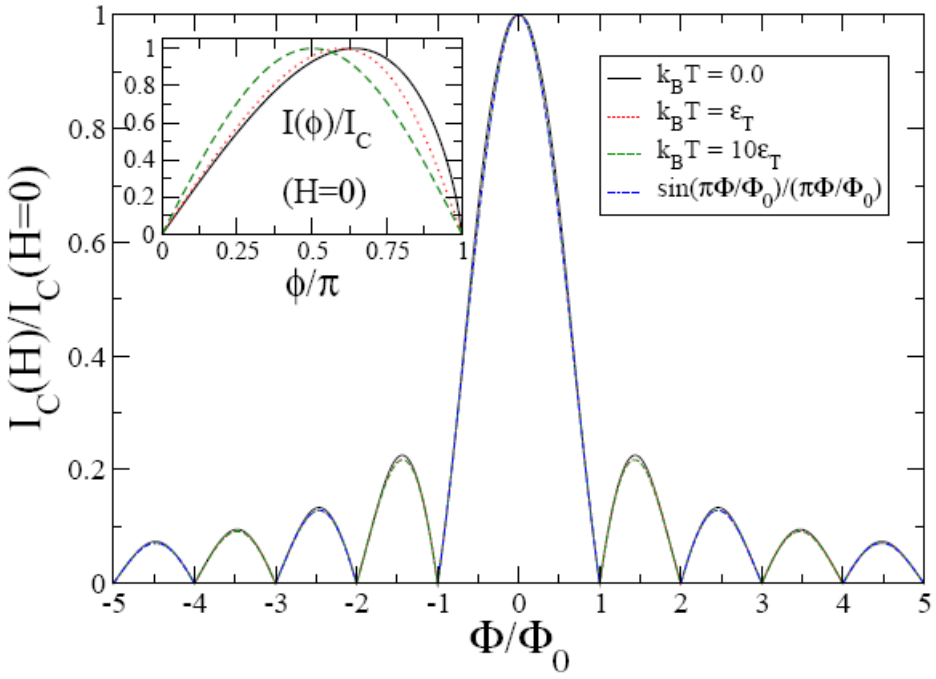

Figure 2.30: *Normalised critical current vs. normalised magnetic flux. For decreasing temperature, the harmonic content of the current-phase relationship $I(\Phi)$ (see inset) increases, but the magnetic field dependence is nearly unchanged from the Fraunhofer dependence of an sinusoidal $I(\Phi)$ (from F.S. Bergeret and J.C. Cuevas, unpublished).*

the diffraction pattern of $I_c(H)$ in SQUIDs and wires, show visible effects of the harmonic content.
As we see in next section, one possible way to access the harmonic content of $I(\delta)$ is to study the fractional Shapiro steps.

To understand completely our experimental $I_c(H)$, it is necessary to take into account not only the aspect ratio of the normal wire, but also the self inductance contribution, particularly important in the WAu-Sq sample (visible in the central peak of the $I_c(H)$ curve, which is tilted around its maximum). Fig. 2.31 shows how a Fraunhofer pattern is modified in presence of a self inductance (a) and when the aspect ratio passes from $L/w < 0.04$ (exact Fraunhofer pattern) to $L/w = 0.7$ (aspect ratio of sample WAu-Sq).

To calculate the effect of the self inductance we have used a model valid for a SIS junction in the case of a width $w > \lambda_L$ [5]. When the field can't completely penetrate, Josephson screening currents circulate in the normal

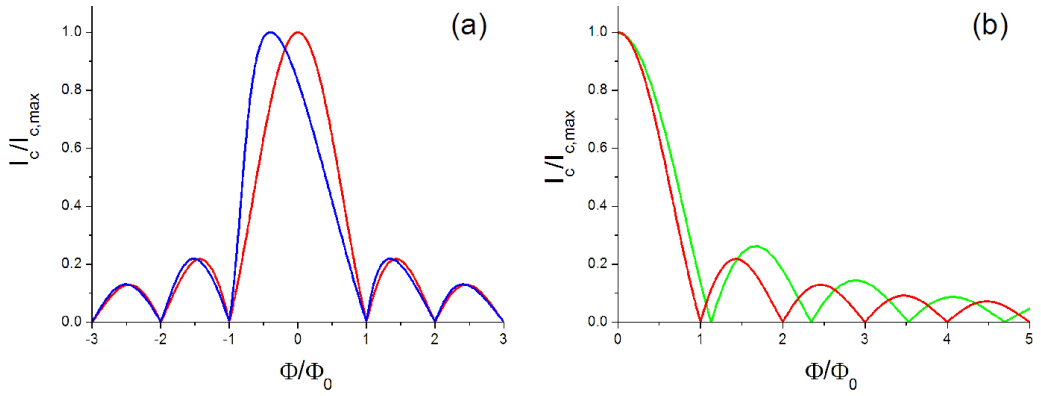

Figure 2.31: *Normalised critical current vs. normalised magnetic flux. Deviations from a Fraunhofer pattern (red line) for (a) an inductive junction (blue line) and (b) a junction with aspect ratio $L/w = 0.7$ (green line).*

part, and the total flux is the sum of the external flux Φ_e and the maximum screening flux that the junction can provide, $\Phi_L = b \times I_c(\Phi_e)$, where $b = \frac{1}{4\pi}(\frac{w}{\lambda_L})^2$. The critical current is then:

$$\frac{I_c(\Phi_e/\Phi_0)}{I_{max}} = \frac{\sin(\pi(\Phi_e/\Phi_0 + b\,\frac{I(\Phi_e/\Phi_0)}{I_{max}}))}{\pi(\Phi_e/\Phi_0 + b\,\frac{I(\Phi_e/\Phi_0)}{I_{max}})} \tag{2.62}$$

The b necessary to account for the inductance contribution in our data is $b = 0.4$. This corresponds to a London penetration length of $0.86\,\mu m$, large for a classic superconductor but reasonable for a proximity superconductor, where the density of pairs is smaller.

Fig. 2.32 shows the field dependence of WAu-Sq critical current: we can see oscillations, just like a Fraunhofer curve, that we had never seen before. When comparing it with the numerical simulation for $L/w = 0.7$, we find a good agreement in the position of the zeros for $H_{zero} = \Phi_0/S$, with $S = 3.45\mu m^2$. This, surprisingly, corresponds to the whole surface of the square normal metal, independently on where the contacts are.
Apart from the minima position, does the simulation fit the shape of our $I_c(H)$? It is difficult to see it, since the experimental curve has minima which do not go to zero for the first four periods. We have then rescaled the theoretical first period field dependence (light blue line), to make it correspond to our data amplitude, and we can now see that the shape is well reproduced. The amplitude of the next periods oscillations decreases however slower than predicted; this could be due to a non uniform current distribu-

tion in the normal metal [5].

The junction WAu-N has instead an aspect ratio of $L/w = 4.5$, big enough to kill the diffraction pattern (see Fig. 2.29). We can see in Fig. 2.33 that, indeed, all oscillations have disappeared, and that the $I_c(H)$ curves is a Gaussian function (red fit).
However, the field decay cannot be fitted by the numerical simulation for the corresponding flux scale Φ/Φ_0: we found a good fit only when decreasing the numerical simulation flux by a factor 2.5.
This can be explained by a non-perfect interface [28], with an interface resistance given roughly by $R_i = 2R_N$ (the ratio $R_i/R_N = 2$ leads to a rescaling

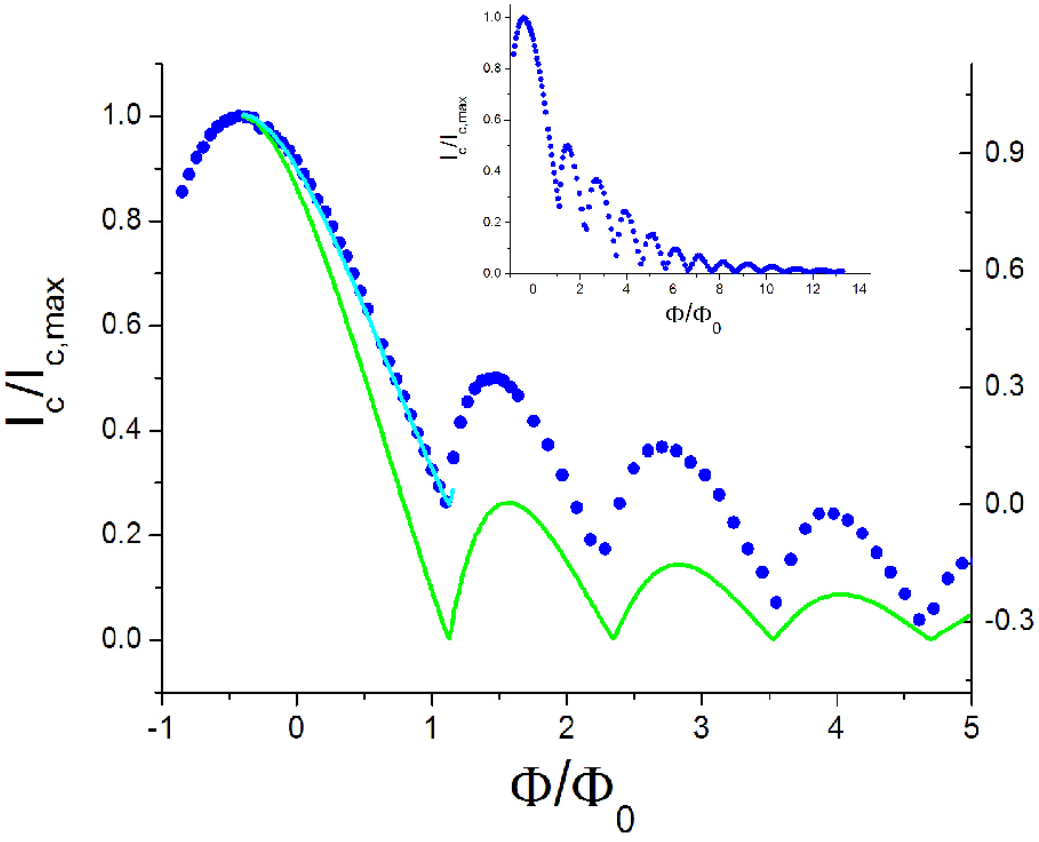

Figure 2.32: *Sample WAu-Sq normalised critical current vs. normalised flux. Green line: theoretical expectation for a junction with aspect ratio $L/w = 0.7$ and inductance given by the dimensionless parameter $b = 0.4$. Light blue line: theoretical curve scaled to fit the first period data amplitude. Inset: global view of $I_c(\Phi/\Phi_0)$.*

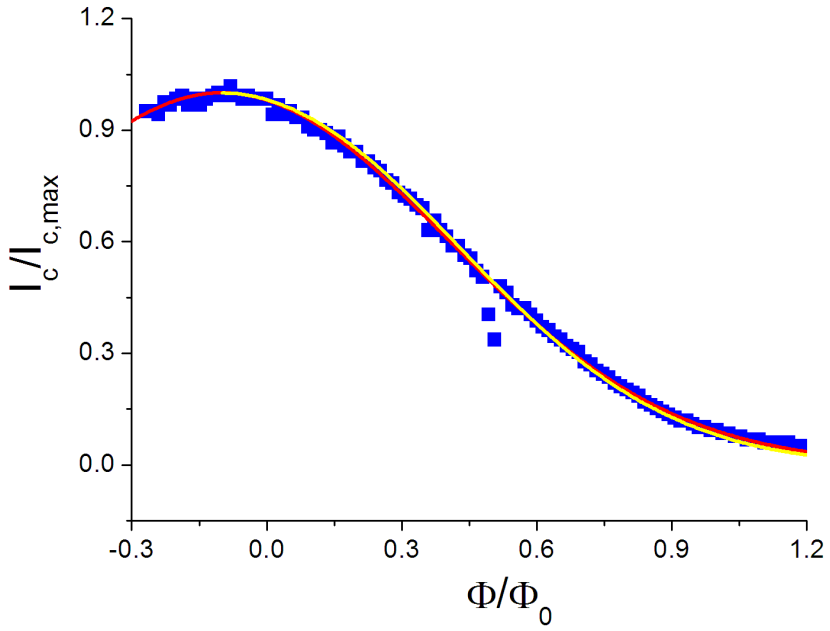

Figure 2.33: *Sample WAu-N normalised critical current vs. normalised flux. Red line: Gaussian function* $e^{-(\Phi/\Phi_0)^2/2*(0.5)^2}$. *Yellow line: numerical simulation of the 2D Usadel equation, where the flux has been rescaled by a factor 2.5.*

of the perfect interface flux by roughly a factor 2).
The origin of this non-perfect interface, may be attributed to the right W contact, which is just at the extremity of the golden wire (see the SEM image 2.4).

2.7.3 Reentrance at low magnetic field

We have observed in certain samples a quite puzzling reentrance of the critical current at low magnetic field ($H < 45\,G$) and low temperatures ($T < 100\,mK$ in sample SQ-AlAu-b).
The samples that present this reentrance are simple junctions or dc SQUIDs (see Fig. 2.34 and 2.35). They were made on different wafers at different moments and have all Al superconducting contacts. Their length varies from $1.25\,\mu m$ of sample AlAu-b to $1.5\,\mu m$ of sample SQ-AlAu-b.
The reentrance is reproducible and doesn't depend on the measurement

setup.
How to explain the field and temperature scales of the reentrance?
We have measured the temperature dependence of the reentrance only for sample SQ-AlAu-b. We find that the reentrance disappear above $T = 100\,mK$. This temperature scale could be connected to the sample mini-gap, $\tilde{\Delta} = 93mK$.
The reentrance disappears when increasing the magnetic field above $H = 32G$ ($\Phi = 0.36\Phi_0$) for sample SQ-AlAu-b, above $H = 43G$ ($\Phi = 0.33\Phi_0$) for sample AlAu-b and above $H = 37G$ ($\Phi = 0.3\Phi_0$) for sample AlAu-c. The field values are very similar, but since the surfaces of those three samples are also very similar, one cannot distinguish if the magnetic field scale is independent of the normal wire or on the contrary is determined by mesoscopic effects in the normal part.

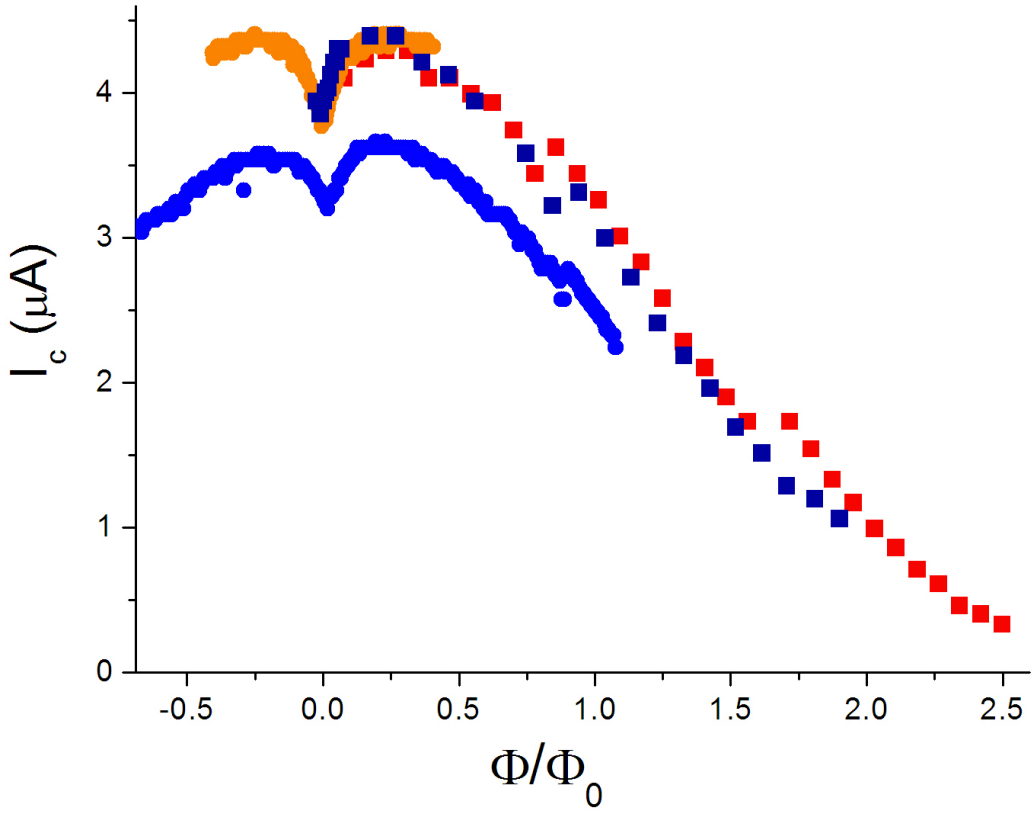

Figure 2.34: *Critical current vs. normalised flux for sample AlAu-b (blue and dark blue squares) and AlAu-c (red and orange squares). For both junctions two different measurements are shown; in the case of sample AlAu-b, the curves are shifted because of a temperature change.*

A possible explanation for the reentrance is the presence of magnetic impurities, causing spin-flips breaking the phase coherence. The magnetic field has two opposite effects on a superconductor: it breaks Andreev pairs, decreasing I_c, but also tend to align the impurities magnetic moments, suppressing the spin-flips and thus increasing I_c. This competition leads to an increase of the critical current for $H \lesssim 0.3\, k_B\, T_c/\mu_B$, above which the depairing is predominant, and for temperatures below $0.4\, T_c$ [60].
The amplitude of the predicted reentrance $\Delta I_c/I_c$ is of the same order of magnitude than our measurements. The temperature scale is also well reproduced when replacing to the T_c of the superconductor the temperature where the proximity superconductivity appears: $0.4\, T_{c,N} \sim 120\, mK$. There are however two problems with this explanation: one is the predicted field scale of the reentrance, $H \sim 2000\, G$; the other, less determinant, is the fact that samples evaporated at the same moment don't present the same features: why should one sample contain more impurities than the others?

A second hypothesis is that the reentrance is caused by a mesoscopic ef-

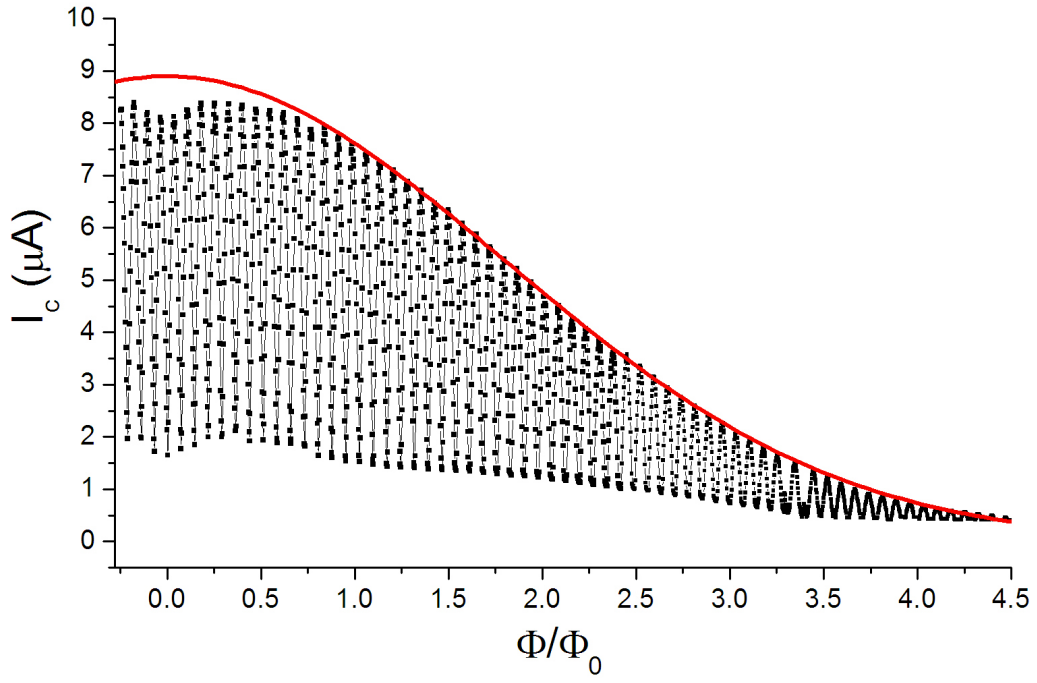

Figure 2.35: *Critical current vs. normalised flux for sample SQ-AlAu-b. Red line: Gaussian function* $I_c(\Phi/\Phi_0) = 8.9e^{-(\Phi/\Phi_0)^2/(2*(1.8)^2)}$.

fect, similar to the weak localization correction to the conductance at low fields.
The weak localization consists in the increase of the probability, at zero magnetic field, for an electron to reverse completely its momentum and come back at its starting point.
In a metallic diffusive coherent wire, at zero field, nearly all interferences are killed by an average over the disorder. Only survive the interferences between time-reversed paths. Thanks to them, the probability to come back at the starting point is twice the classical probability.
The presence of a magnetic field dephases these time-reversed trajectories, and decreases progressively the probability for an electron to come back, thus increasing the conductance.
The weak localisation characteristic field is $H = \Phi_{0,N}/S$, where $\Phi_{0,N} = h/e$ is the normal quantum flux and S is the surface perpendicular to the magnetic field. The characteristic change in conductance is $\Delta G = G_0 \times L_\Phi/L = 2e^2/h \times L_\Phi/L$.
We can then compare the magnitude of the critical current decrease to that of a weak localisation effect. Since at low temperature we are in a saturation regime, we have $RI_c = const$, and thus $\Delta I_c/I_c = \Delta G/G = \Delta G\, R$.
Experimentally, we measure $\Delta I_c/I_c = 14.4\%$ for sample AlAu-b, $\Delta I_c/I_c = 12.3\%$ for sample AlAu-c and $\Delta I_c/I_c = 3.5\%$ for sample SQ-AlAu-b, values one or two order of magnitude larger than the expected $\Delta G/G \sim 0.5\%$.
The magnetic field scales also don't correspond: we measure values three times smaller than the predicted Φ_0/S.
In conclusion, we haven't yet found a satisfactory theory explaining the reentrance, and further measurements would be necessary.

2.8 Shapiro steps

We have measured sample WAu-Sq dc voltage vs. dc current characteristic in presence of microwaves. The microwaves are emitted by an antenna (a coaxial cable) situated just above the sample: the coupling sample-antenna is then weak. In this situation one expects to see Shapiro steps, microwave induced current plateaus for discrete values of the voltage across the junction.
In a tunnel Josephson junction, when a voltage V is present across the junction, the pairs at different sides of the barrier have an energy difference 2eV. If we apply an external radiation of frequency $\omega_{rf}/2\pi$, the absorption of n photons increases the pair tunneling current when:

$$V = n\frac{\hbar}{2e}\omega_{rf} \tag{2.63}$$

generating plateaus in the I(V) curve.
The amplitude of the Shapiro steps varies with the applied rf power, oscillating like a Bessel function of order n for the n^{th} step.
In a long SNS junction, Shapiro steps are also present at voltages such as $V = n\frac{\hbar}{2e}\omega_{rf}$. Their amplitude oscillates, like in a SIS junction, but with a more complicated dependence ([5], sec. 3.7).
We show in Fig. 2.36 the differential resistance of sample WAu-Sq as a function of the applied current when irradiated with microwaves at a frequency $f_{rf} = 2.8\,GHz$. The sharp decrease to zero of the resistance at $I = -5\,\mu A$ corresponds to the retrapping current I_r, while the sharp increase of the resistance at $I = 8.4\,\mu A$ corresponds to the critical current I_c.
When the normal wire is in the resistive state, negative peaks in resistance appear periodically: they are the Shapiro steps.
Their width corresponds to the amplitude of the current plateaus formed in the I(V) curve. We can see that the resistance doesn't decrease to zero for all Shapiro steps; this could be partly due to a insufficient number of points in each peak (in the narrower peaks we have only 5-6 points).
When plotting the voltage as a function of the order n of the step, we expect straight lines, with a slope proportional to the rf frequency. In Fig. 2.37 we show the expected dependences (lines) and the measured Shapiro steps. Even if the agreement is not spectacular (especially for f=1.4 GHz and f=3.6 GHz), it is reasonably good.
We see in Fig. 2.37 that we not only detect the classical, integer Shapiro steps, but also the fractional Shapiro steps at n=1/2, n=1/3, etc.
The position of the steps doesn't vary with temperature or rf power. In Fig. 2.38, we show the resistance of the sample (colour scale) as a function of the

rf power and the bias current.

In contrast to what has been observed by P. Dubos [19] [17] at high temperature ($T = 4\,K$ corresponding to $13\,E_{Th}$), at $T \sim 150\,mK \sim 2.4\,E_{Th}$ we still see Shapiro steps with $n > 1$ at voltages greater than the Thouless energy (for sample WAu-Sq $E_{Th} = 5.33\mu V$). Moreover, we still see Shapiro steps for frequencies up to about three times the minigap ($\tilde{\Delta} = 4\,GHz$).

Fractional Shapiro steps can be explained in the case of an anharmonic current-phase relationship.
For example, the presence of a second harmonic in the current-phase relationship ($I = I_{c1}\sin(\varphi) + I_{c2}\sin(2\varphi)$) produces a step $n = 1/2$.
To demonstrate this statement, let's consider that the microwaves generate an alternative voltage across the junction:

$$V = V_0 + V_\omega \cos(\omega t) \tag{2.64}$$

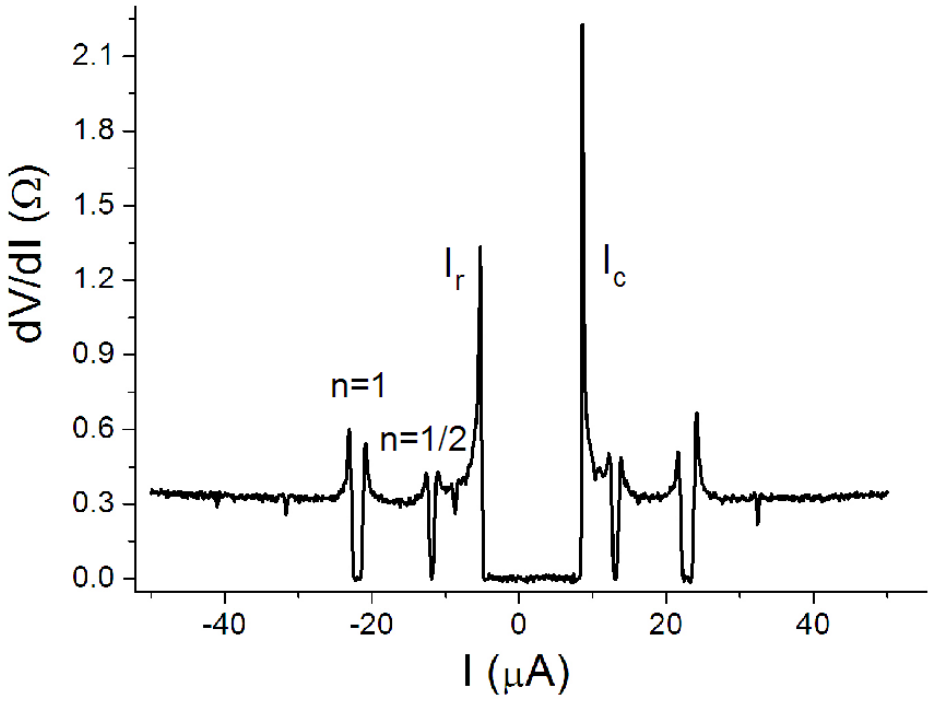

Figure 2.36: *Differential resistance vs. bias current when irradiating sample WAu-Sq with a microwaves of frequency f=2.8 GHz, at* $T = 100\,mK$. *Shapiro steps are clearly visible.*

The ac Josephson effect ($2eV/\hbar = \dot{\varphi}$) yields:

$$\varphi = \varphi_0 + \frac{2eV_0}{\hbar}t + \frac{2eV_\omega}{\hbar\omega}\sin(\omega t) \tag{2.65}$$

The considered current-phase relation then becomes:

$$I = I_{c1}\sin(\varphi_0 + \omega_J t + a\sin(\omega t)) + I_{c2}\sin(2\varphi_0 + 2\omega_J t + 2a\sin(\omega t)) \tag{2.66}$$

where $\omega_J = 2eV_0/\hbar$ and $a = (2eV_\omega)/(\hbar\omega)$. Developing with a Bessel-Fourier

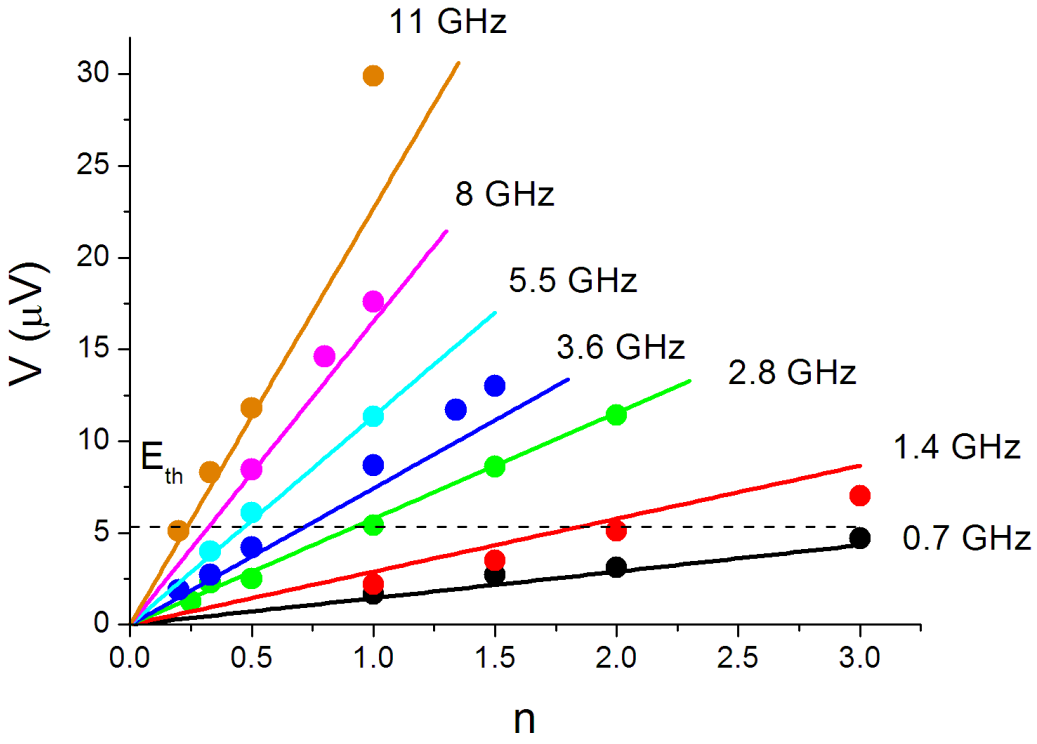

Figure 2.37: *Voltage across the junction vs. Shapiro steps order for sample WAu-Sq. Dots: experimental points. Lines: expected linear dependence given by* $V = n\frac{\hbar}{2e}\omega$. *The microwave frequencies f and powers P used are: f=11 GHz (P=-15 dBm), f=8GHz (P=-4 dBm), f=5.5 GHz (P=-4 dBm), f=3.6 GHz (P=-5dBm), f=2.8GHz (P=-5 dBm), f=1.4GHz (P=7dBm) and f=0.7GHz (P=4dBm). The measurement temperature is T=100-250 mK. We see entire Shapiro steps for n=1, n=2, n=3, and fractional Shapiro steps for n=1/5, n=1/4, n=1/3, n=1/2, n=4/5, n=4/3, n=3/2. It is however difficult to distinguish between n=1/4 and n=1/5.*

transform, we finally obtain:

$$I = I_{c1}\sum(-1)^n J_n(a)\sin(\varphi_0+\omega_J t-n\omega t)+I_{c2}\sum(-1)^n J_n(2a)\sin(2\varphi_0+2\omega_J t-n\omega t) \tag{2.67}$$

A dc current step appears if:

$$V_0 = \frac{\hbar}{2e}\,n\,\omega \quad or \quad V_0 = \frac{\hbar}{2e}\,\frac{n}{2}\,\omega \tag{2.68}$$

We obtain then the Shapiro step $n = 1/2$ and all his multiples. One can easily extend the discussion to a step $n = 1/3$ by adding a third harmonic in the dc Josephson relationship. The step $n = 0$ is simply the critical current. We can then relate the fractional Shapiro steps to anharmonicities in the current-phase characteristic.
These anharmonicity can be due to coherent multiple Andreev reflexions (when L_T, $L_\Phi >> L$, one Andreev pair can cross coherently the normal wire many times, each time adding an harmonic to $I(\delta)$), or to non-equilibrium phenomena (see chapter 4).

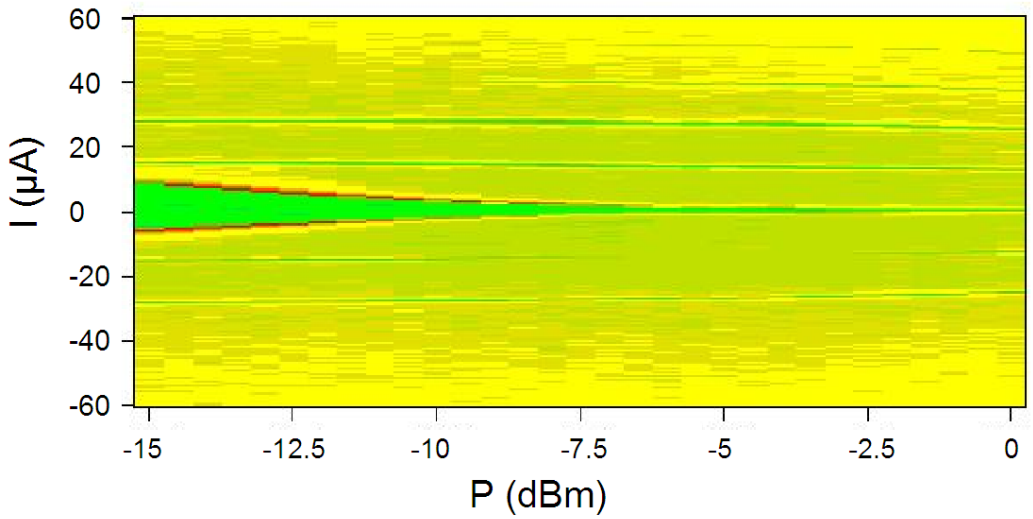

Figure 2.38: *Sample WAu-Sq bias current vs rf power and differential resistance (color scale: green, R=0, increasing resistance yellow and then red). The temperature is $T = 80\,mK$. One can easily see the power dependence of I_c, I_r and of the Shapiro steps.*

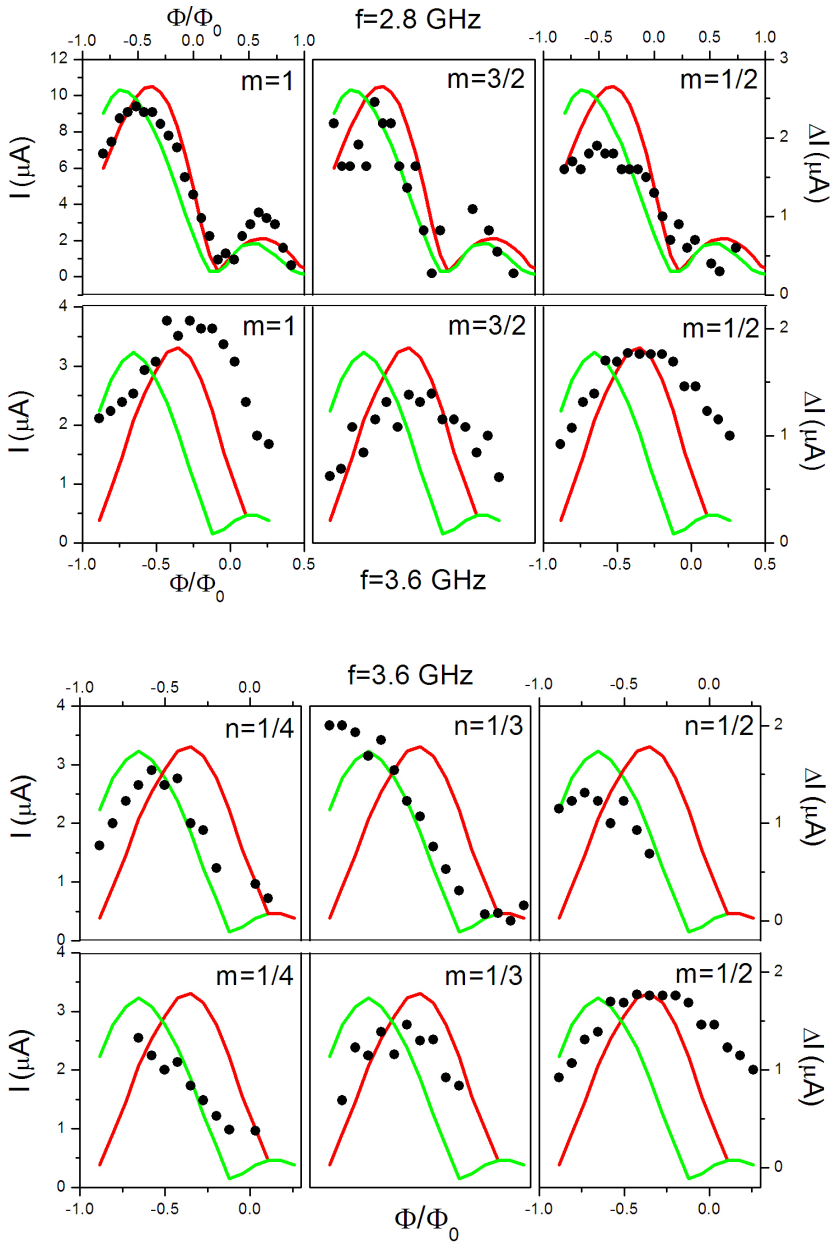

Figure 2.39: *Dots: Shapiro steps current plateau amplitude vs. normalised flux (right scale) with rf frequencies f=2.8 GHz (P=-5 dBm) and f=3.6 GHz (P=-5 dBm). The Shapiro step order is indicated with a m (steps at $I > I_c$) or a n (steps at $I < I_c$). $I_c(\Phi/\Phi_0)$ (red line, maximum on the rigth) and $I_r(\Phi/\Phi_0)$ (green line, maximum on the left) are measured under the same irradiation (left scale). One can see that half quantum flux is trapped in the junction.*

If the fractional Shapiro steps are generated by coherent MAR, we expect the harmonic content to follow [30]:

$$I_{cn} = I_c\,(-1)^n\,\frac{1}{(2n+1)(2n-1)} \tag{2.69}$$

The harmonics, and thus the fractional steps, should disappear faster than the integer steps, in presence of any dephasing mechanism, such as temperature or magnetic field.
We have then measured the dependence of our Shapiro steps on the magnetic field. We show it in Fig. 2.39 for the two rf frequencies $f = 2.8GHz$ and $f = 3.6GHz$, together with the critical and retrapping current dependences. Since our sample has a non negligible inductance, the direction of the magnetic field matters, and we shall compare the Shapiro steps for $I < I_r$, labelled with the n letter, to the $I_r(H)$ curve (in green), and the Shapiro steps for $I > I_c$, labelled with the m letter, to the $I_c(H)$ curve (in red).
Even if these experiments are only preliminary, it is clear that the magnetic field dependence of the integer Shapiro steps is the same as the $n = 0$ step, i.e. the critical or retrapping current.
Let's now look at the fractional Shapiro steps. We have seen in the previous section that the critical current dependence on field is practically the same if the current-phase relation is harmonic or anharmonic. Shapiro steps, instead, should permit to separate the contribution of the higher harmonics one by one.
So, if there is a second harmonic in our $I(\delta)$, this second harmonic would produce a $n = 1/2$ step, which, ignoring for the moment the self inductance and aspect ratio contributions, behaves in magnetic field as

$$I_{c2}(\Phi/\Phi_0) = I_{c2,max}\left|\frac{\sin(2\pi\Phi/\Phi_0)}{2\pi\Phi/\Phi_0}\right| \tag{2.70}$$

This function is similar to a classical Fraunhofer function, but the position of the zeros is at all multiples of $\Phi_0/2$ instead of Φ_0 (see Fig. 2.40).
This is evidently not what we find experimentally, since the field dependence of half integer steps seems to have an equal or greater period than the integer steps.
Our discussion was based on a model without inductance and with an aspect ratio $L/w < 0.04$. However, the self inductance doesn't have any influence on the zeros position, while a bigger aspect ratio could have increased the position of the zeros, but not enough as to match the measurements.
It seems thus improbable that the half integer Shapiro steps we measure are generated by a second harmonic due to the presence, at low temperatures,

of multiple Andreev reflexions.
However, in a out-of-equilibrium situation, in which the response of the junction is not adiabatic, a second harmonic could be generated in the current-phase relation, and an equibrium second harmonic could be modified (see chap. 4). Further measurements, such as the fractional steps temperature dependence, are then still necessary to understand and confirm the origin of the measured half-integer Shapiro steps.

2.9 Conclusion

In this chapter we have examined the DC properties of long SNS junctions and SNS DC SQUIDs. The superconducting contacts have been fabricated with three different metals: Aluminum, Niobium and Tungsten, while the normal part is a high purity golden wire. The Al-Au junctions were made by standard double angle thermal evaporation, the Nb-Au junctions by the etching of a Nb-Au bilayer, and the W-Au junctions by decomposition of a vapour of tungsten hexacarbonyl with a gallium focused ion beam.
Despite the very different fabrication methods and resulting SN interfaces,

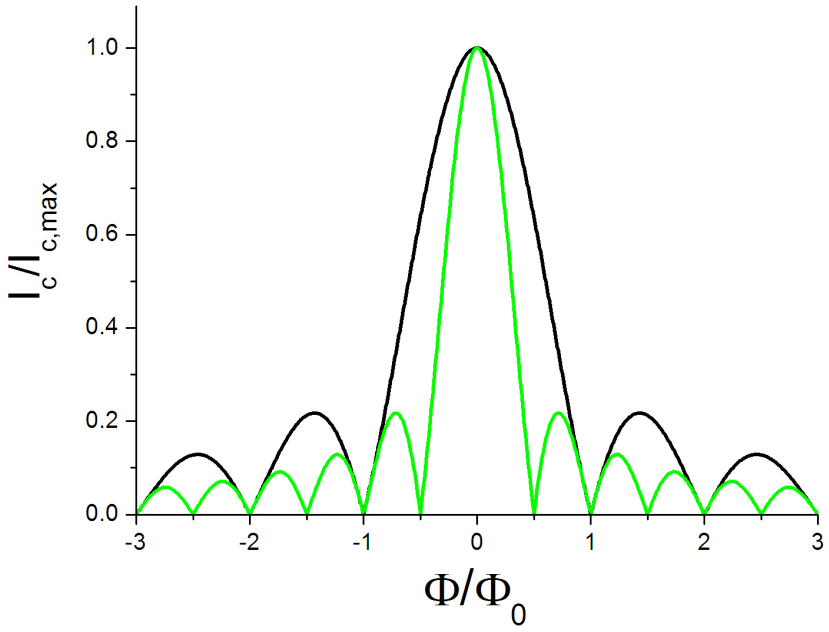

Figure 2.40: *Fraunhofer pattern expected for n=1 Shapiro step (black line) and for a n=1/2 Shapiro step (green line).*

the temperature and magnetic field dependences of the dc voltage-current characteristic could be interpreted within the same framework.

2.9.1 Dc voltage-current characteristics

At low temperature, we observe in all our current-biased samples, hysteretic sharp switches between the normal (N) and the superconducting (S) states. The junction switches from S to N at the critical current I_c, while it switches back from N to S at the retrapping current $I_r < I_c$; we find generally $I_r \sim 0.15 - 0.4\, I_c$.
At high temperature, the hysteresis disappears and the junction transition between S to N is smooth.
We have examined different possible sources of the low temperature hysteretic behavior.
First, we have supposed a thermal origin. The junction, intrinsically non-hysteretic, is heated in the normal state by the Joule dissipated power, and is cooled by the phonons. If the Joule power is greater than the phonon cooling power, the electronic temperature T_e increases, and I_c decreases. The junction then switches from N to S only at $I_r = I_c(T_e)$.
We have found a good agreement with the experiments when modeling the phonon cooling power by $P_{ph} = \Sigma' V (T_e^6 - T_{ph}^6)$, where $\Sigma' \sim 5\ 10^{-8} W\, \mu m^{-3} K^{-6}$, V is the sample volume and T_e and T_{ph} are the electronic and phonon bath temperatures.
We have then supposed an intrinsic hysteresis generated by the phase dynamics, as in a SIS junction.
In a SIS junction, hysteretic curves are predicted for underdamped junctions with a quality factor greater than one: $Q = \tau\, \omega_p > 1$. $\tau = RC$ is the relaxation time and ω_p is the plasma frequency. To use the same model for a SNS junction, we need to replace the RC and ω_p^{-1} times with the corresponding characteristic times in the SNS case. We use the parallel found in sec. 3.6.1: $RC \leftrightarrow \tau_{in}$, where τ_{in} is the inelastic time. Indeed, the time the phase needs to lose its kinetic energy and be retrapped in a potential well could correspond in a SNS junction to the time the electrons need to lose their kinetic energy by inelastic scattering.
From the RCSJ relations $Q = (4/\pi)\, (I_c/I_r)$ and $Q = RC\, \omega_p = \tau_{in}\, \omega_p'$ we can deduce ω_p' from the experimental $I_c(T)$, $I_r(T)$ and $\tau_{in}(T)$ curves. The effective plasma frequency we find is temperature independent and roughly proportional to the diffusion rate τ_D^{-1}.
To confirm these deductions, we assume $\omega_p' \propto \tau_D^{-1}$, and we trace the effective RC time vs. temperature for the samples in which we don't measure

directly the inelastic time. If our assumptions are good, we should find the temperature dependence of the electron-electron time for $T \lesssim 1\,K$, and of the electron-phonon time for $T \gtrsim 1\,K$.
We observe a saturation at low temperature, possibly due to the magnetic impurities scattering, and at higher temperatures a rate decaying with temperature as $\tau^{-1} \sim 1.3\ 10^8\ T^{1.5}\,s^{-1}\,K^{-1.5}$. These results are consistent with the inelastic scattering rate predicted in a limited system.

2.9.2 Temperature dependence

At low temperature, we observe a saturation of the critical current I_c. At high temperature, instead, $I_c(T)$ is exponentially suppressed on a temperature scale corresponding to the minigap induced in the normal metal by the proximity effect.
We reproduce succesfully all our $I_c(T)$ dependences using the analytical expressions obtained by P. Dubos by fitting the numerical calculation of the Usadel equation.
The only deviation from the theory is the low temperature regime, where we observe a saturation region wider than expected, and at a lower critical current. We have not found a satisfying explanation for this behavior.

2.9.3 Magnetic field dependence

We have measured the critical current dependence on a perperndicular magnetic field.
In the dc SQUIDs, we observe two magnetic field scales, corresponding to a quantum flux in the surface of the ring Φ_0/S and to a quantum flux in the surface of the junction normal wire Φ_0/S_j.
At low fields, I_c oscillates with a period Φ_0/S. We explain completely the shape and period of the oscillations using a model developped by F. Balestro for a SIS junction.
At higher fields, the junctions and SQUIDs behavior departs from the SIS expected Fraunhofer pattern.
We have observed an important dependence of the $I_c(H)$ curves on the normal part geometry: for long and narrow normal wires, $I_c(H)$ decreases following a Gaussian dependence, while for larger wires (we have tested a square geometry) $I_c(H)$ approaches continuously a Fraunhofer pattern.
The 1D semiclassical model developped by G. Montambaux and the 2D numerical calculations of the Usadel equations porposed by J. C. Cuevas are in

good agreement with our measurements.

In some Al-Au samples, we have found a surprising reentrance of the critical current at low magnetic fields ($B \lesssim 45\,G$) and at low temperature ($T \lesssim 100mK$).
A possible explanation is the presence of a low magnetic impurities content in the normal metal: at low field, the magnetic field aligns the impurities moments, decreasing the spin-flip scattering and increasing the superconductivity, while at larger fields, the depairing action of the magnetic field is predominant. This theory explains the temperature scale of the reentrance and its amplitude, but the expected magnetic field scale is two order of magnitudes greater than the observed one!
A second hypothesis is a mesoscopic effect similar to the weak localisation. In this case, however, the reentrance amplitude predicted is at least one order of magnitude smaller than the measured one.

2.9.4 Shapiro steps

We have irradiated WAu-Sq with microwaves in order to measure the Shapiro steps.
At low temperature ($T \sim 150\,mK$), we have observed both integer and fractional Shapiro steps.
Neither the Thouless energy nor the minigap seem to limit the Shapiro steps: we have found steps up to voltages greater than the Thouless energy and up to frequencies greater than the minigap ($f \sim 3\,\tilde{\Delta}$).
We have measured the magnetic field dependence of different integer and fractional Shapiro steps. We have found that the integer steps depend on the magnetic field just like the zero-th order step, the critical current. The steps n=1/2 and n=1/3, instead, seem to decay slower than $I_c(H)$.
Fractional Shapiro steps are generated by harmonics in the current-phase relationhip. We can exclude that the harmonics we observe are generated by multiple Andreev reflexions: we would in that case expect the steps to decay with the magnetic field faster than $I_c(H)$. We believe that the harmonics in $I_s(\varphi)$ come from a non-equilibrium response of the supercurrent.

Chapter 3

High frequency current modulation

3.1 Introduction

While an extensive study has been done to understand the dc properties of SNS junctions, their dynamics is still a open question. The main reason is that the Josephson effect, well understood in tunnel junctions and point contact junctions, interferes here with the dynamics of Andreev pairs in the normal metal. In long SNS junctions, this is even more important since the properties of the long junctions are set by the normal metal properties: their energy scale is the Thouless energy $E_{Th} = \frac{\hbar D}{L^2}$, where L is normal wire length, and D is the normal metal diffusion coefficient in the normal metal. As we have seen, the Thouless energy determines the amplitude of the minigap induced in the density of states by the proximity effect and the temperature decay of the critical current.
Probably the simplest way to probe the junction dynamics is to measure its dc response to an ac excitation. By varying the frequency of the excitation, the relevant time scales can be revealed. Different regimes then appear, in which the critical and retrapping currents are strongly modified giving an insight of the dynamics in the SNS junction.

3.2 Microwaves and superconductors

A BCS superconductor driven out-of-equilibrium by microwave radiation experiences increased superconductivity.
This counterintuitive phenomenon is known as Dayem-Wyatt effect [15] [20], first observed in microbridges, thin films and strips, and then in supercon-

ducting tunnel junctions [27] [14] [57].

It is based on the fact that the BCS gap Δ is related in a self-consistent way to the energy distribution of the quasiparticles $f(\epsilon)$ by:

$$1 = \lambda \int_0^\infty \rho(\epsilon)[1 - 2f(\epsilon)]d\epsilon \tag{3.1}$$

where λ quantifies the strength of the electron-phonon interaction and $\rho(\epsilon)$ is the BCS density of states, which depends on Δ.
The thermodynamic gap $\Delta(T)$ is obtained solving the self-consistent equation 3.1 at equilibrium; the distribution function is then a Fermi-Dirac function at temperature T.
Driving the system out-of-equilibrium with microwaves modifies the energy distribution of the excitations. To bring the quasiparticles significantly out of equilibrium clearly demands enough power, but also enough speed: inelastic processes tend to restore equilibrium. If the microwaves frequency exceeds the relaxation rate for the inelastic scattering of quasiparticles, a stationary non-equilibrium distribution of quasiparticles is reached.
When the distribution function is out-of-equilibrium, it differs from a Fermi-

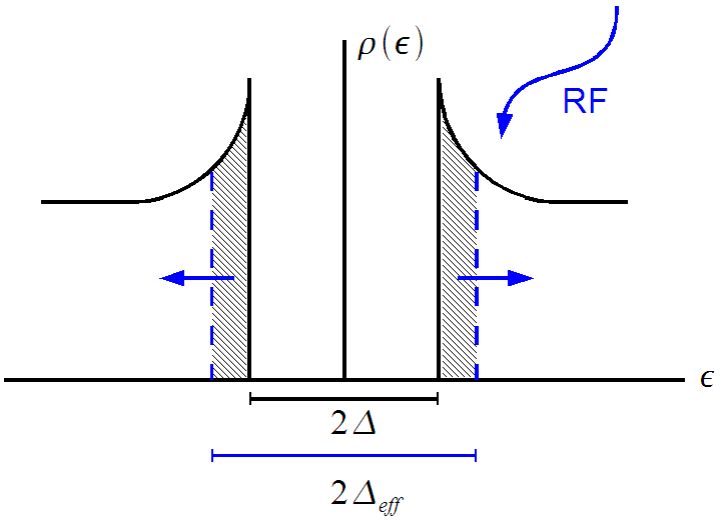

Figure 3.1: *Scheme of the RF induced superconducting gap enhancement.*

Dirac function, and the superconducting gap, derived from eq. 3.1, is modified. In particular, the gap is enhanced for a strong ac excitation whose frequency f is greater than the inverse of the dominant inelastic process,

electron-phonon in usual superconductors.
The equilibrium $\Delta(T)$ is fairly insensitive to T at low temperature whereas it varies strongly close to the critical temperature T_c. This reflects the sensitivity of $\Delta(T)$ to a small change in the distribution function, and translates into the fact that microwave pumping is effective only very close to T_c, experimentally for T within of few percent of T_c.
In a series of articles, Eliashberg analysed the changes in the properties of a

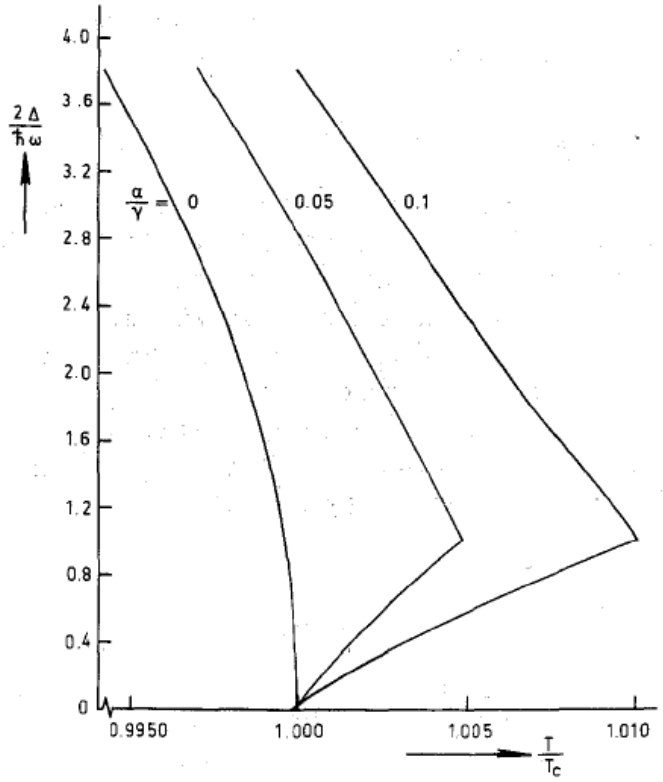

Figure 3.2: *Energy gap calculated for an Al strip, as a function of temperature, in the presence of microwave radiation for various power values. The microwave frequency is $f = \omega/2\pi = 3GHz$, α is the applied microwave power and $\gamma = \hbar/\tau_{e-ph}$ is the relaxation energy. The equilibrium case corresponds to $\alpha/\gamma = 0$.*[35]

superconductor under the influence of a microwave field [31]. He solved the gap equation 3.1 in presence of a small rf power, that he modeled by adding to the distribution function a small term to take into account the absorption, spontaneous emission, and pair-breaking contributions.
Fig. 3.2 shows the results of his calculation: the gap is plotted as a function

of temperature, for various microwave powers. We can see that for $T > T_c$ a non-zero gap solution exists, and that for $T < T_c$ the gap is larger than in the equilibrium case.
From the experimental point of view, Eliashberg's theory is able to account reasonably well for the Dayem-Wyatt effect in superconducting strips [35] and bridges. We can then attribute to Eliashberg's gap enhancement mechanism the increased superconductivity that appears when we irradiate a superconductor with high frequency ($f > \tau_{e-ph}^{-1}$) microwaves.
Dayem-Wyatt is characterised by:

- an enhanced gap for $T \sim T_c$, on a few mK range [36].
- an enhanced critical temperature T_c [20] (see also Fig. 3.3).
- a strong increase of the critical current for $T \sim T_c$ up to several times the original value (see Fig. 3.3).
- an I_c enhancement that increases, then gradually decreases, with the rf frequency and power. The frequency of the maximum increase, as well as the critical frequency, above which the enhancement appears, depend both on temperature [35].

3.3 Microwaves and superconducting hybrid junctions

Hybrid structures made of superconductors and normal metals offer a rich extension of the physics of superconductivity.
Experiments aimed to discover their dynamics have been made on short and long SNS junctions [43] [22].
Both kind of junctions present dynamical effects with features similar to the Dayem-Wyatt effect. In particular, a strong enhancement of the critical current and of the critical temperature of the junctions is observed. The enhancement amplitude is comparable to the superconducting samples results, but some important differences are nevertheless present:

- the critical current enhancement is present on a large range of temperatures (see Fig. 3.4).
- the critical frequency is larger than the inelastic rate.
  More precisely, an enhancement was found if $\omega_{rf} > \omega_J = 2\pi R I_c/\Phi_0$

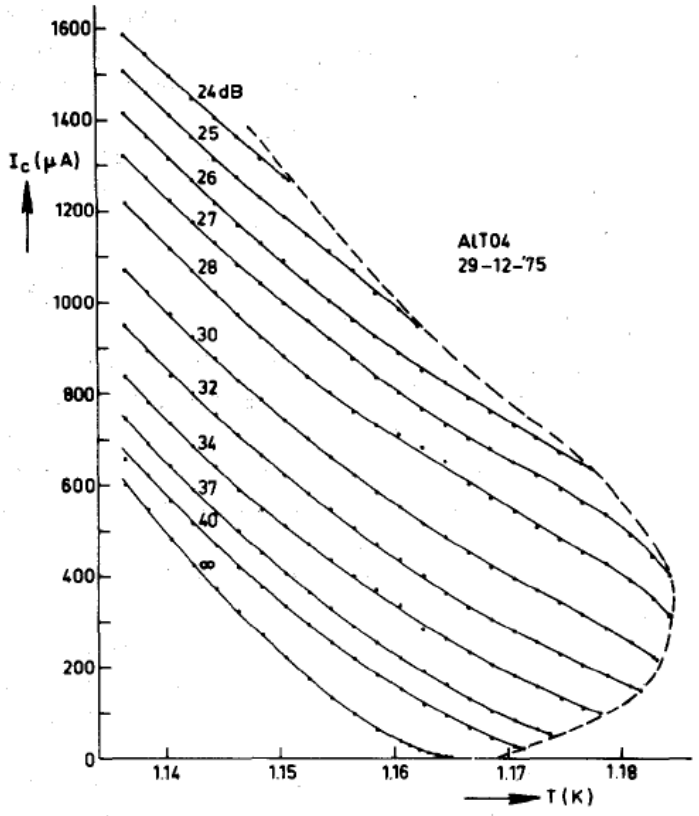

Figure 3.3: *Critical current of a Al strip as a function of temperature at various levels of microwave power (the value of attenuation is noted on each curve). The dashed line encloses the region where critical current can be observed. On passing this line the critical current jumps to zero.*[35]

or if $\omega_{rf} > A/\tau^*$, where $A \sim 2$ and τ^* is the effective time-dependent Ginzburg-Landau relaxation time for a normal metal [22]. It is easy to show that $\tau^* = (\pi/2)^2 \tau_D$.

- the enhanced supercurrent oscillates with rf power as a Bessel function (see Fig. 3.5).

What are the differences between long SNS junctions and superconducting strips that cause these changes?
A first proposition [43] involved the important spatial dependence of the phase in a long SNS junction. The Aslamazov-Larkin (AL) model for proximity junctions was thus modified to take into account this spatial dependence. It was found that for large Josephson current densities (as it is the case in

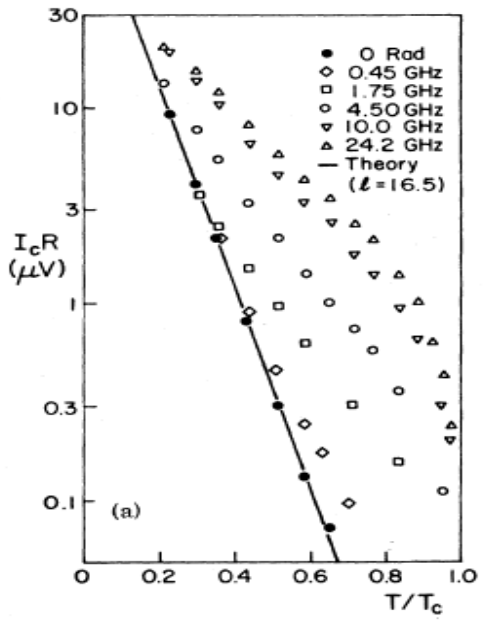

Figure 3.4: *$I_c R$ as a function of several rf frequencies for a long SNS junction of thickness $t = 0.15\mu m$, width $w = 1\mu m$ and length $L = 1\mu m$. The solid line is the theoretical prediction at equilibrium.*[22]

the absence of tunnel contacts) this could lead to an excess supercurrent, depending on rf power as a Bessel function and appearing for $\omega_r f > 2\pi\, R\, I_c/\Phi_0$. A second explanation [22] proposed that the presence of microwaves would change the pair correlations in the normal wire. The rf excitation would increase the coupling of the centre of the normal junction to the superconducting leads, utterly increasing the supercurrent for frequencies higher than the diffusion rate.

Both propositions can explain some of the peculiarities of long SNS junctions, but neither is completely satisfactory.

In section 3.7 we present some more experiments that, we hope, help clearing this complicated panorama. In particular, we show that, indeed, the critical frequency f_c is related to the diffusion rate. However, f_c varies strongly as a function of the magnetic field and temperature, revealing a competiton between the out-of-equilibrium distribution function and the out-of-equilibrium density of states. A recent theoretical paper from P. Virtanen and al. [58] confirms the importance of the diffusion time in the microwave-assisted critical current enhancement.

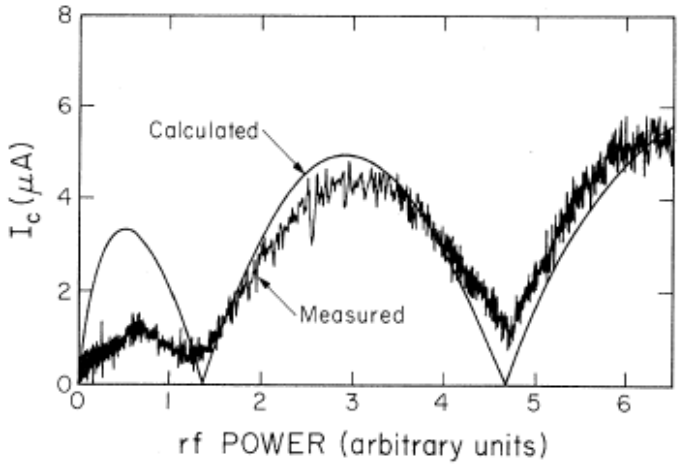

Figure 3.5: *Enhanced supercurrent of a Sn-Au long junction when a 10 GHz microwave power is applied. The data are taken at* $T = 3.6\,K > T_c$*, so that no supercurrent is observed without the external radiation. The smooth solid line is the power dependence to be expected from the modified AL model. The junction is* $1\,\mu m$ *long,* $39\,\mu m$ *wide and* $100\,nm$ *thick.*[43]

3.4 Sample fabrication

The samples fabricated for these experiments are SNS Nb-Al Josephson junctions, in which the superconducting leads are made of Niobium (Nb), while the thin normal wire is made of Aluminium (Al).
The normal wires are $300\,nm$ wide, $9\,nm$ thick and have a length ranging from $300\,nm$ to $5\mu m$. The superconducting contacts are $60\,nm$ thick.
The junctions were measured for temperatures above the critical temperature of Al, $T_c \sim 1.2\,K$, between $T = 1.4\,K$ and the liquid He^4 temperature, $T = 4\,K$. We observe no evidence for superconducting fluctuations in Al in this temperature range [12].
All the junctions were made in ultra-high vacuum (UHV) by double angle deposition through a suspended mask, a trilayer PMMA-Si_3N_4-PES resist, developped by P. Dubos [24]. We have chosen this particular resist because it can sustain high temperatures, condition which is essential to e-gun evaporate a refractory metal like Nb.
We obtain with this technique much better results than with the conventional resists, the Nb superconducting leads having a critical temperature ranging from $6.8\,K$ to $8\,K$. Furthermore, the contact resistance between Nb and Al is negligible, the two evaporations being made one just after the other in a 10^{-8} mbar vacuum.

The mask, deposited on a Si-SiO_2 substrate, consists of a 400 nm PES layer (Poly Ether Sulfone - commercially known as Victrex), a 60 nm layer of rigid Si_3N_4 and a 350 nm layer of electron-sensitive polymer PMMA (Poly Methyl Methacrylate).
The main stages of sample fabrication are illustrated in Fig. 3.6.

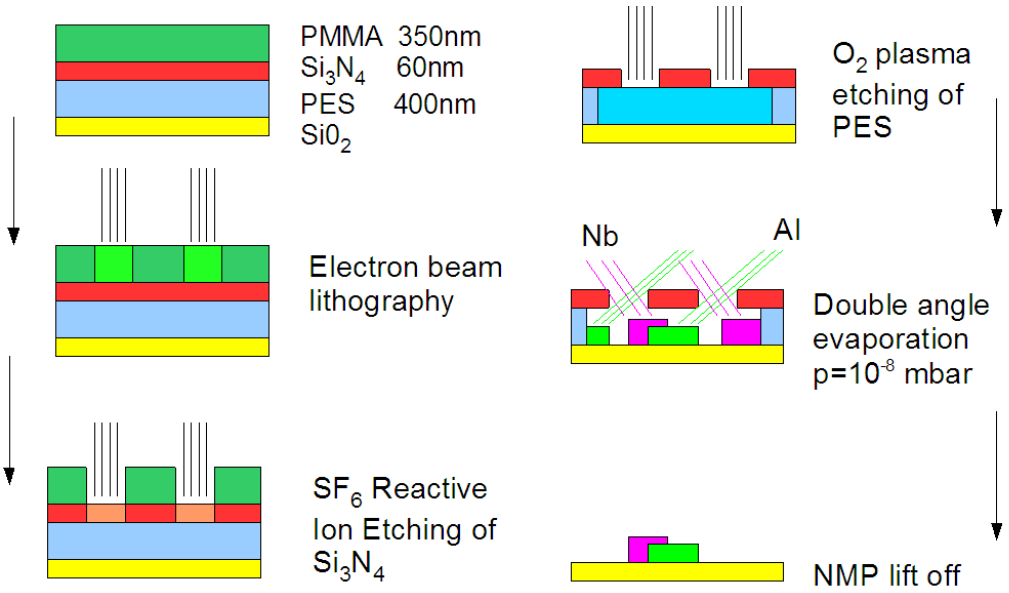

Figure 3.6: *Sample fabrication: from top to bottom and from left to right, schematic vision of the mask etching and junction deposition.*

Lithography First, we draw the pattern on the PMMA layer by electron-beam lithography with a Scanning Electron Microscope (SEM): the PMMA polymer chains are broken by the electron beam and can be removed by immersing the sample in a Methylisobutylcetone (MIBK)-Propanol(IPA) solution for 40 s. The pattern is defined with a precision of the order of tens of nanometers.

Rigid mask Through the PMMA mask, we etch the Si_3N_4 layer with a SF_6 Reactive Ion Etching (RIE) for 2 min 30 s. The Si_3N_4 provides a rigid structure which can be suspended over more than 500 nm without falling or breaking. Since the SF_6 RIE also etches the PMMA, it is crucial to have a good control on etching times to avoid an overetching. At the end of the process, there is no more PMMA on top of the Si_3N_4 layer.

Undercut We etch the PES layer with a high pressure Oxygen plasma. The pattern is etched for 1 min; a further 7 min etching creates a 500 nm undercut, leaving the Si_3N_4 intact. Using a high pressure plasma (p$\sim$ 280 mTorr) permits an isotropic etching and increases the undercut.

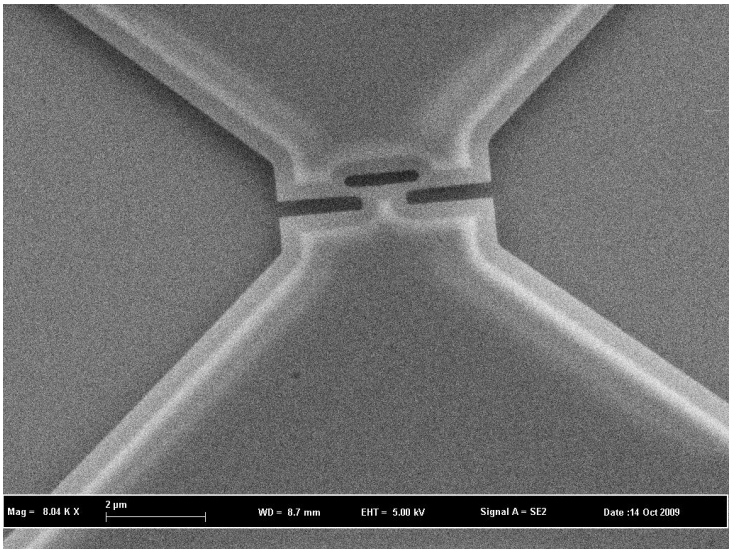

Figure 3.7: *SEM image of a trilayer mask. The dark regions correspond to the pattern, which is completely etched; the grey regions around the pattern show the undercut, where the PES is etched and the Si_3N_4 is suspended.*

The SEM image of a completed mask is shown in Fig. 3.7.
Even though this process is quite demanding, it offers good control of dimensions, stability and reproducibility.
The RIE was performed at Laboratoire de Photonique et Nanostructures (LPN) in Marcoussis, with the help of L. Ferlazzo.

Evaporation Once the mask is ready, the sample is placed in a UHV evaporator whose base pressure is of 10^{-9} mbar.
First, we deposit a 9 nm layer of Aluminium under an angle of $+26°$, at a rate of 5 $\mathring{A}/s$ and at a pressure $p = 1\,10^{-7}$ at the level of the sample. Then, we deposit a 60 nm layer of Niobium under an angle of $-26°$, at a rate of 3 $\mathring{A}/s$ and a pression of $p = 8\,10^{-8}$. The overlap of the two metals forms the SN junctions.
While evaporating Nb we use liquid nitrogen to cool down the walls of the evaporating chamber, ensuring better Nb quality. The choice of the mask is determinant at this stage, since the Nb is very sensitive to contamination by

oxygen and other compounds that could outgas from the mask. The Si_3N_4-PES mask is stable up to 400°C, and doesn't outgas.

Lift-off The remaining resist is eliminated by immersing the sample in a NMP (N Methyl 2 Pyrrolidone) solution at 60° for 10 min.

SEM images of the finished SNS junctions are shown in Fig. 3.8.

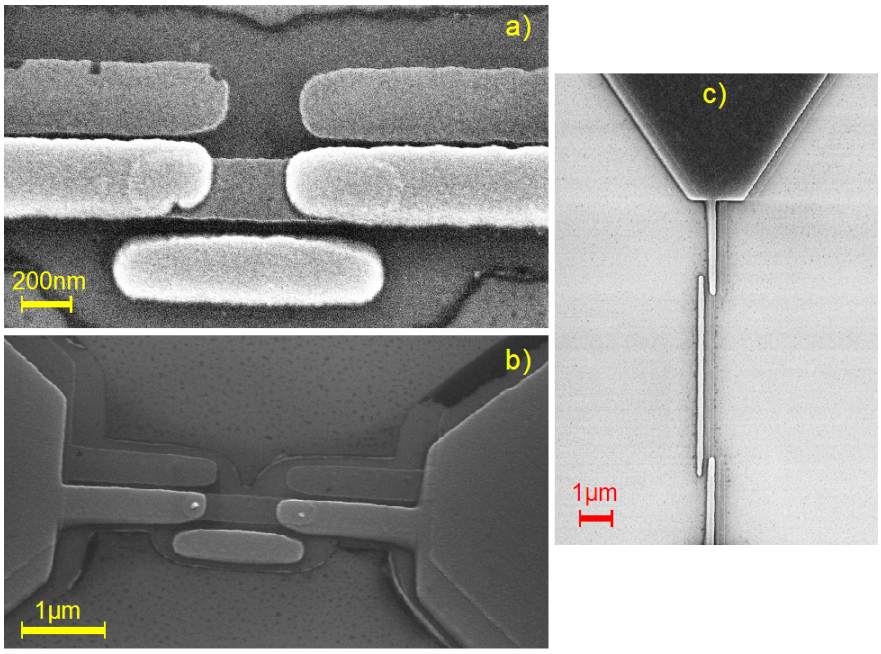

Figure 3.8: *SEM images of three different Nb-Al junctions. a) Short junction (NbAl-S), L=330 nm ; b) Long junction (NbAl-L), L=780 nm; c) example of the longest junction we made with the trilayer technique, L= 5 µm.*

sample	L (nm)	w (nm)	R (Ω)	$\tau_{D,geom}^{-1}$ (GHz)	$\tau_{D,fit}^{-1}$ (GHz)	Δ/E_{Th}
NbAl-L	780	320	14.5	8.2	8.2	118
NbAl-S	330	300	6.5	46	29	21

Table 3.1: *Average characteristic of the long (NbAl-L) and short (NbAl-S) samples: length L, width w, resistance R, diffusion rate* $\tau_D^{-1} = D/L^2$ *and ratio between the superconduting gap* Δ *and the Thouless energy* $E_{Th} = \hbar\tau_D^{-1}$. *These parameters vary in the different samples of:* $\Delta L = \pm 20nm$, $\Delta w = \pm 20nm$, $\Delta R = \pm 1.5\,\Omega$.

We have measured ten samples, of two different lengths, whose average characteristics are summarised in the table 3.1. The diffusion rate is calculated from the resistance and geometry of the samples, and is given by eq. 3.2:

$$D = \frac{L}{w\,t}\,\frac{1}{e^2\,\nu_F\,R} \tag{3.2}$$

where $\nu_F = 1.46\ 10^{47} J^{-1}\,m^{-3}$ is the density of states at the Fermi level for Aluminum.
We calculate an average diffusion coefficient of $D = 5\ 10^{-3}\ m^2/s$. The average diffusion rate for samples NbAl-S and NbAl-L, measured from this diffusion coefficient are listed in table 3.1.
We have also fitted the temperature dependence of I_c using eq. 2.4 as before, to confirm and precise the value of the diffusion rate.
Despite the very good agreement for sample NbAl-L, the fit of sample NbAl-S gives $\tau_{D,fit}^{-1} = 29\ GHz$. This corresponds to a length $L = 400\,nm$.
Looking at the SEM image of the NbAl-S sample we used the most (see Fig. 3.9), one remarks that the superconducting contacts are not perfectly aligned to the normal wire: a sligthly longer normal part should then be expected.

3.5 Static measurements: experimental setup

The experimental setup is sketched in Fig. 3.9.

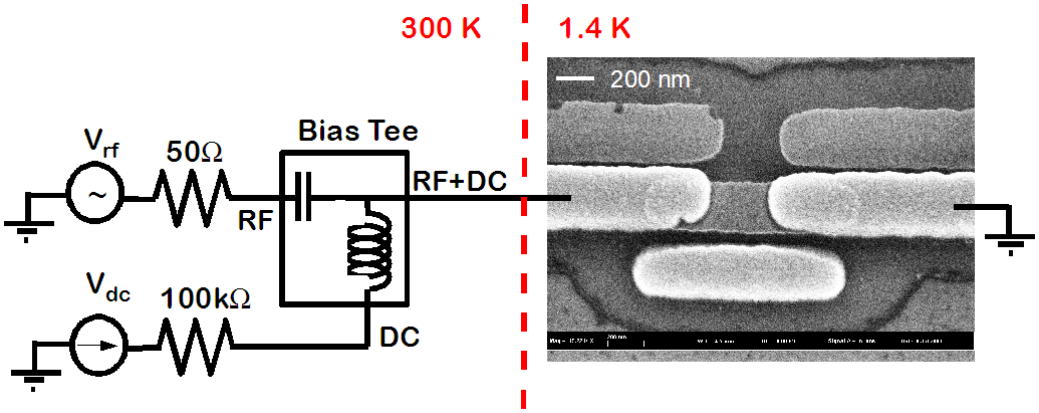

Figure 3.9: *Experimental setup for static measurements.*

The sample is dc current-biased through a $100\,k\Omega$ resistor. An ac current bias of frequencies up to $40\,GHz$ is also applied by a microwave generator.

A Bias-Tee adds the high frequency current bias to the dc bias.
The bias tee is essential for this experiment because it provides a wideband, good coupling of the sample to the rf source. [1]
The sample is placed at the end of a 50 Ω stainless steel coaxial line and sits in the liquid of a pumped He^4 cryostat. The temperature is controlled by adjusting the bath pressure and varies from 1.4 K to 4 K.
In this range, sample NbAl-S is always proximity superconducting, while for sample NbAl-L the proximity effects occurs at $T < 1.92\,K$.
When it is superconducting, the sample has a very small impedance, so that the rf generator of output impedance $R_0 = 50\ \Omega$ acts as a current source. This is not strongly modified when the sample is in the normal state since its resistance is $\sim$ 0.1 - 0.3 R_0.
At high frequency the sample has a complex impedance that can be of order of R_0 [42]. However, it is wire bonded to the microstrip on the sample holder by several (four at most) Al-Si wires in parallel. The inductance in series with the sample is $\mathcal{L} = 3.35$ nH. This is the dominant impedance at high frequency ($\mathcal{L}\,\omega \sim 200\Omega$ at 10 GHz), so the sample is still current-biased at high frequency, but the current is reduced. We take into account this reduction, together with the attenuation of the cables, that we have measured separately, to estimate the rf power at the sample level.

We have then two contributions to take into account: the attenuation due to the cables and bias tee, and the effect of the bonding wire inductance.
To know the attenuation, we have measured with a diode the reflected power P_{att}, when the sample is replaced by a short circuit. The reflected power P_{att} is given by:

$$P_{att} = P_0 * \alpha^2 * \mid \Gamma_{short} \mid^2 \tag{3.3}$$

where P_0 is the injected power, $\Gamma_{short} = -1$ is the reflexion coefficient for a short circuit, and α^2 is the power attenuation coefficient.
We can then access directly the attenuation of the signal traveling down to the sample and back: the one-way attenuation is simply $\sqrt{P_0/P_{att}}$.
In Fig. 3.10 we show the attenuation as a function of the rf frequency. We can notice an absorption peak at f=21 GHz.

Let's see now how we can take into account the effect of the bonding wires inductance.
We can model a rf generator as a ideal voltage generator with a $50\,\Omega$ resistance

[1] We used two different Bias-Tee: an Aeroflex Bias-Tee, working in the frequency range $50\,kHz - 26.5\,GHz$ with less than 3 dB attenuation, and up to $40\,GHz$ with an attenuation of less than 20 dB; and a Anritsu Bias-Tee K252, working in the frequency range $100\,MHz - 40\,GHz$ with less than 2.5 dB attenuation.

in series (see Fig. 3.11 (a)). The output voltage V of the ideal generator is such that a 50 Ω impedance would dissipate the required power P.
We then have:

$$P = 50I^2 \qquad V = (50 + 50)I \tag{3.4}$$

The relationship between the voltage V and nominal power is simply:

$$V = 2\sqrt{50P} \tag{3.5}$$

The real circuit is of course not always adapted to a 50 Ω impedance. In our case, the impedance of the circuit, including the rf generator (its 50Ω in series), is $Z_c = 50 + Z_j + i\omega L$, where Z_j is the SNS junction impedance and $\mathcal{L}$ the bonding wires inductance (see Fig. 3.11 (b)).
The current flowing in the circuit is then:

$$I = \frac{V}{Z_c} = \frac{2\sqrt{50P}}{50 + Z_j + i\omega L} \tag{3.6}$$

In a circuit with only a generator and the sample (see Fig. 3.11 (c)), this current would be generated by a voltage V' such as $V' = (Z_j + 50)I$:

$$I = \frac{V'}{Z_j + 50} = \frac{V}{Z_c} = \frac{2\sqrt{50P}}{50 + Z_j + i\omega L} \tag{3.7}$$

$$V' = (Z_j + 50)\frac{2\sqrt{50P}}{50 + Z_j + i\omega L} \tag{3.8}$$

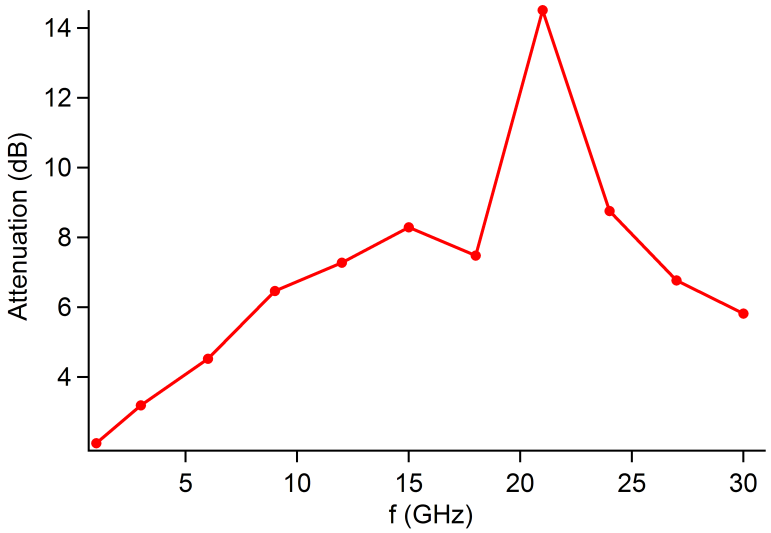

Figure 3.10: *Cables attenuation as a function of the rf frequency.*

We can thus calculate the nominal power of a generator situated just before the sample. The nominal power of this generator directly connected to the sample is related to the nominal power imposed by:

$$P' = \frac{1}{50}\left(\frac{V'}{2}\right)^2 = P \left|\frac{Z_j + 50}{Z_j + 50 + i\omega L}\right|^2 \tag{3.9}$$

When the sample is superconducting, its resistance is zero and its Josephson inductance is much smaller than the bonding wires inductance, so that $Z_j \sim 0$:

$$P' = P/(1 + (\omega L/50)^2) \tag{3.10}$$

Finally, the nominal power of a generator connected to the sample is:

$$P_{sample} = P_0 - \frac{1}{2}\left(10\ log\left(\frac{P_0}{P_{att}}\right)\right) - 10\ log\left(1 + \left(\omega L/50\right)^2\right) \tag{3.11}$$

To estimate the value of the inductance in series, we have measured the reflected power of a NbAl-S junction at T=1.7 K, in the range 0.5-3 GHz with a diode, while the junction was biased with a dc current.
The reflected power P_r is given by:

$$P_r = P_0 * \alpha^2 * \mid \Gamma_{sample} \mid^2 \qquad \Gamma_{sample} = \frac{Z - 50}{Z + 50} \tag{3.12}$$

where Γ_{sample} is the reflexion coefficient of the sample and Z is the junction and bonding wires impedance.

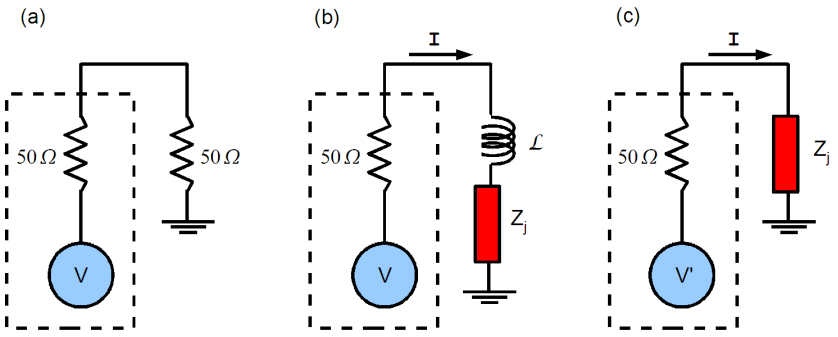

Figure 3.11: *Determination of the power at the sample level. The blue circle is the ideal generator, the dotted square represent the real generator. (a) Relationship between the nominal power and the output voltage of an ideal generator; (b) real circuit; (c) power variation due to the bonding inductance.*

When $I_{dc} = 0$, the junction is in the superconducting state, and

$$Z = i\omega L \qquad |\Gamma_S|^2 = 1 \tag{3.13}$$

When $I_{dc} = 60\mu A$, the sample is normal, and

$$Z = R + i\omega L \qquad |\Gamma_N|^2 = \left|\frac{R + i\omega L - 50}{R + i\omega L + 50}\right|^2 \tag{3.14}$$

By dividing the measured power in the normal state ($P_{r,N}$) by that in the superconducting state ($P_{r,S}$), we can obtain directly Γ_N, independently of the system attenuation.
The ratio $P_{r,N}/P_{r_S}$ is shown in Fig. 3.12, where Γ_N^2 is fitted by $\mathcal{L} = 3.35\,nH$ and $R = 10.6\,\Omega$.
The value found is consistent with the expression for the inductance of a cylindric wire at high frequency $\mathcal{L} = \frac{\mu_0}{2\pi} l\,(log(2l/r) - 1) \sim 3nH$, where $l = 1.5\,mm$ is the length of the wire and $r = 10\,\mu m$ is its radius.
To extend to other samples with two or three bonding wires in parallel, we will simply consider the inductance to be inversely proportional to the number of bonding wires, their length being quite the same for each sample.

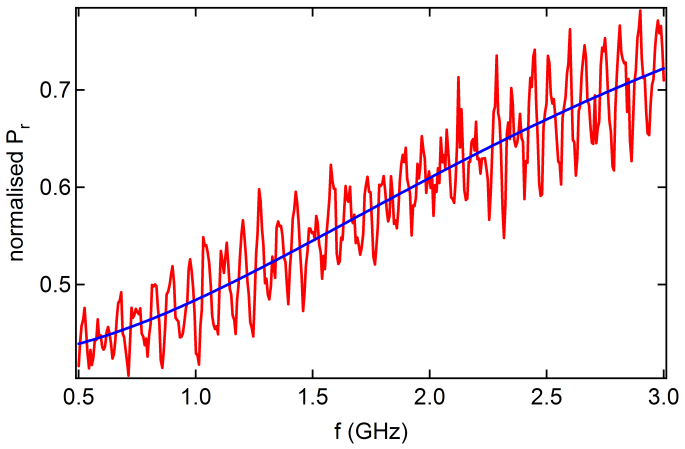

Figure 3.12: *Ratio between the power reflected by the sample in the normal state and in the superconducting state, equal to* Γ_N^2. *The fit correspond to an inductance* $\mathcal{L} = 3.35\,nH$ *and a resistance* $R = 10.6\,\Omega$. *The oscillations come from a phase difference between the normal and superconducting state.*

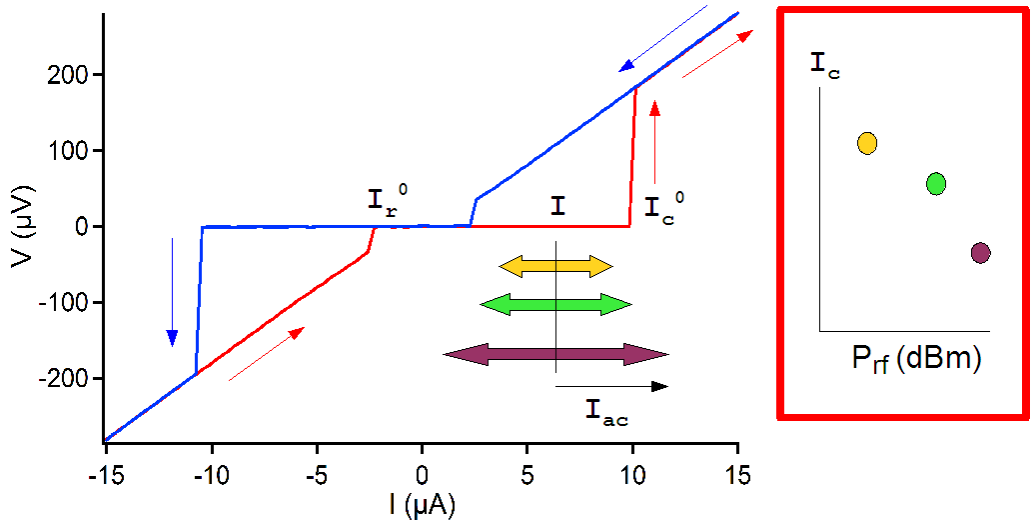

Figure 3.13: *Dc voltage vs. dc current characteristic when sweeping the current up and down at T=1.4 K for sample NbAl-L. The ac excitation modulates the dc current and changes the measured switching current.*

3.6 Low frequency regime

A dc voltage vs. dc current characteristic for sample NbAl-L at T=1.4 K in the absence of rf excitation is shown on Fig. 3.13.
We observe a hysteresis when sweeping the dc current up and down. This hysteresis is present up to 1.6 K for the long junctions and up to 2.23 K for the short junctions (see Fig. 3.25).
From such V(I) we deduce the critical current I_c^0 and the retrapping current I_r^0 with no excitation.
In Fig. 3.14 we show the temperature dependence of the critical current I_c^0 for NbAl-L and NbAl-S samples in normalised units. The continuous lines are the theoretical expectations for long SNS junctions (see sec. 2.3), calculated using eq. 2.4, but with an amplitude increased by a factor 18.5 for NbAl-S junctions and 710 for NbAl-L junctions.
We think that the prefactor is due to the non zero superconducting coupling constant in the Al.
The fact that our normal wires aren't normal metals, but instead superconductors above their critical temperatures, doesn't change the temperature dependence of I_c^0, but only acts as a scaling factor. Indeed, the $I_c(T)$ decay is well described by eq. 2.4.
We then believe that the results we obtain on our Nb-Al junctions are qual-

itatively valid for any SNS junctions containing a normal metal.

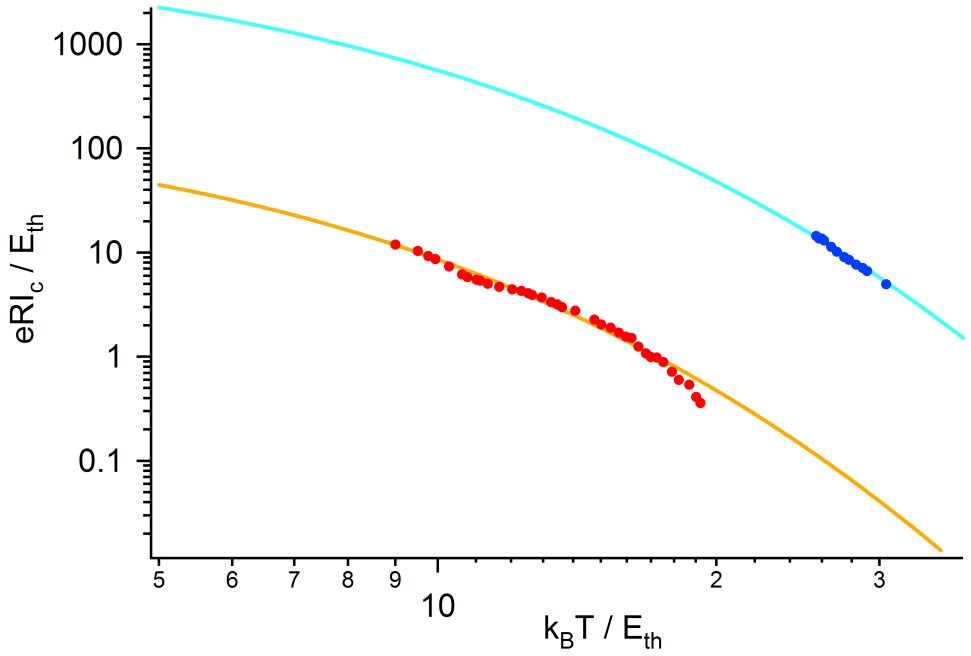

Figure 3.14: *Renormalized critical current vs. renormalized temperature for NbAl-L and NbAl-S samples. Each sample is fitted by the theoretical expectation given by Dubos, with the amplitude increased by a factor a. We used for sample NbAl-S* $\Delta/E_{Th} = 57$ *and* $a = 18.5$*, and for sample NbAl-L* $\Delta/E_Th = 201$ *and* $a = 710$.

We are interested in the changes occurring in the V(I) curves under irradiation. In particular, we concentrate on I_c and I_r.
Increasing the rf frequency, we expect different regimes, the junction behavior being modified each time the ac frequency crosses one of the system characteristic frequencies. This is indeed what we observe.
We now focus on the low frequency regime, between 10kHz and a few hundred MHz, where the frequency becomes of the order of the inelastic rate and much smaller than the temperature.
Let us first consider what happens when a slow ac current of small amplitude I_{ac} is added to the dc current (see Fig. 3.15 (a)). Increasing the dc current I from zero we expect the sample to jump to the normal (N) state when $I + I_{ac} = I_c^0$. Thus, for small ac amplitudes ($2\,I_{ac} < I_c^0 - I_r^0$), one expects one jump at $I_c = I_c^0 - I_{ac}$, i.e. the apparent critical current I_c decreases with

increased rf power (see Fig. 3.13).
Decreasing I from the N state, the sample stays normal as long as $I - I_{ac} > I_r^0$.

At larger ac amplitudes, i.e. when $2\,I_{ac} > I_c^0 - I_r^0$, the sample cycles from S to N and vice-versa, as long as $I_c^0 - I_{ac} < I < I_r^0 + I_{ac}$. Thus in this regime the V(I) characteristic should have two steps at $I_c^1 = I_c^0 - I_{ac}$ and $I_c^2 = I_r^0 + I_{ac}$. Between the two steps the junction is ohmic, with a resistance intermediate between zero and the normal state resistance (see Fig. 3.15 (b)).

The two regimes with one step for small I_{ac} and then a double step for larger I_{ac} is exactly what we observe at 10 MHz, see Fig. 3.16(a). Thus the sample follows adiabatically the 10 MHz excitation.
We have calculated the V(I) curve in the case of an adiabatic excitation using the RCSJ model, as explained in section 3.6.1. The numerical calcutation is shown in Fig. 3.16 as a green dotted line. The good agreement between the measurement and the expected low frequency curve also shows that we can calibrate precisely the rf power arriving to the sample.
A further confirmation of the validity of our interpretation is the temperature dependence of the V(I) curves in the double steps regime: the first step, $I_c^1 = I_c^0 - I_{ac}$, depends strongly on the temperature like $I_c^0(T)$, while the second step, $I_c^2 = I_r^0 + I_{ac}$, doesn't depend on temperature, exactly like $I_r^0(T)$ (see Fig. 3.17 and 3.25).

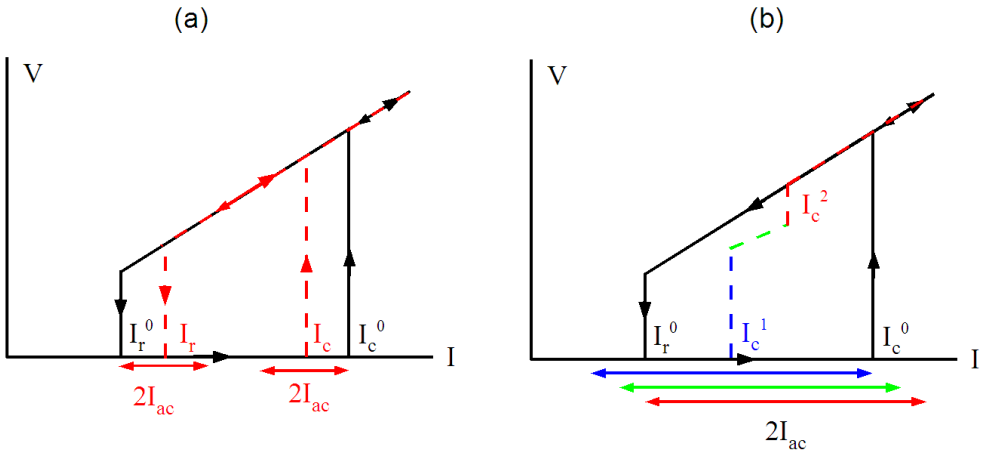

Figure 3.15: *Hysteresis cycle with and without irradiation (a) for a small ac amplitude, $2\,I_{ac} < I_c^0 - I_r^0$ (up and down curves) and (b) for an amplitude larger than the hysteresis cycle, $2\,I_{ac} > I_c^0 - I_r^0$ (only the up curve).*

When we increase the excitation frequency up to 100 MHz, the double steps disappear (see Fig. 3.16(b)).
We show in Fig. 3.18 and 3.19 the V(I) curves for a sample NbAl-S, irradiated with a constant rf power when increasing the rf frequency, at $T = 1.5\,K$ and $T = 1.59\,K$. When the frequency increases, the double steps close in continuously, until there is only one step left.
We also note that the V(I) curve is symmetric up to the frequency corresponding to the one step regime. If we increase further the frequency, the critical current is not affected, while the retrapping current decreases.

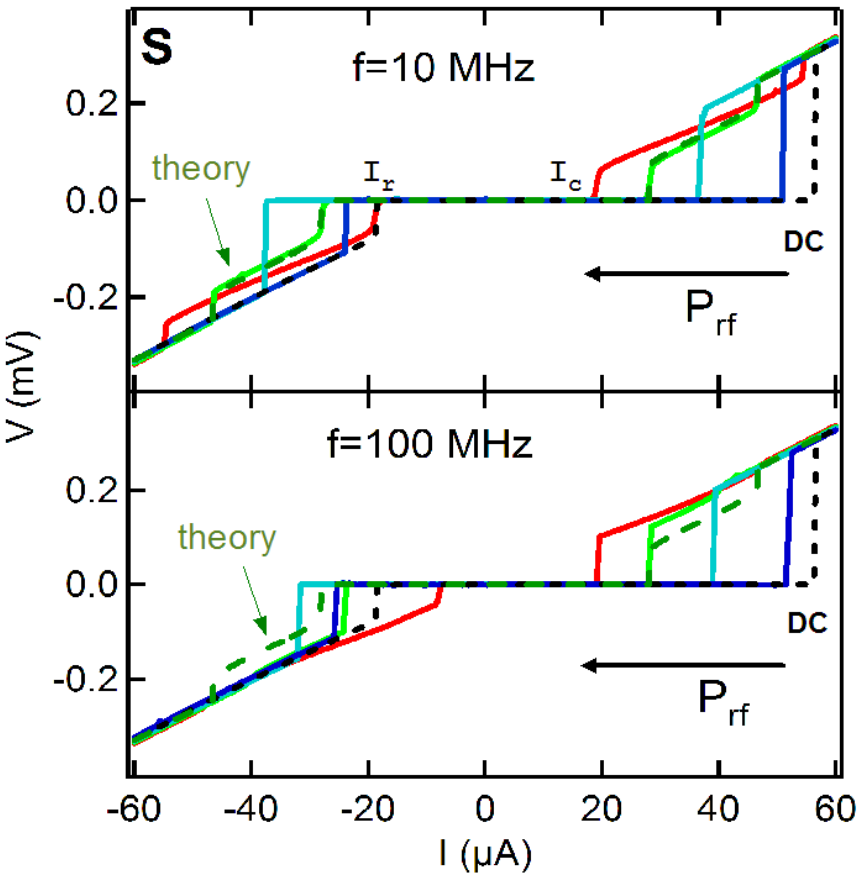

Figure 3.16: *Dc voltage vs. dc current characteristic measured on sample NbAl-S with a 10 MHz (a) or 100 MHz (b) rf excitation at several powers: from right to left, P= -66dB, -52dB, -48dB and -46dB. The dotted black line corresponds to no rf excitation. The dotted green line corresponds to the characteristic expected in the adiabatic regime. The temperature is T=1.5 K.*

An explanation to this behaviour is that, when the sample becomes normal, it never jumps back into the superconducting state even though the current I(t) spends some time below the dc retrapping current I_r^0.
This dynamical effect can be understood if we suppose that the hysteresis in the V(I) curve is at least partially due to heating of the electrons by the dissipative current, as suggested in [21]: the sample can return to the N state only if its temperature is low enough, i.e. when the power injected by the dc current I is completely dissipated through the substrate by inelastic processes.
At low temperature and at high frequency (see Fig. 3.16) the phonon cooling is not efficient enough and the junction heats up as soon as in the normal state, thus decreasing the retrapping current. The second step $I_c^2 = I_r^0 + I_{ac}$ is then expected to decrease. The normal part cools down during the time spent in the superconducting state, so that the critical current, and thus the first step $I_c^1 = I_c^0 - I_{ac}$, aren't affected.
When the frequency is larger than the inverse thermalization time of the electrons, the instantaneous current may be below I_r^0 but electrons are still hot and the sample remains in the normal state instead of cycling between

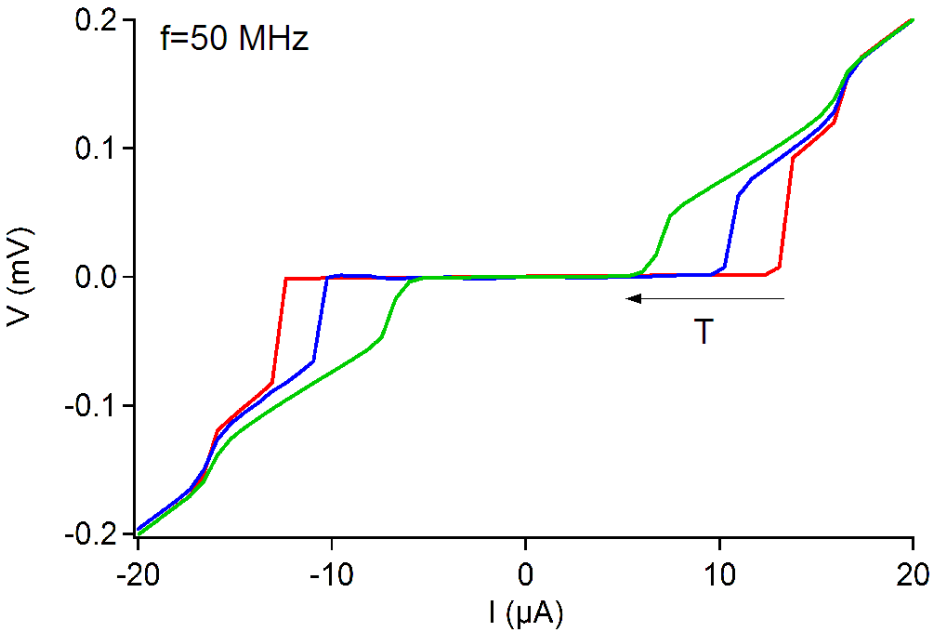

Figure 3.17: *Sample NbAl-S V(I) curves for different temperatures at* $P = -38\,dB$ *and* $f = 50\,MHz$*:* $T = 1.59\,K$ *(red line),* $T = 1.7\,K$ *(blue line) and* $T = 1.82\,K$ *(green line).*

the N and S states. Without cycling, the double steps structure disappears, and the characteristic frequency for the one-step regime should then be the inelastic rate.
Since the thermalization of the electrons occurs via phonon emission, we have compared the temperature dependence of the frequency f_r, corresponding to the transition from two-step to one-step V(I) curves, to a $A * T^3$ law.
In Fig. 3.20 we present the cubic law that best fits f_r. The coefficient A we find is 2.1 times larger than the theoretical value $A_{th} = 9.1\,10^6\,s^{-1}\,K^{-3}$, in good agreement with previous measurements on Al wires [51].
We can therefore assume that the frequency which determines the transition frequency from an adiabatic to a out-of-equilibrium regime is indeed the electron-phonon scattering rate. This strongly suggests that the retrapping is related to energy relaxation by electron-phonon interaction, as has been predicted for superconducting weak links [3].

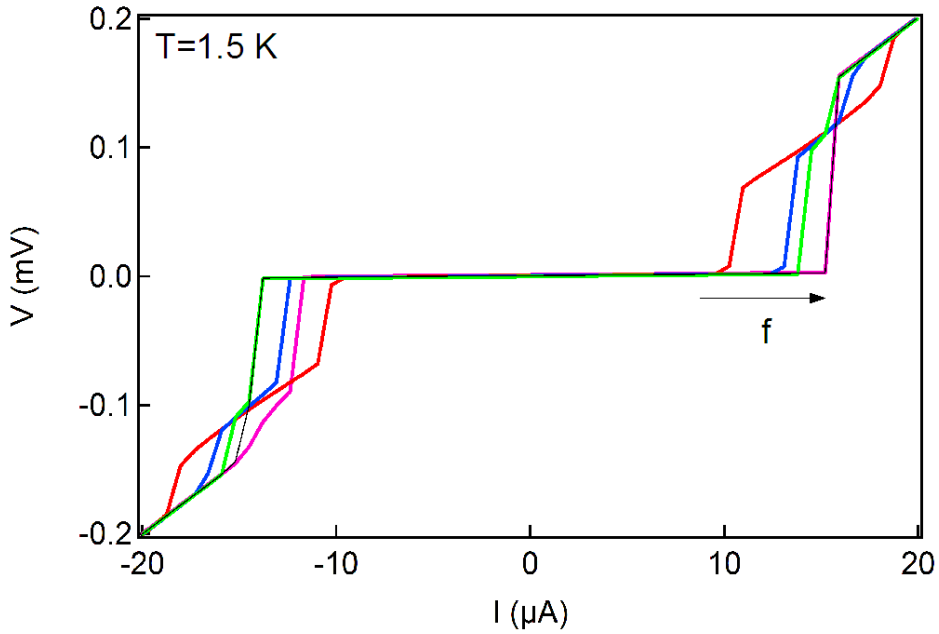

Figure 3.18: *Sample NbAl-S V(I) curves for different rf frequencies at* $T = 1.5\,K$. *The rf power is P=-38 dB. The ac frequencies are: f= 40 MHz (red line), 50 MHz (blue line), 55 MHz (green line), 60 MHz (black narrow line, no more double steps), and 100 MHz (magenta line).*

3.6.1 RCSJ calculations

We have seen in section 2.4 that the phase dynamics of a SIS junction is well understood in the Resistive Capacitive Shunted Junction model. Y. Song has proposed [54] that the same model could well describe also the phase dynamics of a SNS junction, as long as the SIS characteristic frequencies are replaced with the corresponding frequencies in SNS junctions.
It could then be interesting to see if there are any similarities between the frequency dependence of V(I) curves, calculated within the RCSJ model, and the low frequency behavior of a SNS junction (see sec. 3.6). In particular, this comparison could help us understand if the phase dynamics is important in the SNS dynamics, and how to replace the characteristic times of the RCSJ model.
We have solved numerically with the Runge-Kutta method (see B) the differential equation given by:

$$I_{dc} + I_{ac}\,\cos(\omega\tau) - \sin\,\varphi - \dot{\varphi}/Q = \ddot{\varphi} \tag{3.15}$$

where φ is the phase difference across the junction, I_{dc} and I_{ac} are the dc and ac current bias renormalised to the critical current I_c, ω is the excitation

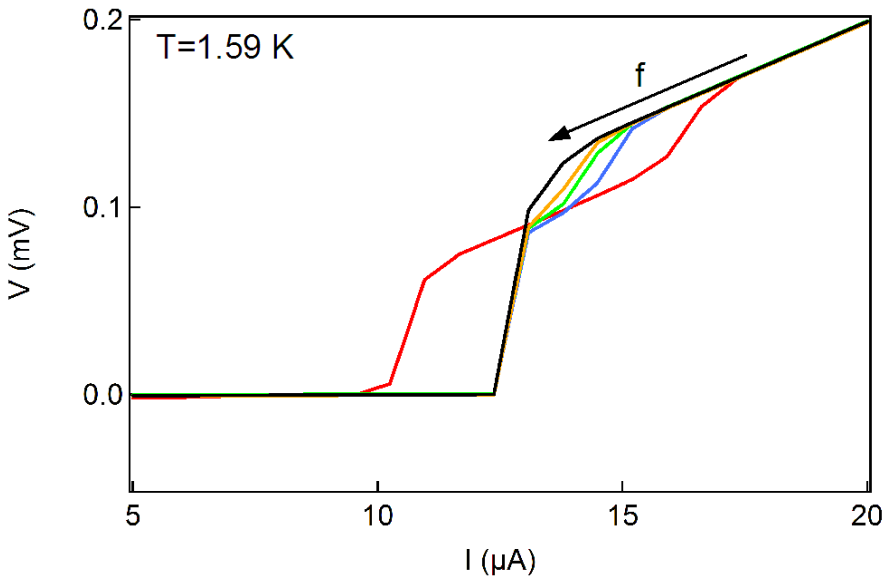

Figure 3.19: *Sample NbAl-S V(I) curves for different rf frequencies at $T = 1.59\,K$. The rf power is P=-38 dB. The ac frequencies are: f= 50 MHz (red line), 60 MHz (blue line), 65 MHz (green line), 70 MHz (orange line), and 80 MHz (black line).*

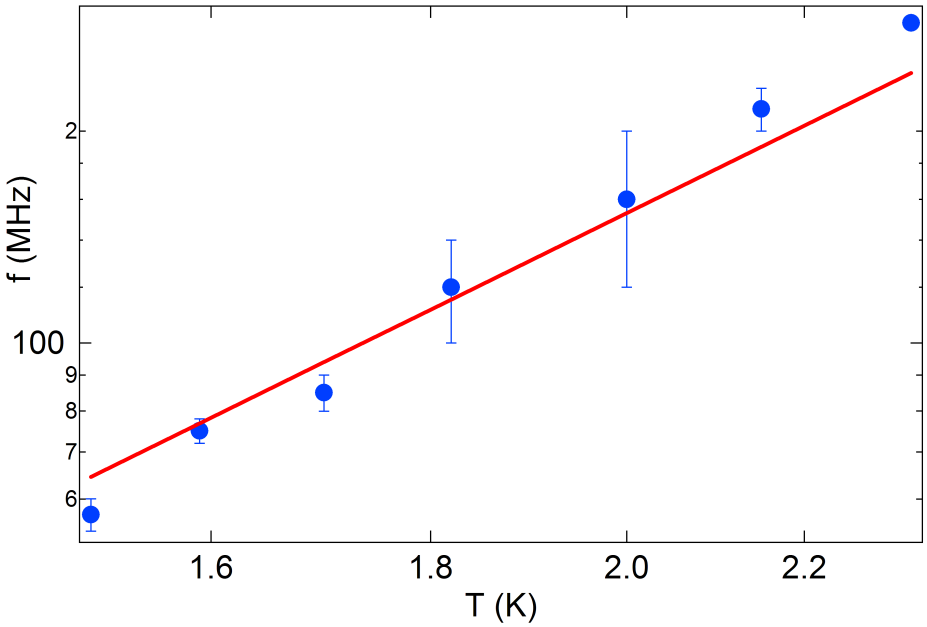

Figure 3.20: *Symbols: temperature dependence of f_r for sample NbAl-S; solid line: temperature dependence of electron-phonon scattering rate for Al.*

frequency, renormalised to the plasma frequency ω_p, $\tau = \omega_p t$ is the adimensional time and $Q = RC\omega_p$ is the junction quality factor.
In a SIS junction, the quality factor Q determines the hysteresis in V(I) curves:

$$Q = \frac{4}{\pi}\frac{I_c}{I_r} \tag{3.16}$$

In our SNS junctions, the experimental ratio $4/\pi\ I_c/I_r$ corresponds to a quality factor $Q \sim 3-4$. To be able to compare later on the results of SIS and SNS junctions, we take the SIS junction quality factor Q of this order of magnitude, i.e. Q=3.
Two characteristic frequencies are present in the model: the relaxation rate $1/RC$ and the plasma frequency ω_p. Since frequencies are renormalised to the plasma frequency, we have $\omega_p = 1$ and $1/RC = 1/Q = 0.33$. The low frequency curves ($\omega = 0.01$) are shown in Fig. 3.21. The junction behavior is exactly what we have observed in our SNS junctions: at low ac amplitudes, I_c is decreased when increasing the rf power, verifying exactly $I_c = I_c^0 - I_{ac}$. For $2\,I_{ac} > I_c^0 - I_r^0$, we find double steps, at $I_c^1 = I_c^0 - I_{ac}$ and $I_c^2 = I_r^0 + I_{ac}$.

When we increase the frequency in the simulations, we see in Fig. 3.22

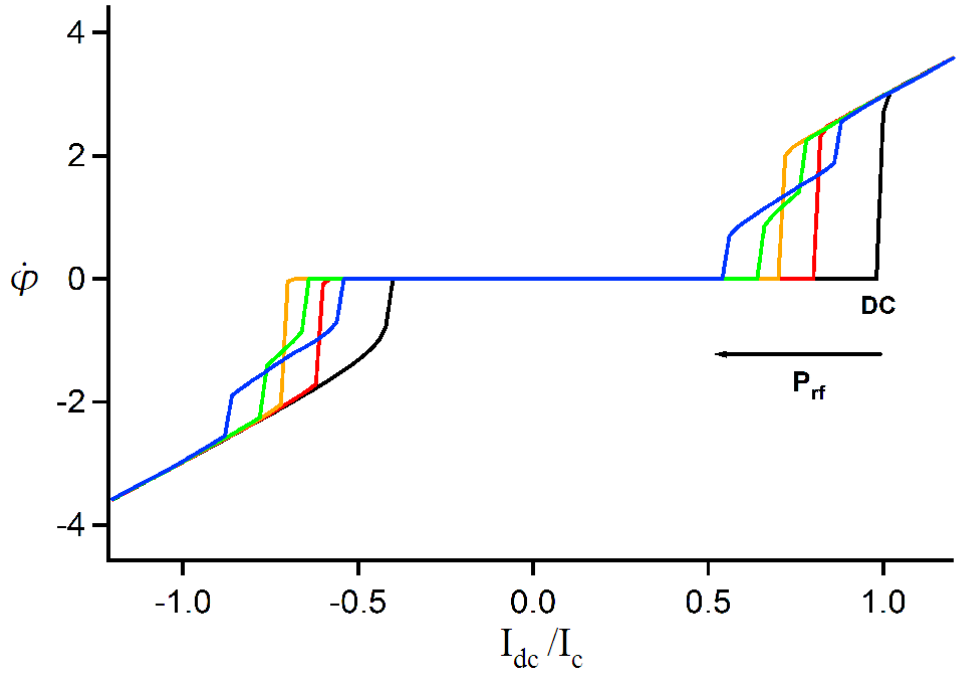

Figure 3.21: *Simulated V(I) curves for Q=3, ω =0.01 and several I_{ac} amplitudes: from right to left I_{ac}=0 (black line), I_{ac}=0.2 (red line), I_{ac}=0.3 (yellow line), I_{ac}=0.35 (green line), and I_{ac}=0.45 (blue line).*

that the two steps decrease gradually and disappear when $\omega = 1/RC$. Simulations for different Q factors (2,3,5,10) confirmed that $1/RC$ is indeed the relevant frequency.
The curves are very noisy since at high frequency and high rf power the response of the model begins to be chaotic.
A correspondance at low frequency can thus be done between the RCSJ model for SIS junctions and for SNS junctions just replacing the relaxation time RC by the inelastic time τ_{e-ph}.

Indeed, coming back to the mechanic interpretation of the RCSJ model, the time RC (the Q factor of the junction) determines the friction, i.e. the time the particle needs to lose the kinetic energy acquired in the normal state and slow down enough to stop in a potential pit of the phase.
In an analogous way, the electron-phonon time is the time the junction needs to lose the energy coming from the heating in the normal state, to come back to the superconducting state.

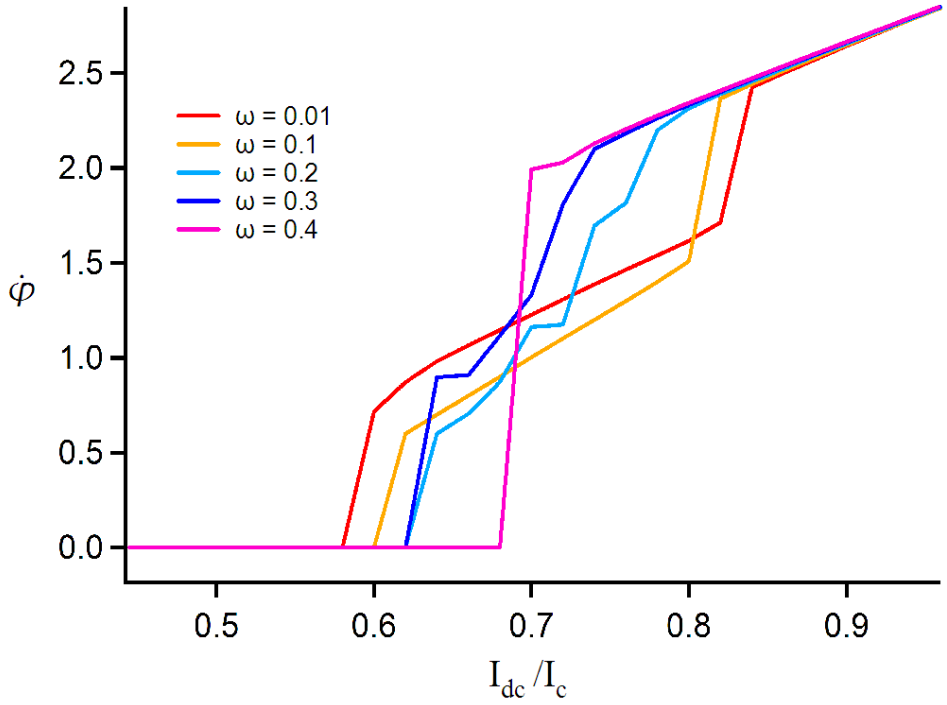

Figure 3.22: *Simulated V(I) curves for Q=3, I_{ac}=0.41 and several excitation frequencies: ω=0.01 (red line), ω=0.1 (yellow line), ω=0.2 (light blue line), ω=0.3 (blue line), and ω=0.4 (magenta line), where the two steps have completely disappeared.*

3.7 High frequency regime

Let's now increase the frequency beyond the electron-phonon rate τ_{e-ph}^{-1}. The V(I) curves have only single jumps, and up to frequencies of the order of a few GHz their features remain qualitatively unchanged. We study now a regime where the rf frequency f is of the order of the diffusion rate τ_D^{-1}, but still smaller than the temperature T.

3.7.1 Shapiro steps

When applying a microwave excitation on a SNS junction, Shapiro steps appear in the resistive part of the I(V) curve, i.e. the current forms a plateau when $V = n \frac{\hbar}{2e} \omega_{rf}$.
We show in Fig. 3.23 the differential resistance $R = dV/dI$ as a function

of the current I for sample NbAl-S at $f = 39\,GHz$. We see negative peaks, corresponding to plateaus in a I(V) curve.
The shift visible in Fig. 3.23 is due to the filters and Bias-Tee resistance, $R_{ext} = 2.3\,\Omega$, which of the same order of magnitude than the sample resistance. When plotting the differential resistance vs. the voltage across the sample, $V - R_{ext}I$, we find the expected plateaus position.
In tunnel Josephson junctions, the amplitude of the Shapiro steps when increasing the rf power is described by a Bessel function. In the case of a

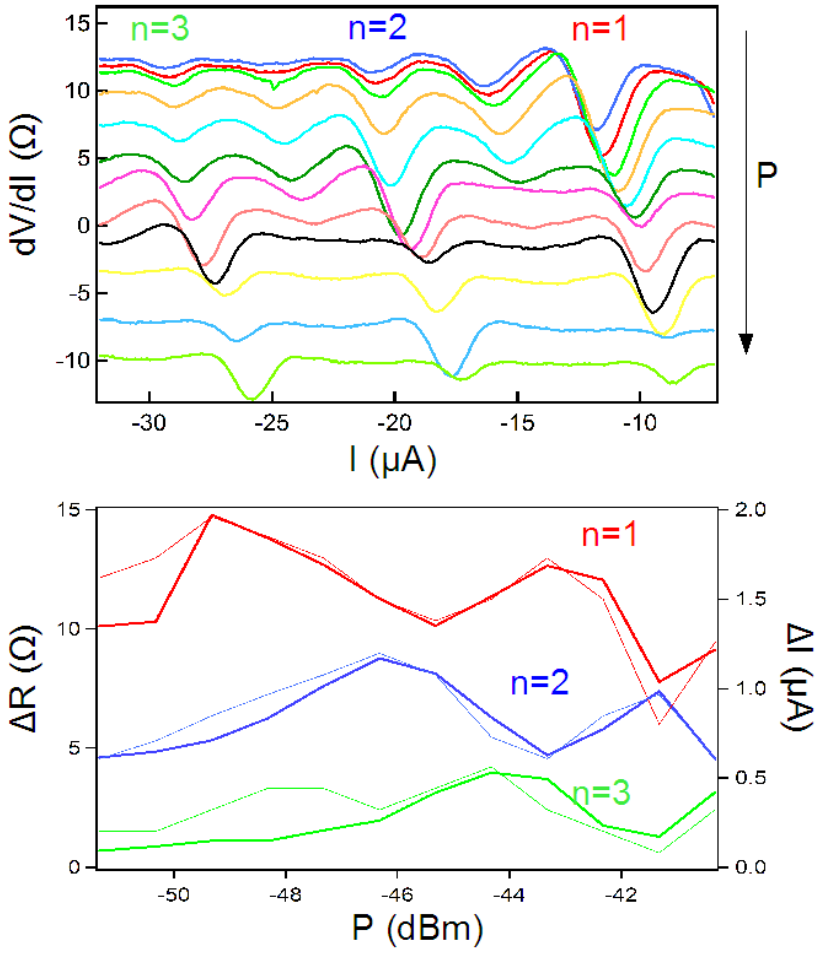

Figure 3.23: *(a) Differential resistance vs. dc current for NbAl-S sample at $T = 2\,K$ when irradiated with a 39 GHz excitation for several rf powers; curves are vertically shifted for clarity (b) resistance variation (left scale, continuous line) and amplitude of the current plateaus (right scale, dotted line) as a function of the rf power for n=1,2,3.*

resistive shunted, current polarised, junction, the amplitude of the current steps as a function of rf power can be calculated [5] and is qualitatively similar to what we found (see Fig. 3.23).
We see integer Shapiro steps up to $f = 8.5\,E_{Th}/h = 2.1\,\tilde{\Delta}/h$. Moreover, at a temperature $T = 2\,K$, we measure Shapiro steps with $n > 1$ up to $V = 13\,E_{Th}/e$. This confirms what we found in sample WAu-Sq (see section 2.8).
On the contrary, we don't see any fractional Shapiro step, possibly because of the difference in the ac bias: in sample WAu-Sq the ac excitation was given by an antenna, while in the case of sample NbAl-S, the ac current is directly injected in the junction, giving a much stronger coupling.

3.7.2 Critical current enhancement

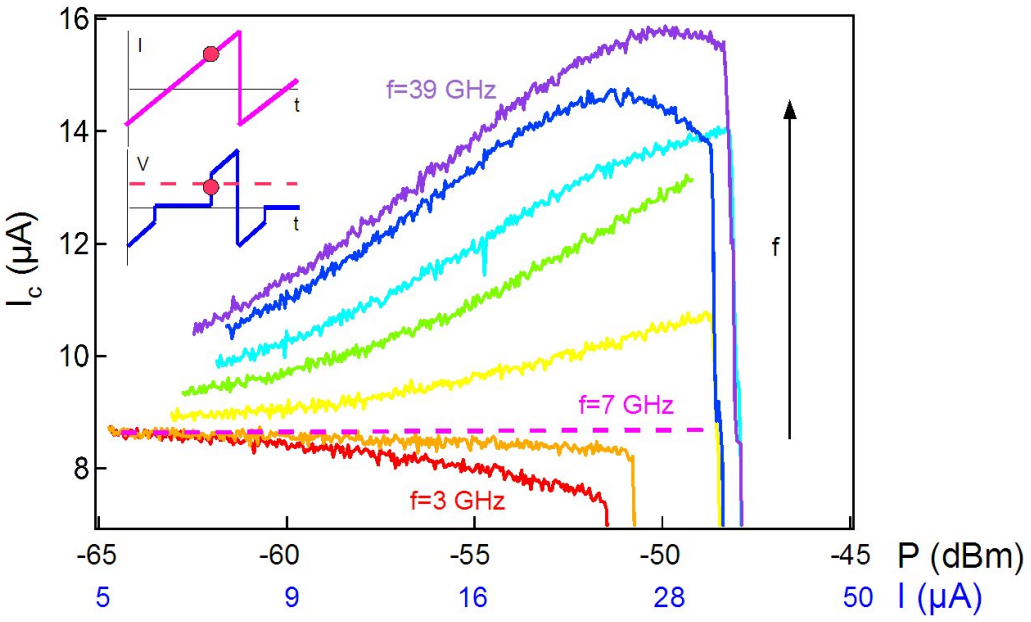

Figure 3.24: *Critical current vs. rf power and bias current in sample NbAl-L at $T = 1.6\,K$ for different frequencies: from bottom to top f=3,6,12,21,33,36,39 GHz.*

The critical current behavior is instead not standard: I_c is strongly increased by the microwaves at high frequency.
To measure I_c we current-bias the junction with an 83 Hz linear ramp and measure the time before dissipation.

We report in Fig. 3.24 for sample NbAl-L the effect of the microwaves on I_c for various frequencies.
We observe that, below a certain frequency f_c, the critical current is decreased by the rf excitation, as in our previous measurements. For $f > f_c$, instead, I_c is enhanced more and more with increasing rf frequency.
As a function of the microwave power, the enhancement initially increases, then begins to decrease (which we could interpret as the fist part of an oscillation, as in Fig. 3.5). We never see a complete oscillation because, around the rf power P=-47 dB, the sample becomes suddenly normal.
The maximum increase amplitude (two times I_c^0 in NbAl-L sample) is consistent with the classical Dayem-Wyatt effect (see sec. 3.2). The frequency f_c, instead, is much greater than the expected inelastic rate, as was also observed in ref (ref Warlaumont, Notarys).
Fig. 3.25 shows I_c and I_r temperature dependence for NbAl-S sample, with and without microwave irradiation ($f = 39GHz, P = -48dBm$). We observe that I_c is markedly increased by the rf excitation over the whole temperature range, which again is in strong contrast with what has been observed in superconducting strips, where the enhanced superconductivity is restricted to a very narrow region around T_c, of the order of a few mK. Our data are instead consistent with Warlaumont et al. [22] and with Notarys et al. [43] .

When applying a magnetic field we see, as expected, a monotonic Gaussian decrease of I_c (see section 2.7.2). Fig. 3.26 shows the critical and retrapping currents I_c and I_r as a function of magnetic field with and without microwave excitation. We can see that the critical current is enhanced even in a magnetic field, but the amplitude of the enhancement decreases quickly. At strong magnetic fields ($B \sim 70G$) the rf excitation destroys the supercurrent.
On the other hand, the retrapping current is slightly decreased when the microwaves are switched on, but its dependence in magnetic field is essentially the same with or without rf.

To understand those data, we have to consider the interplay between the known Dayem-Wyatt effect, i.e. the distribution functions dynamics, and the normal density of states dynamics.
In the SNS geometry, due to coherent Andreev reflections at the N/S interface, a finite gap $\tilde{\Delta}$, the so-called mini-gap, develops inside the normal metal. In a way similar to the BCS gap equation, $\tilde{\Delta}$ is determined by the Andreev bound states as well as by the distribution function of the quasiparticles. It is thus natural to expect an enhanced induced superconductivity by ac irradiation.

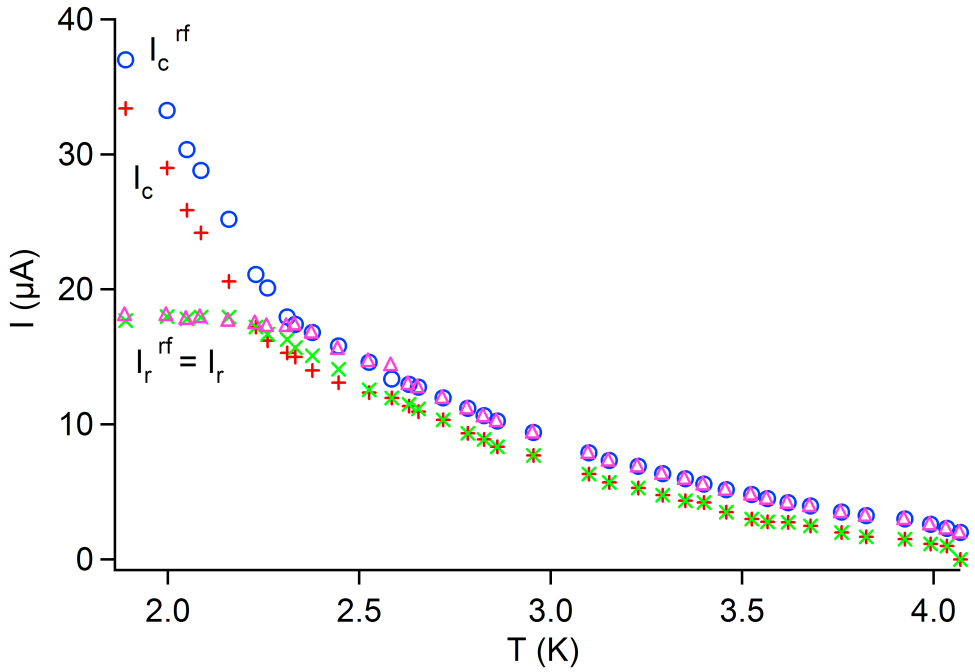

Figure 3.25: *$I_c(T)$ (+ rf off, ◯ rf on) and $I_r(T)$ (X rf off, △ rf on), with and without rf excitation (f=39 GHz, P=-48 dBm) on sample NbAl-S.*

However, two facts make the physics of SNS samples more complex than that of superconductors:

- the distribution functions involve not only the inelastic time but also the diffusion time τ_D of quasiparticles along the N part, since Andreev pairs diffuse from the N/S interfaces to the centre of the N part
- the density of states is affected by the rf field through the phase of the Andreev pairs being modified by the ac vector potential

In order to elucidate the mechanism that sets the critical current enhancement, we have:

1) varied the normal length

2) varied the temperature

3) applied a magnetic field H perpendicular to the substrate

We have observed that:

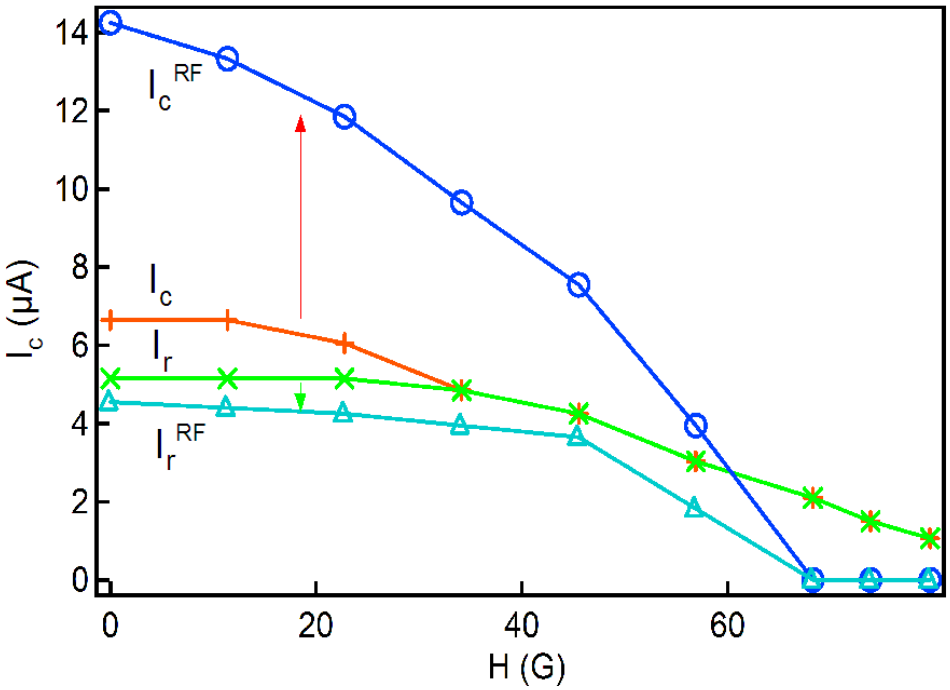

Figure 3.26: *(a) $I_c(H)$ (+ rf off, ◯ rf on) and $I_r(H)$ (X rf off, △ rf on), with and without rf excitation (f=39 GHz, P=-48 dBm) on sample NbAl-L.*

1) I_c vs. rf power has a similar behavior for NbAl-L and NbAl-S samples, but with a frequency f_c that is larger for shorter samples:

   sample NbAl-S: $f_c = 17GHz = 0.59\,\tau_D^{-1}$

   sample NbAl-L: $f_c = 7GHz = 0.85\,\tau_D^{-1}$

   The frequency f_c seems then to be related to the Thouless energy, or to an energy scale depending on the Thouless energy, such as the minigap. Already in Notarys et al. [43] it was mentioned that the relevant time scale may be the effective time-dependent Ginzburg-Landau relaxation time, which is proportional to the diffusion time: $\tau^* = (\pi/2)^2\tau_D$.

2) f_c doesn't depend on temperature at zero magnetic field

3) $f_c(H)$ has a non-monotonic behavior, and depends strongly on temperature (see Fig. 3.27).

In particular, if we note the ratio between the temperature and the normal part critical temperature $T_{c,N}$, i.e. the temperature where the normal part resistance goes to zero, we observe at high temperatures, near to $T_{c,N}$, a parabolic $f_c(H)$ dependence, while at lower temperatures f_c decreases and then increases.
We can understand the parabolic increase if we consider the effect of the magnetic field on the Andreev pairs.
The characteristic time to break an Andreev pair is τ_H, defined as:

$$\frac{1}{\tau_H} = \frac{De^2w^2}{3\hbar^2}H^2 \tag{3.17}$$

The faster the pairs break (high τ_H^{-1}), the faster one should pump the quasiparticles out of the increased effective gap.
We can then fit the f_c curve at the higher temperatures with the law:

$$f_c = \alpha\frac{1}{\tau_D} + \beta\frac{1}{\tau_H} \tag{3.18}$$

which gives:

$$f_c/f_c(0) = 1 + \frac{\beta}{\alpha}\frac{\pi^2}{3}\Big(\frac{\Phi}{\Phi_0}\Big)^2 \tag{3.19}$$

The fit, shown in Fig. 3.27 is good, and we have $\beta = 0.23$ for the sample NbAl-L, and $\beta = 0.05$ for the sample NbAl-S. Of course, those fits are not very significant because of the low number of points and further measurements are needed.

We now look at what happens to the retrapping current when applying a high frequency excitation.
In Fig. 3.25 we can distinguish two temperature ranges: for $T < 2.23K$, when the V(I) characteristic is hysteretic ($I_r \neq I_c$), the microwaves have no effect on I_r, which saturates. For $T > 2.23K$, instead, I_c and I_r are identical, and they are both enhanced by the rf excitation. Thus, as soon as I_r is a relevant quantity, its response to the rf excitation is radically different from that of I_c. Similar results are obtained for the NbAl-L sample.
The behavior of the retrapping current under irradiation could help understand the origin of the hysteresis in SNS junctions (see sec. 2.4). If I_r is only due to thermal effects (electrons heated up to $T_e > T$ because of the power injected in the normal state), its value would be $I_r = I_c(T_e)$. In this case, I_r should be increased by the rf exactly the same way I_c is. But I_r is not enhanced, suggesting that the origin of the hysteresis is not completely

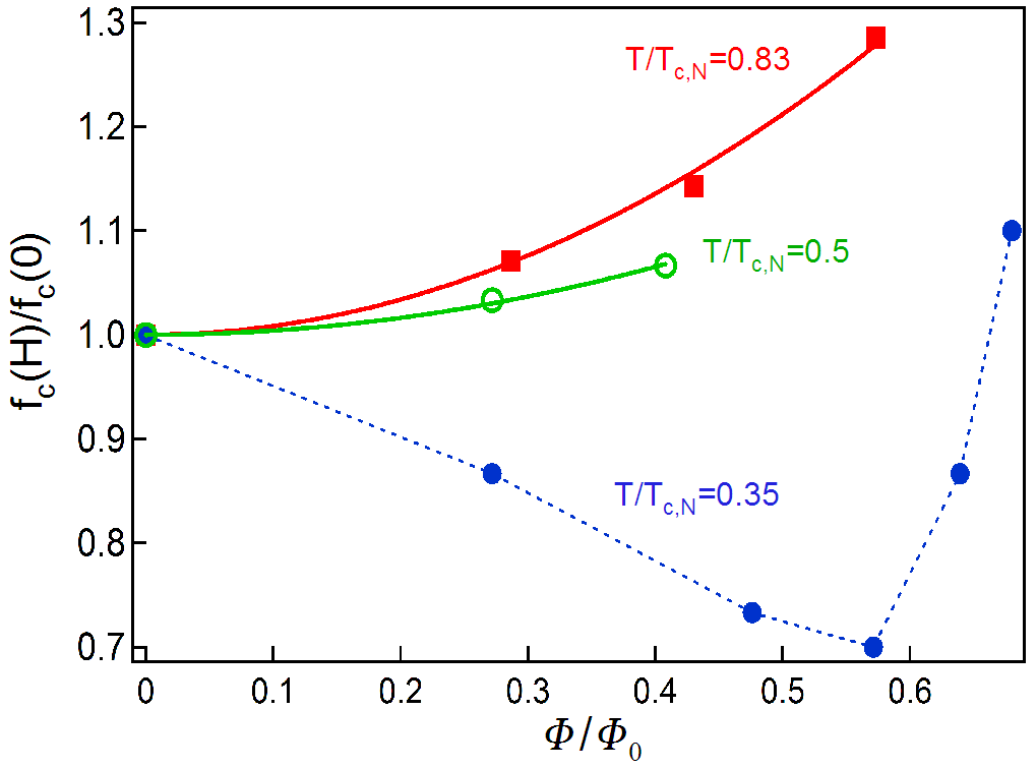

Figure 3.27: *Renormalized cross-over frequency $f_c(H)/f_c(0)$ vs. renormalized magnetic field H/H_0, where H_0 corresponds to one flux quantum in the N part. Full red squares: sample NbAl-L at T=1.6 K; full blue dots: sample NbAl-S at T=1.4 K; green circles: sample NbAl-S at T=2 K.*

explained within a heating model.

3.8 Conclusion

We have measured the dc voltage vs dc current characteristic of a long SNS Nb-Al junctions excited by an ac current in the frequency range 100 kHz - 40 GHz.
Our junctions are made by double angle deposition of Nb (forming the superconducting contacts) and Al (the normal part). To fabricate the suspended mask we used a special resist, a PMMA-Si_3N_4-PES trilayer. This resist can indeed sustain high temperatures, condition which is essential to e-gun evaporate a refractory metal like Nb.
The junctions were measured at temperatures between the critical temperature of Al, $T \sim 1.2\,K$ and the liquid He^4 temperature, $T \sim 4\,K$. At these temperatures, the Al superconducting nature doesn't affect the qualitative results, even if the critical current is globally increased.
We observe several regimes in the V(I) characteristics, depending on the frequency of the microwaves.

At low frequency ($f \lesssim 50\,MHz$), the voltage follows adiabatically the dc measured V(I) curve. For a strong ac current amplitude $2\,I_{ac} > I_c - I_r$ the V(I) characteristic presents two voltage steps, one at $I_c^1 = I_c - I_{ac}$ and the other at $I_c^2 = I_r + I_{ac}$. Between I_c^1 and I_c^2 the junction cycles from the normal to the superconducting state and vice versa. In this region the measured average resistance is smaller than the normal state resistance.
Our measurements in this regime are in very good agreement with the predictions.

At intermediate frequency ($50\,MHz < f < 500\,MHz$), the critical current and, particularly, the retrapping current are affected when the frequency crosses the frequency f_r. In particular, the double step structure is replaced continuously by a single step characteristic.
By measuring its temperature dependence, we have found that f_r corresponds to the electron-phonon scattering rate τ_{e-ph}^{-1}. We measure $f_r = 1.9\ 10^7\,T^3\ s^{-1}\,K^{-3}$, in good agreement with previous measurements on Al wires [51].
This dynamical effect can be understood if we suppose that the hysteresis is partially due to heating of electrons by the dissipative current: the junction can switch from the normal to the superconducting state only if the elec-

tronic temperature is low enough, i.e. if the power injected in the normal state is completely dissipated through the substrate by inelastic processes.
When the frequency is higher than the electron-phonon time, the power dissipated by the junction in the N state hasn't the time to be evacuated through the phonons, which are the main inelastic process at high temperature. The junction then heats up, and the retrapping current decreases. The hysteresis cycle increases, and the excitation amplitude is not large enough anymore to cycle between N and S. The double step region is thus suppressed.
A similar effect is reproduced by the RCSJ model for junctions of $Q = 4/\pi\ I_c/I_r \sim 1.5 - 10$ (of the same order of magnitude than the experimental one) when the ac frequency crosses $f_r = 1/RC$. We can then establish a parallel between the kinetic energy relaxation time RC in a SIS junction, and the energy relaxation time τ_{e-ph} in a SNS junction at $T \gtrsim 1\,K$.

At high frequency ($f > 5\,GHz$), we observe a strong enhancement of the critical current over a large temperature range.
In particular, the microwaves nearly double the critical current in sample NbAl-L, while the increase of I_c in sample NbAl-S is about 11%. The retrapping current is not affected at all.
This enhancement increases with the rf frequency and seems to oscillate with the rf power (we observe only one oscillation period).
The characteristic frequency f_c for the critical current enhancement seems related to the diffusion rate τ_D^{-1}, and like τ_D^{-1} doesn't vary with temperature and depends strongly on the normal wire length.
When applying a dc magnetic field, we observe a parabolical increase of f_c near the proximity superconductivity critical temperature, while, at lower temperatures, f_c is not monotonic.
Indeed, at high temperature the magnetic field acts as a pair breaking mechanism, with a typical breaking rate $\tau_H^{-1} \propto H^2$. This excess of quasiparticles weakens the superconductivity, so that an enhanced critical current is atteined only if the excitation is faster than the pair breaking.
At low temperature, f_c first decreases, then, at strong magnetic field, increases. We guess a competition between the pair breaking mechanism at large fields, and the desity of states dependence on H at low fields (the minigap decreases with the magnetic field).

Chapter 4

High frequency phase modulation

To measure the high frequency current-phase relation of an isolated SQUID is not easy.
One first needs to control and modulate at high frequency the phase difference across the junction.
Then, one needs to access the high frequency response of the supercurrent (possibly separating the part of the current that follows the excitation in phase from the one that is out-of-phase).
One possibility to measure, in a dc configuration, the current-phase relation when the junction is excited at high frequency, is to impose a dc magnetic flux into the ring, to set the dc phase, an antenna to provide the high frequency phase modulation, and a micro-Hall bar to detect the magnetic moment of the supercurrent circulating in the ring [25].
However, the micro-Hall bar itself can be sensitive to the rf irradiation, making it difficult to separate the signal coming from the supercurrent from the signal due to the bar [8]. Moreover, it is not possible within this method to measure independently the in and out-of-phase responses to the high frequency excitation.
In our setup we use a superconducting coil to set the dc phase across the junction, and a superconducting multimode resonator both to provide the phase modulation (modulation possible at all the frequencies multiples of the resonator base frequency) and the readout: the variation of the resonator frequency gives the in-phase response, while the variation of the quality factor gives the out-of-phase response of the supercurrent.
This technique was developped in the group for contactless measurements of the response of the persistent currents in 10^4 normal Aharonov Bohm rings [16] [47]. Thanks to the fact that the supercurrent in a SNS junction

is greater than the persistent current in a normal ring by a factor $g \sim 10^4$ (g being the dimensionless conductance of the normal wire), we are able to measure a single ring. Moreover, it is possible in a SNS ring to adapt the length of the superconductors to maximise the coupling to the resonator, thus maximising the signal.

4.1 Superconducting multimode resonator

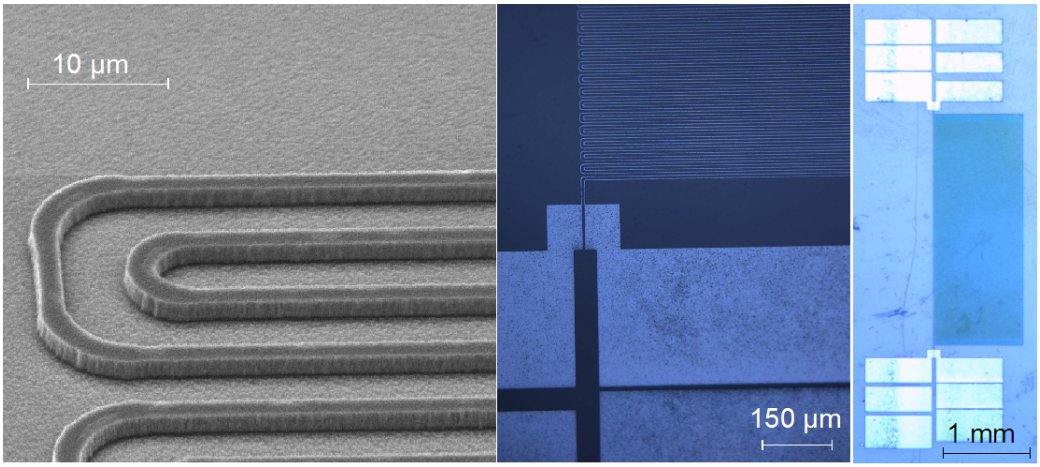

Figure 4.1: *Nb superconducting multimode resonator.*

The superconducting resonators we have fabricated (see Fig. 4.1) were conceived by B. Reulet and H. Bouchiat [48]. They are formed by two parallel Nb meanders on a sapphire or silicon dioxide substrate.
Each line is $20\,cm$ long, $1.7\,\mu m$ wide and $1\,\mu m$ thick, and the distance between the two wires is $6.7\,\mu m$. The two-wire line is folded into a $3\,mm$ x $1\,mm$ structure (see Fig. 4.1).
As shown in Fig. 4.1, at both ends of each line there are several capacitors in series. By choosing where to connect the rf generator, one can control the strength of the capacitive coupling of the resonator to the environment. In particular, we aim to be in the under-coupled regime, with a quality factor at its highest, providing a maximum sensitivity. When the frequency increases, however, the coupling also increases, so that sometimes we are forced in the over-coupled regime.

4.1.1 Resonance frequency and quality factor

We characterise the resonance by two parameters: the resonance frequency f and the quality factor Q.
The quality factor Q is defined as the ratio between the energy stored and the energy dissipated in a time $1/\omega$. Experimentally, Q is related to the sharpness of the resonance: $Q = f/\delta f$, where δf is the width of the resonance at half height.
Both the resonance frequency and the quality factor depend strongly on the temperature T, the magnetic field H and the measurement frequency f (see appendix C).
In order to minimize the dependence of the resonance with the temperature and magnetic field, a thick Nb structure has been chosen for the superconducting resonator.
Indeed, a thick structure has properties close to those of the bulk, and bulk Nb has a high T_c ($T_c = 9.2\,K$), and a relatively high critical magnetic field ($H_{c1} \sim 1000\,G$). Since we work at temperatures $T < 1.5K$ and with magnetic fields $H < 10\,G$, very low in comparison to T_c and H_{c1}, we expect Q and f to be practically independent of temperature and magnetic field.
It is indeed the case, since we observe that Q varies less than 1% and f less than 10^{-5}.

4.1.2 Resonant conditions

The resonant conditions are given by:

$$L_r = n\frac{\lambda}{2} = n\,\frac{c/\sqrt{\epsilon_r}}{2\,f} \tag{4.1}$$

L_r is the resonator length. The relative dielectric constant ϵ_r is the average between the sapphire substrate and the vacuum dielectric constants: $\epsilon_r \simeq (1+10)/2 = 5.5$.
The base resonance frequency is then $f = 320\,MHz$, in agreement with the measured first harmonic of the resonator, which is $f = 365MHz$.
Eq. 4.1 is exactly the same one would use for a bifilar straight line with current zeros at both ends (this condition in our case is imposed by the capacitors): the fact that the resonator is folded doesn't seem to affect its resonances. However, the electro-magnetic field is confined, thanks to the folding, within $5\mu m$ from the resonator.

In a bifilar line, the inductance and capacitance are:

$$\mathcal{L}_r = \frac{\mu_0}{\pi}\, ln\left(\frac{D}{r}\right) L_r = 1.52\ 10^{-7}\ He \tag{4.2}$$

$$C_r = \pi\, \frac{\epsilon_0\, \epsilon_r}{ln(D/r)}\, L_r = 1.31\ 10^{-11}\ F \tag{4.3}$$

where D is the distance between the two wires and r the radius of the wires. The resonance frequency of a bifilar line,

$$2\,\pi\, f = \frac{\pi}{\sqrt{\mathcal{L}_r\, C_r}} \tag{4.4}$$

is equivalent to eq. 4.1.

Our base resonance frequency $f_1 = 365$ MHz is followed by harmonics up to more than 6 GHz with a quality factor $Q = 10^4$ at f_1 and $Q \gtrsim 5\ 10^2$ for frequencies up to the 17^{th} harmonic.
Thanks to the high Q factor, we are able to detect extremely small variations of f and $1/Q$:

$$\frac{\delta f}{f} \sim 10^{-9} \qquad \delta(\frac{1}{Q}) \sim 10^{-10} \tag{4.5}$$

4.1.3 Fabrication method

To fabricate the Nb wires thick enough, one can't use standard evaporation/lift-off method.
Instead, we deposit by sputtering a Nb film $1\mu m$ thick over the substrate (adherence is good for both sapphire and $Si0_2$ substrates).
By optical lithography, we expose the resonator pattern, in which, after developing the resist, we evaporate a 50 nm Al film.
The Al film acting as a mask, we etch all the non-protected Nb with a SF_6 Reactive Ion Etching (Nb being more reactive than Al to the fluorine). Finally, we dissolve the remaining Al in a KOH solution.

4.2 ac SQUID fabrication

4.2.1 Nb-Au AC SQUIDs

Two types of AC SQUIDs were measured.
First, we fabricated on a sapphire substrate a pattern of 25 Nb-Au AC SQUIDs from a Nb-Au bilayer, following the same procedure detailed in

sec. 2.1.2 for SQ-NbAu samples.
After SEM observation, we erased by FIB etching 16 rings, leaving 9 rings without defaults and with a similar normal part length.
The etched rings are shown in Fig. 4.2 (b), while the rings we measured are

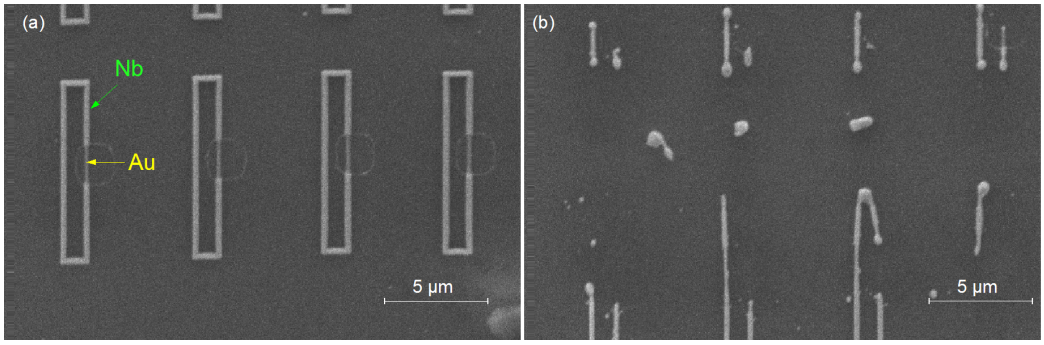

Figure 4.2: *(a) SEM image of four of the Nb-Au AC SQUIDs measured and (b) SEM image of what is left after the FIB etching.*

shown in Fig. 4.2(a).
To couple the rings to the resonator we deposit on the resonator a droplet of PMMA A6, and a MYLAR sheet of thickness $1.4\,\mu m$. As soon as the PMMA has dried, we deposit a second PMMA drop, on which we pose the sapphire face containing the rings. While the PMMA is still liquid, the sapphire substrate is shifted to align the SQUIDs between two resonator lines (see Fig. 4.3); this is possible since the sapphire is transparent. A good alignement assures that the flux of the magnetic field, generated by the resonator into the rings, is maximum.
The preliminary results obtained on this pattern confirmed that the measurement tecnique we use is sensitive enough to detect a single ac SQUID.

4.2.2 W-Au ac SQUID

In a second moment, we have then fabricated a single SNS ac SQUID directly on the resonator sapphire substrate.
The fabrication method is exactly the same as the one used for the samples W-Au on a SiO_2 substrate described in section 2.1.3. However, the insulating nature of the sapphire substrate complicates the process, because the charge accumulation on the substrate deflects the ion beam. We found that connecting to the ground the Nb lines mostly solves the problem.
Let's now detail the SQUID fabrication process. First, we deposit a Au wire

between two resonator lines, by e-beam lithography and thermal evaporation. We use the FIB to contact the Au wire with thin superconducting W wires. We then connect the thin W wires to the Nb thick resonator line, whose surface oxide is previously etched with the FIB. To create wide and thick W wires that don't break when stepping over the $1\mu m$ thick resonator line, we need to increase the beam current and the deposition time.
Fig. 4.4 shows the final SQUID.

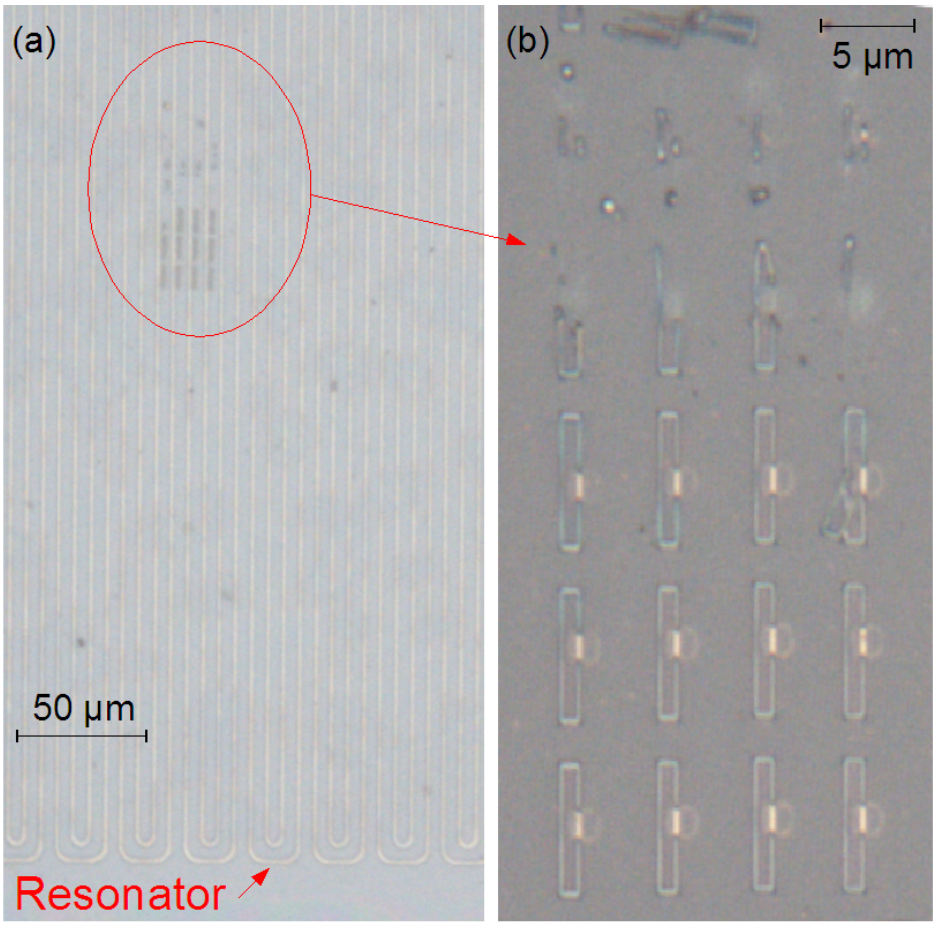

Figure 4.3: *(a) Optical microscope image through the sapphire substrate of the rings, which is superposed to the resonator fabricated on a $Si0_2$ substrate. One can see on the bottom of the image the folding of the resonator lines. On top, dark rectangles are visible: they are the AC SQUIDs. A good focus is very difficult to obtain since the resonator and the SQUIDs have a height difference of about $1-2\,\mu m$. (b) Optical microscope image of SQAC-NbAu. Before the measurement, two of the 11 visible SQUIDs have been removed.*

A first set of measurements revealed that the field screening, due to the ring inductance, was too large. We thus had to reduce the ring perimeter to decrease the ring inductance. We then made new contacts between the thin W wires and the resonator, interrupting the previous ring by FIB etching (see Fig. 4.5).

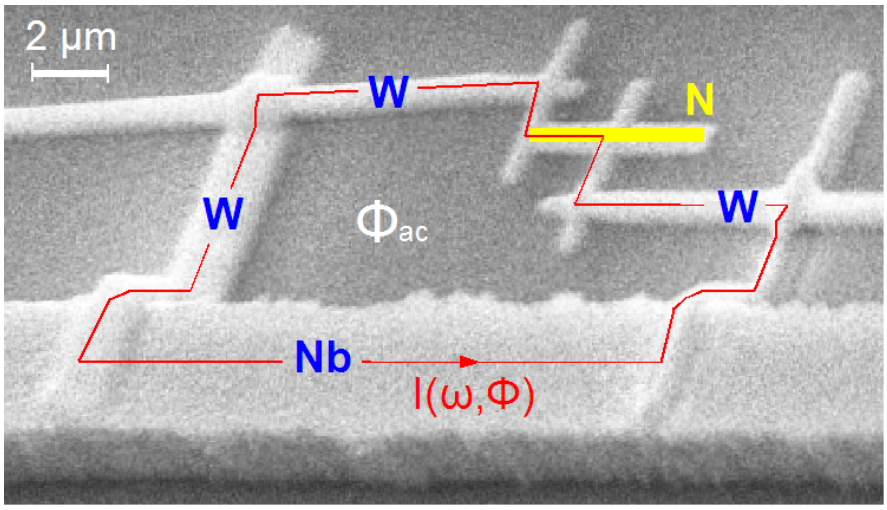

Figure 4.4: *SEM tilted image of AC2 ring. The Au wire is contacted with thin W wires. The thin wires are connected to the* 1 *µm thick resonator by wide and thick W wires. The Au wire is indicated with a yellow line.*

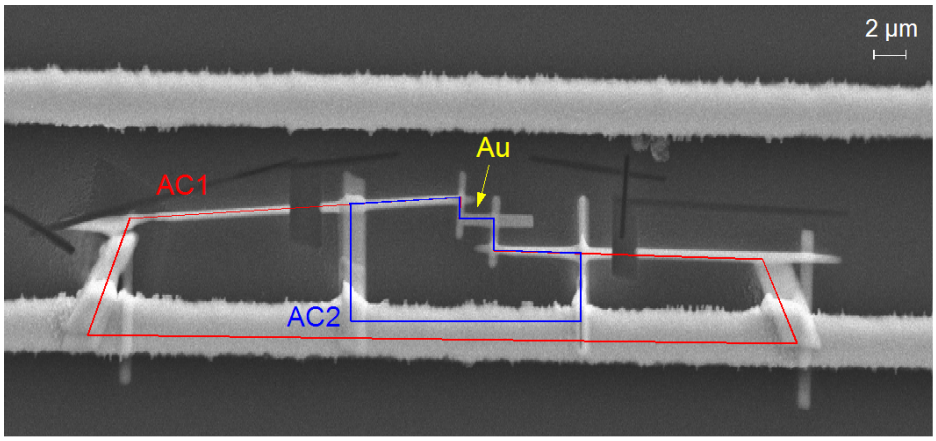

Figure 4.5: *SEM image of SQUIDs SQAC-WAu-1 and SQAC-WAu-2. A red line passes on the bigger ring SQAC-WAu-1, while a blue line passes on the reduced ring SQAC-WAu-2.*

All those steps left unchanged the W wires contacting the Au part, thus conserving exactly the same SNS junction, which was measured again and gave the results described in section 4.5. We call SQAC-WAu-1 the sample with the original ring perimeter, and SQAC-WAu-2 that with the reduced ring.

This modification of the sample is a good example of the many possibilities offered by the FIB fabrication method. However, finding the good deposition parameters and learning the technique is not simple, and many attempts were necessary before atteining a good fabrication control.
We show in Fig. 4.6 (a) the approach of the nozzles injecting the W gas to the sample. The nozzles have to be as close as possible to the sample for a good deposition of W, and they are lowered gradually. The nozzles-sample distance is estimated from the intensity of the nozzles shadow on the resonator. In Fig. 4.6 (b) we show the effect of an accident during the lowering of the nozzles, causing a big scratch in the resonator!

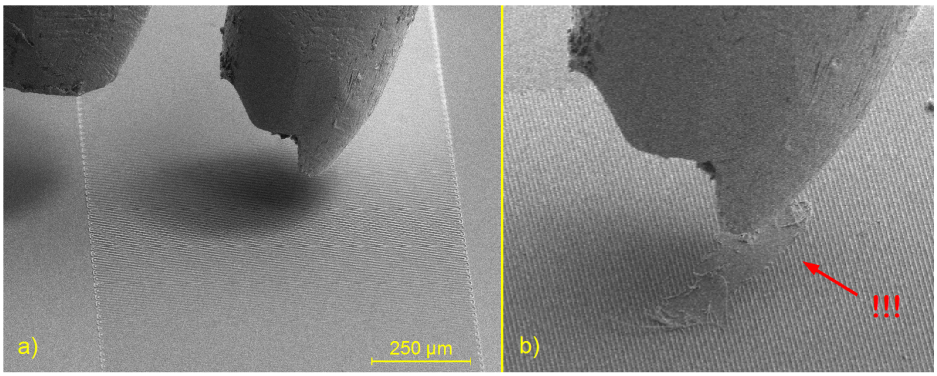

Figure 4.6: *(a) Nozzle injecting the W gas in proximity of the resonator. (b) Result of an excessive lowering of the nozzle.*

4.2.3 AC rings geometry

The geometrical characteristics of the SNS junction, deduced from the SEM pictures, are listed in Table 4.1.
To determine the Thouless energy and the resistance of the wire of these isolated samples, we used the characteristics of the similar samples measured in a dc current bias configuration.

From the comparison with samples SQ-NbAu, we find for sample SQAC-NbAu a resistance $R = 1.7\,\Omega$ and a Thouless energy $E_{Th}/k_B = 30\,mK$, using

sample	$L(\mu m)$	$w(\mu m)$	$t(nm)$	$S(\mu m^2)$	$p(\mu m)$
SQAC-NbAu	1.56	0.28	50	8.9	17.8
SQAC-WAu-1	1.51	0.33	50	93.4	80.2
SQAC-WAu-2	1.51	0.33	50	34.6	32

Table 4.1: *Geometrical characteristics of SQUIDs SQAC-WAu-1 and SQAC-WAu-2, deduced from SEM images. The two SQUIDs consist in the same SNS junction, connected differently to the Nb resonator.*

the same diffusion coefficient as samples SQ-NbAu, $D = 1.02\ 10^{-2}\, m^2/s$.

For samples SQAC-WAu, starting from the resistance per square of samples W-Au, $R_\square = 0.45\,\Omega$, we obtain $R = 2.2\,\Omega$. The diffusion coefficient of the two W-Au samples, $D = 1.3\ 10^{-2}\, m^2/s$, gives a Thouless energy of $E_{Th}/k_B = 41\, mK$.
But these values of resistance and Thouless energy can't reproduce the data, such as the temperature dependence of the critical current, which is described by $E_{Th}/k_B = 90\, mK$.
It is however possible that part of the normal wire is contamined by W particles, as we already observed in sample WAu-N (Fig. 2.4). Considering a contamination of about $250\, nm$ at each NS contact (like in sample WAu-N), the effective normal length becomes $1\, \mu m$, giving a Thouless energy of $E_{Th}/k_B \sim 90\, mK$, which corresponds the the value deduced from the fit of $I_c(T)$.

From the geometrical characteristic of the AC SQUIDs we deduce two of the most important parameters needed to correctly understand our data: the ring self inductance $\mathcal{L}$ and the mutual inductance between the ring and the resonator line $\mathcal{L}'$ (see appendix D for the detailed calculation).
The ring self inductance $\mathcal{L}$ quantifies the screening of the external magnetic field. The mutual inductance between the ring and the resonator line $\mathcal{L}'$ determines the coupling between the current in the SQUID and the resonator.

4.3 Measurement setup

The aim of this experiment is to measure the in-phase (non dissipative) and out-of-phase (dissipative) response of the current as a function of the phase difference across the junction.
In a SQUID one can control the phase difference by just applying a magnetic

sample	$\mathcal{L}$ (pH)	$\mathcal{L}'$ (pH)
SQAC-NbAu	8	1.2
SQAC-WAu-1	36.5	22.5
SQAC-WAu-2	15	5

Table 4.2: *Summary of samples SQAC-WAu-1 and SQAC-WAu-2 inductances: self inductance $\mathcal{L}$ and effective mutual inductance $\mathcal{L}'$ with the resonator line.*

field into the ring:

$$\Delta\varphi = -2\pi\frac{\Phi_{dc}}{\Phi_0} \tag{4.6}$$

where $\Phi_{dc} = H_{dc}\,S$ is the dc magnetic flux in the ring surface.

In addition to the dc flux Φ_{dc} through the ring, an ac flux $\delta\Phi\,\cos(\omega\,t)$ is generated by the resonator line. The response of the ac current δi flowing in the SQUID is then:

$$\delta i\,(\Phi_{dc}) = \chi'(\Phi_{dc},\,\omega)\,\delta\Phi\,\cos(\omega t) + \chi''(\Phi_{dc},\,\omega)\,\delta\Phi\,\sin(\omega t) \tag{4.7}$$

At low frequency, we expect the supercurrent to follow adiabatically the ac excitation, thus giving a response completely in-phase:

$$\chi'(\omega = 0) = \frac{\partial I_J}{\partial\Phi_{dc}} \qquad\qquad \chi''(\omega = 0) = 0 \tag{4.8}$$

where I_J is the non-dissipative Josephson current.
When increasing the frequency above the characteristic rates of the SNS junction, we expect an out-of-phase, dissipative part to appear, and the susceptibility of the junction to become complex: $\chi = \chi' + i\,\chi''$.

The resonator, besides providing the high frequency excitation, is a very sensitive detector of the SQUID response.
We can access the in-phase and out-of-phase responses χ' and χ'' by measuring the resonance frequency shift δf and the variation of the resonance width, proportional to $\delta(1/Q)$, with the dc flux:

$$-2\,\frac{\delta\,f}{f} = k_n^2\,\frac{\mathcal{L}'^2}{\mathcal{L}_r}\,\frac{\chi' - \mathcal{L}\,(\chi'^2 + \chi''^2)}{(1 - \mathcal{L}\,\chi')^2 + \mathcal{L}^2\,\chi''^2} \tag{4.9}$$

$$\delta\left(\frac{1}{Q}\right) = k_n^2\,\frac{\mathcal{L}'^2}{\mathcal{L}_r}\,\frac{\chi''}{(1 - \mathcal{L}\,\chi')^2 + \mathcal{L}^2\,\chi''^2} \tag{4.10}$$

k_n quantifies the ac current at the sample position for the n^{th} resonance frequency. $\mathcal{L}'$ is the effective mutual inductance between the sample and the resonator, $\mathcal{L}$ is the ring self inductance and $\mathcal{L}_r$ is the resonator self inductance.
The derivation of eq. 4.9 and 4.10 is detailed in chapter 5.

Defining F_v and Q_v as quantities proportional to the resonance frequency variation and the $1/Q$ variation due to the sample:

$$F_v = \frac{\mathcal{L}_r}{k_n^2\,\mathcal{L}'^2}\left(-2\,\frac{\delta f}{f}\right) \qquad\qquad Q_v = \frac{\mathcal{L}_r}{k_n^2\,\mathcal{L}'^2}\,\delta\left(\frac{1}{Q}\right) \tag{4.11}$$

we can invert eq. 4.9 and 4.10 to find the real and imaginary parts of the response function χ:

$$\chi' = \frac{F_v + \mathcal{L}(F_v^2 + Q_v^2)}{L^2\,Q_v^2 + (1 + F_v\mathcal{L})^2} \qquad\qquad \chi'' = \frac{Q_v}{L^2\,Q_v^2 + (1 + F_v\mathcal{L})^2} \tag{4.12}$$

Note that, for a ring with a very small inductance or a very small response χ ($\mathcal{L}\,\chi << 1$), we obtain:

$$\chi'(\Phi_{dc}) = F_v(\Phi_{dc}) \qquad\qquad \chi''(\Phi_{dc}) = Q_v(\Phi_{dc}) \tag{4.13}$$

Experimentally, we measure the frequency and quality factor shift with the dc magnetic field. We have then the F_v and Q_v variations with Φ_{dc}, but we have no information about their absolute value.
To use eq. 4.12, we need to know the absolute value of $F_v(\Phi_{dc})$ and $Q_v(\Phi_{dc})$. We have then to determine $F_v(\Phi_{dc} = 0)$ and $Q_v(\Phi_{dc} = 0)$.
For χ'', we assume in our frequency and temperature range ($f_{max} = 1.36\,E_{Th}/h$, $T_{max} = 11.1\,E_{Th}/k_B$):

$$\chi''(\Phi_{dc} = 0) = 0 \tag{4.14}$$

because the dissipation, always positive, is zero at $\Phi_{dc} = 0$, where the gap is completely open ($\hbar\,\omega < \tilde{\Delta}(\Phi_{dc} = 0)$). Since Q_v is proportional to χ'', we have $Q_v(\Phi_{dc} = 0) = 0$.
The $\chi'(\Phi_{dc})$ curve is instead assumed to be centred around zero ($|\chi'_{max}| = |\chi'_{min}|$). F_v is then shifted to obtain a centred χ'.
These hypothesis are essential when, the product $\mathcal{L}\,\chi$ being large, we need to use eq. 4.12. However, we see in sec. 4.5 that at high temperature ($T \sim 1\,K$), the current in the ring, and thus the response χ, are small: we can then neglect the field screening. In this case, eq. 4.13 is valid, and we can access $\chi'(\Phi_{dc})$ and $\chi''(\Phi_{dc})$ without needing the flux independent contribution of F_v and Q_v.

At lower temperature, $\chi'(\Phi_{dc})$ and $\chi''(\Phi_{dc})$ are instead deduced by eq. 4.12, using the above assumptions for the F_v and Q_v values at zero flux. The curves we obtain are similar to the high temperature ones, confirming our assumptions for $F_v(\Phi_{dc} = 0)$ and $Q_v(\Phi_{dc} = 0)$.

In conclusion, using eq. 4.12 and 4.13, we can access the phase dependence of the in-phase and out-of-phase responses $\chi'(\varphi)$ and $\chi''(\varphi)$ just by measuring the resonance frequency shift δf and the inverse quality factor change $\delta(1/Q)$ as a function of the dc flux Φ_{dc}.
This is valid only in the linear regime, where the modulation amplitude of the dc flux is much smaller than Φ_0.

4.4 Measurements on sample SQAC-NbAu

Preliminary measurements were done on sample SQAC-NbAu, a pattern of 9 AC SQUIDs glued on top of a resonator.
We see in Fig. 4.7 the resonance frequency shift δf vs. the external flux Φ_{ext} for $f_1 = 380\,MHz$, $T = 50\,K$ and an applied rf power $P = 5\,nW$.

We notice that oscillations of period Φ_0/S, where S is the ring surface, are superposed to a parabola. The parabola is due to the resonator line dependence on the magnetic field (see Fig. C.1), while the oscillations are proportional to the in-phase response of sample SQAC-NbAu.
When substracting the parabola, we observe an in-phase signal strongly anharmonic, with a ratio between the second and the first harmonic $r_{21} \sim 0.4$.
When varying the temperature from $50\,mK$ to $700\,mK$ the signal amplitude remains constant. This is a very surprising behavior, since the in-phase response is expected to decrease with the temperature exponentially, like $I_c(T)$.
A possible explanation is that the applied rf power heats the sample, so that the electronic temperature, and thus the response amplitude, don't vary much between $50\,mK$ and $700\,mK$.
We then want to reduce the rf power, to avoid the heating and to be in the linear regime, but without much decreasing the signal.
To do that, we fabricated an ac SQUID directly on the resonator substrate. We thus increased the mutual inductive coupling, and we were able to measure a single ac SQUID in the linear regime.

4.5 High frequency linear response

We present in this section the main features of the in-phase and out-of phase linear response of sample SQAC-WAu-2 for

- T : $0.55\,K - 1\,K$, corresponding to $6.1\,E_{Th} < k_B\,T < 11.1\,E_{Th}$
- f : $365\,MHz - 2.57\,GHz$, corresponding to $0.2\,E_{Th} < hf < 1.37\,E_{Th}$

The power injected is of the order of $P_{rf} \sim 5\,pW$.
To estimate the flux modulation in the ring, we first calculate the current I_r in the resonator via

$$I_r = \sqrt{\frac{P\,Q}{\mathcal{L}_r\,\omega}} \tag{4.15}$$

We find the above equation from the quality factor definition: Q is the ratio between the stored energy $\mathcal{L}_r\,I_r^2$ and the energy dissipated in a time $1/\omega$, equal to $P\,/\omega$.
Knowing the mutual inductance, we can derive the ac flux induced through the ring:

$$\delta\Phi = \mathcal{M}\,I_r \tag{4.16}$$

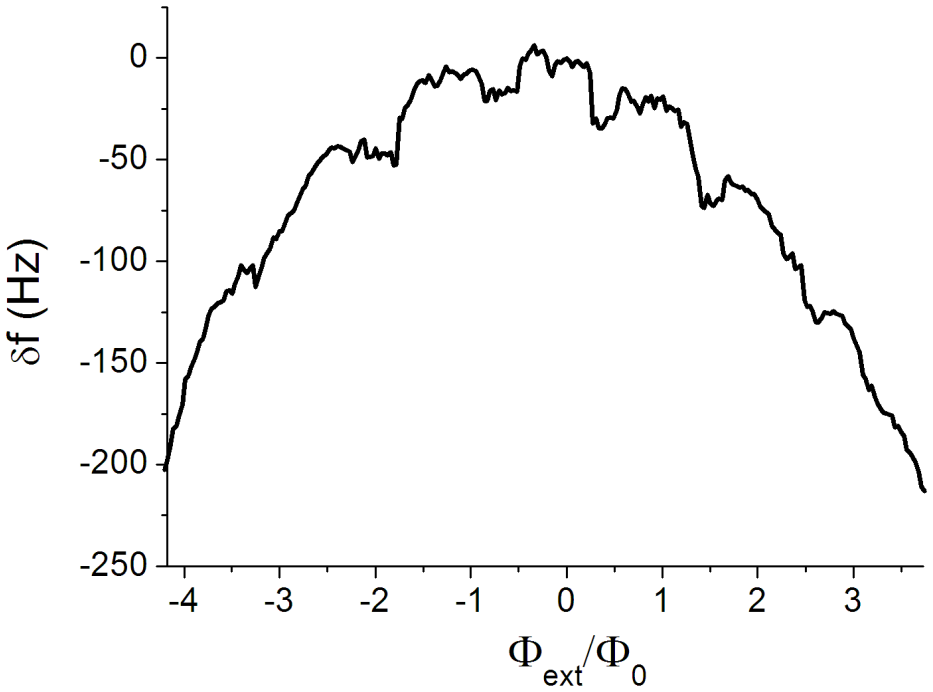

Figure 4.7: *Resonance frequency shift vs applied flux of sample SQAC-NbAu at* $f_1 = 380\,MHz$, $T = 50\,mK$ *and for an applied rf power* $P = 5\,nW$.

We find a flux modulation $\delta\Phi \sim 0.01\,\Phi_0$, confirming that we are indeed in the linear regime.

Characteristic examples of our SQUID response are given in Fig. 4.8 and 4.9, where we show the in-phase and dissipative response at $T = 1\,K$ and $T = 0.67\,K$ for the lowest resonance frequency $f_1 = 365\,MHz$. At $T = 1\,K$, the in-phase and out-of-phase response are directly proportional to $F_v(\Phi_{dc})$ and $Q_v(\Phi_{dc})$ (see eq. 4.13), while at $T = 0.67\,K$, the screening is important and we use eq. 4.12.
All the experimental curves presented in this section are the average of 30 to 100 field scans on sample SQAC-WAu-2.
At high temperatures compared to the minigap, the expected response at zero frequency is harmonic, and entirely in-phase:

$$\chi'(\omega = 0) = \frac{\partial I_J}{\partial \Phi} = -\frac{2\pi\, I_c}{\Phi_0} \cos\left(\frac{2\pi\Phi}{\Phi_0}\right) \qquad \chi''(\omega = 0) = 0 \qquad (4.17)$$

Just like the zero frequency case, the observed χ' and χ'' oscillate with the dc flux with a periodicity corresponding to a quantum flux Φ_0 into the ring surface.

But, apart from the periodicity, the finite frequency case of Fig. 4.8 and

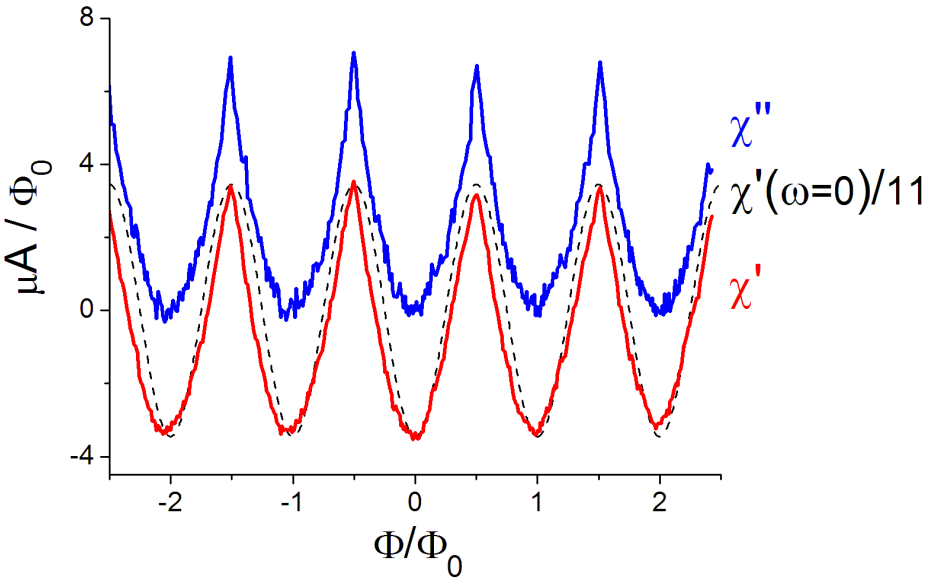

Figure 4.8: *In-phase (red line) and out-of-phase (blue line) response vs. the dc flux into the ring Φ_{int} for the first resonant harmonic f_1 and at $T = 1\,K$, compared to the low frequency in-phase response $\chi'(\omega = 0)$ (black dotted line).*

4.9 is clearly very different from the zero frequency one, even at a frequency lower than E_{Th}: $f_1 = 0.2\,E_{Th}/h$. We observe an in-phase response strongly anharmonic with the dc flux, and an out-of-phase response, that, far from being zero, is even greater than the in-phase response and has its maximum at $n\,\Phi_0/2$.
This shows that, at high frequency, the non dissipative response is not simply the flux derivative of the supercurrent, and that the dissipation is enhanced at phase differences such that the minigap closes.

Before proceeding further in the analysis, let's detail how we deduce the exact χ' and χ'' in presence of a finite ring inductance.

4.5.1 Data treatment

As we have seen, if the ring inductance $\mathcal{L}$ is negligible, the in-phase and out-of-phase responses χ' and χ'' are given by the resonance shift and the quality factor variations:

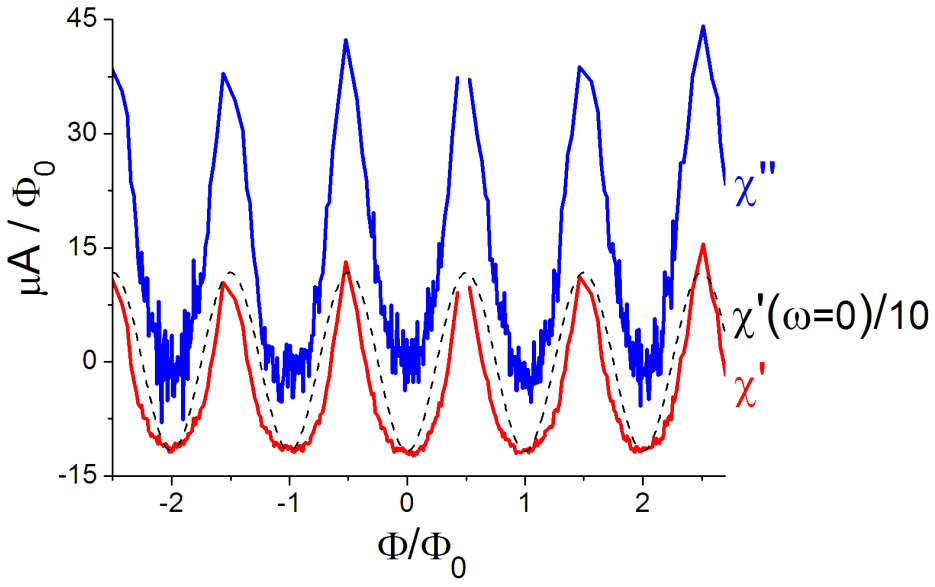

Figure 4.9: *In-phase (red line) and out-of-phase (blue line) response vs. the dc flux into the ring Φ_{int} for the first resonant harmonic f_1 and at $T = 0.67\,K$, compared to the low frequency in-phase response $\chi'(\omega = 0)$ (black dotted line).*

$$\chi' = F_v = \frac{\mathcal{L}_r}{k_n^2\,\mathcal{L}'^2}\left(-2\,\frac{\delta f}{f}\right) \qquad \chi'' = Q_v = \frac{\mathcal{L}_r}{k_n^2\,\mathcal{L}'^2}\,\delta\left(\frac{1}{Q}\right) \tag{4.18}$$

However, if the ring inductance is important, the response is given by the more complex eq. 4.12.

To determine the influence of the inductance, we compare the measured F_v to the χ' calculated from eq. 4.12 using the measured F_v and Q_v: if they are equal, the inductance can be neglected, while a great difference between F_v and χ' means that $\mathcal{L}$ needs to be taken into account.

Fig. 4.10 shows F_v, Q_v, χ' and χ'' at $T = 0.67\,K$ for $f_1 = 365\,MHz$. We see

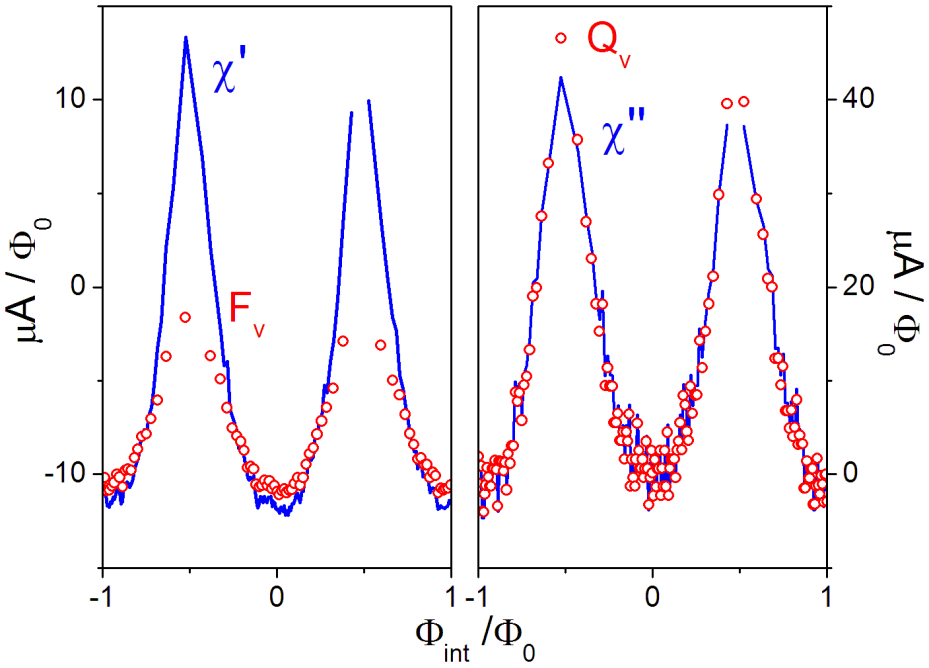

Figure 4.10: *Influence of the ring geometrical inductance on the measured F_v and Q_v at $T = 0.67\,K$ and $f_1 = 365\,MHz$. Left: comparison between F_v (red circles) and χ' (blue line). Right: comparison between Q_v (red circles) and χ'' (blue line).*

that the ring geometrical inductance is indeed non-negligible, particularly for the χ' curve.

χ'' is not strongly affected. This is in general true at all the temperatures and frequencies studied.

On the contrary, the χ' amplitude is sensitive to the ring inductance: at $T = 0.67\,K$ and $f = 365MHz$ the difference between F_v and χ' is about a factor two. However, the amplitude variation is less and less marked when

increasing the frequency and the temperature, so that at $T = 1\,K$ F_v and χ' coincide and we can neglect $\mathcal{L}$ (see Fig. 4.11).

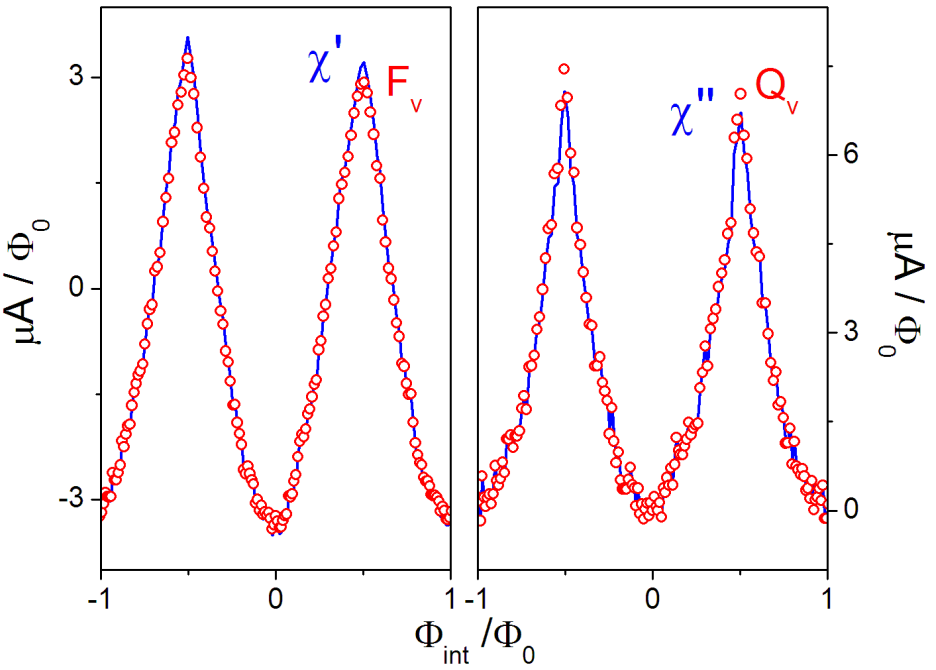

Figure 4.11: *Influence of the ring geometrical inductance on the measured F_v and Q_v at $T = 1\,K$ and $f_1 = 365\,MHz$. Left: comparison between F_v (red circles) and χ' (blue line). Right: comparison between Q_v (red circles) and χ'' (blue line).*

A second important effect due to the finite ring inductance is the screening of the dc applied flux by the supercurrent. The flux through the ring, that we call internal flux, is given by:

$$\Phi_{int} = \Phi_{ext} + \mathcal{L}\, I_J(\Phi_{int}) \tag{4.19}$$

Fig. 4.12 shows $\chi'(T = 0.67\,K,\ f = 365\,MHz)$ as a function of the internal and external flux Φ_{int} and Φ_{ext}. As a function of the internal flux, the curve appears shrinked around the multiples of Φ_0, and the peak at $\Phi_0/2$ appears widened.

This effect is stronger when the temperature decreases, since I_J increases. When

$$2\pi \frac{\mathcal{L}\, I_c}{\Phi_0} = \beta > 1 \tag{4.20}$$

the screening effect leads to a hysteretic behavior.

In Fig. 4.13 we illustrate the hysteresis present when $\beta > 1$, by tracing $\Phi_{int}(\Phi_{ext})$. To do so we have calculated Φ_{ext} as a function of Φ_{int} from eq. 4.19, supposing a sinusoidal relation $I_J(\Phi_{int}) = -I_c \sin(2\pi\,\Phi_{int}/\Phi_0)$:

$$\Phi_{ext} = \Phi_{int} + \mathcal{L}\, I_c \sin\left(2\pi \frac{\Phi_{int}}{\Phi_0}\right) \tag{4.21}$$

and then, we have traced $\Phi_{int}(\Phi_{ext})$.
We see that when the external flux increases from zero, the internal flux increases first linearly as $\Phi_{int} = \Phi_{ext}/(1+\beta)$, then increases faster and in A it jumps to B. When decreasing the external flux from B, the internal flux jumps back only at C. Because of the hysteresis cycle ABCD, the entire range of internal flux between A and C is not accessible.

In sample SQAC-WAu-2 we see an hysteresis up to a temperature $T_h \sim 0.6\,K$. The complete flux response of the SQUID is thus accessible only for $T > 0.6\,K$.
In Fig. 4.14 we show the curve $\Phi_{int}(\Phi_{ext})$ for the three different temperatures

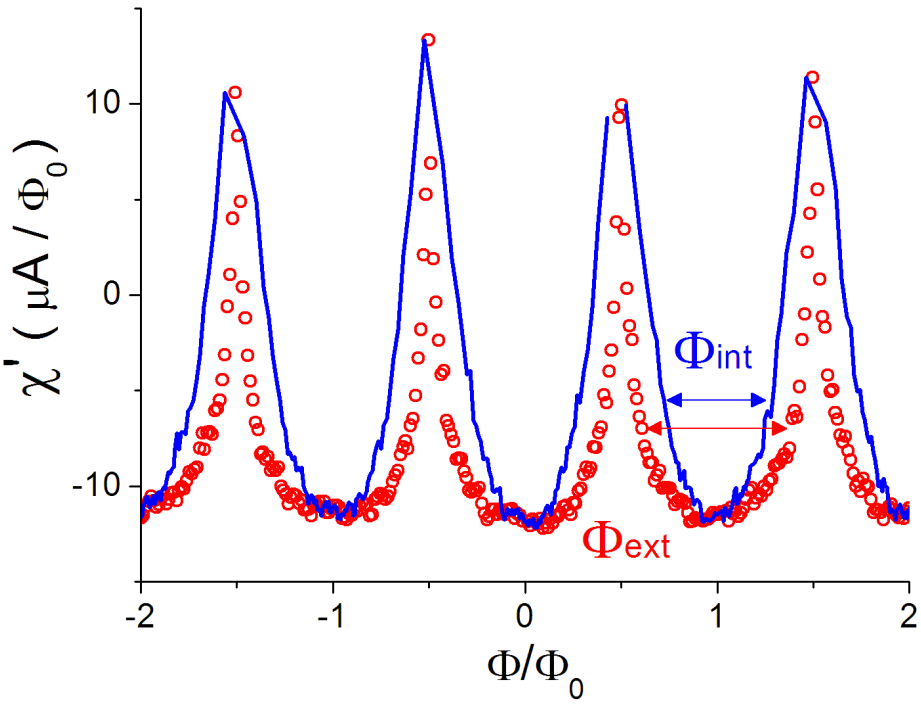

Figure 4.12: *χ' at $T = 0.67\,K$ and $f = 365\,MHz$ as a function of the internal flux Φ_{int} (blue line) and the external flux Φ_{ext} (red circles)*

we studied during this experiment. Since the hysteresis is still present at $T = 0.55\,K$, we need the contribution of the up curve (external field increased) and the down curve (external field decreased) to explore the whole permitted range of fields.
In Fig. 4.15 (left) we show χ' as a function of the external flux Φ_{ext}. The hysteresis is clear. In Fig. 4.15 (right) we trace χ' as a function of the internal flux. A flux interval of amplitude $0.32\,\Phi_0$, centred around the multiples of $\Phi_0/2$, is not accessible.

4.5.2 Thouless energy

The temperature at which the hysteresis appears is in our case $T_h = 0.63\,K$. For temperatures lower than T_h we aren't able to access the whole field dependence of the response, so we concentrate on the high temperature regime. However, even if the curves at the lowest temperatures suffer an important loss of information, they can nevertheless be useful.

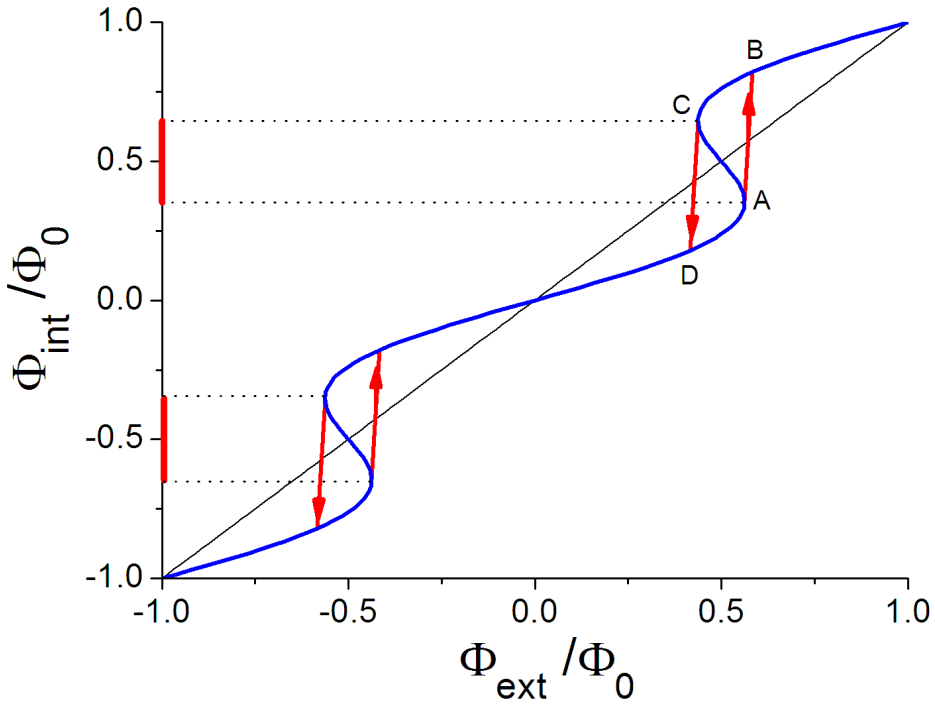

Figure 4.13: *Internal flux vs. external flux for $\beta = 1.65$. When increasing the external flux, the internal flux follows up to A, where it jumps to B. Decreasing the external flux, the internal flux only jumps back in C, creating an hysteresis cycle. The red lines mark the internal flux range not accessible.*

In fact, it is possible to deduce exactly the value of the critical current that causes a particular hysteresis, and thus access the $I_c(T)$ curve. Indeed, the values of Φ_{ext} corresponding to the sharp jumps in the measured χ' and χ'' curves are directly related to the critical current. We have then traced the

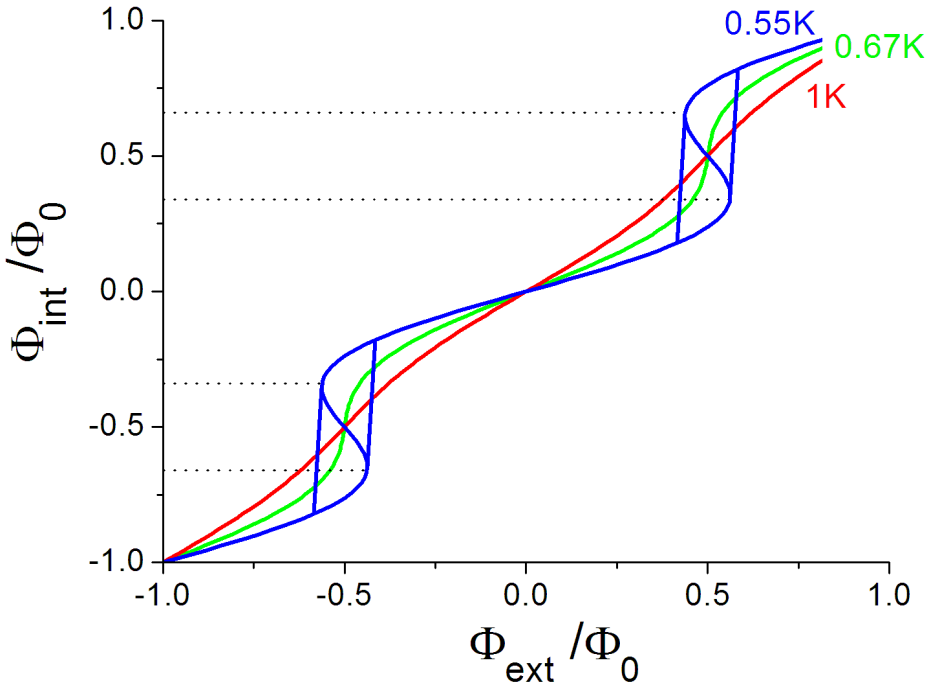

Figure 4.14: *Internal flux vs. external flux for* $T = 0.55\,K$, $T = 0.67\,K$ *and* $T = 1\,K$.

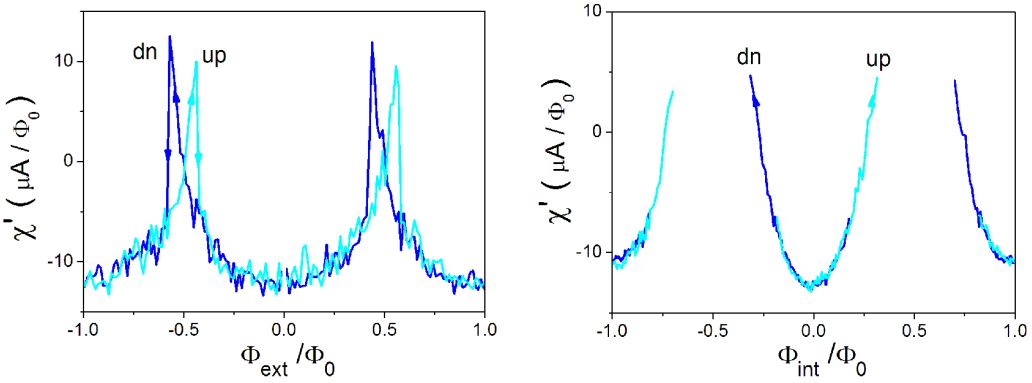

Figure 4.15: *In-phase response at* $T = 0.55\,K$. *Left)* $\chi'(\Phi_{ext})$, *up curve (light blue) and down curve (blue). Right)* $\chi'(\Phi_{int})$, *up curve (light blue) and down curve (blue).*

$\Phi_{int}(\Phi_{ext})$ curves as explained before, varying the critical current to find the I_c that gives a jump at the observed Φ_{ext}.
As we have seen in section 2.3, from the temperature dependence of the critical current one can deduce the Thouless energy.
We recall that this information is particularly precious, since we can't measure directly the transport properties of our SNS junction.
From the fit of the obtained $I_c(T)$ curve we have:

- $E_{Th} = 90\,mK$
- $R = 0.52\,\Omega$

The Thouless energy we had calculated from the geometry of the wire and an estimated diffusion coefficient was $E_{Th} = 41\,mK$. How to explain this discrepancy?
Due to the fabrication method, we can suppose a W contamination in proximity of the superconducting contacts of about $250\,nm$ on each side (comparable to the contamination seen for sample WAu-N). This leaves a normal wire of length $L = 1\,\mu m$, and thus a Thouless energy $E_{Th} = 90\,mK$ when using the same diffusion coefficient that sample WAu-N, $D = 1.3\,10^{-2}\,m^2\,s^{-1}$.
The square resistance accounting for $R = 0.52\,\Omega$ is $R_\square \sim 0.17\,\Omega$, which is smaller than in the case of the two samples W-Au, and about half of the square resistances measured (see table 2.2). It is possible that the contact resistance of this wire is lower than in the other samples as a consequence of the FIB etching step before the W deposition.

4.5.3 Temperature dependence of χ' and χ''

In this section we investigate the in-phase and out-of phase response dependence on temperature.
We show in Fig. 4.16 and 4.17 $\chi'(\Phi_{int})$ and $\chi''(\Phi_{int})$ at $f_1 = 365\,MHz$, the lowest frequency studied, for three different temperatures: $T = 1\,K$, $T = 0.67\,K$ and $T = 0.55\,K$. Since this last temperature is below T_h, we miss a whole range of fluxes around $\Phi_0/2$.

The oscillation amplitude of the in and out-of-phase response for $T = 0.67\,K$ and $T = 1\,K$ is reported in table 4.3.
At zero frequency, $\delta\chi'$, the amplitude of χ', decreases exponentially with the temperature. At finite frequency, $\delta\chi'(T)$ still decreases roughly like $I_c(T)$:

$$\frac{\delta\chi'(0.67K)}{\delta\chi'(1K)} = 3.3 \qquad \frac{\chi_J(0.67K)}{\chi_J(1K)} = 3.1 \tag{4.22}$$

The dissipative response amplitude $\delta\chi''$ also decreases with temperature, roughly like $\delta\chi'$.
To quantify the effect of the finite frequency, we can compare the amplitude of non dissipative response $\delta\chi'$ to the amplitude of the zero frequency response, $\delta\chi_J(T) = 2 \times 2\pi\, I_c(T)/\Phi_0$, and the amplitude of the dissipative response $\delta\chi''$ to ωG, where $G = 1/R$ is the normal state conductance.
We observe in Fig. 4.17 that $\delta\chi''(1\,K) \sim 0.8\,\omega_1\,G$, while $\delta\chi''(0.67\,K) \sim 4.4\,\omega_1\,G$.
$\delta\chi'$ is on the contrary smaller than $\delta\chi_J(T)$: $\delta\chi'(1\,K) = 0.1\,\delta\chi_J$, and $\delta\chi'(0.67\,K) = 0.09\,\delta\chi_J$.

For all temperatures we observe a great anharmonicity in χ' and χ''. To estimate the anharmonicity we report in table 4.4 the ratio r_{21} between the second and the first harmonic.
We notice that the second harmonic in χ' and χ'' is quite important at both

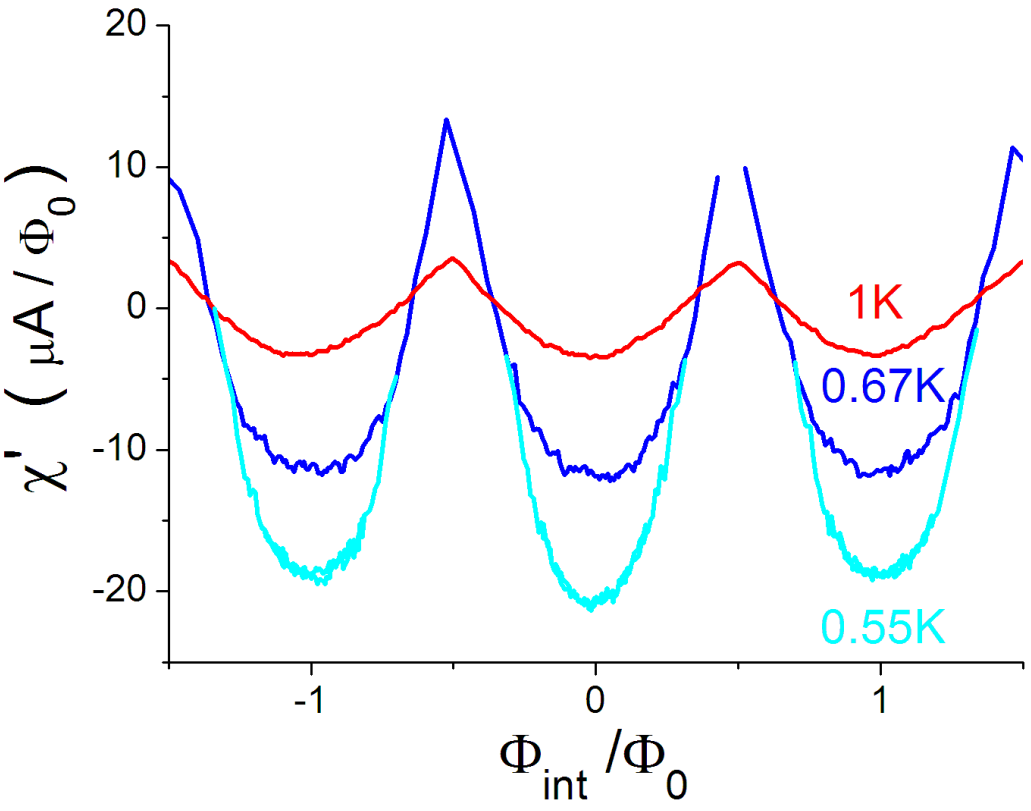

Figure 4.16: *In-phase response at $T = 1\,K$ (red line), $T = 0.67\,K$ (blue line) and $T = 0.55\,K$ (light blue line) for $f = 365\,MHz$.*

temperatures, being at least 20% of the first harmonic. When increasing the temperature, χ' becomes more harmonic, while χ'' seems to become more anharmonic.

4.5.4 Frequency dependence of χ' and χ''

Fig. 4.18 and 4.19 show the response at $T = 0.67\,K$ for two different frequencies: $f_1 = 365\,MHz$ and $f_4 = 1.56\,GHz$.

$\delta\chi'$ and $\delta\chi''$ greatly decrease when increasing the frequency. $\delta\chi'$ decreases faster than $\delta\chi''$:

$$\delta\chi''(f_1)/\delta\chi''(f_4) = 2.8 \qquad \delta\chi'(f_1)/\delta\chi'(f_4) = 10.9 \tag{4.23}$$

The χ' harmonic content decreases with the frequency, while the χ'' harmonic

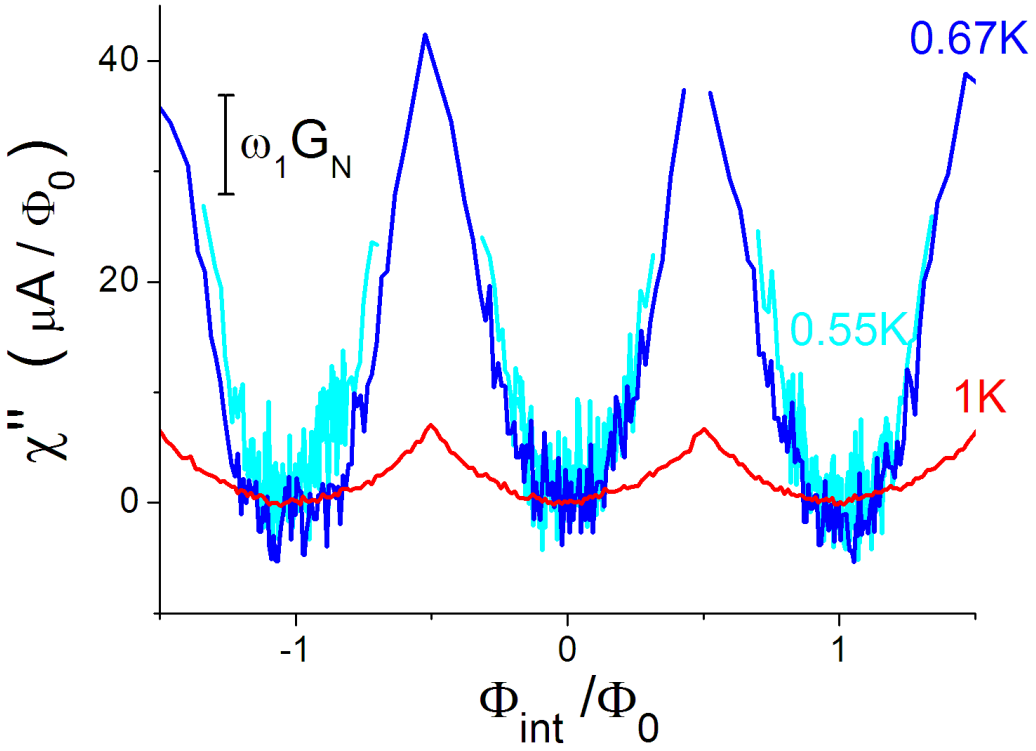

Figure 4.17: *Dissipative response at $T = 1\,K$ (red line), $T = 0.67\,K$ (blue line) and $T = 0.55\,K$ (light blue line) for $f = 365\,MHz$.*

$(\mu A/\Phi_0)$	$T = 0.67\,K$	$T = 1\,K$
$\delta\chi'$	22.9	6.87
$\delta\chi''$	39	6.98
$\delta\chi_J(T) = 4\pi\, I_c/\Phi_0$	234	76.6

Table 4.3: *Comparison between the amplitude of the zero frequency response* $\delta\chi_J$ *and the oscillation amplitudes* $\delta\chi'$ *and* $\delta\chi''$*, for* $T = 1\,K$ *and* $T = 0.67\,K$*.*

r_{21}	$T = 0.67\,K$	$T = 1\,K$
χ'	0.33	0.18
χ''	0.19	0.26

Table 4.4: *Ratio between the second and the first harmonic of the in-phase and out-of-phase response at* $T = 0.67\,K$ *and* $T = 1\,K$*.*

content remains stable, with a ratio between the second and the first harmonic of $r_{21} \sim 0.2$.

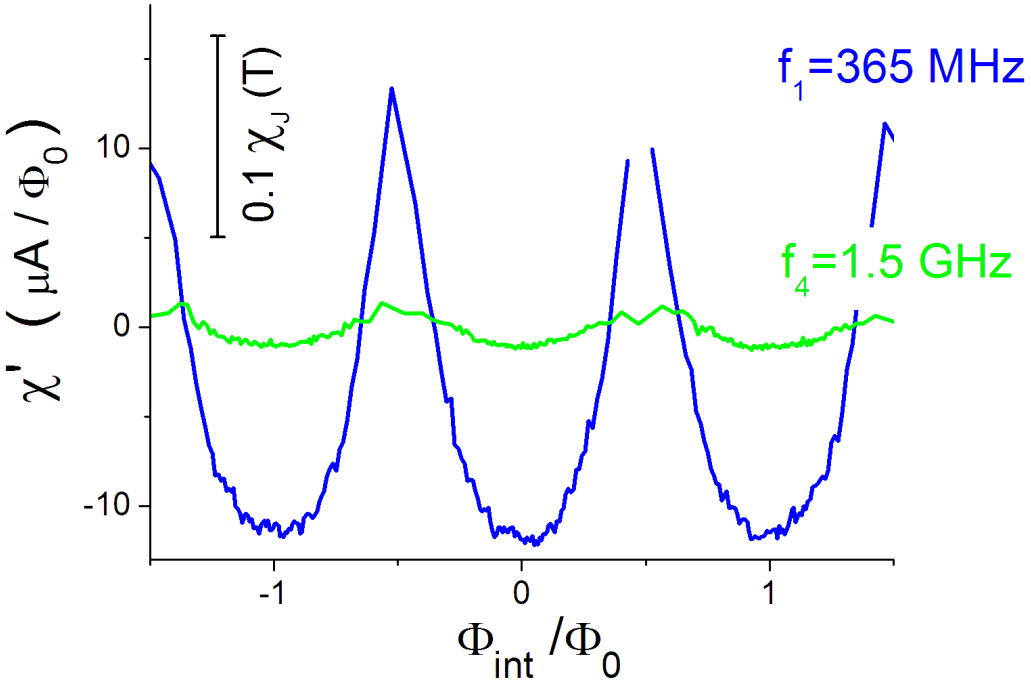

Figure 4.18: *In-phase response at* $T = 0.67\,K$ *for* $f_1 = 365\,MHz$ *(blue line) and* $f_4 = 1.5\,GHz$ *(green line).*

To find the important relaxation times, we have traced the oscillation amplitudes $\delta\chi'$ and $\delta\chi''$ as a function of the frequency, at the temperatures $T = 0.67\,K$ and $T = 1\,K$ (Fig. 4.20). We find that the frequency dependence follows a simple Debye relaxation law:

$$\delta\chi'(\omega) = \delta\chi(0,T)\,\frac{1}{1+(\omega\tau)^2} \tag{4.24}$$

$$\delta\chi''(\omega) = \delta\chi(0,T)\,\frac{\omega\tau}{1+(\omega\tau)^2} \tag{4.25}$$

$\chi(0,T)$ is the zero frequency, temperature dependent, $\delta\chi'$, that we expect equal to $\delta\chi_J$, and τ is the relaxation time.

To confirm the values of τ deduced from the $\delta\chi'(\omega)$ and $\delta\chi''(\omega)$ fits, we also plot in Fig. 4.21 the ratio $\delta\chi''/\delta\chi'$. This ratio is proportional to τ in a Debye relaxation model, and doesn't depend on $\mathcal{L}'$, $\mathcal{L}_r$ and k_n, parameters that are all subject to an error.

The found fitting parameters are:

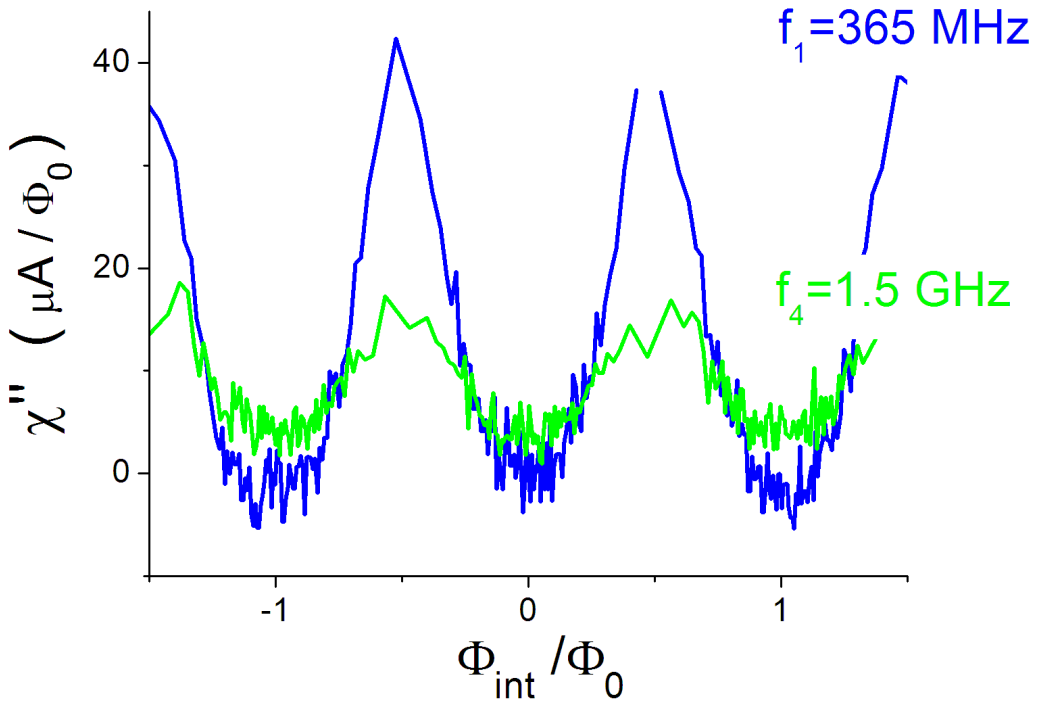

Figure 4.19: *Out-of-phase response at* $T = 0.67\,K$ *for* $f_1 = 365\,MHz$ *(blue line) and* $f_4 = 1.5\,GHz$ *(green line).*

- $T = 0.67\,K \quad \tau = 0.6 \pm 0.2\,ns \quad \delta\chi(0) = 70\,\mu A/\Phi_0 = 3.3\delta\chi_J$

- $T = 1\,K \quad \tau = 0.6 \pm 0.2\,ns \quad \delta\chi(0) = 24\,\mu A/\Phi_0 = 3.2\delta\chi_J$

The $\delta\chi(0)$ found are of the same order of magnitude than $\delta\chi_J$, but they are reduced by the same factor 3.2, due probably to the uncertainty of determination of the SQUID-resonator coupling. It is however worthwhile to note that

$$\frac{\chi(\omega = 0, T = 0.67\,K)}{\chi(\omega = 0, T = 1\,K)} = \frac{\chi_J(T = 0.67\,K)}{\chi_J(T = 1\,K)} \tag{4.26}$$

The relaxation time τ is in the nanosecond range, and doesn't vary with temperature. When comparing it to the diffusion time, we find $\tau = 7.5\,\tau_D$.

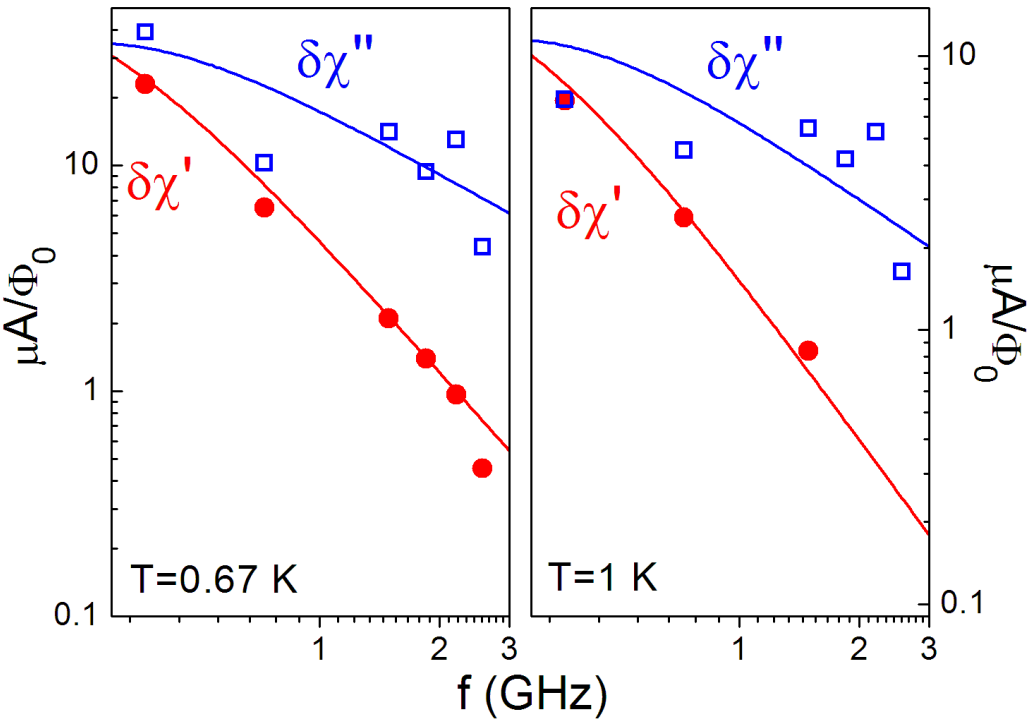

Figure 4.20: *Amplitudes of the in-phase and out-of-phase response $\delta\chi'$ (red circles) and $\delta\chi''$ (blue squares) as a function of frequency at $T = 0.67\,K$ and $T = 1\,K$. The fits are Debye relaxation laws with relaxation time $\tau = 0.6ns$.*

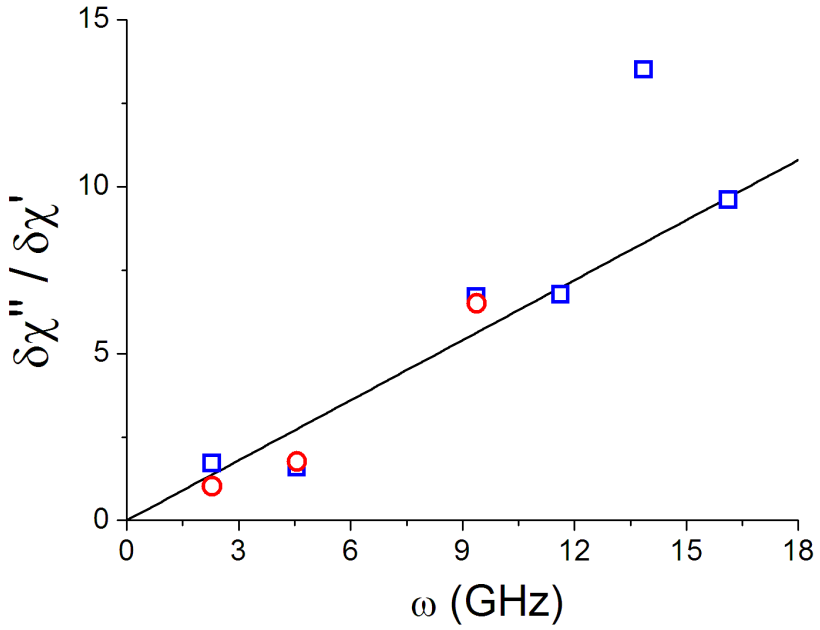

Figure 4.21: *Ratio $\delta\chi''/\delta\chi'$ as a function of $\omega = 2\pi f$ for $T = 0.67\,K$ (blue squares) and for $T = 1\,K$ (red circles). The black line has a slope of $0.6\,ns$.*

4.6 Theoretical predictions

In this section we discuss a possible explanation of the χ' and χ'' flux dependence in the linear regime.
The current flowing in a SNS junction is carried by the Andreev levels. Each Andreev level of energy ϵ_n carries a current

$$i_n = -\frac{\partial \epsilon_n}{\partial \Phi} \tag{4.27}$$

where Φ is the flux through the ring.
We write for simplicity the current in the case of a discrete spectrum, but the same can easily be transposed to a continuum spectrum.
The flux dependent Josephson current at equilibrium sums the contributions of each Andreev level:

$$I_{eq} = \sum_n p_n(\epsilon_n(\Phi))\, i_n(\Phi) \tag{4.28}$$

where p_n is the level occupation factor.
The equilibrium response is thus:

$$\chi(\omega = 0) = \frac{\partial I_{eq}}{\partial \Phi} = \sum_n i_n \frac{\partial p_n}{\partial \Phi} + \sum_n p_n \frac{\partial i_n}{\partial \Phi} \tag{4.29}$$

$$= \sum_n i_n \frac{\partial p_n}{\partial \epsilon_n} \frac{\partial \epsilon_n}{\partial \Phi} + \sum_n p_n \frac{\partial i_n}{\partial \Phi} \tag{4.30}$$

When exciting an SNS junction with a finite frequency flux modulation, we affect both the energy levels and their populations.
We should then detect two characteristic times: the response time of the distribution function p_n appearing explicitly in the current expression, and the diffusion time of Andreev pairs. In fact, if the pairs don't have the time to cross the normal wire during the measuring time, the adiabatic approximation fails. The Andreev bound states aren't then defined any more, and the density of states becomes out-of-equilibrium. In this case, the Josephson current is affected through the currents i_n.
The response of the distribution function is well understood (see sec. 4.6.1). The response time is given by the inelastic time τ_{in}, the minimum between the electron-phonon time τ_{e-ph} and the electron-electron time τ_{e-e}. We estimate that at $T = 1\,K$ the inelastic time in our golden wires is about $\tau_{in} \sim 5\,10^{-8} s$, which corresponds to a frequency $f_{in} \sim 3\,MHz$, much smaller than the frequency range of the resonator.
We then expect the populations of our normal wires to be completely frozen, and the only relaxation we should observe is that of the density of states.

4.6.1 Distribution function relaxation time

In this section we derive the response of the current through a SNS junction to a small phase modulation at a frequency of the order of the distribution relaxation time, i.e. the inelastic time.
In the relaxation time approximation, the population p_n of the n^{th} level obeys:

$$\frac{dp_n}{dt} = -\frac{1}{\tau_{in}}(p_n - p_{n,eq}) \tag{4.31}$$

where $p_{n,eq}$ is the equilibrium Fermi-Dirac distribution at the energy ϵ_n:

$$p_{n,eq} = \frac{1}{1 + e^{\epsilon_n/(k_B T)}} \tag{4.32}$$

and τ_{in} is for simplicity independent of n.
If the phase difference φ across the junction is modulated with a small modulation amplitude $\delta\varphi$:

$$\varphi(t) = \varphi_{dc} + \delta\varphi\, e^{i\,\omega\,t} \tag{4.33}$$

We have:

$$i_n(\varphi) = i_n(\varphi_{dc}) + \frac{\partial i_n}{\partial\varphi}\,\delta\varphi\, e^{i\,\omega\,t} \tag{4.34}$$

$$p_{n,eq}(\varphi) = p_{n,eq}(\varphi_{dc}) + \frac{\partial p_{n,eq}}{\partial\varphi}\,\delta\varphi\, e^{i\,\omega\,t} \tag{4.35}$$

$$p_n = p_n(\varphi_{dc}) + \delta p_n\, e^{i\,\omega\,t} \tag{4.36}$$

Introducing the expressions 4.34, 4.35 and 4.36 in eq. 4.31, we obtain:

$$i\,\omega\,\delta p_n\, e^{i\,\omega\,t} = -\frac{1}{\tau_{in}}\, e^{i\,\omega\,t}\left(\delta p_n - \frac{\partial p_n}{\partial\varphi}\delta\varphi\right) \tag{4.37}$$

So that the distribution function variation $\delta\, p_n$ due to the high frequency phase excitation is:

$$\delta\, p_n = \frac{1}{1 + i\,\omega\,\tau_{in}}\,\frac{\partial p_n}{\partial\varphi}\delta\varphi \tag{4.38}$$

Using the relation between the phase and the flux $\varphi = -2\,\pi\,\Phi/\Phi_0$, we find that:

$$\delta\, p_n = \frac{1}{1 + i\,\omega\,\tau_{in}}\,\frac{\partial p_n}{\partial\Phi}\delta\Phi \tag{4.39}$$

The linear response of the current is then:

$$\chi = \frac{\partial I}{\partial\Phi} = \sum_n i_n\,\frac{\partial p_n}{\partial\Phi}\,\frac{1}{1 + i\,\omega\,\tau_{in}} + \sum_n p_n\,\frac{\partial i_n}{\partial\Phi} \tag{4.40}$$

When the frequency is of the order of the inelastic rate, the populations can't follow the excitation, and an out-of-phase, dissipative response appears. This dissipative response is proportional to $-\omega\,\tau_{in}/(1 + \omega^2\,\tau_{in}^2)$.

4.6.2 Current response for $\omega\,\tau_{in} \sim 1$

As we have seen in the previous section, when the excitation frequency approaches the inelastic rate, we have to take into account the relaxation of the populations. If we consider for the moment that the Andreev levels respond

instantly to the excitation, the only relaxation time is the inelastic time. The current response χ becomes:

$$\chi_{in} = \sum_n i_n \frac{\partial p_n}{\partial \epsilon_n} \frac{\partial \epsilon_n}{\partial \Phi} \frac{1}{1 + i\,\omega\,\tau_{in}} + \sum_n p_n \frac{\partial i_n}{\partial \Phi} \tag{4.41}$$

and, since $i_n = -\partial \epsilon_n / \partial \Phi$,

$$\chi_{in} = -\sum_n i_n^2 \frac{\partial p_n}{\partial \epsilon_n} \frac{1}{1 + i\,\omega\,\tau_{in}} + \sum_n p_n \frac{\partial i_n}{\partial \Phi} \tag{4.42}$$

At zero frequency, the response is:

$$\chi(\omega = 0) = \sum_n i_n^2 \frac{\partial p_n}{\partial \epsilon_n} + \sum_n p_n \frac{\partial i_n}{\partial \Phi} \tag{4.43}$$

$$= -\frac{2\pi\, I_c(T)}{\Phi_0} \cos\left(\frac{2\pi\,\Phi}{\Phi_0}\right) \tag{4.44}$$

Since we can easily calculate the zero frequency response, it can be useful to express χ_{in} as a function of $\chi(\omega = 0)$:

$$\chi_{in} = \chi(\omega = 0) + \frac{i\,\omega\,\tau_{in}}{1 + i\,\omega\,\tau_{in}} \sum_n i_n^2 \frac{\partial p_n}{\partial \epsilon_n} \tag{4.45}$$

The in-phase and out-of-phase responses are then:

$$\chi'_{in} = \chi'(\omega = 0) + \frac{\omega^2\,\tau_{in}^2}{1 + \omega^2\,\tau_{in}^2} \sum_n i_n^2 \frac{\partial p_n}{\partial \epsilon_n} \tag{4.46}$$

$$\chi''_{in} = \frac{\omega\,\tau_{in}}{1 + \omega^2\,\tau_{in}^2} \sum_n i_n^2 \frac{\partial p_n}{\partial \epsilon_n} \tag{4.47}$$

If $\tau_{in}^{-1} << \omega$, the populations are completely frozen, and the response is:

$$\chi_{in} = \chi(\omega = 0) + \sum_n i_n^2 \frac{\partial p_n}{\partial \epsilon_n} = \chi(\omega = 0) - F(\Phi, T) \tag{4.48}$$

where

$$F(\Phi, T) = -\sum_n i_n^2 \frac{\partial p_n}{\partial \epsilon_n} \tag{4.49}$$

$F(\Phi, T)$ can be rewritten in the continuous spectrum limit for $k_B\,T >> E_{Th}$:

$$F(\Phi, T) = \int \frac{1}{k_B\,T\ \rho(\epsilon)}\, j^2(\Phi, \epsilon) d\epsilon \tag{4.50}$$

where $j(\Phi, \epsilon)$ is the current density and $\rho(\epsilon)$ the density of states. The distribution function p_n is replaced by its high temperature dependence $1-\epsilon/k_B\,T$, so that $\partial p/\partial\epsilon \sim -1/k_B\,T$.
This expression, valid in the limit $k_B\,T \gtrsim 5\,E_{Th}$ and $\hbar\omega \sim E_{Th}$, was calculated using Usadel equations by T. Heikkila and P. Virtanen.
Fig. 4.22 shows the normalised $\chi(\omega = 0)$, the calculateed $F(\Phi)$ and the χ'_{in} resulting from eq. 4.47 for $T = 8\,E_{Th}$ and $\omega\,\tau_{in} \sim 100$. Since $\omega\,\tau_{in} >> 1$, using the simpler eq. 4.48 would have given the same result.

We notice in Fig. 4.22 that the amplitude of χ is not modified even at

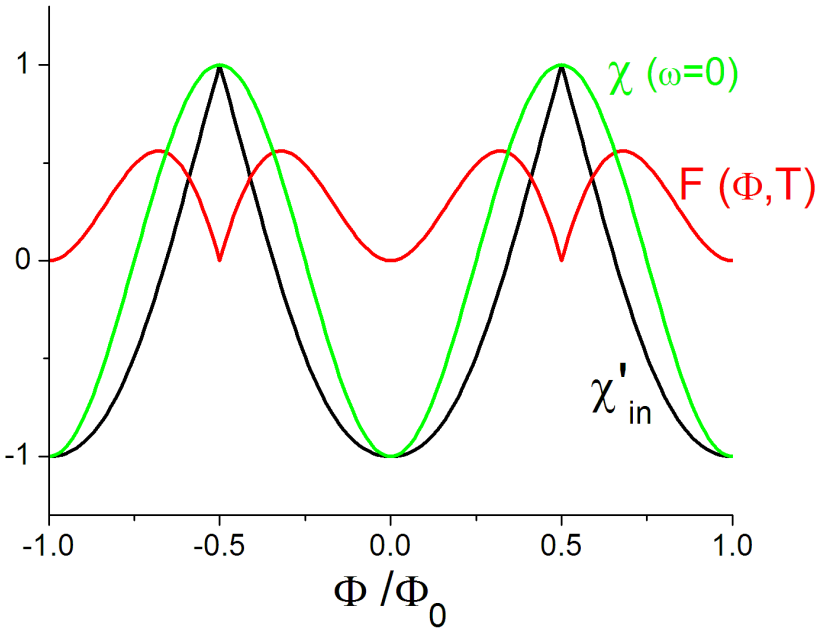

Figure 4.22: *Normalised* $\chi(\omega = 0)$ *(green line),* $F(\Phi)$ *(red line) and in-phase high frequency response* χ'_{in} *calculated from eq. 4.47 for* $T = 8\,E_{Th}$, $\omega\,\tau_{in} \sim 100$ *and* $\omega\tau_A << 1$.

$\omega\,\tau_{in} >> 1$, but a sharp peak appear at $\Phi_0/2$, where the minigap closes, similar to the peaks we observe.
However, eq. 4.48 cannot reproduce our measurements. Indeed, at high frequency compared to the inelastic rate, the relaxation of the populations doesn't predict any out-of-phase response, in contrast to our observations. Moreover, the frequency dependence of $\delta\chi'$ and $\delta\chi''$ observed in sec. 4.5.4 remains completely unexplained.

This relaxation of the χ' and χ'' amplitude is described by a faster dynamics, that we attribute to the relaxation of the Andreev levels, characterised by a time τ_A. The high frequency response for $\omega >> \tau_{in}^{-1}$ and $\omega \sim \tau_A$ can then be written phenomenologically:

$$\chi = \chi_{in} \frac{1}{1 + i\,\omega\,\tau_A} = \sum_n p_n \frac{\partial i_n}{\partial \Phi} \frac{1}{1 + i\,\omega\,\tau_A} \tag{4.51}$$

We now compare the in-phase experimental response at finite frequency with the theoretical expression 4.51. We assume that τ_A is the temperature independent relaxation time $\tau = 0.6\,ns = 7.5\,\tau_D$, that we have measured in sec. 4.5.4.
In Fig. 4.23 we show the numerical calculations of eq. 4.51, compared to the experimental $\chi'(\Phi)$ and $\chi''(\Phi)$ measured for $f_1 = 365MHz$ at $T = 0.55\,K$, $T = 0.67\,K$ and $T = 1\,K$ and for $f_4 = 1.5\,GHz$ at $T = 0.67\,K$.
Eq. 4.51 has been calculated for the ratios $T/E_{Th} = 5$, $T/E_{Th} = 6$ and $T/E_{Th} = 9$; these values are slightly below the experimental ones, but are consistent with the error in the determination of the Thouless energy. The amplitude of the theoretical simulations for χ' has been rescaled by a factor 0.28, while the amplitude for χ'' has been rescaled by a factor 0.36. We have probably underestimated the amplitude of the experimental curves, due to an error in the determination of the SQUID-resonator coupling parameters.
We observe that the agreement of the numerical calculation with the experimental $\chi'(\Phi)$ is very good. Both the shape of the curves (their flux anharmonicity) and the temperature and frequency dependences are well reproduced. In particular, we see that the Andreev levels relaxation only affects the amplitude of the response, while the harmonic content remains unchanged, like in our phenomenological model.
The $\chi''(\Phi)$ curves are also well reproduced, with the exception of the response at $T = 1\,K$.

In conclusion, the model presented predicts strongly anharmonic $\chi'(\Phi)$ and $\chi''(\Phi)$ at high temperatures $k_B T > 5\,E_{Th}$, at frequencies larger than the inelastic rate $\omega > \tau_{in}^{-1}$ and up to roughly the diffusion rate $\omega \lesssim \tau_D^{-1}$. To explain the frequency dependence, we introduced phenomenologically a relaxation time $\tau_A \sim \tau_D$ associated to the relaxation of the current carried by the Andreev levels.
We thus reproduce very well the shape and amplitude of the measured $\chi'(\Phi)$ and $\chi''(\Phi)$, up to $f_4 = 1.5\,GHz$.

4.7 High frequency out-of-equilibrium response

So far, we have discussed the linear response regime, where a small rf power is injected in the resonator leading to a small flux modulation $\delta\Phi << \Phi_0$.
In this section we present the response of SQUIDs SQAC-WAu-1 and SQAC-WAu-2 when increasing the rf power, so that the flux modulation becomes of the order and bigger than Φ_0.
Because we are no longer in the linear regime, we cannot deduce easily χ' and χ'' from F_v and Q_v. We present then in this section the field dependence of the frequency shift F_v and the quality factor variation Q_v.
When entering the non-linear regime, both F_v and Q_v change abruptly their dependence in flux.
As shown in Fig. 4.24 and 4.25, the dissipative response increases greatly at

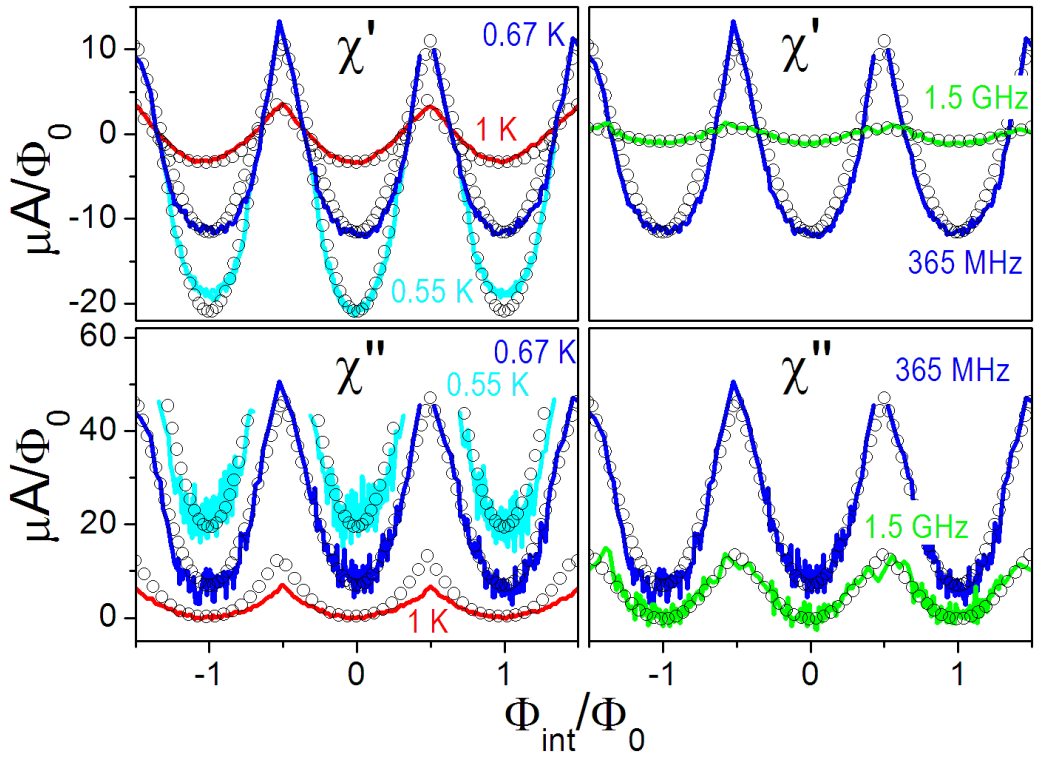

Figure 4.23: *$\chi'(\Phi)$ and $\chi''(\Phi)$ for $f_1 = 365\,MHz$ at $T = 0.55\,K$, $T = 0.67\,K$ and $T = 1\,K$ and for $f_4 = 1.5\,GHz$ at $T = 0.67\,K$ (lines). Numerical simulation for $T/E_{Th} = 5$, $T/E_{Th} = 6$ and $T/E_{Th} = 9$ of eq. 4.51 (circles) with $\tau_A = 7.5\,\tau_D$. The amplitude of the theoretical simulations for χ' has been rescaled by a factor 0.28, while the amplitude for χ'' has been rescaled by a factor 0.36.*

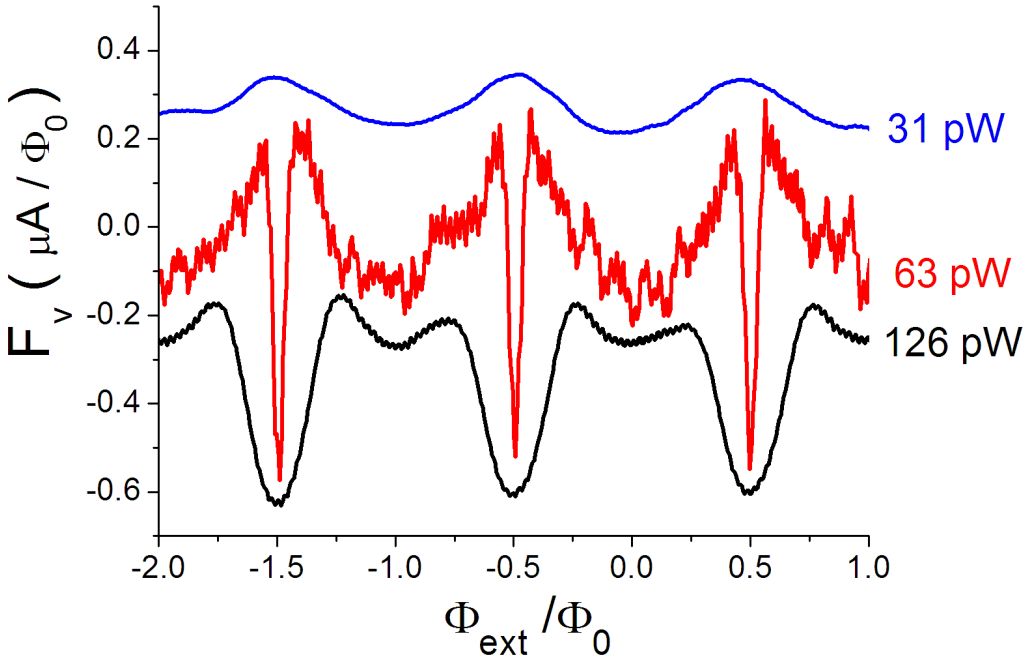

Figure 4.24: *$F_v(\Phi_{ext})$ for sample SQAC-WAu-1 at $T = 0.82\,K$, $f = 365\,MHz$ and for P= 31 pW ($\Phi_{ac} = 0.34\,\Phi_0$), P=63 pW ($\Phi_{ac} = 0.48\,\Phi_0$) and P=126 pW ($\Phi_{ac} = 0.67\,\Phi_0$).*

the odd multiples of $\Phi_0/2$. When raising the rf power, the dissipation peaks become plateaus, centred around $\Phi_0/2$, and whose width increases with the power (see 4.25). The in-phase response presents, also at the odd multiples of $\Phi_0/2$, sharp negative peaks (see 4.24).

The non-linear effects appear in the dissipative and non-dissipative response above a critical power P_c. We observe that:

- P_c decreases when increasing the excitation frequency. At high frequency, even at the lowest powers the response is non-linear.
- P_c decreases when the temperature increases. Temperature and frequency have a similar effect.

We detail in table 4.5 the evolution of P_c with the frequency, at $T = 0.67\,K$ and $T = 1\,K$, in sample SQAC-WAu-2. From f_1 to f_3, we never observe the non-linear regime when increasing the power up to $P = 5\,nW$, corresponding to one quantum flux through the ring. For frequencies above f_6 we never observe the linear regime, even when lowering the power below $P = 0.3\,pW$.

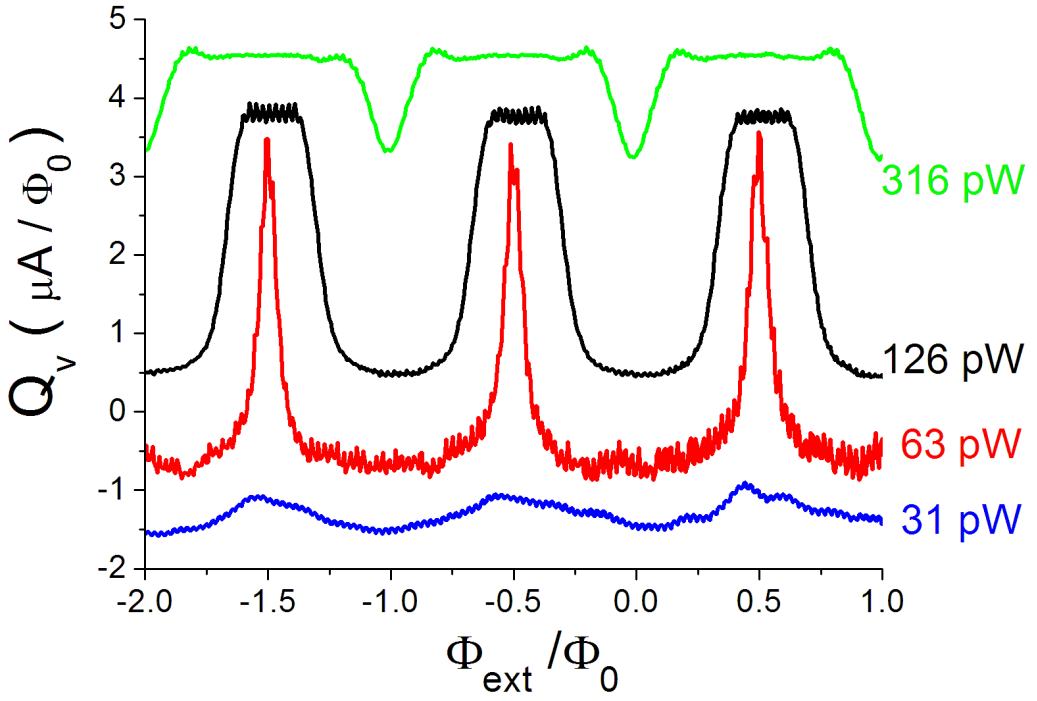

Figure 4.25: *$Q_v(\Phi_{ext})$ for sample SQAC-WAu-1 at $T = 0.82\,K$, $f = 365\,MHz$ and for P= 31 pW ($\Phi_{ac} = 0.34\,\Phi_0$), P=63 pW ($\Phi_{ac} = 0.48\,\Phi_0$) and P=126 pW ($\Phi_{ac} = 0.67\,\Phi_0$).*

We remark that the Thouless energy correspond to $f = E_{Th}/h = 1.88\,GHz$, which is roughly the observed frequency threshold for the non-linearity appearance at $T = 0.67\,K$ and $P \sim 0.1\,pW$, which corresponds to a flux of $0.001\,\Phi_0$.

To explain approximately the dependence of Q with the magnetic flux, it is necessary to remember that the minigap $\tilde{\Delta}$ closes at the odd multiples of $\Phi_0/2$. In the proximity of $\Phi_0/2$, the minigap is very small, and when applying a small ac excitation the quasiparticles are pumped easily to the

	$f_1 = 365\,MHz$	$f_4 = 1.5\,GHz$	$f_5 = 1.85\,GHz$	$f_6 = 2.2\,GHz$
$P_c(0.67\,K)$	$> 5\,nW$	$0.28\,nW$	$1.9\,pW$	$< 0.4\,pW$
$P_c(1\,K)$	$> 5\,nW$	$2.8\,pW$	$< 0.6\,pW$	$< 0.4\,pW$

Table 4.5: *Critical power for the appearence of non-linear effects in sample SQAC-WAu-2 at $T = 0.67\,K$ and $T = 1\,K$.*

conduction band, increasing the dissipation.
When increasing the excitation frequency, the energy transferred to the quasiparticles increases, and the transitions are possible as soon as $h\,f \sim 2\,\tilde{\Delta}$, and not only at $\Phi_0/2$.
Moreover, the microwaves induce an important pair breaking of Andreev pairs, that increases when the rf power and frequency increase, and that also occur preferentially when the minigap is minimal.
Of course, these arguments give just an idea of the causes of the large dissipation increase. In fact, on should note that the temperature is already greater than the minigap.
In conclusion, as the frequency and the temperature increase, the SQUID response is more and more non-linear. The dissipation, maximal around the odd multiples of $\Phi_0/2$, is caused by the microwave-induced quasiparticle transitions across the minigap and the Andreev pair breaking. A quantitative description, however is still lacking.

We note that the observed F_v behavior recalls the strong modification of the dc current/phase relation under microwave irradiation observed by Strunk [25], where a strong second harmonic appears at the odd harmonics of $\Phi_0/2$.
It is interesting to compare our data with the supercurrent-phase relation $I_s(\varphi)$ found by Strunk (Fig. 4.26, right). Since F_v, the frequency shift, is related to the non-dissipative response of the SQUID, we trace the normalised integral of $F_v(\varphi)$ (Fig. 4.26, left), proportional to $I_s(\varphi)$.
What we find is very similar to the curve in the inset of Fig. 4.26 (right), showing $I_s(\varphi)$ for $T = 2.8\,K$ and $f = 7.4\,GHz$. The frequency and temperature correspond to $T = 10\,E_{Th}/k_B$ and $f = 1.27\,E_{Th}/h$.
These ranges of temperatures and frequencies are compatible with ours: $T = 9.1\,E_{Th}/k_B$ and $f = 0.2\,E_{Th}/h$.
What distinguish the curve in the inset from the others is the fact that the excitation frequency for the inset is near a cavity resonance. The power arriving to the sample is thus greater than for the other curves.
Thus, an important second harmonic appear when the power on the sample crosses a certain threshold, which is exactly what we observe.

4.8 Conclusion

We have measured the current response of a long W-Au SNS junction to a high frequency phase modulation for $6\,E_{Th} < k_B\,T < 11\,E_{Th}$ and $0.2\,E_{Th} <$

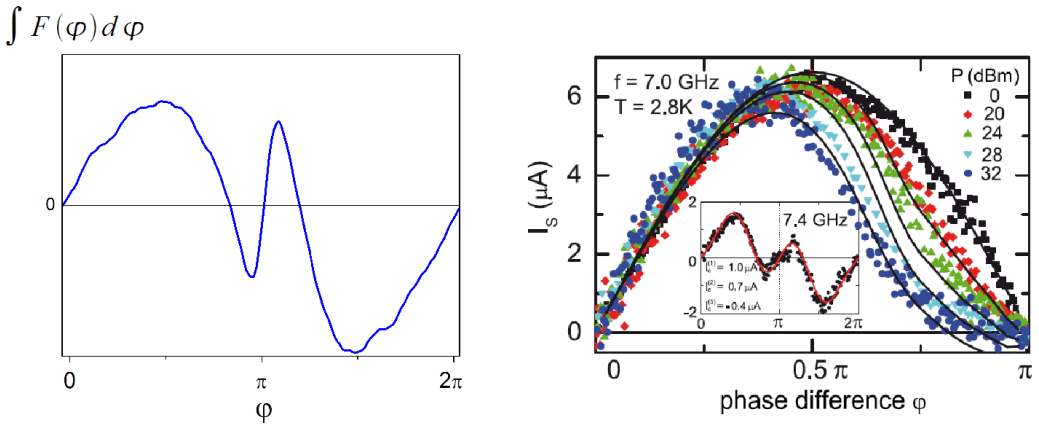

Figure 4.26: *Left: normalised integral of* $F_v(\varphi)$ *for* $\Phi_{ac} = 0.48\,\Phi_0$, $T = 9.1\,E_{Th}/k_B$ *and* $f = 0.2\,E_{Th}/h$. *Right, inset:* $I_s(\Phi)$ *for* $T = 10\,E_{Th}/k_B$ *and* $f = 1.27\,E_{Th}/h$ *[25].*

$h\,f < 1.37\,E_{Th}$.
To this end we have inductively coupled a SNS ring to a multimode superconducting resonator operating in a wide range of frequency.

The golden normal wire is fabricated directly on the resonator substrate, and then contacted to a resonator line with W wires, deposited by Focused Ion Beam irradiation of a tungsten gas. Thanks to the ductility of this fabrication method, it was possible to modify many times the ring shape to adapt its geometry to the measurement requirements.
The Nb multimode resonator provides the high frequency flux (and thus phase) modulation in the ring, but is also a high frequency detector: by measuring the resonance frequency shift and the quality factor variation of the resonator as a function of the dc phase, we can access the in-phase and out-of-phase response of the SQUID current.
Thanks to the high resonator quality factor $Q \sim 10^4$, we are able to detect extremely small variations of f and Q: $\delta f/f \sim 10^{-9}$ and $\delta(1/Q) \sim 10^{-10}$. We can then afford to measure a single SNS ac SQUID.

At low frequency, the supercurrent is expected to follow adiabatically the ac excitation, so that the response, completely in phase, is equal to $\partial I_J/\partial\Phi \propto I_c\,cos(2\pi\,\Phi/\Phi_0)$.
When increasing the frequency above the characteristic rates of the SNS junction, we expect that the dynamic response also contains an out-of-phase, dissipative, part.

Indeed, we observe, besides the expected non-dissipative in-phase response χ', a sizable dissipative out-of-phase response χ'', larger than χ' in all the temperature and frequency range explored.
As in the zero-frequency case, both χ' and χ'' exhibit Φ_0 periodic flux oscillations. However, both quantities present a large harmonic content in a range of temperature where the Josephson current is purely sinusoidal.
When increasing the temperature, the amplitude of χ' decreases exponentially like the critical current, similarly to the low-frequency case. The amplitude of χ'', instead, decreases with the temperature twice as fast as χ'.
When increasing the frequency, the response amplitudes $\delta\chi'$ and $\delta\chi''$ follow a Debye relaxation law characterised by a relaxation time $\tau_A = 0.6 \pm 0.2ns$.

It is possible to reproduce theoretically the amplitude and flux dependence of the in-phase response at $f = 365\,MHz$, assuming that the populations of the Andreev levels are frozen for frequencies larger than the inelastic rate. We estimate $\tau_{in}^{-1} \sim 3\,MHz$, a frequency much smaller than the lower measurement frequency of our setup.
When increasing further the frequency, a second relaxation mechanism appears, possibly related to the relaxation of the current carried by the Andreev levels. This second relaxation time τ_A is temperature independent, and of the same order of magnitude than the diffusion time $\tau_A \sim 7.5\,\tau_D$.
Introducing phenomenologically this time in the theoretical predictions, we have:

$$\chi'(\omega >> \tau_{in}^{-1}) = \left[\sum_n p_n \frac{\partial i_n}{\partial \Phi}\right] \frac{1}{1+\omega^2\,\tau_A^2} \tag{4.52}$$

where p_n is the n^{th} level occupation factor and i_n the current carried by the n^{th} Andreev level.
P. Virtanen and T. T. Heikkilä have calculated the previous expression in the continuous limit using Usadel equations.
The agreement between the shape and amplitude of experimental curves and the theoretical ones is very good.

Abandoning the linear response regime, we have also explored the out-of-equilibrium response of the current.
We observe that non-linear effects appear above a critical power P_c, which decreases when increasing the excitation frequency and the temperature: at the highest frequencies and temperatures, the system is out of equilibrium even at the at the lowest powers.
In the out-of-equilibrium regime, the dissipative response increases greatly at odd multiples of $\Phi_0/2$. In proximity of $\Phi_0/2$, indeed, the minigap closes

and even small excitation frequencies can transfer the quasiparticules to the conduction band, increasing the dissipation. When increasing the rf power, the dissipation peaks become plateaus of increasing width.
The in-phase response is also modified at the odd multiples of $\Phi_0/2$, with the apparition of sharp negative peaks.
The observed behavior of the in-phase response recalls the dc current-phase relation under microwave irradiation observed by C. Strunk: a strong second harmonic appears at the odd multiples of $\Phi_0/2$ [25].

Chapter 5

Details on the AC measurements

In this chapter we detail the measurement of the in-phase and out-of-phase response of a long SNS ac SQUID inductively coupled to a multimode superconducting resonator.
First, we calculate the variation of the resonator self inductance due to the SQUID presence.
Then, we study how this self inductance variation modifies the resonance frequency and the quality factor of the resonator.
We thus derive the relations 5.27 and 5.28, relying the resonance shift δf and the quality factor variation $\delta(1/Q)$ to the SQUID response $\chi = \chi' + i\chi''$.
Finally, we detail the measurement circuit and how we extract δf and $\delta(1/Q)$ from the reflected power of the sample.

5.1 SQUID-resonator system - disconnected ring

In this section we study the variation of the resonator self inductance caused by the current flowing into the SQUID.
We begin modelling the resonator-ac SQUID system as a straight wire coupled by mutual inductance to a ring (see Fig. 5.1).
We can neglect the folding of the resonator, since the resonator's straight segments are about 100 times larger than the ring size, and since the ring is roughly in their middle. The magnetic field created by the resonator is then perpendicular to the substrate and constant over the ring surface.
The small ac current i_r flowing through the resonator creates an ac magnetic

field, and thus an ac flux $\delta\Phi$ into the ring:

$$\delta\Phi = \mathcal{M}(x)\, i_r + \mathcal{L}\, \delta i \tag{5.1}$$

where $\mathcal{M}(x)$ is the position-dependent, mutual inductance between the ring and the resonator, $\mathcal{L}$ the self inductance of the ring and δi the current in the SQUID induced by i_r.
In the small excitation regime, $\delta i = (\partial i/\partial\Phi)\ \delta\Phi$, and the flux into the ring is:

$$\delta\Phi = \frac{\mathcal{M}(x)\, i_r}{1 - \mathcal{L}\, \frac{\partial i}{\partial \Phi}} \tag{5.2}$$

The flux created on the resonator by the SQUID current is then:

$$\delta\Phi_r = \mathcal{M}(x)\, \delta i = \mathcal{M}(x)\, \frac{\partial i}{\partial \Phi}\, \delta\Phi \tag{5.3}$$

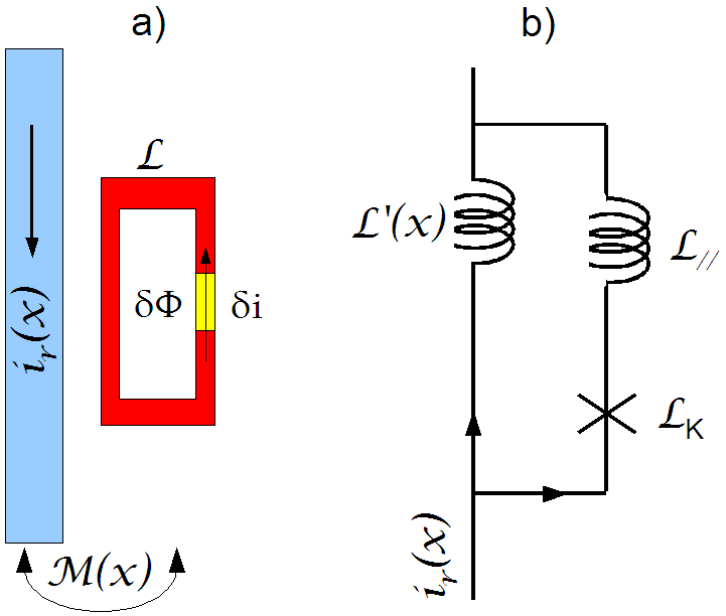

Figure 5.1: *Schematics of the SQUID-resonator line system. a) Disconnected ring. The resonator current i_r produces by mutual inductance an ac flux $\delta\Phi$ in the ring. A current δi flows in the ring of inductance $\mathcal{L}$. b) Equivalent circuit in the case of a connected ring. $\mathcal{L}_K$ is the kinetic inductance of the SNS junction, $\mathcal{L}'$ is the self inductance of the resonator line included in the ring and $\mathcal{L}_{//}$ is the geometric inductance of the W wires.*

The changes of this flux can be seen as due to a self inductance variation of the resonator $\delta\mathcal{L}_r$:

$$\delta\Phi_r = \delta\mathcal{L}_r\, i_r \qquad with \qquad \delta\mathcal{L}_r = \frac{\mathcal{M}(x)^2\, \partial i/\partial\Phi}{1 - \mathcal{L}\, \partial i/\partial\Phi} \tag{5.4}$$

The mutual inductance $\mathcal{M}(x)$ depends on the sample position. Indeed, we can write the flux induced in the ring as:

$$\delta\Phi = \mathcal{M}(x)\, i_r = \mathcal{M}\, i_r(x) \tag{5.5}$$

where the current $i_r(x)$ in the resonator varies with the position. For instance, for the first resonance frequency, the current is maximum in the centre. When changing the frequency, the current amplitude at a given point of the resonant line changes. We define

$$i_r(x) = k_n\, i_r \qquad k_n = \sin(n\,\pi\, x/L_r) \tag{5.6}$$

where n label the harmonic number, x is the sample position and L_r the resonator length.
We show in Fig. 5.2 the amplitude of the first seven harmonics as a function of the position along the resonator; the ring is at $x = 0.35L_r$.

Since

$$\partial i/\partial\Phi = \chi = \chi' + i\,\chi'' \tag{5.7}$$

we find:

$$\delta\mathcal{L}_r = k_n^2\, \mathcal{M}^2\, \frac{\chi' + i\,\chi''}{1 - \mathcal{L}\,(\chi' + i\,\chi'')} \tag{5.8}$$

with a real and imaginary part:

$$\delta\mathcal{L}_r = k_n^2\, \mathcal{M}^2 \left[\frac{\chi' - \mathcal{L}\,(\chi'^2 + \chi''^2)}{(1 - \mathcal{L}\,\chi')^2 + \mathcal{L}^2\,\chi''^2} + i\, \frac{\chi''}{(1 - \mathcal{L}\,\chi')^2 + \mathcal{L}^2\,\chi''^2} \right] \tag{5.9}$$

5.2 SQUID-resonator system - connected ring

In this section we check that the results found in the previous section also hold if the SQUID is not, as supposed before, isolated from the resonator but is, as in reality, directly connected to one resonator line.
We consider the system as the sum of different inductances, as shown in Fig. 5.1 b). $\mathcal{L}'(x)$ is the position-dependent, self inductance of the resonator portion included in the ring, $\mathcal{L}_{//}$ is the geometrical inductance in parallel

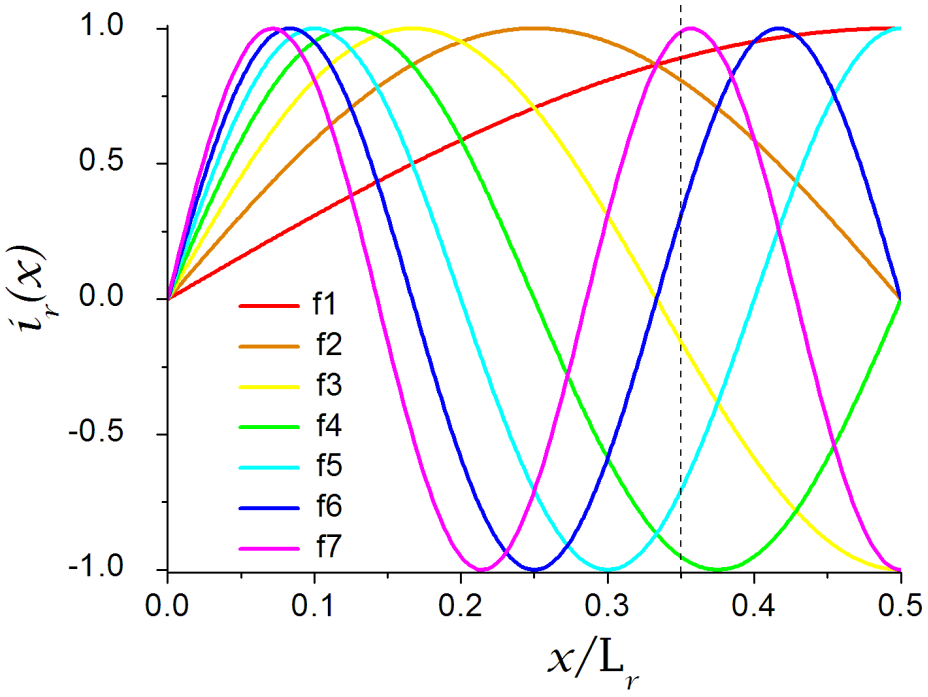

Figure 5.2: *Amplitude of the resonator current $i_r(x)$ as a function of the position along the resonator, for the first seven resonances. The sample position is indicated by a dotted line.*

with the resonator and $\mathcal{L}_J$, is the Josephson inductance of the SNS junction. From the AC and DC Josephson effect:

$$V = \frac{\hbar}{2\,e}\,\dot{\varphi} = \frac{\hbar}{2\,e}\,\frac{1}{I_c\,\cos(\varphi)}\,\frac{dI}{d\varphi} = \mathcal{L}_J\,\frac{dI}{d\varphi} \tag{5.10}$$

so that the Josephson inductance is:

$$\mathcal{L}_J = \frac{\hbar}{2\,e}\,\frac{1}{I_c\,\cos(\varphi)} = -\left(\frac{dI}{d\Phi}\right)^{-1} \tag{5.11}$$

The total inductance of the circuit is:

$$\frac{1}{\mathcal{L}_{tot}} = \frac{1}{\mathcal{L}'(x)} + \frac{1}{\mathcal{L}_{//} + \mathcal{L}_K} \tag{5.12}$$

The inductance relative change due to the SQUID is then:

$$\mathcal{L}_{tot} - \mathcal{L}'(x) = -\frac{\mathcal{L}'(x)^2}{\mathcal{L} + \mathcal{L}_K} \tag{5.13}$$

where $\mathcal{L} = \mathcal{L}_{//} + \mathcal{L}'(x)$ is the geometrical inductance of the SQUID. Writing the explicit expression of the kinetic inductance we have:

$$\mathcal{L}_{tot} - \mathcal{L}'(x) = \mathcal{L}'(x)^2 \frac{\partial i/\partial \Phi}{1 - \mathcal{L}\,\partial i/\partial \Phi} \tag{5.14}$$

The flux in the resonator line is thus:

$$\delta\Phi_r = (\mathcal{L}_{tot} - \mathcal{L}'(x))\, i_r = \delta\mathcal{L}_r\, i_r \tag{5.15}$$

and, using as in the previous section the relation $\mathcal{L}'(x) = k_n\,\mathcal{L}'$ we find:

$$\delta\mathcal{L}_r = k_n^2\,\mathcal{L}'^2 \frac{\partial i/\partial \Phi}{1 - \mathcal{L}\,\partial i/\partial \Phi} \tag{5.16}$$

which is exactly eq. 5.4 with $\mathcal{L}'$ replacing $\mathcal{M}$. We have also seen in sec. D.2 that the mutual inductance $\mathcal{M}$ and the self inductance $\mathcal{L}'$ have similar numerical values.

5.3 Resonance changes due to the SQUID

In this section we show how the variation of the resonator self inductance $\delta\mathcal{L}_r$ enters into the resonance frequency and quality factor. Since the SQUID response is generally complex, $\delta\mathcal{L}_r$ is also complex: $\delta\mathcal{L}_r = \delta\mathcal{L}'_r + i\,\delta\mathcal{L}''_r$.
We model the resonator as a parallel $R\,\mathcal{L}\,C$ circuit with impedance

$$\frac{1}{Z} = \frac{1}{R} + \frac{1}{i\,\omega\,\mathcal{L}} + i\,\omega\,C \tag{5.17}$$

$$Z = \frac{R\,\omega^2\mathcal{L}^2 \;+\; i\,R^2\omega\mathcal{L}(1 - \omega^2\,\mathcal{L}C)}{\omega^2\mathcal{L}^2 + R^2(1 - \omega^2\,\mathcal{L}C)} \tag{5.18}$$

At the resonance the imaginary part of the impedance is zero; the resonance frequency is then:

$$\omega_0 = \frac{1}{\sqrt{\mathcal{L}C}} \tag{5.19}$$

The quality factor is defined as the ratio between the stored energy and the power dissipated in a time $1/\omega$. This gives:

$$Q = R\sqrt{\frac{C}{\mathcal{L}}} \tag{5.20}$$

A small change in the real part of the resonator inductance $\delta\mathcal{L}'_r$ changes the circuit inductance by $\delta\mathcal{L}$, and shifts the resonance frequency $f = \omega_0/2\pi$:

$$\frac{\delta\,\mathcal{L}'_r}{\mathcal{L}_r} = -2\,\frac{\delta\omega_0}{\omega_0} = -2\,\frac{\delta\,f}{f} \tag{5.21}$$

A small change in the imaginary part of the inductance $\delta\mathcal{L}''_r$ corresponds to a small resistance r, added in series to the inductance, whose value is:

$$r = i\,\omega\,(i\,\delta\mathcal{L}''_r) = -\omega\,\delta\mathcal{L}''_r \tag{5.22}$$

This small resistance r changes the circuit resistance R by:

$$\delta R = \frac{R^2}{\omega^2\,\mathcal{L}^2}\,r \tag{5.23}$$

and thus the inverse quality factor becomes:

$$\delta\left(\frac{1}{Q}\right) = -\frac{1}{Q}\frac{\delta R}{R} + \frac{1}{2Q}\frac{\delta\mathcal{L}}{\mathcal{L}} \tag{5.24}$$

Introducing eq. 5.23 and 5.22 in the previous equation we obtain:

$$\delta\left(\frac{1}{Q}\right) = \frac{\delta\mathcal{L}''_r}{\mathcal{L}_r} + \frac{1}{2Q}\frac{\delta\mathcal{L}'_r}{\mathcal{L}_r} \tag{5.25}$$

The second term of this equation can be neglected, since in our case $Q > 10^3$ and $\mathcal{L}''_r \gtrsim \mathcal{L}'_r$, so that finally:

$$\delta\left(\frac{1}{Q}\right) = \frac{\delta\mathcal{L}''_r}{\mathcal{L}_r} \tag{5.26}$$

Summarising, the resonance frequency f and the quality factor Q change according to:

$$-2\,\frac{\delta\,f}{f} = \frac{\delta\,\mathcal{L}'_r}{\mathcal{L}_r} = k_n^2\,\frac{\mathcal{L}'^2}{\mathcal{L}_r}\,\frac{\chi' - \mathcal{L}\,(\chi'^2 + \chi''^2)}{(1-\mathcal{L}\,\chi')^2 + \mathcal{L}^2\,\chi''^2} \tag{5.27}$$

$$\delta\left(\frac{1}{Q}\right) = \frac{\delta\mathcal{L}''_r}{\mathcal{L}_r} = k_n^2\,\frac{\mathcal{L}'^2}{\mathcal{L}_r}\,\frac{\chi''}{(1-\mathcal{L}\,\chi')^2 + \mathcal{L}^2\,\chi''^2} \tag{5.28}$$

5.4 Measurement of $\delta f/f$ and $\delta(1/Q)$

The schematics of the measurement setup is traced in Fig. 5.4 and Fig. 5.6. We begin by summarising the action of each component of the measurement circuit:

- **Splitter** The splitter splits a rf signal in half; the signal of each branch then loses 3 dBm.
- **Magic T** The magic T is a four port device where each port is connected to the two nearest ports (see Fig. 5.3 (a)).
  In our circuit, the excitation enters the magic T in 1, and is splitted into the ports 2 and 4; the wave going to 4 is dephased by π and directed into a 50Ω impedance, while the wave going to 2 is directed to the sample. The signal reflected by the sample is sent back to 1 towards the generator, but is greatly reduced by the attenuators; the signal reflected to 3, added to the one reflected by the 50Ω, which is assumed to be zero, enters the measurement circuit.
  For $f > 1.2\,GHz$, the magic T is replaced by a directional coupler, a three terminal device where the transmission between the ports IN and OUT is optimal, while an attenuator is placed between IN and CPL (see Fig. 5.3 (b)).
  In our circuit, the rf excitation enters in CPL, is attenuated, exit in IN and goes to the sample. The power reflected by the sample enters the directional coupler in IN and exits in OUT.

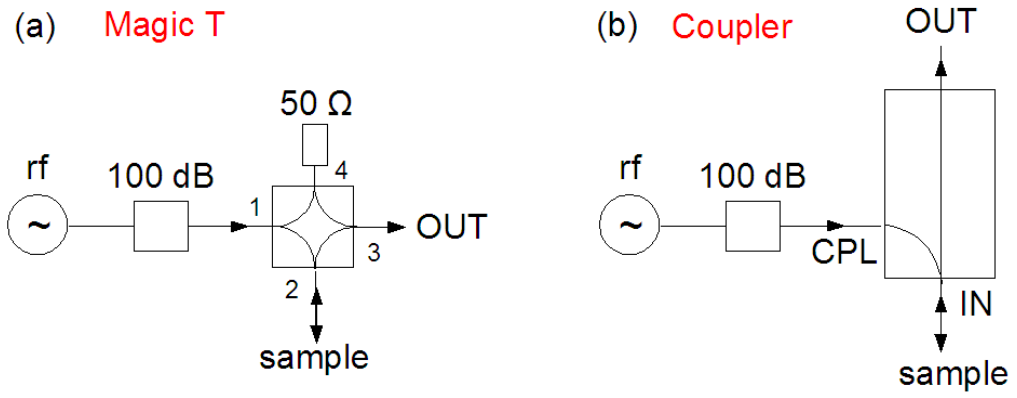

Figure 5.3: *Magic T (a) and Coupler (b) configuration.*

- **Mixer** The mixer multiplies two high-frequency signals.
  In our circuit, the mixer multiplies part of the rf generator excitation with the high frequency sample response to that excitation. If we

write the generator ac voltage as $V_0\, e^{i\,\omega\, t+\varphi}$ and the sample response as $V_1(\omega)\, e^{i\omega\, t+\varphi'}$, with $V_1 = V_1' + i\, V_1''$ complex, their product is:

$$V_{out} = Re\left(V_0\, e^{i\,\omega\, t+\varphi}\right) * Re\left(V_1\, e^{i\omega\, t+\varphi'}\right) = \tag{5.29}$$

$$\frac{1}{2}\, V_0\, V_1' \left[\cos(2\omega\, t + \varphi + \varphi') + \cos(\varphi - \varphi')\right] \tag{5.30}$$

$$-\frac{1}{2}\, V_0\, V_1''[\sin(2\omega\, t + \varphi + \varphi') - \sin(\varphi - \varphi')] \tag{5.31}$$

By dephasing the reference generator signal before entering the mixer, we can set the two waves in-phase ($\varphi = \varphi'$), maximising the dc output:

$$V_{out} = \frac{1}{2}\, V_0\, V_1'[\cos(2\omega\, t + 2\varphi) + 1] - \frac{1}{2}\, V_0\, V_1''[\sin(2\omega\, t + 2\varphi)] \tag{5.32}$$

Filtering the high frequency part of V_{out} we obtain a dc signal proportional to the sample response:

$$V_{out,dc} = \frac{1}{2}\, V_0\, V_1' \tag{5.33}$$

- **Integral-Proportional** The Integral-Proportional circuit multiplies and integrates the input signal $A_{in}(t)$, giving a output:

$$A_{out}(t) = P\, A_{in}(t) + I \int_0^t A_{in}(t')dt' \tag{5.34}$$

where the parameters P and I can be adjusted.

Now that we have introduced the principal components of the measurement circuit, let's follow the signal step by step.

The rf generator output is a voltage oscillating at a resonance frequency of the resonator ($f_n = n\, f_1 = n \times 365 MHz$). The output power is the maximum permitted by the generator, i.e. +13 dBm.

We apply a frequency modulation of amplitude $\delta\omega$ and frequency $\omega_1/\, 2\pi$ to gain in sensitivity.

The output voltage of the splitter is:

$$V_g(t) = V_0\, e^{i(\omega_n\, t + \frac{\delta\omega}{\omega_1}\, \sin(\omega_1\, t))} \tag{5.35}$$

$\omega_n = 2\pi f_n \sim 10 GHz$ and $\omega_1 \sim 30 - 80\, kHz$.

$\delta\omega$ is chosen to be half the resonance width; $\delta\omega \sim 100\, kHz$ at ω_1, and increases up to $1 GHz$ at the highest frequencies.

After the splitter, one half of the excitation, attenuated between 90 dB and 110 dB (depending on the measurement temperature and frequency), is directed to the sample. The other half is dephased and enters the mixer.
The voltage reflected by the sample is proportional to the reflexion coefficient

$$\Gamma = \frac{Z - Z_0}{Z + Z_0} \tag{5.36}$$

where Z is the impedance of the resonator and the coupling capacitor, and $Z_0 = 50\,\Omega$ is the characteristic impedance of the coaxial cables.
The voltage reflected by the resonator is:

$$V_r(t) = V_0\,\Gamma(\omega, \omega_1)\,e^{i(\omega_n\,t + \frac{\delta\omega}{\omega_1}\,\sin(\omega_1\,t))} \tag{5.37}$$

In the mixer, this voltage is multiplied with $V_g(t)$, dephased to be in-phase with the sample reflexion.
The dc component of the mixer output is proportional to the real part of the reflexion coefficient Γ':

$$V_1 = \frac{1}{2}\,V_0^2\,\Gamma'(\omega, \omega_1) \tag{5.38}$$

where Γ' oscillates at a frequency ω_n, modulated at ω_1 with a small amplitude $\delta\omega$.
Since $\delta\omega << \omega_n$, we can develop V_1:

$$V_1 = V_0\left[\Gamma'(\omega_n) + \frac{\partial\Gamma'}{\partial\omega}(\omega_n)\,\delta\omega\,\cos(\omega_1\,t) + \frac{1}{2}\frac{\partial^2\Gamma'}{\partial\omega^2}(\omega_n)\,\delta\omega^2\,\cos(\omega_1\,t)^2\right] \tag{5.39}$$

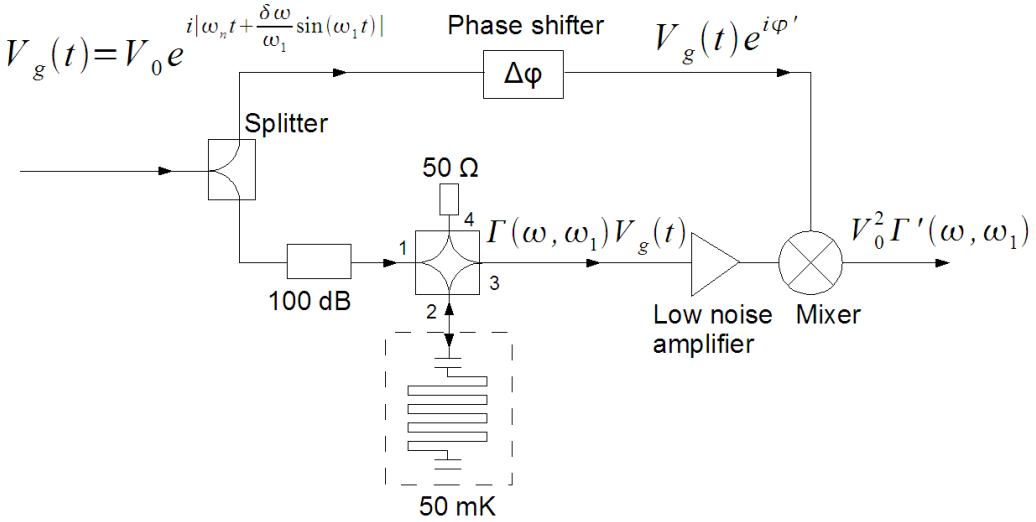

Figure 5.4: *Measurement circuit from the rf generator to the mixer output.*

where $\cos(\omega_1 t)^2 = 1/2\,(1 + \cos(2\,\omega_1 t))$.
A Lock-in working at ω_1 selects $(\partial\Gamma'/\partial\omega)(\omega_n)$, which is proportional to δf.
A Lock-in working at $2\omega_1$ selects $(\partial^2\Gamma'/\partial\omega^2)(\omega_n)$,which is proportional to Q^2.

In the under-coupled regime, the coupling capacitor has an impedance larger than that of the resonator, to isolate the resonator from the environment. In this case, the variations of the reflection coefficient Γ are proportional to the resonator impedance Z_r.
We can write the real part of the resonator impedance near the resonance using eq. 5.18:

$$Z'_r = R\,\frac{1}{1 + \frac{R^2}{\omega^2/\omega_n^2}(1 - \omega^2\mathcal{L}C)^2} \sim R\left[1 - 4\,Q^2\left(\frac{\omega - \omega_n}{\omega_n}\right)^2\right] \tag{5.40}$$

where the approximation to a Lorentzian is valid for $\delta\omega_n/\omega_n << Q^{-1}$, which is our case since $\delta\omega_n/\omega_n < 10^{-6}$ and $Q^{-1} > 10^{-4}$.
At the resonance, the real part of the impedance is minimal, and its derivative vs. ω is zero. Near the resonance the first derivative is proportional to the resonance frequency shift:

$$\delta\dot{Z}'_r = -8\,R\,\frac{Q^2}{\omega_n^2}\,(\omega - \omega_n) \tag{5.41}$$

The variation of the second derivative of Z_r is instead proportional to the quality factor variation:

$$\delta\ddot{Z}'_r = -8\,R\,\frac{Q^2}{\omega_n^2} \tag{5.42}$$

and thus:

$$\frac{\delta\ddot{Z}'_r}{\ddot{Z}'_r} = 2\,\frac{\delta Q}{Q} \tag{5.43}$$

The output of the Lock-in working at ω_1, which is proportional to the resonance frequency shift $\omega - \omega_n$, is sent to the proportional-integral, whose output controls the generator frequency. Thanks to this retroactive circuit, the generator changes its output frequency to follow the resonance.
The proportional-integral parameters P and I control the quality of the retroactive circuit: if P is too big, the generator frequency oscillates around the resonance frequency without ever reaching it, while if I is too big, the time needed to reach the resonance frequency is very long, and the generator can't follow the resonance frequency changes.
Using the retroactive circuit, we can directly measure, without any calibration, the resonance frequency shift: we just look at the change in the generator frequency needed to be at resonance again.

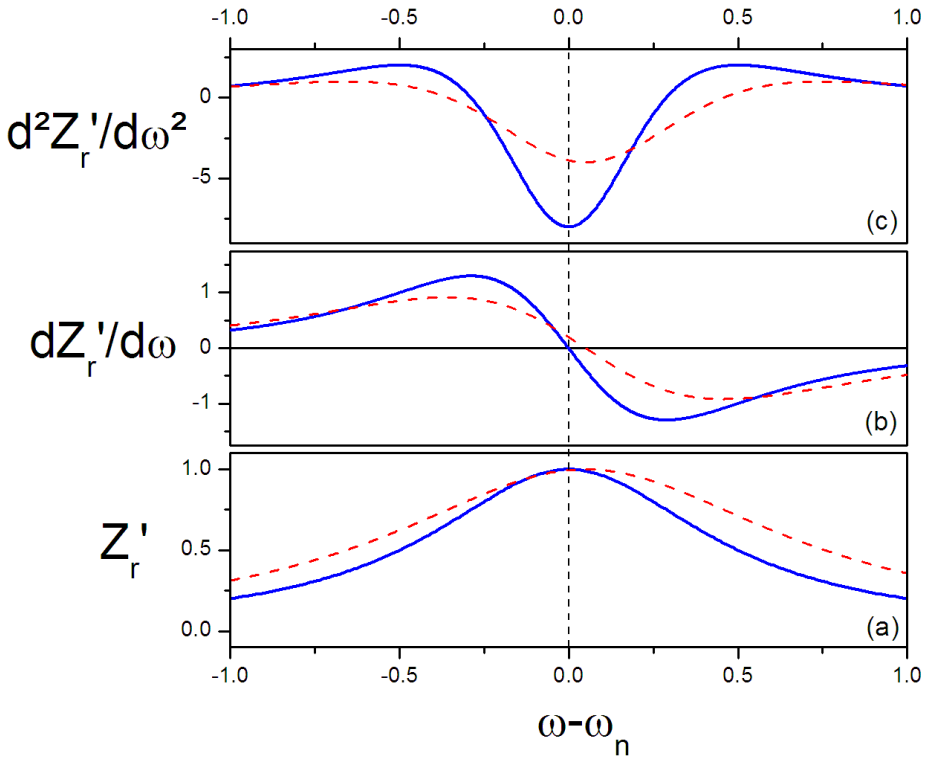

Figure 5.5: *Effect of a resonance frequency shift and quality factor variation in the (a) real part of the resonator impedance $Z_r'(\omega)$, in the (b) first derivative of $Z_r'(\omega)$ and in the (c) second derivative of $Z_r'(\omega)$.*

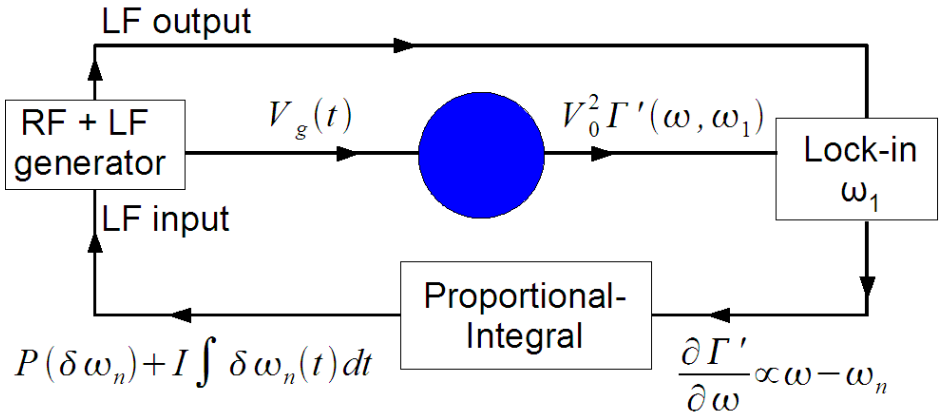

Figure 5.6: *Retro-action circuit that permits to the generator to follow the resonance frequency changes caused by the magnetic flux into the SQUID. The blue circle corresponds to the circuit detailed in Fig. 5.4*

Chapter 6

Conclusions

In this thesis we have addressed the dynamics of Superconductor/Normal metal/Superconductor long junctions.
A wide range of samples were used, in which we varied the superconducting and normal metals, the length and geometry of the normal wire, and the N-S interfaces.
In order to explore the dynamics of such junctions, we have imposed a high frequency excitation in two different ways. In a first set of experiments we have modulated the bias current, and observed the sharp transitions between the superconducting and the normal state in the V(I) characteristic, while in a second set of experiments we have modulated the phase difference across an isolated junction, and observed the current response. In the first case, the measurement was in a strongly non-linear regime, while in the second case we explored both the linear and the non-linear response regimes by varying the phase modulation amplitude.
The aim of these experiments is to understand which microscopic mechanisms govern the dynamics of a long coherent normal wire in which superconducting correlations penetrate completely. A precious insight can be gained by studying the relevant time scales. Many time-scales may indeed play a role: the inelastic scattering times (the electron-electron time τ_{e-e} and the electron-phonon time τ_{e-ph}), the diffusion time τ_D, the dephasing time τ_φ...

6.1 Relaxation times

6.1.1 Inelastic scattering time

In both experiments, two relevant times emerge: the inelastic relaxation time and the diffusion time.
In the current-biased experiment, we observe that the junction is at equilibrium and follows adiabatically the excitation for frequencies below the electron-phonon rate (the inelastic rate at the measurement temperatures). This is indirectly confirmed by the phase-biased experiment, where at frequencies above the inelastic rate, but lower than the other characteristic rates, the junction is already out-of-equilibrium.
When we impose a small amplitude phase modulation faster than the inelastic rate, the current response develops an imaginary, dissipative component. Thus the current, far from being non-dissipative and sinusoidal with the phase, as in the equilibrium case, has now a dissipative contribution and depends non-sinusoidally on the phase.
We can understand the large harmonic content in the current-phase relation at high frequency by considering that the occupation of the Andreev levels is frozen. Indeed, when varying the phase, the energy of Andreev levels change, and quasiparticles relax to the new Fermi distribution. But when $f > \tau_{in}^{-1}$ they have no time to relax, and the distribution remains frozen at its dc value.
Thus, a frequency larger than the inelastic scattering rate prevents the energy relaxation, and results in an out-of-equilibrium, modulation-independent Andreev states population.
A similar effect is also observed in the current-biased experiment. In this case, when the frequency exceeds the inelastic scattering rate, the switching from the normal to the superconducting state is strongly affected. This can be attributed to a global heating of the junction. Indeed, when switching to the normal state, the junction becomes resistive and is heated by the Joule power. If the bias current, and thus the injected Joule power, varies faster than the inelastic scattering rate, quasiparticles cannot evacuate the excess heat fast enough to be able to switch back in the superconducting state when the current becomes lower than the equilibrium retrapping current.
Thus, when the frequency is larger than the inelastic scattering rate, because of the lack of energy relaxation, the distribution function is a Fermi function with an effective temperature higher than the bath temperature.

6.1.2 Diffusion time

A second important time scale is the diffusion time. This 'macroscopic' time is associated with the length of the normal wire, since it is defined as the time quasiparticles take to cross the junction.
We observe in the current-biased experiment that for frequencies larger than the diffusion rate, the critical current is strongly modified, while the retrapping current is completely unaffected. Indeed, the critical current is markedly increased in the whole range of temperatures studied.
A similar effect is observed in superconducting bridges, but only for temperatures near the superconductor's transition temperature. The enhancement being due in that case to a non-equilibrium quasiparticles distribution, the characteristic frequency is given by the inelastic rate.
In the case of long SNS junctions the situation is more complicated, as microwaves generate not only a non-equilibrium quasiparticles distribution, but also modify the density of states. The amplitude of the minigap in the normal wire, proportional to the diffusion rate, sets then the critical frequency for the enhancement.
Excitations faster than the diffusion rate have also a strong effect in the phase-biased experiment: the current response decays indeed on the diffusion time-scale. This relaxation time could then be interpreted as the response time of the Andreev levels. Indeed, Andreev levels are the eigenstates of the system for a given phase difference across the wire. The information about the phase boundaries conditions, however, is not instantaneously transmitted, since it takes a time τ_D to diffuse across the wire. This delay, the response time of Andreev levels, could be responsible for the current relaxation.

6.2 Hysteresis

A topic which profited from the two different experiments in parallel is the interpretation of the hysteresis in V(I) curves.
We examined two possibilities for the hysteresis of the switching current between the normal and the superconducting state: heating effects and phase dynamics.

6.2.1 Heating

We suppose in this case that the junction is intrinsically non-hysteretic. The retrapping current is then equal to the critical current.
When the sample switches from the superconducting to the normal state,

the resistance goes abruptly from zero to a finite value, the sample dissipates a Joule power $P_J = R\,I^2$ and its electronic temperature T_e increases. The Joule power can be evacuated to the substrate by phonon emission.
Usually, the phonon cooling power is modeled as $P = \Sigma\,V\,(T_e^5 - T_{ph}^5)$, where T_{ph} is the phonon temperature, V the normal wire volume and Σ a material dependent parameter.
By equating Joule power and phonon cooling power, the electronic temperature is deduced. Using the experimental $I_c(T)$ curve, one can then find $I_r = I_c(T_e)$.
This simple model reproduces well the nearly constant temperature dependence of I_r, but predicts retrapping current amplitudes too small by a factor two compared to the measured ones.
We then examine the case of a sixth power law for the phonons cooling power: $P = \Sigma'\,V\,(T_e^6 - T_{ph}^6)$. Such a law was indeed first predicted by A. Schmid, and then measured by J. T. Karvonen et al. in 57 nm thick Au wires and Cu wires thinner than 140 nm.
Recalculating the temperature dependence of the retrapping current within this model leads to a very good agreement with the experimental $I_r(T)$ in samples SQ-NbAu-L, SQ-NbAu-S and WAu-Sq. Moreover, the fitting parameters Σ' are consistent with those found by J. T. Karvonen.
However, when trying to fit the retrapping current dependence in samples NbAl-L and NbAl-S, neither the fifth power law nor the sixth power law give the good temperature dependence, I_r decreasing slower than predicted.
In conclusion, the heating model is satisfactory for the Nb-Au SQUIDs and the W-Au wires, if we accept the unusual sixth power law. It is not clear though why measurements of the sixth power law are so rare in standard metal films.
In the case of Nb-Al wires, the heating model does not work. This is also confirmed by the retrapping current behavior, when the sample is irradiated by microwaves with $f > \tau_D^{-1}$. Indeed, while the critical current is strongly enhanced over the whole temperature range, the retrapping current is completely unaffected. Whereas if the relation $I_r = I_c(T_e)$ were valid, the retrapping current should also be enhanced by the excitation. It is thus necessary to consider a different explanation for hysteresis in Nb-Al samples.

6.2.2 Phase dynamics

SIS junctions with a high quality factor present an hysteresis which is the result of phase dynamics. The phase, fixed in the superconducting state, turns in the resistive state at a velocity proportional to the voltage. To switch from the normal to the superconducting state, the phase has to decrease its

velocity. The phase deceleration is related to the environment properties through the RC time and the plasma frequency ω_p: for a large quality factor $Q = RC\,\omega_p$, the deceleration is small and the hysteresis is large.
Since SIS and SNS junctions often behave similarly, we can try to apply this model also to SNS junctions. To do this, we have to replace the RC time and the plasma frequency with the proper characteristic times in SNS junctions. We find that it is possible to explain the hysteresis in Nb-Al samples when replacing the RC time with the electron-phonon time τ_{e-ph} and the plasma frequency ω_p with a temperature-independent, size-dependent frequency proportional to the diffusion rate τ_D^{-1}.
Unfortunately, we could not check this hypothesis in the other samples, since we lacked an independent measurement of the electron-phonon time.

6.2.3 Intrinsic hysteresis in presence of heating

Finally, the hysteresis could result from a combination of the two phenomena described above: SNS junctions could be intrinsically hysteretic, but the hysteresis could be increased by heating effects.
In the case of Nb-Al samples, then, the hysteresis we observe would be mostly intrinsic, and thus explainable with the phase dynamics model controlled by the two times τ_{e-ph} and τ_D. At the measurement temperatures, between 1.5 K and 4 K, the heating would be indeed a small effect.
In the case of Nb-Au or W-Au samples, which in contrast were measured between 50 mK and 1 K, the main effect would be due to heating, even in the presence of an intrinsic hysteresis. We confirmed with numerical simulations that very similar hysteresis are obtained at low temperature from heating only, or from heating added to an intrinsic hysteresis.

Appendix A

SQUID Phase-Flux relation

A.1 Meissner effect

The macroscopic wave function of a superconducting ring is $\psi = \sqrt{n_s}\, e^{i\,\theta(\vec{r})}$. The current density $\vec{j}$ in the ring is:

$$\vec{j} = 2e\,\psi^*\,\vec{v}\,\psi = \frac{2e\,n_s}{2m}\,(\hbar\vec{\nabla}\theta - 2e\vec{A}) \tag{A.1}$$

From eq. A.1 we derive the second London equation:

$$\vec{\nabla} \times \vec{j} = -\frac{(2e)^2\,n_s}{2m}\,\vec{B} \tag{A.2}$$

Using Maxwell equation $\vec{\nabla} \times \vec{B} = \mu_0\,\vec{j}$, we find

$$\vec{\nabla} \times (\vec{\nabla} \times \vec{B}) = \mu_0 \vec{\nabla} \times \vec{j} = -\frac{(2e)^2\,n_s}{2m}\,\vec{B} = -\frac{1}{\lambda_L^2}\,\vec{B} \tag{A.3}$$

and

$$\vec{\nabla} \times (\vec{\nabla} \times \vec{B}) = -\vec{\nabla}^2\vec{B} = -\frac{1}{\lambda_L^2}\vec{B} \tag{A.4}$$

The magnetic field penetrates then in the superconductor only over a length λ_L, called the London penetration length.

A.2 SIS SQUID

We now interrupt the superconducting ring with a thin insulating layer. If the ring is wide enough, far from the ring borders the magnetic field cannot penetrate, and $\vec{B}$ and $\vec{j}$ are zero. Then, from eq. A.1:

$$\hbar\vec{\nabla}\theta = 2e\vec{A} \tag{A.5}$$

We now integrate over a path far from the borders (see Fig. A.1). We can neglect the field in the insulating layer, since the layer is very thin. We then obtain:

$$\int_1^2 \vec{A} \cdot d\vec{l} \approx \oint \vec{A} \cdot d\vec{l} = \Phi \tag{A.6}$$

$$\int_1^2 \vec{\nabla}\theta \cdot d\vec{l} = \theta_2 - \theta_1 \tag{A.7}$$

So that the relation between the phase difference δ and the magnetic flux in the ring Φ is

$$\delta = \theta_1 - \theta_2 = -\frac{2e}{\hbar}\Phi = -2\pi \frac{\Phi}{\Phi_0} \tag{A.8}$$

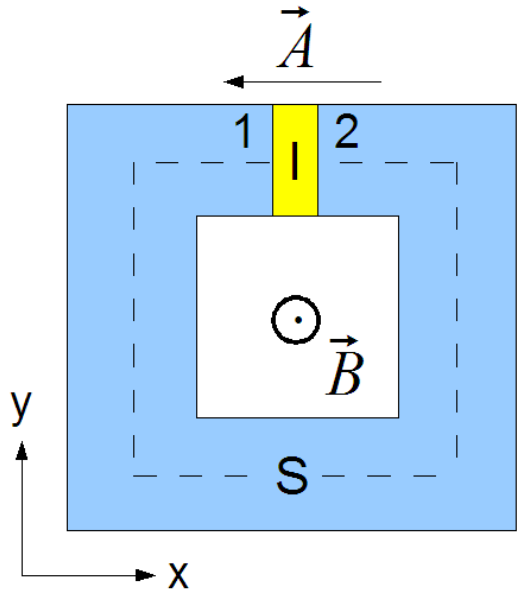

Figure A.1: *Schematics of an SIS ring in presence of a magnetic field.*

Appendix B

Runge Kutta method

Problems involving ordinary differential equations of order N can be reduced to the study of a system of N first-order differential equations of the type:

$$\frac{dy_i(x)}{dx} = f_i(x, y_1 ... y_N) \tag{B.1}$$

In initial value problems, the y_i values are known at a initial point x_0, and the aim is to find the y_i at a final point x_f.
The simplest solution is to define small discrete steps Δx and Δy_i, and to solve at the first order the N equations. This is called the Euler method.

$$x_{n+1} = x_n + \Delta x = x_n + h \tag{B.2}$$

$$y_i(x_n + h) = y_i(x_n) + h\, f_i(x_n, y_i(x_n)) + O(h^2) \tag{B.3}$$

However, the accuracy of this method is moderate.
Runge-Kutta methods are based on the Euler method, but they use intermediate steps to evaluate the derivative one or more times in the interval Δx, so to decrease the error [46].
We demonstrate here the second-order, or midpoint, Runge-Kutta method, which has an error $O(h^3)$.
In the following we neglect the index i in y_i and f_i for simplicity.
As we have seen, at the first order we have:

$$y(x_n + h) = y(x_n) + h\, f(x_n, y(x_n)) \tag{B.4}$$

Instead of using the derivative evaluated in x_n, we use to determine $y(x_n + h)$ the derivative of the middlepoint $x_n + h/2$:

$$y(x_n + \frac{h}{2}) = y(x_n) + \frac{h}{2}\, f(x_n, y(x_n)) + \frac{h^2}{8}\, f'(x_n, y(x_n)) + O(h^3) \tag{B.5}$$

and

$$y(x_n+h) = y(x_n+\frac{h}{2})+\frac{h}{2}\,f(x_n+\frac{h}{2}, y(x_n+\frac{h}{2}))+\frac{h^2}{8}\,f'(x_n+\frac{h}{2}, y(x_n+\frac{h}{2}))+O(h^3) \tag{B.6}$$

Developping

$$f(x_n, y_n) = f(x_n + \frac{h}{2}, y(x_n + \frac{h}{2})) - \frac{h}{2}f'(x_n + \frac{h}{2}, y(x_n + \frac{h}{2})) \tag{B.7}$$

we finally obtain:

$$y(x_n + h) = y(x_n) + h\,f(x_n + \frac{h}{2}, y(x_n + \frac{h}{2})) + O(h^3) \tag{B.8}$$

When increasing the number of intermediate evaluations, the error decreases. The most used Runge-Kutta method is the fourth-order one, which has an error $O(h^5)$.

Appendix C

Resonance dependence on temperature and magnetic field

To describe the resonance frequency dependence on temperature and magnetic field, we model the superconducting resonator by a circuit formed by the geometrical inductance of the line $\mathcal{L}$ and the capacitance between the two wires C. When applying a rf excitation, a dissipative density of current, generated by the ac electric field, adds to the non-dissipative one. In this case a surface resistance appears; its magnitude depends on the normal electron density n_n, on the penetration depth λ_L and on the excitation frequency f [62]:

$$R_s \propto n_n \lambda_L^3 f^2 \tag{C.1}$$

n_n and λ_L depend on the temperature as $n_n \sim e^{-\Delta/k_B T}$ and $\lambda_L \sim 1/\sqrt{1-e^{-\Delta/k_B T}}$, where Δ is the superconductor gap.
For $H << H_c$, where H_c is the critical magnetic field of Nb, λ_L and n_n depend linearly on the magnetic field.
If we add this resistance in series with the inductance, the resonance frequency changes:

$$\frac{f}{f_0} = \sqrt{1 - \frac{C}{\mathcal{L}} R^2} \tag{C.2}$$

so that the resonance frequency decreases parabolically when the resistance is increased by the temperature (bigger n_n), by the magnetic field (bigger λ_L) or by the frequency.

The quality factor is inversely proportional to the dissipation. At low temperature, the most important source of dissipation affecting the quality factor is the presence in the substrate of magnetic impurities: substrates of sapphire or silicon dioxide were thus chosen because of their low impurities

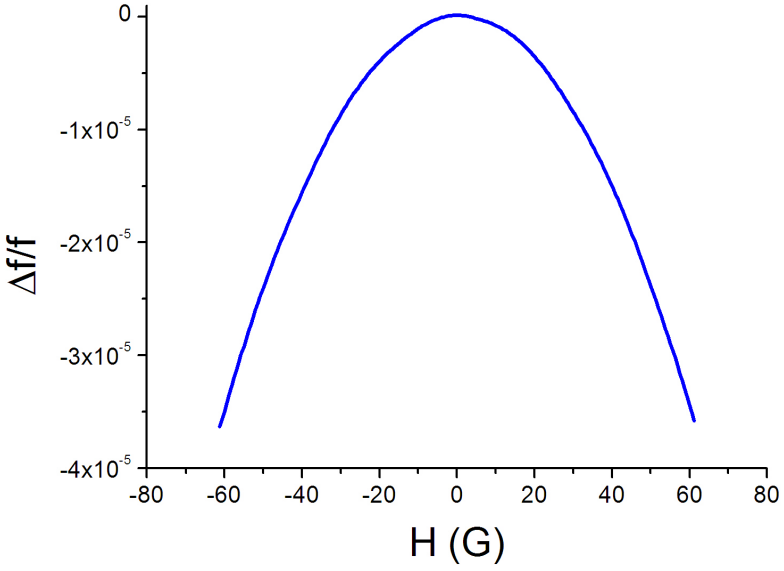

Figure C.1: *Normalised variation of the first resonance frequency as a function of the magnetic field at T=50mK*

content.
These impurities are stable in our magnetic field and temperature range. The Q-factor, however, depends on frequency, temperature and magnetic field. This can be explained as due to the rf biasing of the resonator. As we have seen before, the high frequency bias of the resonator produces a surface resistance R_s, that increases with the frequency, the temperature and the magnetic field. We then expect for 1/Q a dependence similar to that of R_s.

Appendix D

Self inductance and mutual inductance calculation

D.1 AC ring self inductance

We have calculated the ring self inductance from the following formula, describing the high frequency self inductance of a rectangular ring with sides a and b of wire radius r:

$$\mathcal{L} = \frac{\mu_0}{2\pi}\left[2a\,ln\left(\frac{2a}{r}\right) + 2b\,ln\left(\frac{2b}{r}\right) - 4(a+b)\right. \tag{D.1}$$

$$\left. + 4\sqrt{a^2+b^2} - 2a\,sinh^{-1}\left(\frac{a}{b}\right) - 2b\,sinh^{-1}\left(\frac{b}{a}\right)\right] \tag{D.2}$$

The ring is not exactly a rectangle, but we can find two effective sides a and b by forcing the effective rectangle to have the same surface and perimeter of our ring. In this way we find:

- SQAC-WAu-1: $a = 37.6\,\mu m$ and $b = 2.485\,\mu m$
- SQAC-WAu-2: $a = 13.42\,\mu m$ and $b = 2.578\,\mu m$

We can note that the long side a is practically equal to the part of the resonator line included in the ring: $37.4\,\mu m$ for SQAC-WAu-1 and $12.9\,\mu m$ for SQAC-WAu-2.

The radius of the wires composing the SQUID is in our case not uniform: one long side a is a part of the Nb resonator, and has an approximate radius $r_{Nb} \sim 1.35\mu m$, while the other three sides of the rectangle are W wires with an approximate radius of $r_W \sim 50nm$. To take this difference of thickness

in account, we decompose the term $2a\,ln(2a/r)$ corresponding to two equal wires in two:

$$2a\,ln\frac{2a}{r} \longleftrightarrow a\,ln\frac{2a}{r_W} + a\,ln\frac{2a}{r_{Nb}} \tag{D.3}$$

The results of this calculation are: for SQAC-WAu-1, $\mathcal{L} = 36.5pH$ and for SQAC-WAu-2 $\mathcal{L} = 15pH$.

D.2 AC ring-resonator mutual inductance

To calculate the mutual inductance between the ring and the resonator line, we used the expression:

$$\mathcal{M} = \frac{\mu_0}{2\pi}\,a\,ln\left(\frac{2d+b}{2d-b}\right) \tag{D.4}$$

valid in the case of a ring isolated from the current line. a is the length of the side facing the resonator line, b is the other side and d is the center-to-center distance between the ring and the line.

If we let the distance between the ring and the resonator go to zero, and

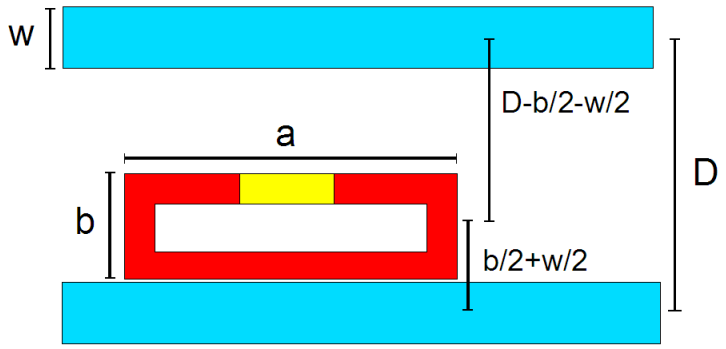

Figure D.1: *Schematic of the system SQUID-resonator for the mutual inductance calculation.*

if we take into account the contribution of the two lines, above (first term) and below (second term) the ring, we obtain:

$$\mathcal{M} = \frac{\mu_0}{2\pi}\,a\,ln\left(\frac{2b+w}{w}\right) + \frac{\mu_0}{2\pi}\,a\,ln\left(\frac{2D-w}{2D-w-2b}\right) \tag{D.5}$$

where w is the line width and D is the distance between the two lines (see Fig. D.1).

sample	$\mathcal{L}$ (pH)	$\mathcal{M}$ (pH)	$\mathcal{L}'$ (pH)
SQAC-WAu-1	36.5	14.4	22.5
SQAC-WAu-2	15	5.3	5

Table D.1: *Summary of samples SQAC-WAu-1 and SQAC-WAu-2 inductances: self inductance $\mathcal{L}$, mutual inductance $\mathcal{M}$ with the resonator line and self inductance of the resonator part facing the ring $\mathcal{L}'$.*

We obtain for sample SQAC-WAu-1 $\mathcal{M} = 14.4\,pH$ and for sample SQAC-WAu-2 $\mathcal{M} = 5.3\,pH$.

The mutual inductance $\mathcal{L}'$ of a SQUID directly connected to the resonator is given by the self inductance of the resonator part included in the SQUID (see sec. 5.2). For sample SQAC-WAu-1 we find $\mathcal{L}' = 22.5pH$ and for sample SQAC-WAu-2 is $\mathcal{L}' = 5pH$.
Because of the complicated shape of our ring, however, the uncertainty in our estimation of the inductance is roughly 30%.

Remerciements

Je voudrais tout d'abord remercier Bertrand Reulet et Hélène Bouchiat pour avoir été mes directeurs de thèse: j'ai beaucoup profité de toutes mes discussions avec eux, et leur enthousiasme a été contagieux!
Merci Betrand pour tes explications toujours très claires, pour tous tes encouragement au cours de ces années, pour m'avoir laissé me débrouiller toute seule tout en étant toujours là pour me donner un coup de main! Grâce à cette atmosphère sereine et détendue mais pleine de discussions scientifiques, j'ai vraiment eu plaisir à travailler!
Merci Hélène pour les nombreuses discussions avec toi, dans lesquelles il y avait toujours tellement d'idées nouvelles et de suggestions que même après des jours je continuais à comprendre ce que tu voulais dire, merci pour ton attitude tolérante et ton ouverture d'esprit (dans une mémorable discussion avec Sophie, tu défendais la possibilité pour moi d'être camionneuse si je le souhaitais!), et pour ta présence tout au long des expériences et de la compréhension des données!
Ensuite, je voudrais remercier Sophie Guéron et Meydi Ferrier, qui ont été pour moi aussi des directeurs de thèse.
Merci Sophie pour avoir été toujours là pour reprendre les modèles et arguments avec calme, les examiner en détail et bien les comprendre, toujours avec patience et bonne humeur! Merci aussi de tout ton aide en dehors du labo, d'avoir été mon garant en signant un contrat semblable à un pacte avec le diable, de m'avoir passé ta vieille machine à laver (et surtout à avoir pensé pour son transport à un chariot!!!)...
Merci Meydi pour avoir toujours compris où je ne comprenais pas, et avoir souvent ajouté une toute petite précision qui faisait la lumière dans mon esprit, et merci aussi pour ta disponibilité et ta patience!
En général, je voudrais remercier les groupes NS2 et MESO pour la bonne ambiance, le chocolat toujours présent, les déjeuners sur l'herbe, et les nombreuses discussions, scientifiques et non, qui ont ponctué les dernières 4 années.
Merci Marco pour ton franc-parler, pour t'être toujours intéressé à tout ar-

gument scientifique qui soit ou pas en relation avec ta recherche, et pour avoir compris cet étrange mélange d'italien, français et de mots dérivé d'une langue et passés sans scrupules dans l'autre qu'il m'arrive souvent de parler!
Merci Julien d'avoir été toujours prêt à m'aider, et d'avoir été un vrai puits d'informations pendant les discussions du café: j'ai vraiment beaucoup appris!
Merci Ivana pour avoir été une excellente copine de bureau, prête à discuter de science, mais aussi de cinéma, de vacances au bord de la mer et de chocolat!
Merci Richard, d'avoir gardé ton calme et ta bonne humeur tout au long de ces 4 années, en répondant toujours sans surprise (manifeste) aux questions les plus disparates que je t'ai posé à l'imprévu!
Merci Lionel de m'avoir aidé au début de ma thèse en me passant ton expérience!
Merci Charis, pour m'avoir aidé pendant la préparation de la soutenance avec tes conseils et tes rires tonitruants!
Merci Claudia, Julien, Miguel, Sandrine et Alik pour les pauses café toujours agrémentés de sucreries internationales!
Merci à Frank Fortuna, Alik Kasumov et Laurence Ferlazzo pour votre aide avec la fabrication des échantillons: ça aurait été dur sans vous! Merci aussi à Marie-France Mariotto, Marie-France Cozic, Alain Clément, Sophie Tourlet, Michel Heritier, Sylvie Falcinelli, Jean-Luc Picot, Martine, aux services informatique et électronique, qui m'ont toujours beaucoup et promptement aidé.
Je voudrais aussi remercier Olivier Buisson et Christophe Strunk d'avoir accepté d'être mes rapporteurs: les discussions avec eux ont été très fructueuses, me donnant envie de continuer, plutôt que finir ma thèse!
Merci aussi aux membres de mon jury: Frank Hekking, le président, qui a conduit avec humour la soutenance, Alfredo Levy-Yeyati et Hugues Pothier, avec qui j'espère je pourrai continuer à discuter dans le futur.
Finalement, je voudrais remercier Alexei de toujours avoir été là, même quand il était au Japon :) Merci Alexei d'avoir su avec un gros rire dissiper mes préoccupations, me rassurer et m'encourager! Vraiment merci! Infine, vorrei ringraziare tutta la mia famiglia, i miei genitori, Filippo, i miei zii, le mie cugine, mia nonna e la mia prozia, che mi sono stati vicini, che mi hanno aiutato, spronato e tranquillizzato durante tutti questi anni.
Grazie soprattutto papà e mamma, senza di voi tutto sarebbe stato molto più difficile. E grazie per l'eccellente rinfresco che avete organizzato!
Grazie Fili di aver riascoltato 50 volte la mia presentazione senza (troppo) protestare! Ricambierò!

Bibliography

[1] Vinay Ambegaokar and B. I. Halperin. *Phys. Rev. Lett.*, **22**, 25, 1969.

[2] Nathan Argaman. *Superlattices and microstructures*, **25**, 861-875, 1999.

[3] S. N. Artemenko, A. F. Volkov, and A.V. Zaitsev. *Sov. Phys. JETP*, **49**, 924, 1979.

[4] Frank Balestro. *Dynamique quantique d'un SQUID-DC.* PhD thesis, Université Joseph Fourier - Grenoble I, 2003.

[5] Antonio Barone and Gianfranco Paternó. *Physics and Applications of the Josephson effect.* John Wiley and Sons, 1982.

[6] Ya. M. Blanter. *Phys. Rev. B*, **54**, 18, 1996.

[7] Jérôme Cayssol. *Etudes de propriéttes thermodynamiques de structures hybrides métal normal/métal ferromagnétique-supraconducteur.* PhD thesis, Université de Paris-7 Jussieu, 2003.

[8] A.D. Chepelianskii and H. Bouchiat. *Phys. Rev. Lett.*, **102**, 086810, 2009.

[9] J. Clarke. *Phys. Rev. B*, **4**, 2963, 1971.

[10] John Clarke and James L. Paterson. *Appl. Phys. Lett.*, **19**, 496, 1971.

[11] H. Courtois, Ph. Gandit, D. Mailly, and B. Pannetier. *Phys. Rev. Lett.*, **76**, 130, 1996.

[12] R.A Craven, G. A. Thomas, and R. D. Parks. *Phys. Rev. B*, **4**, 2185, 1971.

[13] J.C. Cuevas and F.S. Bergeret. *Phys. Rev. Lett.*, **99**, 217002, 2007.

[14] E. D. Dahlberg, R. L. Orbach, and I. Schuller. *J. Low Temp. Phys.*, **36**, 367, 1979.

[15] A. H. Dayem and J. J. Wiegand. *Phys. Rev. Lett.*, **155**, 419, 1976.

[16] R. Deblock, Y. Noat, B. Reulet, H. Bouchiat, and D. Mailly. *Phys. Rev. B*, **65**, 075301, 2002.

[17] P. Dubos, H. Courtois, O. Buisson, and B. Pannetier. *Phys. Rev. Lett.*, **87**, 206801, 2001.

[18] P. Dubos, H. Courtois, B. Pannetier, F. K.Wilhelm, A. D. Zaikin, and G. Schön. *Phys. Rev. B*, **63**, 064502, 2001.

[19] Pascal Dubos. *Transport électronique dans des nanojonctions supraconducteur - métal normal - supraconducteur*. PhD thesis, Université Joseph Fourier - Grenoble I, 2000.

[20] A. F. G. Wyatt et al. *Phys. Rev. Lett.*, **16**, 1166, 1966.

[21] H. Courtois et al. *Phys. Rev. Lett.*, **101**, 067002, 2008.

[22] J. M. Warlaumont et al. *Phys. Rev. Lett.*, **43**, 169, 1979.

[23] L. Angers et al. *Phys. Rev. B*, **77**, 165408, 2008.

[24] P. Dubos et al. *J. Vac. Sci. Technol.*, **18**, 122, 2000.

[25] M. Fuechsle, J. Bentner, D.A. Ryndyk, M. Reinwald, W. Wegscheider, and C. Strunk. *Phys. Rev. Lett.*, **102**, 1217001, 2009.

[26] Anupam Garg. *Phys. Rev. B*, **51**, 21, 1995.

[27] J. T. Hall, L. B. Holdeman, and Jr. R. J. Soulen. *Phys. Rev. Lett.*, **45**, 1011, 1980.

[28] J.C. Hammer, J.C. Cuevas, F.S. Bergeret, and W. Belzig. *Phys. Rev. B*, **76**, 6, 2007.

[29] J. P. Heida, B. J. van Wees, T. M. Klapwijk, and G. Borghs. *Phys. Rev. B*, **57**, 10, 1998.

[30] Tero T. Heikkilä, Jani Särkkä, and Frank K. Wilhelm. *Phys. Rev. B*, **66**, 184513, 2002.

[31] B. I. Ivlev, S. G. Lisitsyn, and G. M. Eliashberg. *J. Low Temp. Phys.*, **10**, 449, 1973.

[32] B. D. Josephson. *Phys. Lett.*, **1**, 251, 1962.

[33] J. T. Karvonen, L. J. Taskinen, and I. J. Maasilta. *Phys. Rev. B*, **72**, 012302, 2005.

[34] A. Yu. Kasumov, K. Tsukagoshi, M. Kawamura, T. Kobayashi, Y. Aoyagi, K. Senba, T. Kodama, H. Nishikawa, I. Ikemoto, K. Kikuchi, V. T. Volkov, Yu. A. Kasumov, R. Deblock, S. Guéron, and H. Bouchiat. *Phys. Rev. B*, **72**, 033414, 2005.

[35] T. M. Klapwijk, J. N. van der Bergh, and J. E. Mooij. *J. Low Temp. Phys.*, **26**, 385, 1977.

[36] T. Kommers and J. Clarke. *Phys. Rev. Lett.*, **38**, 1091, 1977.

[37] H. le Sueur, P. Joyez, H. Pothier, C. Urbina, and D. Esteve. *Phys. Rev. Lett.*, **100**, 197002, 2008.

[38] V. Lefevre-Seguin, E. Turlot, C. Urbina, D. Estève, and M. H. Devoret. *Phys. Rev. B*, 46, 1992.

[39] Laurent-Patrick Lévy. *Magnétisme et supraconductivité*. CNRS editions, 1997.

[40] K. K. Likharev. *Dynamics of Josephson Junctions and Circuits*. Gordon and Breach, 1991.

[41] Gilles Montambaux. *cond-mat.mes-hall*, 07070411v1, 2007.

[42] J. E. Mooij and T. M. Klapwijk. *Phys. Rev. B*, **27**, 3054, 1983.

[43] H. A. Notarys, M. L. Yu, and J. E. Mercereau. *Phys. Rev. Lett.*, **30**, 743, 1973.

[44] V. T. Petrashov, V. N. Antonov, P. Delsing, and T. Claeson. *Phys. Rev. Lett.*, **74**, 5268, 1995.

[45] Frédéric Pierre. *Interactions électron-électron dans les fils mésoscopiques*. PhD thesis, Université Paris 6, 2000.

[46] W. H. Press, S. A. Teukolsky, W. T. Wetterling, and B. P. Flannery. *Numerical Recipes in C - The Art of Scientific Computing*. Cambridge University Press, 1992.

[47] B. Reulet, M. Ramin, H. Bouchiat, and D. Mailly. *Phys. Rev. Lett.*, **75**, 124, 1995.

[48] Bertrand Reulet. *Susceptibilité magnétique orbitale et conductance AC d'anneaux mésoscopiques isolés*. PhD thesis, Université Paris-Sud, 2004.

[49] M. L. Roukes, M. R. Freeman, R. S. Germain, R. C. Richardson, and M. B. Ketchen. *Phys. Rev. Lett.*, **55**, 4, 1985.

[50] J. M. Rowell. *Phys. Lett.*, **30**, 5, 1973.

[51] P. Santhanam and D. E. Prober. *Phys. Rev. B*, **29**, 3733, 1984.

[52] A. Sergeev and V. Mitin. *Phys. Rev. B*, **61**, 6041, 2000.

[53] Minghao Shen. *Low Temperature Electron-Phonon Interaction in Disordered Metal Thin Films and Applications to Fast, Sensitive Sub-Millimeter Photon Sources and Detectors*. PhD thesis, Yale University, 2005.

[54] Y. Song. *J. Appl. Phys.*, **47**, 2651, 1976.

[55] C. D. Tesche and J. Clarke. *J. Low Temp. Phys.*, 29, 1977.

[56] Michael Tinkham. *Introduction to Superconductivity*. McGraw-Hill, 1996.

[57] P. van den Hamer, T.M. Klapwijk, and J. E. Mooij. *J. Low Temp. Phys.*, **54**, 607, 1984.

[58] Pauli Virtanen, Tero T. Heikkilä, F. Sebastián Bergeret, and Juan Carlos Cuevas. *arXiv*, 1001.5149v1, 2010.

[59] J. Warlaumont, J. C. Brown, and R. A. Buhrman. *Appl. Phys. Lett.*, **34**, 415, 1979.

[60] T.-C. Wei, D. Pekker, A. Rogachev, A. Bezryadin, and P. Goldbart. *Europhys. Lett.*, **75**, 943-949, 2006.

[61] F. C. Wellstood, C. Urbina, and John Clarke. *Phys. Rev. B*, **49**, 9, 1994.

[62] Shu-Ang Zhou. *Electrodynamics of Solids and Microwave Superconductivity*. John Wiley and Sons, 1999.